THE UNIVERSITY OF NOTTINGHAM

SCHOOL OF ELECTRICAL AND ELECTRONIC ENGINEERING

Developments in Time-Reversal of Electromagnetic Fields using the Transmission-Line Modelling Method

by

Ian Scott, BSc (Hons.)

Thesis submitted to the University of Nottingham
for the degree of Doctor of Philosophy, September 2009

Developments in Time-Reversal of Electromagnetic Fields using the Transmission-Line Modelling Method

by

Ian Scott, BSc (Hons.)

Abstract

Inverse modelling methods are receiving significant interest, due to their simplicity and ease of use in the design of modern microwave components. This study investigates and further develops the technique of numerical time-reversal, in the context of automated component design, for modelling metal waveguide devices.

The thesis demonstrates that time-reversal methods suffer from temporal truncation, evanescent wave decay and significant computational resource requirements and will investigate different methods to solve these problems. In order to reduce the runtime, the use of Prony's method for temporal extrapolation of a discrete waveform is proposed. Lossy materials are investigated, with particular attention given to the loss of modal content from the reverse model due to material loss present in the forward phase of the time-reversal process.

The memory and time requirements of a successful time-reversal design simulation are significant. Temporal, spatial and modal filtering are used to minimise the computational demands of time-reversal. Further, in order to accelerate convergence of the time-reversal design process, a number of linear acceleration methods are developed, notably successive over relaxation, conjugate gradients and generalised minimal residual. A convergence acceleration factor of two is achieved.

It is shown that local evanescent content around optimised scattering elements is not always captured by the time-reversal process, and is dependant upon the component order, numerical sampling and machine precision. Internal mirrors are developed which capture the fast decaying fields around the metal features of a designed component and further increase the accuracy and speed of the time-reversal convergence. Their use for higher order component design is shown to be paramount in achieving convergence. Further, combined with the linear acceleration methods, the

capture of local evanescent content is shown to greatly improve the viability of the time-reversal technique to practical microwave component design.

The time-reversal methodology is implemented using the numerical transmission-line modelling (TLM) method for transverse magnetic polarisation in two-dimensions. A brief examination of the three-dimensional time-reversal using the symmetrical condensed TLM node is also given.

Publications by the author relevant to the thesis

1. Scott, I, Vukovic, A, Sewell, P, "Reducing Numerical Limitations in Time-Reversal Simulations", Proc. of the 4th International Association of Science and Technology for Development (IASTED) International Conf. on Antennas, Radar, and Wave Propagation, Montreal, Quebec, Canada, pp.186-191, May 30th - June 1st, 2007.

2. Scott, I, Vukovic, A, Sewell, P, "Time Reversal in Lossy Material; An Assessment", Proc. of the 22nd Progress in Electromagnetics Research Symposium (PIERS), Prague, Czech Republic, pp.535-539, 27-30th August, 2007, Selected for PIERS Online, Vol. 3, No. 8, pp.1259-1263, 2007.

3. Scott, I, Vukovic, A, Sewell, P, "Convergence Acceleration for Simulated Time-Reversal", The 10th International Workshop on Optimization and Inverse Problems in Electromagnetism (OIPE), Ilmenau, Germany, pp.182-183, 14-17th September, 2008.

4. Scott, I, Vukovic, A, Sewell, P, "Convergence Acceleration for Simulated Time-Reversal", The International Journal for Computation and Mathematics in Electrical and Electronic Engineering (COMPEL), Vol. 28, No. 5, pp. 1290-1297, 2009.

5. Scott, I, Vukovic, A, Sewell, P, "Reducing the Computational Requirements of Time-Reversal Device Optimizations", Accepted, International Journal of Numerical Modelling: Electronic Networks, Devices and Fields.

6. Scott, I, Vukovic, A, Sewell, P, “Krylov Acceleration Techniques for Time-Reversal Design Applications”, Accepted, IEEE Microwave Theory and Techniques.

7. Scott, I, Vukovic, A, Sewell, P, “Internal Mirrors for Time-Reversal Optimization”, Accepted, IET Microwaves, Antennas & Propagation.

8. Scott, I, Vukovic, A, Sewell, P, “Finite Precision Limitations in Numerical Time-Reversal Simulations”, Submitted, Electromagnetics.

Acknowledgements

I would like to express my gratitude to my supervisors, Dr Ana Vukovic and Professor Phillip Sewell for their support and guidance throughout the course of my research. I would also like to thank the many members of the George Green Institute for Electromagnetics Research (GGIEMR), who offered their guidance and expertise, especially during the early months of my time at GGIEMR.

I would also like to express deepest thanks to Dr Donard de Cogan from the University of East Anglia (UEA), for introducing me to numerical simulation for electromagnetics, and pointing me in the direction of the George Green Institute, without this guidance I would not be where I am today.

Finally, I would like to thank my family for their support throughout my time in academia.

This project was supported financially by the Engineering and Physical Sciences Research Council (EPSRC).

Contents

List of Symbols and Terms

The symbols and variables used throughout the thesis are as now defined, unless otherwise stated during use.

E, D	Electric field intensity and flux density
H, B	Magnetic field intensity and flux density
J, ρ	Electric current density and charge density
x, y, z	Rectangular coordinate system
X, Y, Z	Nodal mesh size
k	Temporal iteration number
k_0	Wave number
N	Total temporal iterations
Δl	Spatial sampling
Δt	Temporal sampling
κ	Iteration of time-reversal procedure
N_{TR}	Total number of time-reversal iterations
v	Velocity of propagation
α	Damping factor
T	Threshold
Z_0	Intrinsic impedance
Z_g	Waveguide impedance
$\varepsilon_0, \varepsilon_r$	Vacuum and relative permittivity
μ_0, μ_r	Vacuum and relative permeability
σ	Material loss, or half width of Gaussian pulse
ω	Angular frequency
γ	Propagation constant ($\alpha + j\beta$)
λ	Wavelength
n, m	Mode number
ϕ	Modal distribution
$\vec{a}$	Vector

$\underline{a}$	Array
$\underline{\underline{a}}$	Matrix
$\underline{a}(b)$	Array a indexed at b
$a(b)$	Function a at b
^	Denotes frequency domain
$\left\|\underline{a}\right\|_2$	Euclidean norm of the array a, $\sqrt{\sum_{b=0}^{B-1}\underline{a}(b)^2}$

1. Introduction

1.1 Introduction and Objective of the Thesis

The design of complex electromagnetic devices is an expensive and time consuming process and over the years predictive computer simulations have proved themselves a cost effective and essential tool for the designer. Of the many design methods available, broadly speaking, all are categorised into frequency or time domain and forward or inverse domain. Of the four categories each can then be further subdivided into analytical or numerical methods.

Forward domain implementations of analytical or numerical schemes such as integral equation or finite element [1.1], often require considerable knowledge of the component being designed to be used successfully. In comparison inverse implementations determine a component given a desired output, and hence require minimal input from the engineer. For this reason, with the addition of a numerical scheme, they can often lead to non-intuitive device configurations. Unfortunately, due to the need to use a numerical scheme to maintain generality; the inverse method often becomes intractable with even the simplest of components to design [1.2].

Inverse simulation, or time-reversal, forms the subject of this thesis. In [1.3] the problem of time-reversal around a spherical scatterer in an electromagnetic field was investigated using an analytical derivation.

Similarly to forward domain methods, inverse methods using a numerical scheme are more general in application. In [1.4] a similar problem was investigated using the finite differences numerical scheme, which shows the simplicity and generality associated with the numerical implementation. In this thesis numerical time-reversal is of primary focus.

Time-reversal, due to its perturbative nature [1.2], is particularly suited to electromagnetic component optimisation over a wide frequency bandwidth, for which forward-time methods such as genetic algorithms are often slow to converge [1.5].

The objective of the thesis is to implement and further develop the method of time-reversal for microwave component design.

1.1.1 Inverse Time-Domain Methods

Inverse time domain methods, or time-reversal methods, are developed from reversal of the temporal wave equation [1.6]. The majority of research using time-reversal is in the field of image reconstruction and component design. Historically, more successful work has been reported using time-reversal for imaging, for example source location in cluttered environments [1.7] [1.8] [1.9], than has in the field of microwave component design [1.2]. This is most likely attributed to the problems of intensive memory and limited spatial resolution when time-reversal is applied iteratively, factors that are not as prevalent when only a single time-reversal iteration is used.

1.1.1.1 Imaging

The research of Fink *et al.* [1.10] [1.11] [1.12] demonstrates time-reversal for acoustic frequencies. Namely, the derivation of time-reversal for acoustics, the derivation of a time-reversal-cavity, and the associated experimental setup and results are given. This is commonly attributed as the

first in depth investigation into time-reversal techniques, and is the underpinning theory of much work using time-reversal.

The time-reversal-cavity [1.10] is a surface of receivers enclosing the modelling space where time-reversal is performed. During the forward stage of the process, the receivers measure and store the incident field in time. In the reverse stage of the simulation, the receivers become sources, exciting the cavity with the forward field in reverse time order.

Time-reversal has been used for image reconstruction of cancerous tumours within healthy biological tissue in [1.8] [1.13] [1.14]. The data for the time-reversal algorithm was provided through the use of magnetic-resonance-imaging measurements. The finite difference time domain method [1.1] was used, from which it was shown that loss in the forward stage of a time-reversal simulation is modelled as gain in the reverse stage. The choice of numerical method limits the use of gain, since instability is created. In reported practical scenarios, time-reversal with loss is usually successful without the need to include gain, providing the loss is small within the frequency band of interest [1.15].

Time-reversal for image reconstruction is also ideally suited to non-destructive testing [1.16] [1.17], since the transmitting and receiving antenna array are non-intrusive for the material under test. To date, limited research has been performed in this area, probably due to the already established and successful ultrasonic methods [1.18].

The time-reversal method has also been used to locate a source, while an environment, composed of a number of dielectric rods, continually changed representing a cluttered medium [1.9] [1.19]. A similar scenario has been investigated in [1.7] for an urban environment. A further example of

imaging is found in [1.15], where novel configurations of the experimental setup are compared to improve the focusing upon the source location.

Imaging in anisotropic materials has also been investigated in [1.20] and [1.21]. Again, focusing was the primary concern. Theoretical analysis was completed into the properties of time-reversal, with a view to improving the focusing in the reverse stage. This is still an early area of research for time-reversal. The work of [1.22] and [1.23] develops the theory for time-reversal in random media.

The focusing of the time-reversal-cavity was reported in [1.24]. In the paper, the effect of limited sampling at the time-reversal-mirrors, was demonstrated to impact the directivity of the source. In this thesis, an investigation into focusing of the time-reversal-cavity at microwave frequencies is performed. Attention is given to the spreading of the recovered source in comparison to the input, a topic not covered by [1.24].

1.1.1.2 Component Design

The design of an electromagnetic component, whether through inverse or forward domain methods, usually requires multiple design iterations in order to optimise the components response. Generally, iterative design approaches perturb the object geometry from an initial estimate until the difference between its predicted and the specified response is minimised. For inverse design, the known desired response is used to determine the physical dimensions of the structure. This form often leads to non-intuitive designs. Inverse simulation techniques are complementary to evolutionary approaches [1.5] and are particularly suited to perturbative design.

The use of time-reversal as a component design technique, which is a primary area of this thesis, exploits much of the framework of the image reconstruction method. In the early work of Sorrentino *et al.* [1.25] [1.26]

time-reversal for microwave frequencies is proposed. Time-reversal iterates the design geometry by first extracting the part of the scattered field on the problem's bounding surface that is supported by sources on the surface of the object. If this field were applied as an excitation on the problem boundary then, given that Maxwell's equations are time reversible, the surface of the object can be identified from the resulting field distributions [1.25] [1.26]. However, if this extracted field is perturbed toward the desired distribution, then the corresponding perturbations in the object geometry will be identifiable in the time-reversal stage of the simulation. Clearly, an arbitrary change to the scattered field may be inconsistent with any real object geometry and this process must proceed perturbatively. Component design using time-reversal of electromagnetic waves has been numerically demonstrated using both the finite difference and transmission-line modelling (TLM) methods [1.13] [1.27].

In [1.27] it was shown the time-reversal method for component design requires significant memory and runtime, and at the time more complicated structures could not be designed due to this limitation. This thesis addresses issues regarding reduction of computer memory and runtime, using a variety of novel techniques, namely filtering at the time-reversal-mirrors to remove redundant information, and convergence acceleration through the use of stationary and non-stationary linear acceleration methods.

1.2 Outline of the Thesis

Chapter two begins by introducing the basic theory of electromagnetics used throughout the thesis. The wave equation for time-harmonic fields is derived from Maxwell's equations, Lorentz reciprocity is introduced in the concept of time-reversal and the inverse wave equation is derived. The definition of the Poynting vector is given and Green's functions are covered. The chapter concludes with the analytical derivation of the time-reversal process and demonstrates the reversal of a single source in a cavity.

Chapter three covers the numerical transmission-line modelling (TLM) method. The two-dimensional (2D) and three-dimensional (3D) TLM nodes for transverse magnetic propagation are derived, and the travelling wave form for numerical simulation is shown. The time-reversal-cavity for use with the TLM method is derived.

Chapter four begins the original research of this thesis by investigating the properties of the time-reversal-cavity with the TLM method for reconstruction of a point source. Prony's method to temporally extrapolate the inverse stage of the time-reversal algorithm is investigated. Lossy materials are covered, and Argand diagrams [1.28] are demonstrated as a novel method to predict the performance of the time-reversal algorithm in the presence of conductive material loss.

In Chapter five the general time-reversal procedure is shown for the design of microwave components. Time-reversal is applied to the design of band pass microwave filters, a waveguide bend and coupler. The convergence of the algorithm is controlled through the use of damping. Optimum threshold selection for parameter measurement is also shown.

Time-reversal using the conventional numerical algorithm of Chapter five requires excessive computational resources. Chapter six investigates the problem of memory limitations of time-reversal. Temporal and spatial filtering methods are proposed as a solution. The concept of a modal time-reversal-mirror for use with a time-reversal-cavity is introduced, and the application of modal filtering is shown. The algorithm of Chapter five is used to demonstrate memory reduction in the design of the microwave filters, waveguide bend and coupler examples.

In Chapter seven, stationary and non-stationary linear solvers, are introduced to optimise the convergence of the time-reversal design process. Gram-Schmidt conjugation, successive over relaxation, conjugate gradients and generalised minimal residual are applied to time-reversal. Convergence acceleration of the time-reversal design algorithm is demonstrated for the design case studies.

Loss of spatial resolution due to evanescent mode decay in the presence of finite machine precision restricts the scope for optimising large complex devices. In Chapter eight internal-time-reversal-mirrors are developed to capture evanescent electromagnetic fields around the internal scattering elements of a device, which enables the design of a higher order microwave filter.

In Chapter nine the 2D time-reversal method is extended to 3D. A simple waveguide filter is designed and optimised using the 3D time-reversal method. This chapter implements the thin wire formulation for the symmetrical condensed TLM node [1.29], and demonstrates the design of a dipole antenna using time-reversal, an example of component design within an open cavity structure.

Chapter ten concludes the research of the thesis and lists suggestions for further work.

Throughout the thesis the C++ language [1.30] [1.31] [1.32] was used to implement the time-reversal algorithm and the Matlab [1.33] [1.34] environment is used to display graphical results.

1.3 References

[1.1] T. Itoh, ed., *Numerical Techniques for Microwave and Millimeter-wave Passive Structures*. John Wiley & Sons Inc, New York, NY, 1989.

[1.2] M. Forest and W. J. R. Hoefer, "A Novel Synthesis Technique for Conducting Scatterers Using TLM Time Reversal," *IEEE Transactions on Microwave Theory and Techniques*, vol. 43, pp. 1371–1378, June 1995.

[1.3] D. H. Chambers and J. G. Berryman, "Analysis of the Time-Reversal Operator for a Small Spherical Scatterer in an Electromagnetic Field," *IEEE Transactions on Antennas and Propagation*, vol. 52, pp. 1729–1738, July 2004.

[1.4] T. Tanaka, T. Takenaka, and S. He, "An FDTD Approach to the Time-Domain Inverse Scattering Problem for an Inhomogeneous Cylindrical Object," *Microwave and Optical Technology Letters*, vol. 20, pp. 461–464, January 1999.

[1.5] J. H. Holland, *Adaptation in Natural and Artificial Systems*. MIT Press, Cambridge, MA, USA, 2nd ed., 1992.

[1.6] D. K. Cheng, *Field and Wave Electromagnetics*. Prentice-Hall, Reading, MA, 2nd ed., 1989.

[1.7] D. G. Albert, L. Liu, and M. L. Moran, "Time Reversal Processing for Source Location in an Urban Environment," *Journal of the Acoustical Society of America*, vol. 118, pp. 616–619, August 2005.

[1.8] P. Kosmas and C. M. Rappaport, "FDTD-Based Time Reversal for Microwave Breast Cancer Detection - Localization in Three Dimensions," *IEEE Transactions on Microwave Theory and Techniques*, vol. 54, pp. 1921–1927, April 2006.

[1.9] D. Liu, J. Krolik, and L. Carin, "Electromagnetic Target Detection in Uncertain Media: Time-Reversal and Minimum-Variance

Algorithms," *IEEE Transactions on Geoscience and Remote Sensing*, vol. 45, pp. 934–944, April 2007.

[1.10] D. Cassereau and M. Fink, "Time Reversal of Ultrasonic Fields - Part III: Theory of the Closed Time-Reversed Cavity," *IEEE Transactions on Ultrasonics, Ferroelectrics, and Frequency Control*, vol. 39, pp. 579–592, September 1992.

[1.11] M. Fink, "Time Reversal of Ultrasonic Fields - Part I: Basic Principles," *IEEE Transactions on Ultrasonics, Ferroelectrics, and Frequency Control*, vol. 39, pp. 555–566, September 1992.

[1.12] F. Wu, J. L. Thomas, and M. Fink, "Time Reversal of Ultrasonic Fields - Part II: Experimental Results," *IEEE Transactions on Ultrasonics, Ferroelectrics, and Frequency Control*, vol. 39, pp. 567–578, September 1992.

[1.13] P. Kosmas and C. M. Rappaport, "Time Reversal With the FDTD Method for Microwave Breast Cancer Detection," *IEEE Transactions on Microwave Theory and Techniques*, vol. 53, pp. 2317–2323, July 2005.

[1.14] P. Kosmas and C. M. Rappaport, "A Matched-Filter FDTD-Based Time Reversal Approach for Microwave Breast Cancer Detection," *IEEE Transactions on Antennas and Propagation*, vol. 54, pp. 1257–1264, April 2006.

[1.15] V. Chatelee, A. Dubois, I. Aliferis, J. Y. Dauvignac, H. E. Yakouti, and C. Pichot, "Time Reversal Imaging Techniques applied to Experimental Data," pp. 121–124, Proceedings of the Mediterranean Microwave Symposium (MMS), Genova, Italy, 19-21 September 2006.

[1.16] O. B. Matar, S. D. Santos, S. Calle, T. S. Goursolle, S. Vanaverbeke, and K. V. D. Abeele, "Simulations of Nonlinear Time Reversal Imaging of Damaged Materials," European NDT Conference (ECNDT), Berlin, Germany, 25-29 September 2006.

[1.17] N. Chakroun, M. Fink, and F. Wu, "Ultrasonic Nondestructive Testing with Time Reversal Mirrors," in *Proceedings of IEEE Ultrasonics Symposium*, vol. 2, pp. 809–814, October 1992.

[1.18] Wiki Entry: http://en.wikipedia.org/wiki/Ultrasonic_testing, Retrieved: 09/02/2009.

[1.19] D. Liu, S. Vasudevan, J. Krolik, G. Bal, and L. Carin, "Electromagnetic Time-Reversal Source Localization in Changing Media: Experiment and Analysis," *IEEE Transactions on Antennas and Propagation*, vol. 55, pp. 344–354, February 2007.

[1.20] D. Colton and R. Potthast, "The Inverse Electromagnetic Scattering Problem for an Anisotropic Medium," *The Quarterly Journal of Mechanics and Applied Mathematics*, vol. 52, pp. 349–372, September 1999.

[1.21] B. Zhang, M. Lu, and C. Wang, "Theoretical and Experimental Study of Time Reversal in Anisotropic Medium," pp. 1070–1073, IEEE Ultrasonics Symposium, Montreal, Canada, 23-27 August 2004.

[1.22] J.-P. Fouque, J. Garnier, and A. Nachbin, "Time reversal for dispersive waves in random media," *SIAM Journal on Applied Mathematics*, vol. 64, no. 5, pp. 1810–1838, 2004.

[1.23] K. J. Mehta, "Numerical Methods to Implement Time Reversal of Waves Propagating in Complex Random Media," MSc Thesis, North Carolina State University, 2003.

[1.24] P. Roux and M. Fink, "Time Reversal in a Waveguide: Study of the Temporal and Spatial Focusing," *Journal of the Acoustical Society of America*, vol. 107, pp. 2418–2429, May 2000.

[1.25] R. Sorrentino, P. P. So, and W. J. R. Hoefer, "Numerical Microwave Synthesis by Inversion of the TLM Process," pp. 1273–1277, 21st European Microwave Conference Digest, Stuttgart, Germany, 4-6 October 1991.

[1.26] R. Sorrentino, L. Roselli, and P. Mezzanotte, "Time Reversal in Finite Difference Time Domain Method," *IEEE Microwave and Guided Wave Letters*, vol. 3, pp. 402–404, November 1993.

[1.27] M. Forest and W. J. R. Hoefer, "TLM Synthesis of Microwave Structures Using Time Reversal," pp. 779–782, IEEE Microwave Theory and Techniques Symposium Digest, Albuquerque, NM, USA, 1-5 Jun 1992.

[1.28] E. Kreyszig, *Advanced Engineering Mathematics*. John Wiley & Sons Inc, New York, NY, 8th ed., 1998.

[1.29] P. Naylor and C. Christopoulos, "A New Wire Node for Modeling Thin Wires in Electromagnetic Field Problems Solved by Transmission Line Modeling," *IEEE Transactions on Microwave Theory and Techniques*, vol. 38, pp. 328–330, March 1990.

[1.30] L. Ullman and A. Signer, *C++ Programming*. Peachpit-Press, Berkeley CA, 2005.

[1.31] W. Savitch, *Absolute C++*. Addison Wesley, Reading, MA, 2nd ed., 2006.

[1.32] W. H. Press, B. P. Flannery, S. A. Teukolsky, and W. T. Vetterling, *Numerical Recipes in C: The Art of Scientific Computing*. Cambridge University Press, Cambridge, 2nd ed., 1992.

[1.33] www.mathworks.co.uk.

[1.34] J. H. Mathews and K. D. Fink, *Numerical Methods using Matlab*. Prentice-Hall, Reading, MA, 3rd ed., 1998.

2. Analytical Time-Reversal

This chapter presents the basic principals of Maxwell's equations, as related to the forward and inverse wave equation in homogenous and inhomogeneous linear media. The Lorentz reciprocity theorem and Poynting's vector for the measurement of power density are covered. The concept of the Greens function is introduced and the example of a point source reconstruction in a time-reversal-cavity is demonstrated.

2.1 Basic Electromagnetics

The properties of waves and fields whether bounded or in free space are governed by a group of laws collectively known as Maxwell's equations [2.1]. The derivation of these laws by James Clerk Maxwell is commonly assumed to have been based upon the empirical data provided by scientists such as Hans Christian Ørsted, Carl Friedrich Gauss, André-Marie Ampère and Michael Faraday. The modern form of Maxwell's equations were rewritten by Oliver Heaviside after the development of vector mathematics, and demonstrated physically by the work of Heinrich Hertz and Guglielmo Marconi [2.2] [2.3]. The differential form of Maxwell's equations which are used throughout this work are:

$$\nabla \times \vec{E} = -\frac{\partial \vec{B}}{\partial t} \tag{2.1a}$$

$$\nabla \times \vec{H} = \vec{J} + \frac{\partial \vec{D}}{\partial t} \tag{2.1b}$$

$$\nabla \cdot \vec{D} = \rho \tag{2.1c}$$

$$\nabla \cdot \vec{B} = 0 \tag{2.1d}$$

where

$\vec{E}$ is the electric field intensity in V/m,

$\vec{B}$ is the magnetic flux density in Wb/m^2,

$\vec{H}$ is the magnetic field intensity in A/m,

$\vec{J}$ is the electric current density in A/m^2,

$\vec{D}$ is the electric flux density in C/m^2 and

ρ is the electric charge density in C/m^3.

If an isotropic linear medium is assumed, the field intensities are related to the flux densities through the constitutive relations [2.1]

$$\vec{D} = \varepsilon \vec{E} \tag{2.2a}$$

$$\vec{B} = \mu \vec{H} \tag{2.2b}$$

where $\varepsilon = \varepsilon_0 \varepsilon_r$ is the permittivity of the medium in F/m, and $\mu = \mu_0 \mu_r$ and is the permeability in H/m.

2.1.1 Wave Equation

The wave equation is a second order partial differential equation that describes the propagation of electromagnetic fields in free space. The wave equation for the electric field is derived by taking the curl of Eqn.2.1a, and substituting in Eqn.2.2b to yield

$$\nabla \times \nabla \times \vec{E} = -\frac{\partial \nabla \times \vec{B}}{\partial t} = -\mu \frac{\partial \nabla \times \vec{H}}{\partial t}. \tag{2.3}$$

Substituting Eqn.2.1b in Eqn.2.3 and making use of Eqn.2.2a gives

$$\nabla \times \nabla \times \vec{E} = -\mu \frac{\partial\left(\vec{J} + \frac{\partial \vec{D}}{\partial t}\right)}{\partial t} = -\mu \frac{\partial \vec{J}}{\partial t} - \mu\varepsilon \frac{\partial^2 \vec{E}}{\partial t^2}. \tag{2.4}$$

Using the identity [2.4]

$$\nabla\left(\nabla \cdot \vec{E}\right) - \nabla^2 \vec{E} = \nabla \times \nabla \times \vec{E} \tag{2.5}$$

and the fact that $\nabla\left(\nabla \cdot \vec{E}\right) = 0$ which follows from Eqn.2.1c and the relation in Eqn.2.2a, Eqn.2.4 can be expressed as

$$\nabla^2 \vec{E} - \mu\varepsilon \frac{\partial^2 \vec{E}}{\partial t^2} = \mu \frac{\partial \vec{J}}{\partial t}. \tag{2.6}$$

The corresponding magnetic form is now derived by taking the curl of Eqn.2.1b and making use of Eqn.2.2a to give

$$\nabla \times \nabla \times \vec{H} = \nabla \times \vec{J} + \frac{\partial \nabla \times \vec{D}}{\partial t} = \nabla \times \vec{J} + \varepsilon \frac{\partial \nabla \times \vec{E}}{\partial t}. \tag{2.7}$$

Substitution of Eqn.2.1a in Eqn.2.7 and use of Eqn.2.2b yields

$$\nabla \times \nabla \times \vec{H} = \nabla \times \vec{J} - \mu\varepsilon \frac{\partial^2 \vec{H}}{\partial t^2}. \tag{2.8}$$

Rearranging and making use of the corresponding form of Eqn.2.5 gives

$$\nabla^2 \vec{H} - \mu\varepsilon \frac{\partial^2 \vec{H}}{\partial t^2} = -\nabla \times \vec{J} . \tag{2.9}$$

The source free wave equation for the electric field is a special case of the general wave equation, and is found by setting the electric current density and electric charge density to zero in Eqns.2.1 giving

$$\nabla^2 \vec{E} - \frac{1}{v^2} \frac{\partial^2 \vec{E}}{\partial t^2} = 0 \tag{2.10}$$

and

$$\nabla^2 \vec{H} - \frac{1}{v^2} \frac{\partial^2 \vec{H}}{\partial t^2} = 0 \tag{2.11}$$

where $v = 1/\sqrt{\mu\varepsilon}$ is the velocity of the wave [2.5].

2.1.2 Vector Potential

The wave equation can also be derived using the concept of vector potentials [2.5]. Since the divergence of the magnetic flux is zero, $\vec{B}$ can be expressed as the curl of another vector, say $\vec{A}$, since $\nabla \cdot \left(\nabla \times \vec{A} \right) = 0$, the vector $\vec{A}$ is known as the magnetic potential. Substitution of $\nabla \times \vec{A}$ in the place of $\vec{B}$ in Eqn.2.1a gives

$$\nabla \times \vec{E} = -\frac{\partial \nabla \times \vec{A}}{\partial t} \tag{2.12}$$

and rearranging Eqn.2.12, gives

$$\nabla \times \left(\vec{E} + \frac{\partial \vec{A}}{\partial t} \right) = 0 . \tag{2.13}$$

It is seen that the term inside the brackets is curl free, and can be expressed as the gradient of a scalar [2.4] [2.5], as

$$-\nabla \Phi = \vec{E} + \frac{\partial \vec{A}}{\partial t} , \tag{2.14}$$

from which it is seen that

$$\vec{E} = -\frac{\partial \vec{A}}{\partial t} - \nabla \Phi . \tag{2.15}$$

Using Eqn.2.15 and the substitution $\vec{B} = \nabla \times \vec{A}$ in Eqns.2.1 it is possible to derive the wave equation for the vector magnetic potential $\vec{A}$ and scalar electric potential Φ.

2.1.3 Time-Harmonic Wave Equation

A time-harmonic field is a field with sinusoidal time dependence [2.5]. In typical form this is expressed as

$$\vec{E}(x, y, z, t) = \vec{E}(x, y, z) \exp(j\omega t) . \tag{2.16}$$

It is seen from Eqn.2.16 that

$$\frac{\partial \vec{E}(x, y, z)}{\partial t} = j\omega \vec{E}(x, y, z) \exp(j\omega t) . \tag{2.17}$$

In general the partial derivative $\partial / \partial t$ is replaced with $j\omega$ in Maxwell's equations for forward time. In a similar manner as was done in the previous section the electric field wave equation is

$$\nabla^2 \vec{E}(x,y,z) + {k_0}^2 \vec{E}(x,y,z) = j\omega\mu\vec{J}(x,y,z) \tag{2.18}$$

where $k_0 = \omega\sqrt{\mu\varepsilon}$ is known as the wave number [2.5].

In reverse time the electric field in Eqn.2.16 has a temporal dependence represented by $\exp(-j\omega t)$, Eqn.2.17 then becomes

$$\frac{\partial \vec{E}(x,y,z)}{\partial t} = -j\omega\vec{E}(x,y,z)\exp(-j\omega t), \tag{2.19}$$

from which it is seen the partial derivative with respect to time in Maxwell's equations can now be replaced with the factor $-j\omega$ giving

$$\nabla^2 \vec{E}(x,y,z) + {k_0}^2 \vec{E}(x,y,z) = -j\omega\mu\vec{J}(x,y,z). \tag{2.20}$$

The left hand side of Eqn.2.20 defining the field propagation is unchanged while the electric current density, $\vec{J}(x,y,z)$ (or source), is negated in reverse time. In general this observation holds, since the source free wave equations for the electric and magnetic fields in Eqns.2.10-2.11 only contain even order partial derivatives with respect to time [2.6], and hence the homogenous wave equations for reverse time are identical to their forward time counterparts.

2.1.4 Power Flow and the Poynting Vector

The Poynting vector is defined as [2.5]

$$\vec{P} = \vec{E} \times \vec{H}, \qquad (\mathrm{W/m^2}) \tag{2.21}$$

and measures the power density of an electromagnetic field. In time-reversal, the Poynting vector is useful to measure the higher power density spaces within a volume. In general, the fields diverging from a source, $\vec{J}$ during forward time, will converge back to the source location during reversal [2.7], and as they converge upon $\vec{J}$ the density of the Poynting vector will increase. This property is important for the recovery of scattering elements, which will be covered in Chapter five when time-reversal is used for component design.

2.1.5 Source and Receiver Reciprocity

The Lorentz reciprocity theorem is an important result in electromagnetic theory [2.8], that states the relationship between a source and receiver is unchanged, if the source and receiver positions are interchanged. Reciprocity can be used to illustrate the time-reversal process, however, due to factors in time-reversal implementations, for example loss of evanescent waves (investigated in Chapter four), reciprocity may be valid in situations where time-reversal is not [2.9], and as such the following should not be taken as a proof of time-reversal validity, but a simple explanation of the time-reversal process.

Figure 2-1 shows two sources $\vec{J}_1$ and $\vec{J}_2$, with respective electric and magnetic fields, in the general free-space volume V, bounded by the surface S, with unit normal $\vec{n}$. The integral form of the Lorentz reciprocity theorem is

$$\oint_S \left(\vec{E}_1 \times \vec{H}_2 - \vec{E}_2 \times \vec{H}_1\right) \cdot \vec{n} dS = \int_V \left(\vec{J}_1 \cdot \vec{E}_2 - \vec{J}_2 \cdot \vec{E}_1\right) dV \,. \tag{2.22}$$

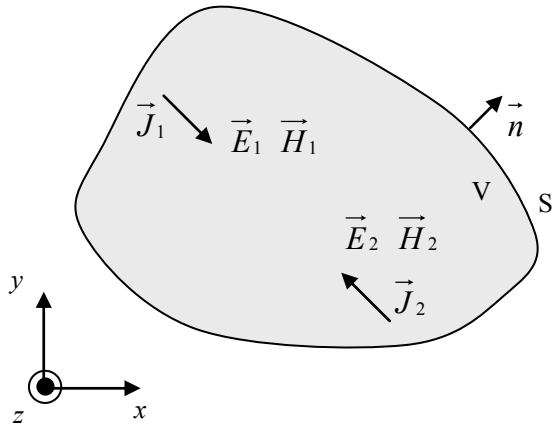

Figure 2-1 - Lorentz reciprocity, relationship between $\vec{\mathbf{J}}_1$ with respective fields $\vec{\mathbf{E}}_1$ and $\vec{\mathbf{H}}_1$ is unchanged if source and measurement points are interchanged with those of $\vec{\mathbf{J}}_2$, $\vec{\mathbf{E}}_2$ and $\vec{\mathbf{H}}_2$ respectively.

In time-reversal, $\vec{J}_2$ will represent the reverse source generating field $\vec{E}_2$ and $\vec{H}_2$ while the forward time source, $\vec{J}_1$ gives fields $\vec{E}_1$ and $\vec{H}_1$.

Using Eqn.2.22 the process behind the time-reversal procedure can be explained. The forward time source, $\vec{J}_1$ with time dependence, t, is $\vec{J}_1(t) = \vec{J}_1 \exp(j\omega t)$. The reverse source is expressed in terms of the forward source as

$$\vec{J}_2(t) = \vec{J}_1(-t) = \vec{J}_1(t) \exp(-j2\omega t) \,, \tag{2.23}$$

from which it is seen that the reverse source is propagating with $-t$ as defined. Making use of Eqn.2.23 the Lorentz theorem in Eqn.2.22 becomes

$$\oint_S \left(\vec{E}_1(t) \times \vec{H}_2(t) - \vec{E}_2(t) \times \vec{H}_1(t)\right) \cdot \vec{n} dS = \int_V \left(\vec{J}_1(t) \cdot \vec{E}_2(t) - \vec{J}_1(t) \exp(-j2\omega t) \cdot \vec{E}_1(t)\right) dV . \tag{2.24}$$

The left hand side of Eqn.2.24 tends to zero as the radius of the surface tends to $+\infty$, hence

$$\int_V \left(\vec{J}_1(t) \cdot \vec{E}_2(t)\right) dV = \int_V \left(\vec{J}_1(t) \exp(-j2\omega t) \cdot \vec{E}_1(t)\right) dV , \tag{2.25}$$

from which it can be seen by comparing like terms

$$\vec{E}_2(t) = \vec{E}_1(t) \exp(-j2\omega t) = \vec{E}_1(-t) . \tag{2.26}$$

Eqn.2.26 illustrates the field $\vec{E}_2$ from the time-reversed source $\vec{J}_2$ can be thought of as a time-reversed form of the field $\vec{E}_1$ from the forward time source $\vec{J}_1$. A similar case can be shown for the magnetic field by using Maxwell's equations with a fictitious magnetic current density [2.8] to derive the Lorentz theorem.

This illustrative use of the reciprocity theorem has served to demonstrate the fundamental process of time-reversal. A more rigorous analysis forms the remainder of this chapter.

2.2 Green's Functions

In brief, a Green's function is an integral kernel solution to a homogenous partial differential equation, which is used to construct the particular solution of the corresponding inhomogeneous partial differential equation [2.10]. For example, if G is the field at an observer, caused by a point source, then the field caused by a source distribution, $\vec{p}$, is the integral of

G over the range occupied by the source $\vec{p}$ [2.11], and is termed the kernel solution. The method of Green's function is typically used where traditional methods such as separation of variables [2.5], or the characteristic equation approach [2.12] are cumbersome.

In the theoretical analysis that follows, a Green's function of the form $G(r,r')$ is used, where r is the coordinate of the observation point, and r' is the source coordinate. The properties of the Green's function are first covered.

2.2.1 Application of Green's Function for Solution of the Wave Equation

The wave equation for the forward electric field, was shown to be

$$\nabla^2 \vec{E}(r) + k_0{}^2 \vec{E}(r) = j\omega\mu\vec{J}(r). \tag{2.27}$$

This form of the wave equation can be expressed in the form of a linear operation, L, upon the electric field

$$L\vec{E}(r) = \vec{p}(r) \tag{2.28}$$

where L is the linear differential operator

$$L = \left(\nabla^2 + k_0{}^2\right) \tag{2.29}$$

and

$$\vec{p}(r) = j\omega\mu\vec{J}(r). \tag{2.30}$$

The Green's function is a solution of the wave equation for the point charge represented by the delta function, and hence the associated Green's function for Eqn.2.28 satisfies

$$LG(r,r') = \delta(r-r') \tag{2.31}$$

where the delta function is given as

$$\delta(r-r') = \begin{cases} 1, & r = r', \\ 0, & r \neq r'. \end{cases} \tag{2.32}$$

The electric field can be expressed in the form [2.10]

$$\vec{E}(r) = \vec{\Phi}(r) + \int_V G(r,r')\vec{p}(r')dV \tag{2.33}$$

where $\vec{\Phi}(r)$ is a solution to the homogenous form of Eqn.2.27, and the volume integral is termed the kernel solution, the derivation of which is beyond the scope of this work.

This completes the application of the Green's function for the wave equation. This illustration is sufficient for our purpose, although it should be noted the formation and application of Green's functions is a significant area of electromagnetics research of which further details can be found in [2.10] and [2.12].

In the remainder of this chapter, the dyadic Green's function will be used, and termed $\vec{\vec{G}}(r,r')$. In 3D Cartesian coordinates the dyadic can be expressed as three vector Green's functions in x, y and z

$$\vec{\vec{G}} = \vec{G}_1\vec{x} + \vec{G}_2\vec{y} + \vec{G}_3\vec{z} \tag{2.34}$$

where, for example, $\vec{G}_1\vec{x}$ is the direct product $\left[g_{11}\vec{x} \quad g_{12}\vec{x} \quad g_{13}\vec{x}\right]^T$. The dyadic form of Green's function is useful to express the Green's function wave equation in vector form, similarly to the electric field wave equation.

2.3 Time-Reversal-Cavity

The time-reversal-cavity technique for simulated time-reversal is used throughout the thesis to perform the numerical time-reversal simulations. This section builds upon the work of [2.13], theoretically investigating the properties of the cavity approach to time-reversal, using a frequency domain formulation at electromagnetic frequencies. The frequency domain form simplifies the analysis, as the temporal inversion in the time domain can be replaced with conjugation in the frequency domain.

The section will begin with an analysis of the forward electric field within the time-reversal-cavity. This is then compared with the reverse field, using only boundary reversal, and the ideal case, where reversal of the source and boundary conditions of the wave equation is possible.

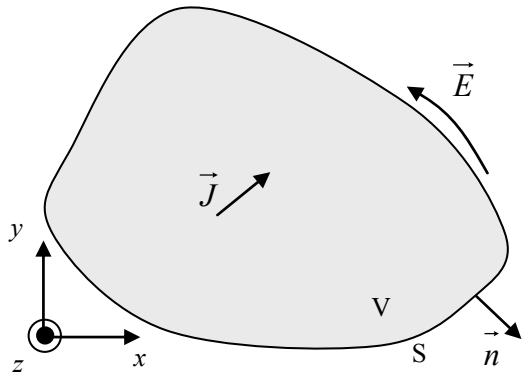

Figure 2-2 - Illustration of time-reversal-cavity for simulated time-reversal, source $\vec{\mathbf{J}}$ generates field $\vec{\mathbf{E}}$, which is stored around closed surface S.

2.3.1 Forward Stage

The time-harmonic form of the wave equation for an electric field derived in section 2.1.1 can be expressed as

$$\nabla \times \nabla \times \vec{E}(r) - {k_0}^2 \vec{E}(r) = -j\omega\mu\vec{J} \tag{2.35}$$

where ${k_0}^2 = \omega^2 \mu\varepsilon$.

The corresponding dyadic Green's function for $\vec{E}(r)$ in Eqn.2.35 must satisfy the equation

$$\nabla \times \nabla \times \overleftrightarrow{G}(r,r') - {k_0}^2 \overleftrightarrow{G}(r,r') = -\delta(r-r')\overleftrightarrow{I}. \tag{2.36}$$

where $\overleftrightarrow{I}$ is the unit dyadic.

Green's second theorem [2.10] can be used to relate the integral of the electric field, $\vec{E}$ over a volume V bounded by the surface S, to the surface integral of $\vec{E}$ around the closed surface S, see Figure 2-2. Defining two arbitrary electric fields, $\vec{E}_1$ and $\vec{E}_2$, this is expressed as [2.14]

$$\int_V \left(\vec{E}_1 \cdot \nabla \times \nabla \times \vec{E}_2\right) - \left(\vec{E}_2 \cdot \nabla \times \nabla \times \vec{E}_1\right) dV = \int_S \left(\vec{E}_2 \times \nabla \times \vec{E}_1\right) - \left(\vec{E}_1 \times \nabla \times \vec{E}_2\right) \vec{n} dS. \tag{2.37}$$

Through application of Green's second theorem in Eqn.2.37 with the substitution of $\vec{E}_1 = \vec{E}(r)$ and $\vec{E}_2 = \overleftrightarrow{G}(r,r')\vec{C}$ where $\vec{C}$ is an arbitrary vector along which the Green's function is defined, the electric field is expressed as

$$\int_V \left(\vec{E}(r)\cdot\nabla\times\nabla\times\overleftrightarrow{G}(r,r')\vec{C}\right)-\left(\overleftrightarrow{G}(r,r')\vec{C}\cdot\nabla\times\nabla\times\vec{E}(r)\right)dV = \int_S \left(\overleftrightarrow{G}(r,r')\vec{C}\times\nabla\times\vec{E}(r)\right)-\left(\vec{E}(r)\times\nabla\times\overleftrightarrow{G}(r,r')\vec{C}\right)\vec{n}dS . \quad (2.38)$$

To investigate the behaviour of the electric field in the time-reversal-cavity, it is necessary to determine $\vec{E}(r)$ from Eqn.2.38. The wave equation of Eqn.2.35 is multiplied throughout by $\overleftrightarrow{G}(r,r')\vec{C}$, giving

$$\overleftrightarrow{G}(r,r')\vec{C}\cdot\nabla\times\nabla\times\vec{E}(r)-k_0{}^2\vec{E}(r)\cdot\overleftrightarrow{G}(r,r')\vec{C}=-j\omega\mu\vec{J}\cdot\overleftrightarrow{G}(r,r')\vec{C} . \quad (2.39)$$

Similarly, from Eqn.2.36, and $\vec{E}(r)\vec{C}$,

$$\vec{E}(r)\vec{C}\cdot\nabla\times\nabla\times\overleftrightarrow{G}(r,r')-k_0{}^2\overleftrightarrow{G}(r,r')\cdot\vec{E}(r)\vec{C}=-\delta(r-r')\overleftrightarrow{I}\cdot\vec{E}(r)\vec{C} . \quad (2.40)$$

Subtracting Eqn.2.39 from Eqn.2.40 and since $k_0{}^2\overleftrightarrow{G}(r,r')\cdot\vec{E}(r)\vec{C}=k_0{}^2\vec{E}(r)\cdot\overleftrightarrow{G}(r,r')\vec{C}$ for all real vectors $\vec{C}$, we have

$$\vec{E}(r)\vec{C}\cdot\nabla\times\nabla\times\overleftrightarrow{G}(r,r')-\overleftrightarrow{G}(r,r')\vec{C}\cdot\nabla\times\nabla\times\vec{E}(r)= -\delta(r-r')\overleftrightarrow{I}\cdot\vec{E}(r)\vec{C}+j\omega\mu\vec{J}\cdot\overleftrightarrow{G}(r,r')\vec{C}. \quad (2.41)$$

Substitution of Eqn.2.41 into the second Green's theorem in Eqn.2.38 gives

$$\int_V \left(-\delta(r-r')\overleftrightarrow{I}\cdot\vec{E}(r)\vec{C}+j\omega\mu\vec{J}\cdot\overleftrightarrow{G}(r,r')\vec{C}\right)dV = \int_S \left(\overleftrightarrow{G}(r,r')\vec{C}\times\nabla\times\vec{E}(r)\right)-\left(\vec{E}(r)\times\nabla\times\overleftrightarrow{G}(r,r')\vec{C}\right)\vec{n}dS . \quad (2.42)$$

Since $\int_r \delta(r-r')\overleftrightarrow{I}\cdot\vec{E}(r)\vec{C}dr=\vec{E}(r')\vec{C}$, Eqn.2.42 is simplified to read

$$\vec{E}(r')\vec{C} = \int_V j\omega\mu\vec{J}\cdot\overleftrightarrow{G}(r,r')\vec{C}dV - \left(\int_S \left(\overleftrightarrow{G}(r,r')\vec{C}\times\nabla\times\vec{E}(r)\right) - \left(\vec{E}(r)\times\nabla\times\overleftrightarrow{G}(r,r')\vec{C}\right)\vec{n}dS\right). \tag{2.43}$$

Eqn.2.43 expresses the forward time electric field at the source $\vec{E}(r')$ along the vector $\vec{C}$ in terms of the volume and surface integrals of the cavity. $\vec{C}$ is arbitrary, so Eqn.2.43 can be used to express the electric field along any direction, x, y, z for example in Cartesian coordinates, hence Eqn.2.43 completely defines the electric field of the cavity. It is informative to compare this case with respect to the use of the time-reversal-cavity, when only the boundary field is stored, and the ideal case, when both the source and boundary are reversed.

2.3.2 Reverse Stage

2.3.2.1 Time-Reversal-Cavity (Boundary Reversal)

For the inverse case of the time-reversal-cavity, the wave equation in Eqn.2.35 becomes a source-free wave equation since the input source excitation of the cavity is removed,

$$\nabla\times\nabla\times\vec{E}^*(r) - k_0{}^2\vec{E}^*(r) = 0 \tag{2.44}$$

where $\vec{E}^*(r)$ is the conjugate of $\vec{E}(r)$, since conjugation in the frequency domain is time-reversal in the time domain [2.13].

The same Green's function used in Eqn.2.36, and the same procedure used to derive $\vec{E}(r')$ is repeated to give

$$\vec{E}^*(r')\vec{C} = -\left(\int_S \left(\overleftrightarrow{G}(r,r')\vec{C} \times \nabla \times \vec{E}^*(r) \right) - \left(\vec{E}^*(r) \times \nabla \times \overleftrightarrow{G}(r,r')\vec{C} \right) \vec{n} dS \right). \quad (2.45)$$

Eqn.2.45 relates the conjugate electric field to the closed surface integral, since this is the form of the inverse field when a time-reversal-cavity is used for time-reversal, the recovered source field, $\vec{E}^*(r')$, is now termed $\vec{E}_R(r')$ and Eqn.2.45 reads

$$\vec{E}_R(r')\vec{C} = -\left(\int_S \left(\overleftrightarrow{G}(r,r')\vec{C} \times \nabla \times \vec{E}^*(r) \right) - \left(\vec{E}^*(r) \times \nabla \times \overleftrightarrow{G}(r,r')\vec{C} \right) \vec{n} dS \right). \quad (2.46)$$

2.3.2.2 Time-Reversal of Source and Boundary

It is seen in Eqn.2.46, the volume integral relating $\vec{J}$ to the electric field has vanished, since the source has been removed in the inverse stage of the simulation. Assuming for now reversed placement of the source is possible, and replacing $\vec{E}(r)$ and $\vec{J}$ with $\vec{E}^*(r)$ and $\vec{J}^*$ respectively in Eqns.2.35-2.43 gives the corresponding form of Eqn.2.46 when both the source and boundary are reversed [2.13] as

$$\begin{aligned} \vec{E}^*(r')\vec{C} = & \int_V j\omega\mu \vec{J}^* \cdot \overleftrightarrow{G}(r,r')\vec{C} dV - \\ & \left(\int_S \left(\overleftrightarrow{G}(r,r')\vec{C} \times \nabla \times \vec{E}^*(r) \right) - \left(\vec{E}^*(r) \times \nabla \times \overleftrightarrow{G}(r,r')\vec{C} \right) \vec{n} dS \right). \end{aligned} \quad (2.47)$$

Eqn.2.47 contains an additional term that is not present when the time-reversal-cavity approach to time-reversal is used. Subtraction of Eqn.2.47, from the case when only the boundary field is reversed using the time-reversal-cavity, Eqn.2.46, gives the remaining field as

$$\vec{E}_R(r')\vec{C} = \vec{E}(r')^*\vec{C} - \int_V j\omega\mu \vec{J}^* \cdot \overleftrightarrow{G}(r,r')\vec{C} dV. \quad (2.48)$$

Referring back to Eqn.2.43, the Green's function and electric field are both forward functions; hence the closed surface integral tends to zero, and Eqn.2.43 is simplified further to read

$$\vec{E}(r')\vec{C} = \int_V j\omega\mu\vec{J}\cdot\overleftrightarrow{G}(r,r')\vec{C}dV\,. \tag{2.49}$$

Conjugation of Eqn.2.49 and substitution into Eqn.2.48 gives

$$\begin{aligned}\vec{E}_R(r')\vec{C} &= \int_V j\omega\mu\vec{J}^*\cdot\overleftrightarrow{G}^*(r,r')\vec{C}dV - \int_V j\omega\mu\vec{J}^*\cdot\overleftrightarrow{G}(r,r')\vec{C}dV \\ &= \int_V j\omega\mu\vec{J}^*\cdot\left(\overleftrightarrow{G}^*(r,r') - \overleftrightarrow{G}(r,r')\right)\vec{C}dV\end{aligned} \tag{2.50}$$

where $\overleftrightarrow{G}^*(r,r')$ is the conjugated Green's function. Simplification of Eqn.2.50 results in

$$\vec{E}_R(r')\vec{C} = 2\int_V \omega\mu\vec{J}^*\cdot im\left\{\overleftrightarrow{G}(r,r')\right\}\vec{C}dV\,. \tag{2.51}$$

The arbitrary vector $\vec{C}$ used for the general derivation is now cancelled and Eqn.2.51 reads [2.13]

$$\vec{E}_R(r') = 2\int_V \omega\mu\vec{J}^*\cdot im\left\{\overleftrightarrow{G}(r,r')\right\}dV\,, \tag{2.52}$$

from which it is seen that the electric field at the source location after time-reversal is complete, is not the original source, but the imaginary component of the corresponding Green's function.

2.3.3 Point Source in Time-Reversal-Cavity

An impulse function point source is a popular method of excitation in electromagnetics. As an example, if a point source excitation is used to excite the time-reversal-cavity,

$$\vec{J} = \delta(r - r')\vec{\mathbf{J}} \tag{2.53}$$

where $\vec{\mathbf{J}}$ is the source. The corresponding Green's function is [2.10]

$$\overleftrightarrow{G}(r, r') = \frac{\delta(r - r')\exp\left(-jk_0(r - r')\right)\overleftrightarrow{I}}{r - r'}. \tag{2.54}$$

Substitution of Eqns.2.53-2.54 into Eqn.2.52 shows

$$\begin{aligned}\vec{E}_R(r') &= 2\int_V \omega\mu\delta(r - r')\vec{\mathbf{J}} * \cdot im\left\{\frac{\delta(r - r')\exp\left(-jk_0(r - r')\right)\overleftrightarrow{I}}{r - r'}\right\}dV \\ &= 2\omega\mu\vec{\mathbf{J}} * \cdot im\left\{\frac{\exp\left(-jk_0 r'\right)\overleftrightarrow{I}}{r'}\right\} \\ &= -2\omega\mu\vec{\mathbf{J}} * \cdot k_0\,\mathrm{sinc}(k_0 r')\overleftrightarrow{I}.\end{aligned} \tag{2.55}$$

Eqn.2.55 states that the recovered point source after time-reversal is a sinc function. The width of the sinc function is related to the wave number k_0, and hence as the frequency increases the recovered sinc function will become narrower.

2.4 Conclusions

The chapter introduced Maxwell's equations and derived the electromagnetic wave equation. Lorentz reciprocity, the Poynting vector and Green's function were covered. The properties of the time-reversal-cavity for simulated time-reversal were investigated, and it was shown that the

cavity only reverses the field measured from the boundary, and does not reverse the initial source conditions. An example of a point source reconstruction was used to demonstrate the recovered point source is a sinc function, with width dependant on frequency.

The next chapter will introduce the transmission-line modelling (TLM) method for numerical simulation of electromagnetic propagation, and the time-reversal-cavity for use with TLM.

2.5 References

[2.1] R. E. Collin, *Foundations for Microwave Engineering*. John Wiley & Sons Inc, New York, NY, 2nd ed., 2001.

[2.2] Online: http://www.ieeeghn.org/wiki/index.php/Heinrich_Hertz_(1857-1894), Retrieved: 18/05/2009.

[2.3] Online: http://www.ieeeghn.org/wiki/index.php/Guglielmo_Marconi, Retrieved: 18/05/2009.

[2.4] P. C. Matthews, *Vector Calculus*. Springer, New York, NY, 2006.

[2.5] D. K. Cheng, *Field and Wave Electromagnetics*. Prentice-Hall, Reading, MA, 2nd ed., 1989.

[2.6] G. Lerosey, J. de Rosny, A. Tourin, A. Derode, G. Montaldo, and M. Fink, "Time Reversal of Electromagnetic Waves," *Physical Review Letters*, vol. 92, pp. 193904–(1–3), May 2004.

[2.7] P. Kosmas and C. M. Rappaport, "Time Reversal With the FDTD Method for Microwave Breast Cancer Detection," *IEEE Transactions on Microwave Theory and Techniques*, vol. 53, pp. 2317–2323, July 2005.

[2.8] D. M. Pozar, *Microwave Engineering*. John Wiley & Sons Inc, New York, NY, 3rd ed., 2007.

[2.9] R. Carminati and M. Nieto-Vesperinas, "Reciprocity of Evanescent Electromagnetic Waves," *Journal of the Optical Society of America*, vol. 15, pp. 706–712, March 1998.

[2.10] P. Russer, *Electromagnetics, Microwave Circuit, and Antenna Design for Communications Engineering*. Artech House, Norwood, MA, 2nd ed., 2006.

[2.11] P. M. Morse and H. Feshbach, *Methods of Theoretical Physics: Part 1*. McGraw Hill, New York, NY, 1953.

[2.12] E. Kreyszig, *Advanced Engineering Mathematics*. John Wiley & Sons Inc, New York, NY, 8th ed., 1998.

[2.13] R. Carminati, R. Pierrat, J. de Rosny, and M. Fink, "Theory of the Time-Reversal Cavity for Electromagnetic Fields," *Optics Letters*, vol. 32, pp. 3107–3109, November 2007.

[2.14] R. E. Collin, *Field Theory of Guided Waves*. John Wiley & Sons Inc, New York, NY, 2nd ed., 1990.

3. The Transmission-Line Modelling Method and Numerical Time-Reversal

The chapter begins by introducing the transmission-line modelling (TLM) method for numerical simulation followed by a derivation of the 2D shunt node for transverse magnetic polarisation. The symmetrical condensed node for 3D electromagnetic propagation is also shown. Finally the TLM time-reversal-cavity for numerical time-reversal simulation is described.

3.1 2D Transmission-Line Modelling Method

Maxwell's equations are often difficult to solve in analytical form for complex geometries. The approximation of Maxwell's equations through the use of numerical schemes has hence proved popular, and a number of numerical methods have emerged. Finite element and finite difference [3.1] are among the most popular and widespread methods.

In this thesis, TLM is used extensively due to its inherent stability, ease of implementation, and widespread use in the Department. The method was originally developed at the University of Nottingham in the early 1970's [3.2]. TLM is a time-domain numerical method based upon the analogy between the evolution of electromagnetic fields to voltage impulses travelling on an interconnected 3D mesh of commensurate transmission-lines and is related to the differential form of Maxwell's equations [3.3].

The resulting algorithm is unconditionally stable, since the underlying formulation is based upon circuit theory and electromagnetics principles [3.4] [3.5] [3.6]. TLM also allows sampling of the electric and magnetic field at the same sample point, and the algorithm can be parallelised to allow efficient computation [3.7].

3.1.1 Transverse Magnetic Polarisation

This section will derive Maxwell's equations for transverse magnetic polarisation, where the electric field is polarised out of the page. Expansion of Maxwell's equations in Cartesian coordinates, and using the constitutive relations of Chapter two, Eqn.2.2, produce the following six equations, where the coordinate axis are as shown in Figure 3-1.

$$\frac{\partial E_x}{\partial y} - \frac{\partial E_y}{\partial x} = -\mu \frac{\partial H_z}{\partial t} \tag{3.1a}$$

$$-\left(\frac{\partial E_x}{\partial z} - \frac{\partial E_z}{\partial x} \right) = -\mu \frac{\partial H_y}{\partial t} \tag{3.1b}$$

$$\frac{\partial E_y}{\partial z} - \frac{\partial E_z}{\partial y} = -\mu \frac{\partial H_x}{\partial t} \tag{3.1c}$$

$$\frac{\partial H_x}{\partial y} - \frac{\partial H_y}{\partial x} = \varepsilon \frac{\partial E_z}{\partial t} \tag{3.1d}$$

$$-\left(\frac{\partial H_x}{\partial z} - \frac{\partial H_z}{\partial x} \right) = \varepsilon \frac{\partial E_y}{\partial t} \tag{3.1e}$$

$$\frac{\partial H_y}{\partial z} - \frac{\partial H_z}{\partial y} = \varepsilon \frac{\partial E_x}{\partial t} \tag{3.1f}$$

For a 2D problem, the field is transverse magnetic polarised if the electric field is orthogonal to the reference plane, while the magnetic fields are parallel to the reference plane. In this respect, the field is defined by the E_z, H_x, and H_y field components, where E_x, E_y, and H_z are zero, and it is seen Eqns.3.1 simplify [3.3]

$$\frac{\partial E_z}{\partial x} = -\mu \frac{\partial H_y}{\partial t} \tag{3.2b}$$

$$-\frac{\partial E_z}{\partial y} = -\mu \frac{\partial H_x}{\partial t} \tag{3.2c}$$

$$\frac{\partial H_x}{\partial y} - \frac{\partial H_y}{\partial x} = \varepsilon \frac{\partial E_z}{\partial t}. \tag{3.2d}$$

Taking the partial derivative of Eqns.3.2b,c with respect to x and y respectively, gives

$$\frac{\partial^2 E_z}{\partial x^2} = -\mu \frac{\partial}{\partial x}\frac{\partial H_y}{\partial t} \tag{3.3a}$$

$$-\frac{\partial^2 E_z}{\partial y^2} = -\mu \frac{\partial}{\partial y}\frac{\partial H_x}{\partial t}. \tag{3.3b}$$

The addition of Eqn.3.3a and Eqn.3.3b gives

$$\begin{aligned}\frac{\partial^2 E_z}{\partial x^2} + \frac{\partial^2 E_z}{\partial y^2} &= \mu \frac{\partial}{\partial y}\frac{\partial H_x}{\partial t} - \mu \frac{\partial}{\partial x}\frac{\partial H_y}{\partial t} \\ &= \mu \frac{\partial}{\partial t}\left(\frac{\partial H_x}{\partial y} - \frac{\partial H_y}{\partial x}\right).\end{aligned} \tag{3.4}$$

Substitution of Eqn.3.2d in Eqn.3.4 gives

$$\begin{aligned}\frac{\partial^2 E_z}{\partial x^2} + \frac{\partial^2 E_z}{\partial y^2} &= \mu \frac{\partial}{\partial t}\left(\varepsilon \frac{\partial E_z}{\partial t}\right) \\ &= \mu\varepsilon \frac{\partial^2 E_z}{\partial t^2}.\end{aligned} \tag{3.5}$$

Eqn.3.5 is the 2D Cartesian form of the wave equation for the field component E_z, in a source free region. The velocity is expressed as

$$v = 1/\sqrt{\mu\varepsilon}\,. \tag{3.6}$$

For free space, where $\mu = \mu_0 = 1.26e-6$ H/m and $\varepsilon = \varepsilon_0 = 8.85e-12$ F/m, the velocity is

$$v = 1/\sqrt{\mu_0\varepsilon_0} = 2.998e8 \text{ m/s}. \tag{3.7}$$

The TLM paradigm is to model the continuous field quantities, $\vec{E}$ and $\vec{H}$ using voltage and current equivalences measured at discrete intervals, Δl. The 2D TLM node for modelling transverse magnetic polarisation will be shown next, and its equivalence to the transverse magnetic field quantities is given.

3.1.2 2D TLM Node

The TLM method models current and voltage, synonymous to magnetic and electric fields. To use the TLM method to model Eqn.3.5, it is necessary to define the transmission-line circuit as shown in Figure 3-1a [3.3]. The structure is referred to as a 2D shunt TLM node, since the intersecting transmission-lines are connected in a parallel configuration, and models a space of area Δl^2.

In Figure 3-1b the equivalent passive element form is shown. The distributed shunt capacitance of each transmission-line of length $\Delta l/2$ and impedance Z_0, is given at the node centre as C.

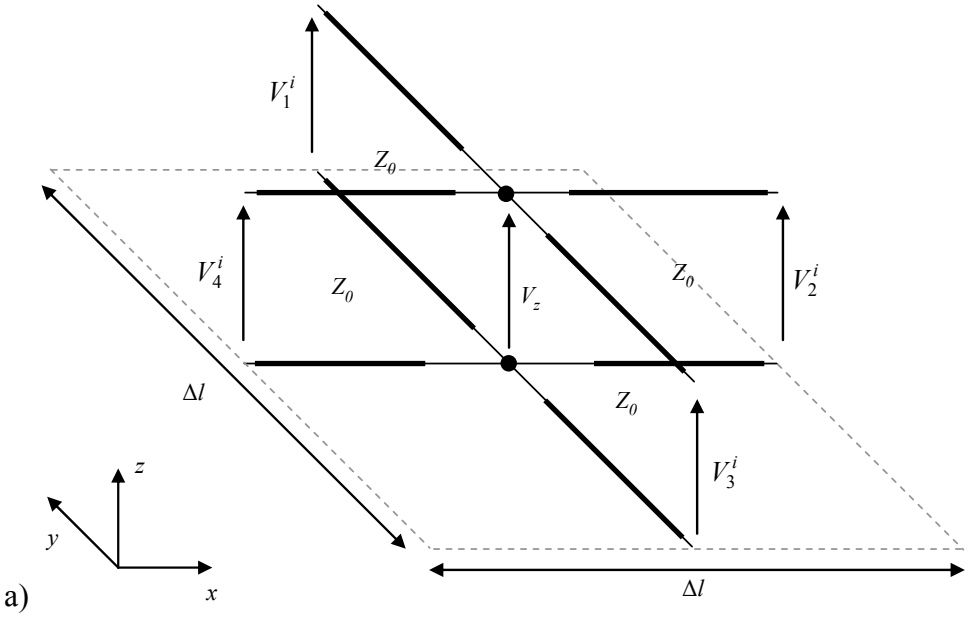

a)

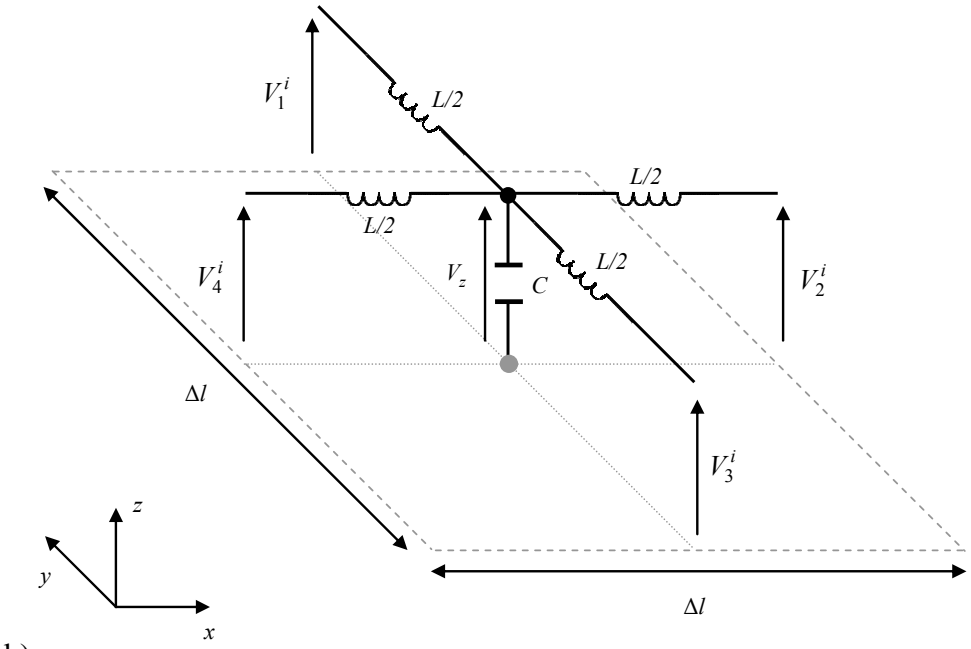

b)

Figure 3-1 - a) 2D TLM shunt node element covering an area of Δl^2, Z_0 is the intrinsic impedance of the transmission-line sections, b) equivalent circuit representation. Distributed capacitance of each line of length $\Delta l/2$ has been combined at the node centre.

Figure 3-2 shows the condensed form of the 2D shunt node, which is commonly used to derive the field equivalences.

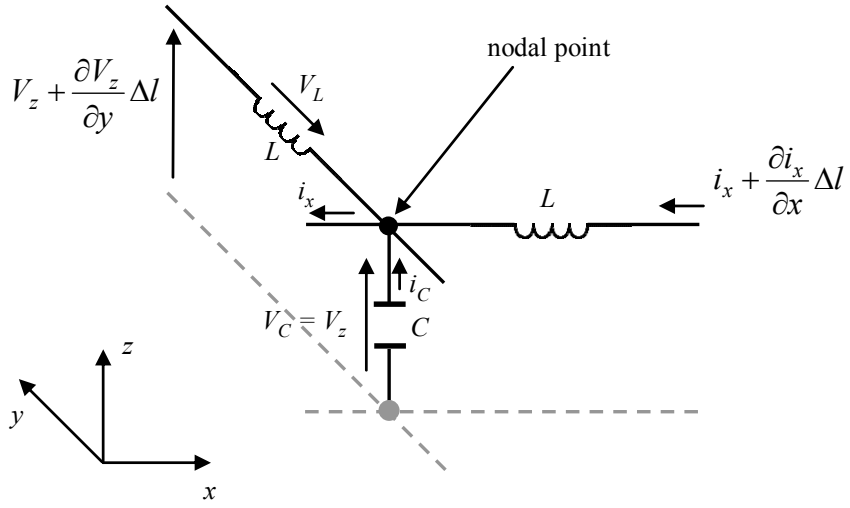

Figure 3-2 - Kirchoffs current law in *x* arm of TLM node and Kirchoffs voltage law in *y* arm.

Kirchoff's current law states the current entering a node must equal the current leaving the node, hence using Kirchoff's current law [3.3] on Figure 3-2, for the x-direction only gives

$$i_C - i_x + i_x + \frac{\partial i_x}{\partial x}\Delta l = 0 \tag{3.8}$$

simplifying, rearranging and replacing the current across the capacitor, i_C with $C\frac{\partial V_z}{\partial t}$ gives

$$C\frac{\partial V_z}{\partial t} = -\frac{\partial i_x}{\partial x}\Delta l\,. \tag{3.9}$$

Taking the partial derivative of Eqn.3.9 with respect to t and rearranging gives

$$\frac{\partial}{\partial t}\left(\frac{\partial i_x}{\partial x}\right) = -\frac{C}{\Delta l}\frac{\partial^2 V_z}{\partial t^2}\,. \tag{3.10}$$

Similarly from Kirchoff's voltage law circulating in x [3.3] and $V_L = L\frac{\partial i_x}{\partial t}$, it is seen

$$\begin{aligned} -V_z + V_L + V_z + \frac{\partial V_z}{\partial x}\Delta l = 0 \\ L\frac{\partial i_x}{\partial t} = -\frac{\partial V_z}{\partial x}\Delta l \end{aligned} \tag{3.11}$$

and again taking the partial derivative with respect to x gives

$$\frac{\partial}{\partial x}\left(\frac{\partial i_x}{\partial t}\right) = -\frac{\partial^2 V_z}{\partial x^2}\frac{\Delta l}{L}. \tag{3.12}$$

Subtracting Eqn.3.12 from Eqn. 3.10 gives

$$\frac{\Delta l^2}{L}\frac{\partial^2 V_z}{\partial x^2} = C\frac{\partial^2 V_z}{\partial t^2}. \tag{3.13}$$

In Figure 3-2 Kirchoff's current law for x and voltage law for y was illustrated. Using Kirchoff's voltage and current laws in y, yields the two equations

$$\begin{aligned} i_C - i_y + i_y + \frac{\partial i_y}{\partial y}\Delta l = 0 \\ C\frac{\partial V_z}{\partial t} = -\frac{\partial i_y}{\partial y}\Delta l \end{aligned} \tag{3.14}$$

and

$$\begin{aligned} -V_z + V_L + V_z + \frac{\partial V_z}{\partial y}\Delta l = 0 \\ L\frac{\partial i_y}{\partial t} = -\frac{\partial V_z}{\partial y}\Delta l. \end{aligned} \tag{3.15}$$

Taking the partial derivative of Eqn.3.14 with respect to t and Eqn.3.15 with respect to y and rearranging gives

$$\frac{\partial}{\partial t}\left(\frac{\partial i_y}{\partial y}\right) = -\frac{C}{\Delta l}\frac{\partial^2 V_z}{\partial t^2} \tag{3.16a}$$

$$\frac{\partial}{\partial y}\left(\frac{\partial i_y}{\partial t}\right) = -\frac{\Delta l}{L}\frac{\partial^2 V_z}{\partial y^2}. \tag{3.16b}$$

Subtracting Eqn.3.16b from Eqn.3.16a gives

$$\frac{\Delta l^2}{L}\frac{\partial^2 V_z}{\partial y^2} = C\frac{\partial^2 V_z}{\partial t^2}. \tag{3.17}$$

Addition of Eqn.3.13 and Eqn.3.17 gives a wave equation for the voltage V_z at the node

$$\frac{\partial^2 V_z}{\partial x^2} + \frac{\partial^2 V_z}{\partial y^2} = \frac{2LC}{\Delta l^2}\frac{\partial^2 V_z}{\partial t^2}. \tag{3.18}$$

Since the inductance of a general inductor is related to the magnetic flux through the current i [3.4], it is seen that

$$L = \frac{\vec{B}}{i} = \frac{\mu_0 i\left(\Delta l^2\right)}{i\Delta l} = \mu_0 \Delta l. \tag{3.19}$$

To determine the capacitance, the general formula for a capacitor of surface area A and plate separation d is used [3.4], where

$$C = \frac{\varepsilon_0 A}{d} = \frac{\varepsilon_0 \Delta l^2}{\Delta l} = \varepsilon_0 \Delta l . \tag{3.20}$$

Substitution of Eqns.3.19,3.20 in Eqn.3.18 yields

$$\frac{\partial^2 V_z}{\partial x^2} + \frac{\partial^2 V_z}{\partial y^2} = 2\varepsilon_0 \mu_0 \frac{\partial^2 V_z}{\partial t^2} . \tag{3.21}$$

Eqn.3.21 shows that the shunt TLM node models a material with constitutive parameters $2\varepsilon_0, \mu_0$.

The impedance of a lossless section of transmission-line is known to be $Z_0 = \sqrt{\mu_0 / \varepsilon_0} = \sqrt{L/C}$ [3.4]. Observing the values of ε_0, μ_0 in Eqn.3.21 it is seen the impedance is $\sqrt{\mu_0 / 2\varepsilon_0}$, hence to model a material with parameters ε_0, μ_0 it is necessary to set

$$Z_0 = \sqrt{2}\sqrt{\frac{\mu_0}{\varepsilon_0}} \tag{3.22}$$

and hence to model free-space Z_0 equates to $\sqrt{2}(376.73)\,\Omega$. The velocity of the material is $v_0 = \Delta l / \sqrt{LC}$ for the section of length Δl. It can be seen here, the velocity will be $1/\sqrt{2\mu_0\varepsilon_0}$, and hence to model a material of ε_0, μ_0 correctly it is necessary to set the velocity to

$$v = \frac{\sqrt{2}}{\sqrt{\varepsilon_0 \mu_0}} . \tag{3.23}$$

The temporal sampling of the model, Δt is defined as

$$\Delta t = \frac{\Delta l}{v}. \tag{3.24}$$

The spatial sampling is defined by the choice of nodal points in the model, for example $\Delta y = D_Y / Y$, where D_Y is the size of the problem in the y direction, and Y is the number of nodes in y. Throughout this thesis, unless otherwise specified, it is assumed $\Delta x = \Delta y = \Delta z = \Delta l$, in this manner the length in the x direction is determined as $X\Delta l$. Providing $\Delta l < \lambda / 10$ it is known the TLM model is of acceptable accuracy [3.8], where λ is the wavelength of the frequency of interest.

The field components are related to the circuit voltage and current as

$$E_z = -\frac{V_z}{\Delta l}, \tag{3.25}$$

$$H_x = \frac{i_y}{\Delta l}, \tag{3.26}$$

and

$$H_y = -\frac{i_x}{\Delta l}. \tag{3.27}$$

3.1.3 Modelling Material Properties

In general, capacitance can be added to the transmission-line sections to model a dielectric material, but the temporal discretisation Δt will not remain constant at the interface between different materials due to the varying propagation velocity between materials [3.3], making the simulation

more difficult. An example of this is shown in Figure 3-3, where two materials of relative permittivity ε_{r1} and ε_{r2} are modelled.

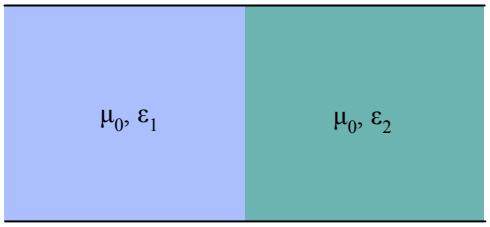

Figure 3-3 - Connection between two materials of varying dielectric permittivity.

For material 1, the velocity of propagation is from Eqn.3.6, $v_1 = 1/\sqrt{\mu\varepsilon_0\varepsilon_{r1}}$, while for material 2, Eqn.3.6 becomes $v_2 = 1/\sqrt{\mu\varepsilon_0\varepsilon_{r2}}$, ignoring the $\sqrt{2}$ factor of TLM. Hence it is seen, the temporal sampling becomes from Eqn.3.24

$$\Delta t_1 = \frac{\Delta l}{v_1}, \tag{3.28a}$$

while for material 2

$$\Delta t_2 = \frac{\Delta l}{v_2}. \tag{3.28b}$$

It is seen, the simulation of material 1 is out of step with material 2. Assuming material 1 is of higher dielectric permittivity, the time step for material 1 is larger than that of material 2, and hence at the interface between the two materials, the computation of material 1 will have to be delayed until field values are ready from material 2.

Alternatively if the time-step is fixed, and the spatial sampling between the two materials is varied, instability and loss of power is caused, as the spatial coordinates will not align between neighbouring nodes.

In light of this, the modelling of dielectric and/or lossy materials is achieved through the use of stubs, which maintains the same velocity throughout the TLM mesh.

Addition of a capacitive stub (open circuit transmission-line) at the node, of length $\Delta l/2$ and hence round trip time, Δt, increases the value of ε (see Eqn.3.20), and allows the simulation of dielectric materials while maintaining temporal and spatial synchronicity at the connection between materials. In a similar manner, the simulation of lossy materials is achieved by inclusion of conductance in the stub.

For a dielectric conductive material Maxwell's equations, are similarly expanded as in Eqns.3.1, with the substitution $\vec{J} = \sigma \vec{E}$, Eqn.3.2 now becomes

$$\frac{\partial H_x}{\partial y} - \frac{\partial H_y}{\partial x} = \varepsilon \frac{\partial E_z}{\partial t} + \sigma E_z \tag{3.29}$$

where σ is the conductivity of the material in S/m.

3.1.4 Modelling Lossy Dielectric Materials

In Figure 3-2 the x directed arm of the free-space shunt node was shown, in Figure 3-4 the x arm of the stub loaded shunt node is given, with the addition of the conductance and capacitance of the stub, where Kirchoff's current law is illustrated.

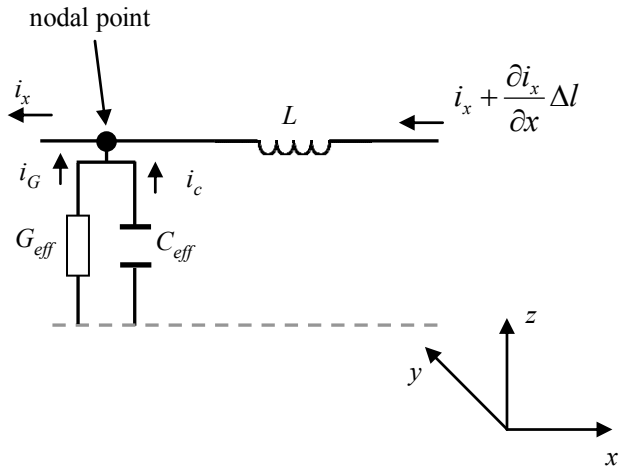

Figure 3-4 - Kirchhoff's current law on stub loaded shunt TLM node, G_{eff} is the effective conductance (stub), and C_{eff} is the effective capacitance (stub + line), the inductance remains unchanged. The dotted grey line is the ground plane.

Using Kirchoff's current law

$$\begin{aligned} -i_x + i_G + i_C + i_x + \frac{\partial i_x}{\partial x}\Delta l = 0 \\ \frac{\partial i_x}{\partial x}\Delta l = -V_z G_{eff} - C_{eff}\frac{\partial V_z}{\partial t} \end{aligned} \tag{3.30}$$

where C_{eff} is the effective capacitance of the stub and node. In a similar manner for the y directed current,

$$\frac{\partial i_y}{\partial y}\Delta l = -V_z G_{eff} - C_{eff}\frac{\partial V_z}{\partial t}. \tag{3.31}$$

Addition of Eqns.3.30-3.31 results in

$$\frac{\partial i_y}{\partial y} + \frac{\partial i_x}{\partial x} = \frac{2}{\Delta l}\left(-V_z G_{eff} - C_{eff}\frac{\partial V_z}{\partial t}\right). \tag{3.32}$$

For a single transmission-line section of length Δl, it was shown $Z_0 = \sqrt{L/C}$, $v = \Delta l / \sqrt{LC}$ and hence $\Delta t = \sqrt{LC}$. Using these it can be shown $L = {Z_0}^2 C$ and $L = \dfrac{\Delta l^2}{v^2 C}$, equating and simplifying gives

$$C = \frac{\Delta t}{Z_0}. \tag{3.33}$$

Similarly, the inductance is related to the time-step as $L = Z_0 \Delta t$ and for the stub $C_{st} = \dfrac{\Delta t}{4 Z_{st}}$ since the line is of length $\Delta l / 2$. In this manner the effective capacitance, inductance and conductance of the stub loaded node in Figure 3-4 is

$$C_{eff} = \frac{\Delta t}{Z_0} + \frac{\Delta t}{4 Z_{st}} \tag{3.34a}$$

$$L = Z_0 \Delta t \tag{3.34b}$$

$$G_{eff} = \frac{G}{2}. \tag{3.34c}$$

Substitution of Eqns.3.34 in Eqn.3.32 yields

$$\frac{\partial i_y}{\partial y} + \frac{\partial i_x}{\partial x} = \frac{1}{\Delta l}\left(- V_z G - \left(\frac{2\Delta t}{Z_0} + \frac{\Delta t}{2 Z_{st}} \right) \frac{\partial V_z}{\partial t} \right). \tag{3.35}$$

Substitution of Eqns.3.25,3.26,3.27 in Eqn.3.35 results in

$$\frac{\partial H_x}{\partial y} - \frac{\partial H_y}{\partial x} = E_z \frac{G}{\Delta l} + \left(\frac{2\Delta t}{Z_0 \Delta l} + \frac{\Delta t}{2 Z_{st} \Delta l} \right) \frac{\partial E_z}{\partial t}, \tag{3.36}$$

from which it is seen by comparison with Eqn.3.29

$$\sigma = \frac{G}{\Delta l} \tag{3.37a}$$

$$\varepsilon = \frac{2\Delta t}{Z_0 \Delta l} + \frac{\Delta t}{2 Z_{st} \Delta l} \tag{3.37b}$$

and $\mu_0 = Z_0 \Delta t / \Delta l$ as before.

Rearranging and simplifying Eqn.3.37b, taking account of the $\sqrt{2}$ factor of propagation and substitution of Eqns.3.22-3.23

$$\varepsilon = \frac{2\Delta t}{Z_0 \Delta l} + \frac{\Delta t / 2}{Z_{st} \Delta l} = \frac{2\Delta t}{Z_0 \Delta l}\left(1 + \frac{Z_0}{4 Z_{st}}\right) = \varepsilon_0 \left(1 + \frac{Z_0}{4 Z_{st}}\right). \tag{3.38}$$

From Eqn.3.38 it is seen

$$\varepsilon_r = 1 + \frac{Z_0}{4 Z_{st}} \tag{3.39}$$

and hence the stub admittance is

$$Y_{st} = \frac{1}{Z_{st}} = \frac{4(\varepsilon_r - 1)}{Z_0}. \tag{3.40}$$

3.1.5 Travelling Wave Form

In the previous section the derivation of the TLM node from Maxwell's equations was shown. To simulate propagation of an electromagnetic field using the node, it is necessary to introduce the travelling wave format.

Figure 3-1a shows the free-space shunt TLM node with four ports labelled from 1 to 4 and corresponding voltage potentials. The node models a cell of

size Δl^2. The Thevenin [3.3] equivalent circuit is formed as in Figure 3-5, and the nodal voltage V_z can be defined in terms of the incident voltage waves on each branch, as

$$
\begin{aligned}
{}_kV_z &= \frac{\dfrac{2V_1^i}{Z_0}+\dfrac{2V_2^i}{Z_0}+\dfrac{2V_3^i}{Z_0}+\dfrac{2V_4^i}{Z_0}}{4\left(\dfrac{1}{Z_0}\right)} \\
&= \frac{V_1^i+V_2^i+V_3^i+V_4^i}{2}.
\end{aligned}
\tag{3.41}
$$

A similar Thevenin circuit is formed for the x and y currents by selecting the nodal ports 1, 3 and 2, 4 respectively. In Figure 3-5 the current flowing in y is shown in the clockwise direction [3.3]

$$i_y = \frac{V_2 - V_4}{Z_0}\ , \tag{3.42}$$

$$i_x = \frac{V_1 - V_3}{Z_0}. \tag{3.43}$$

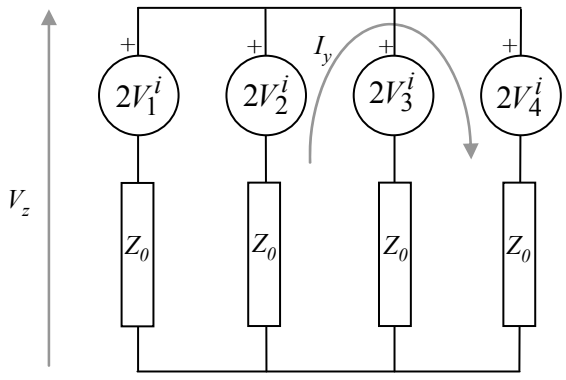

Figure 3-5 - Thevenin equivalent of the 2D shunt TLM node.

The TLM method propagates the voltage waves throughout the mesh by means of a method known as scatter/connection.

The incident voltage upon port 1 of the node, will 'see' a load impedance, Z_L, of three parallel connected lines of impedance Z_0, and hence a reflection at port 1 will be generated. From transmission-line theory,

$$\Gamma = \frac{Z_L - Z_0}{Z_L + Z_0} = \frac{Z_0/3 - Z_0}{Z_0/3 + Z_0} = -\frac{1}{2}, \tag{3.44}$$

while the transmission coefficient is $+1/2$. The reflected voltages can be expressed in matrix form from the incident voltages as

$$\begin{bmatrix} V_1^r \\ V_2^r \\ V_3^r \\ V_4^r \end{bmatrix} = \underline{\underline{S}} \begin{bmatrix} V_1^i \\ V_2^i \\ V_3^i \\ V_4^i \end{bmatrix} \tag{3.45}$$

where $\underline{\underline{S}}$ is the nodal scattering matrix of reflection coefficients, of dimensions 4×4.

In general the total voltage at any port is a sum of reflected and incident voltages, and hence the reflected voltage at port n is

$$V_n^r = V_z - V_n^i. \tag{3.46}$$

Expanding Eqn.3.46 for $n = 1...4$, and placing the resulting four equations in the matrix form of Eqn.3.45, it can be shown the nodal scattering matrix for the shunt TLM node is [3.3]

$$\underline{\underline{S}} = \frac{1}{2}\begin{bmatrix} -1 & 1 & 1 & 1 \\ 1 & -1 & 1 & 1 \\ 1 & 1 & -1 & 1 \\ 1 & 1 & 1 & -1 \end{bmatrix}. \tag{3.47}$$

The connection process states that reflected voltages on ports become incident on neighbouring ports at the next time step as shown in Figure 3-6. In general, the procedure is described by the following four equations

$$\underline{\underline{{}_{k+1}V_1^i}}(x, y-\Delta l) = \underline{\underline{{}_{k}V_3^r}}(x, y) \tag{3.48a}$$

$$\underline{\underline{{}_{k+1}V_2^i}}(x-\Delta l, y) = \underline{\underline{{}_{k}V_4^r}}(x, y) \tag{3.48b}$$

$$\underline{\underline{{}_{k+1}V_3^i}}(x, y+\Delta l) = \underline{\underline{{}_{k}V_1^r}}(x, y) \tag{3.48c}$$

$$\underline{\underline{{}_{k+1}V_4^i}}(x+\Delta l, y) = \underline{\underline{{}_{k}V_2^r}}(x, y) \tag{3.48d}$$

where the subscript k denotes the temporal iteration.

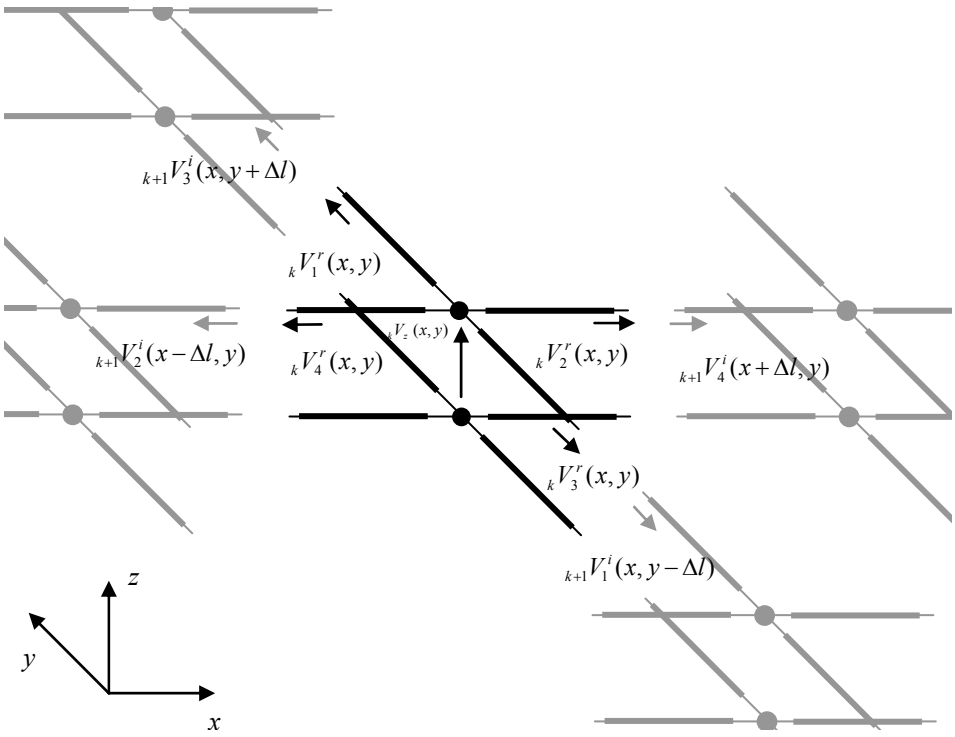

Figure 3-6 - Connection process in 2D TLM, origin is in bottom left.

In a similar manner the travelling wave form for the stub loaded TLM node shown in Figure 3-7 is derived, resulting in [3.3]

$$
\begin{aligned}
{}_kV_z &= \frac{\dfrac{2_kV_1^i}{Z_0}+\dfrac{2_kV_2^i}{Z_0}+\dfrac{2_kV_3^i}{Z_0}+\dfrac{2_kV_4^i}{Z_0}+\dfrac{2_kV_{st}^i}{Z_{st}}}{4\left(\dfrac{1}{Z_0}\right)+\left(\dfrac{1}{Z_{st}}\right)+G_{st}} \\
&= \frac{2_kV_1^i+2_kV_2^i+2_kV_3^i+2_kV_4^i+\dfrac{Z_0\,2_kV_{st}^i}{Z_{st}}}{4+\left(\dfrac{Z_0}{Z_{st}}\right)+Z_0G_{st}}.
\end{aligned}
\tag{3.49}
$$

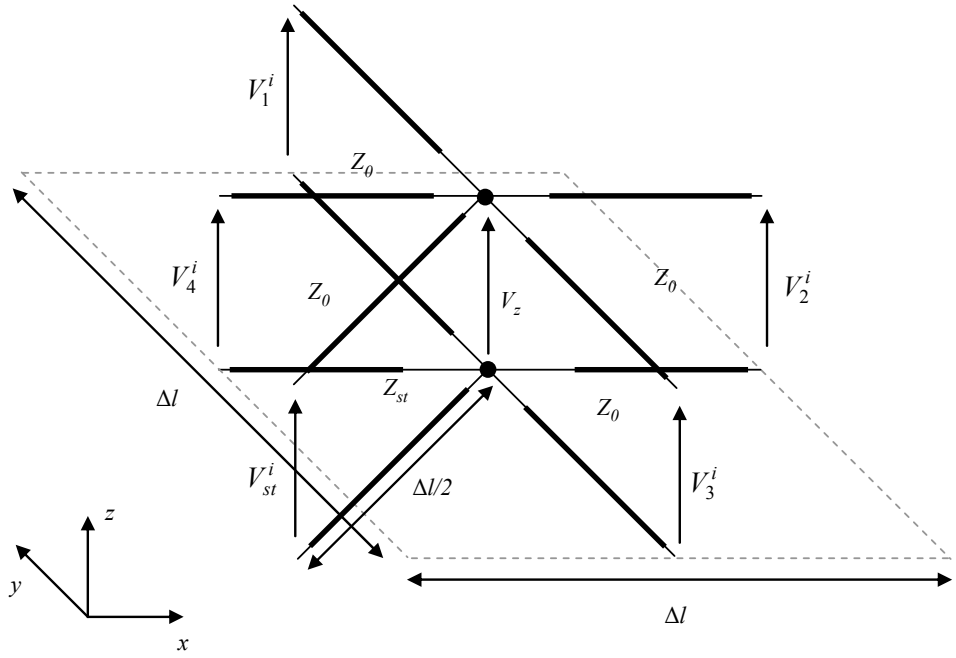

Figure 3-7 - 2D TLM shunt node element with stub, for the modelling of dielectric/lossy materials.

It is customary to define $G_S = Z_0 G_{st}$ and $Z_s = 1/Y_s = Z_{st}/Z_0$, where Y_S is the normalised admittance of the stub, Y_{st}. The reflected voltages are determined from

$$\begin{bmatrix} V_1^r \\ V_2^r \\ V_3^r \\ V_4^r \\ V_{st}^r \end{bmatrix} = \underline{\underline{S}} \begin{bmatrix} V_1^i \\ V_2^i \\ V_3^i \\ V_4^i \\ V_{st}^i \end{bmatrix} \tag{3.50}$$

where $\underline{\underline{S}}$ is the nodal scattering matrix of dimensions 5×5,

$$\underline{\underline{S}} = \left(\frac{1}{Y_{ad}} \right) \begin{bmatrix} 2 - Y_{ad} & 2 & 2 & 2 & 2Y_s \\ 2 & 2 - Y_{ad} & 2 & 2 & 2Y_s \\ 2 & 2 & 2 - Y_{ad} & 2 & 2Y_s \\ 2 & 2 & 2 & 2 - Y_{ad} & 2Y_s \\ 2 & 2 & 2 & 2 & 2Y_s - Y_{ad} \end{bmatrix} \tag{3.51}$$

where $Y_{ad} = 4 + Y_s + G_s$.

The stub connects with itself, as

$$\underline{\underline{{}_{k+1}V_{st}^i}}(x, y) = \underline{\underline{{}_kV_{st}^r}}(x, y). \tag{3.52}$$

From Eqn.3.52 it is seen the stub acts as an energy store. To model magnetic materials inductive stubs are used [3.3].

3.1.6 Boundary Conditions

In electromagnetic simulations of physical problems it is often necessary to define boundary conditions, for example a waveguide has metal walls which define boundary conditions for the electric and magnetic fields. The connection stage of the TLM process for the boundary nodal ports is

$$\underline{\underline{{}_{k+1}V_n^i}}(x, y) = \Gamma \, \underline{\underline{{}_kV_n^r}}(x, y) \tag{3.53}$$

where Γ is a reflection coefficient. For a perfect short circuit boundary condition or electric boundary at a distance of $\Delta l/2$ from nodal port n, the reflection coefficient is

$$\Gamma = \frac{Z_L - Z_0}{Z_L + Z_0} = \frac{0 - Z_0}{0 + Z_0} = -1. \tag{3.54}$$

Similarly, for an open circuit termination, or magnetic boundary, $\Gamma = 1$.

Repetition of Eqns.3.45,3.48 for time $k = 0...N-1$ in the mesh formed by the connection of nodes, constitutes the 2D TLM method for electromagnetic simulation of transverse magnetic fields. A similar derivation is possible for transverse electric fields, which results in the series TLM node [3.3]. It can be shown in this case the scattering matrix $\underline{\underline{S}}$ would become

$$\underline{\underline{S}} = \frac{1}{2}\begin{bmatrix} 1 & 1 & 1 & -1 \\ 1 & 1 & -1 & 1 \\ 1 & -1 & 1 & 1 \\ -1 & 1 & 1 & 1 \end{bmatrix}. \tag{3.55}$$

3.2 3D TLM Symmetrical Condensed Node

In the previous section an in depth derivation of 2D shunt TLM was shown. In this section a node for 3D simulation is derived. The modern form of the 3D TLM node is known as the symmetrical condensed node (SCN). The SCN is considerably more complex, and hence due to space limitations only a working example is given here. Further details can be found in [3.3] [3.8] and [3.9].

The SCN is shown schematically in Figure 3-8, and is visualised as a combination of shunt and series nodes in each direction of propagation. The

scattering matrix for the node is determined through the use of the laws of conservation of power [3.9]. Observation of the expanded Maxwell's equations, Eqns.3.1, relate the electric fields to the magnetic fields, from which the coupling of fields within the node can be determined [3.3]. Eqn.3.56 is derived for the nodal reflected voltages

$$\begin{bmatrix} {}_kV_1^r & {}_kV_2^r & {}_kV_3^r & {}_kV_4^r & {}_kV_5^r & {}_kV_6^r & {}_kV_7^r & {}_kV_8^r & {}_kV_9^r & {}_kV_{10}^r & {}_kV_{11}^r & {}_kV_{12}^r \end{bmatrix}^T \\ = \underline{\underline{S}} \begin{bmatrix} {}_kV_1^i & {}_kV_2^i & {}_kV_3^i & {}_kV_4^i & {}_kV_5^i & {}_kV_6^i & {}_kV_7^i & {}_kV_8^i & {}_kV_9^i & {}_kV_{10}^i & {}_kV_{11}^i & {}_kV_{12}^i \end{bmatrix}^T \quad (3.56)$$

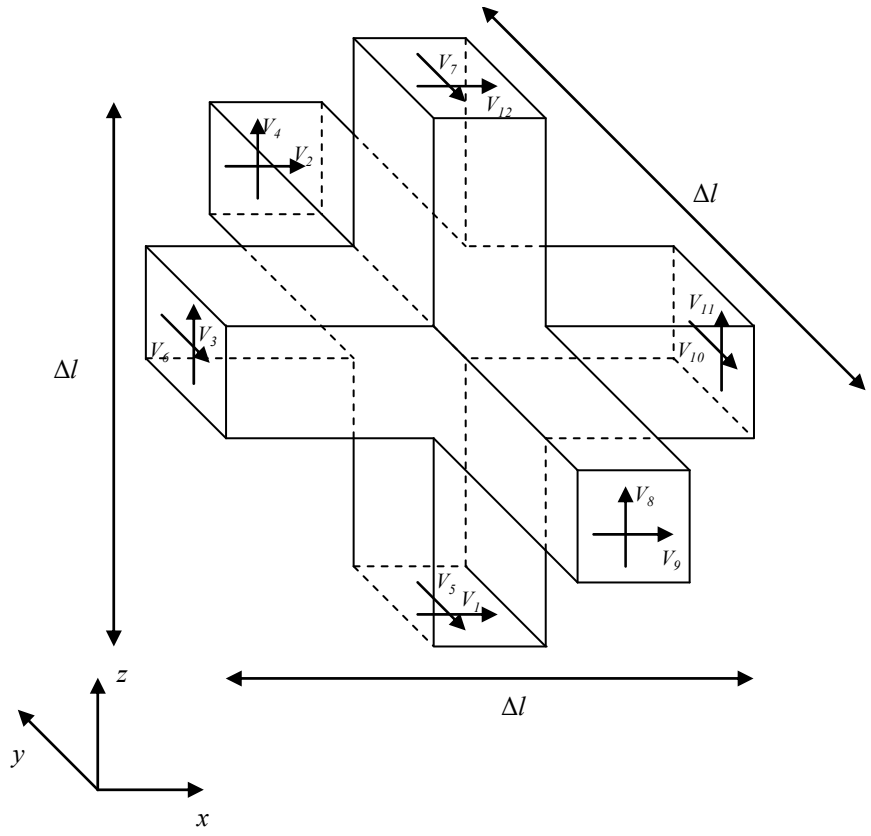

Figure 3-8 - 3D TLM Symmetrical Condensed Node (SCN) equal spatial sampling in *x*, *y* and *z*, the node models a volume of size Δl^3.

where $\underline{\underline{S}}$ is the 12×12 nodal scattering matrix given as [3.3]

$$\underline{\underline{S}} = 0.5\begin{bmatrix} 0 & 1 & 1 & 0 & 0 & 0 & 0 & 0 & 1 & 0 & -1 & 0 \\ 1 & 0 & 0 & 0 & 0 & 1 & 0 & 0 & 0 & -1 & 0 & 1 \\ 1 & 0 & 0 & 1 & 0 & 0 & 0 & 1 & 0 & 0 & 0 & -1 \\ 0 & 0 & 1 & 0 & 1 & 0 & -1 & 0 & 0 & 0 & 1 & 0 \\ 0 & 0 & 0 & 1 & 0 & 1 & 0 & -1 & 0 & 1 & 0 & 0 \\ 0 & 1 & 0 & 0 & 1 & 0 & 1 & 0 & -1 & 0 & 0 & 0 \\ 0 & 0 & 0 & -1 & 0 & 1 & 0 & 1 & 0 & 1 & 0 & 0 \\ 0 & 0 & 1 & 0 & -1 & 0 & 1 & 0 & 0 & 0 & 1 & 0 \\ 1 & 0 & 0 & 0 & 0 & -1 & 0 & 0 & 0 & 1 & 0 & 1 \\ 0 & -1 & 0 & 0 & 1 & 0 & 1 & 0 & 1 & 0 & 0 & 0 \\ -1 & 0 & 0 & 1 & 0 & 0 & 0 & 1 & 0 & 0 & 0 & 1 \\ 0 & 1 & -1 & 0 & 0 & 0 & 0 & 0 & 1 & 0 & 1 & 0 \end{bmatrix}. \quad (3.57)$$

The connection process is identical to that for the 2D node, where for example

$$\underline{\underline{{}_{k+1}V_1^i}}(x, y, z + \Delta l) = \underline{\underline{{}_kV_{12}^r}}(x, y, z), \quad (3.58a)$$

$$\underline{\underline{{}_{k+1}V_2^i}}(x, y - \Delta l, z) = \underline{\underline{{}_kV_9^r}}(x, y, z), \quad (3.58b)$$

$$\underline{\underline{{}_{k+1}V_3^i}}(x + \Delta l, y, z) = \underline{\underline{{}_kV_{11}^r}}(x, y, z), \quad (3.58c)$$

etc.

The electric and magnetic fields are determined from the x, y and z directed voltages and currents respectively, for example

$$E_z = -\frac{V_z}{\Delta l} = -\frac{{}_kV_3^i + {}_kV_4^i + {}_kV_8^i + {}_kV_{11}^i}{2\Delta l}, \quad (3.59a)$$

$$H_x = -\frac{{}_kV_4^i - {}_kV_5^i + {}_kV_7^i - {}_kV_8^i}{2Z_0\Delta l}, \quad (3.59b)$$

$$H_y = -\frac{{}_kV_1^i - {}_kV_3^i + {}_kV_{11}^i - {}_kV_{12}^i}{2Z_0\Delta l}. \quad (3.59c)$$

Similarly open/short circuit boundaries are modelled using Eqn.3.53, with the exception it is now necessary to take both ports at the node connection into account, for example, a short circuit boundary through z would be enforced at ports 7 and 12 of the node below and ports 1 and 5 of the node above the boundary.

The $\sqrt{2}$ factor of the series and shunt nodes combined into the SCN effectively cancel each other [3.3], and the velocity within the 3D SCN simulation is $v = \Delta l / 2\Delta t$. Modelling of dielectric, magnetic and lossy materials are possible through the use of stubs. Modelling of dielectric, magnetic and lossy materials in 3D is not covered here as all time-reversal modelling in 3D is done in the presence of metal.

3.3 Numerical Time-Reversal

This section will describe the time-reversal process using the numerical TLM method. The TLM time-reversal is performed through the use of the time-reversal-cavity [3.10] [3.11] [3.12]. For a 2D rectangular time-reversal-cavity shown in Figure 3-9, the simulation space is bounded on four sides by absorbing boundaries, known as time-reversal-mirrors [3.11]. The time-reversal-mirrors are placed a distance of $\Delta l / 2$ from the neighbouring TLM node, where Δl is the spatial sampling of the model.

The TLM time-reversal process has two stages: forward simulation, during which all time history is recorded at the time-reversal-mirrors, and the reverse stage, at which the recorded information is re-injected into the time-reversal-cavity. In the case of device optimisation, multiple time-reversal simulations are needed in order to converge to a desired performance [3.13].

To capture the forward-time electric field within the cavity, the time-reversal-mirrors sample the reflected voltages scattered from the neighbouring TLM nodes,

$$\underline{\underline{{}_1V_{TRM}}}(x,k) = \underline{\underline{{}_kV_1^r}}(x,Y-1) \tag{3.60a}$$

$$\underline{\underline{{}_2V_{TRM}}}(y,k) = \underline{\underline{{}_kV_2^r}}(X-1,y) \tag{3.60b}$$

$$\underline{\underline{{}_3V_{TRM}}}(x,k) = \underline{\underline{{}_kV_3^r}}(x,0) \tag{3.60c}$$

$$\underline{\underline{{}_4V_{TRM}}}(y,k) = \underline{\underline{{}_kV_4^r}}(0,y)\,. \tag{3.60d}$$

The time-reversal-mirrors act as matched boundaries during the forward simulation. $\underline{\underline{{}_{1,3}V_{TRM}}}$ are of dimensions $X \times N$ and $\underline{\underline{{}_{2,4}V_{TRM}}}$ are of dimensions $Y \times N$, where X, Y and N are the longitudinal nodes, transverse nodes and temporal iterations respectively. To reach steady state in a numerical simulation, N is much larger than X and Y, requiring significant memory.

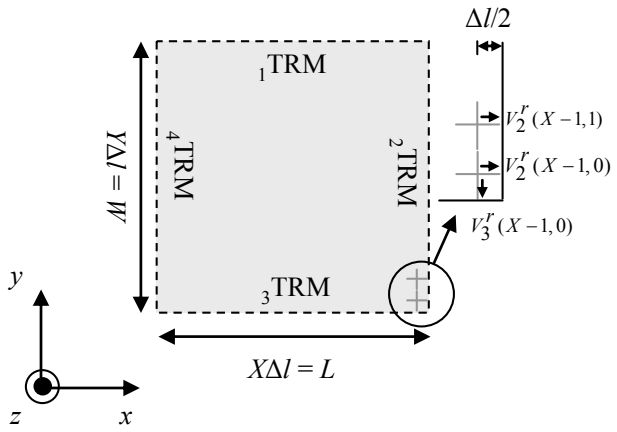

Figure 3-9 - General 2D time-reversal-cavity, electric and magnetic fields are incident upon the bounding surfaces, termed time-reversal-mirrors (TRM).

In the reverse stage of the time-reversal process, the time-reversal-mirrors act as line sources, re-injecting the time sampled reflected voltages from the forward simulation as incident voltages upon the neighbouring TLM nodes in reverse time order

$$\underline{\underline{{}_kV_1^i}}(x,Y-1) = \underline{\underline{{}_1V_{TRM}}}(x,k) \tag{3.61a}$$

$$\underline{\underline{{}_kV_2^i}}(X-1,y) = \underline{\underline{{}_2V_{TRM}}}(y,k) \tag{3.61b}$$

$$\underline{\underline{{}_kV_3^i}}(x,0) = \underline{\underline{{}_3V_{TRM}}}(x,k) \tag{3.61c}$$

$$\underline{\underline{{}_kV_4^i}}(0,y) = \underline{\underline{{}_4V_{TRM}}}(y,k)\,. \tag{3.61d}$$

The reverse process continues for iterations $k = N-1, N-2, \ldots 0$, at which time the reverse simulation stops.

To implement time-reversal within TLM, it is only necessary to reverse the scattering process, i.e. find the incident waves from the known reflected waves. The nodal scattering matrix $\underline{\underline{S}} = \underline{\underline{S}}^{-1}$ for all TLM nodes, and hence the inverse TLM algorithm is identical to the forward TLM. In general this result holds, providing the material is linear and isotropic.

Inversion of the scattering matrix alone does not guarantee time-reversal will be valid. Intuitively, loss in the forward stage, results in gain in reverse. For this reason, lossy materials are more difficult for use with time-reversal, since gain in a numerical procedure, such as TLM, will often result in instability. Investigation of time-reversal in lossy materials is the subject of the following chapter.

3.4 Conclusion

This chapter introduced the 2D and 3D TLM methods. The 2D and 3D nodes were given, and the relation between the wave equation, and the discrete travelling wave form was shown. The chapter concluded by introducing the TLM time-reversal-cavity for numerical simulation of time-reversal. It was shown the scattering matrix for forward propagation in TLM is equal to its inverse, giving the same core algorithm for reverse simulation.

The next chapter begins the original research of this thesis, with an investigation into the spatial filtering of the time-reversal-cavity, and the

effect temporal truncation and evanescent fields have in a time-reversal simulation.

3.5 References

[3.1] T. Itoh, ed., *Numerical Techniques for Microwave and Millimeter-wave Passive Structures*. John Wiley & Sons Inc, New York, NY, 1989.

[3.2] P. B. Johns and R. L. Beurle, "Numerical solution of 2-Dimensional Scattering Problems Using a Transmission Line Matrix," *Proceedings of the IEEE*, vol. 118, pp. 1203–1208, September 1971.

[3.3] C. Christopoulos, *The Transmission-line Modeling Method: TLM*. John Wiley & Sons/IEEE Publications, New York, NY, 1995.

[3.4] R. Ludwig and P. Bretchko, *RF Circuit Design Theory and Applications*. Prentice-Hall, Upper Saddle River, NJ, 2000.

[3.5] J. D. Kraus and D. Fleisch, *Electromagnetics with Applications*. McGraw Hill, New York, NY, 5th ed., 1999.

[3.6] D. de Cogan, W. J. O'Connor, and S. Pulko, *Transmission Line Matrix (TLM) in Computational Mechanics*. CRC Press, London, 2005.

[3.7] "MPICH: Message Passing Interface." Online at: http://www.mcs.anl.gov/research/projects/mpich2/, Retrieved: 03/01/2009.

[3.8] W. J. R. Hoefer, "The Transmission-Line Matrix Method - Theory and Applications," *IEEE Transactions on Microwave Theory and Techniques*, vol. 33, pp. 882–893, October 1985.

[3.9] P. B. Johns, "A Symmetrical Condensed Node for the TLM Method," *IEEE Transactions on Microwave Theory and Techniques*, vol. 35, pp. 370–377, April 1987.

[3.10] R. Carminati, R. Pierrat, J. de Rosny, and M. Fink, "Theory of the Time-Reversal Cavity for Electromagnetic Fields," *Optics Letters*, vol. 32, pp. 3107–3109, November 2007.

[3.11] D. Cassereau and M. Fink, "Time Reversal of Ultrasonic Fields - Part III: Theory of the Closed Time-Reversed Cavity," *IEEE Transactions on Ultrasonics, Ferroelectrics, and Frequency Control*, vol. 39, pp. 579–592, September 1992.

[3.12] R. Sorrentino, P. P. So, and W. J. R. Hoefer, "Numerical Microwave Synthesis by Inversion of the TLM Process," pp. 1273–1277, 21st European Microwave Conference Digest, Stuttgart, Germany, 4-6 October 1991.

[3.13] I. Scott, A. Vukovic, and P. Sewell, "Krylov acceleration techniques for time-reversal design applications," *Accepted, IEEE Microwave Theory and Techniques*.

4. Temporal Truncation and Evanescent Fields

The previous chapter has shown that numerical time-reversal requires significant computational resources. Both the practical need to truncate the simulation time and finite machine precision limit the fidelity of the reverse process and a quantitative study of these effects is undertaken in this chapter. The use of Prony extrapolation to compensate the effects of truncated simulations and in order to significantly reduce the memory requirements is explored. Moreover, the derogatory consequences of finite computational precision are important when evanescent fields are present and theoretical predictions are compared with practical results. The chapter uses the example of single and multiple source reconstruction under time-reversal to demonstrate the above problems. The impact of lossy materials is also briefly discussed.

4.1 Temporal Truncation and Prony's Method

This section will investigate the effect of temporal truncation of the simulation and then proceed with the implementation of Prony's series to predict future behaviour of a wave form.

A forward numerical simulation of a physical structure reaches the steady state after N temporal iterations, at time $N\Delta t$, where Δt is the temporal

discretisation. In the case of numerical time-reversal, the situation is complicated by the need to store the full time-history of the forward simulation. Theoretically the original source will be perfectly reconstructed in both time and space by an ideal time-reversal process. However, when the forward simulation is truncated, even for large N, there are waves in the cavity that do not reach the time-reversal-mirrors. It can hence be assumed that source power remains in the cavity; this power is lost when the cavity is reset for the reverse stage.

In order to ameliorate the need for long run times, the temporal Prony series can be used to predict the future behaviour of a discrete temporal waveform, based on a given set of known samples. Its use has been successfully demonstrated in the finite difference time domain [4.1] and transmission-line modelling (TLM) [4.2] methods, to extrapolate the temporal history of a simulation for accurate computation of scattering parameters. However, perhaps because of the complexity of the Prony method, due to the need to solve a least squares optimisation problem in the formulation of the series, it has received limited attention. It is emphasised here that the solution to the least squares problem is of minimal computational impact in comparison to the numerical simulation.

The Prony series is effectively used to predict the effect of field transients still within the structure when the forward simulation is truncated. Using the Prony series, a time sampled waveform is approximated as

$$\underline{F_P}(k) = \sum_{u=0}^{U-1} \underline{B}(u) \exp\left(\underline{\Lambda}(u) k \Delta t\right) \tag{4.1}$$

where U is the number of poles in the series and $\underline{B}$, the weightings of each basis function.

The objective is to obtain the closest match possible between the Prony generated waveform, $\underline{F_P}(k)$, and the true waveform stored in the time-reversal-mirrors, termed $\underline{F}(k)$ in this discussion, using the minimum number of poles, U.

The term $\underline{\Lambda}(u)$ represents a pole on an Argand diagram [4.3]. The process of determining the values of $\underline{\Lambda}$ and $\underline{B}$ can be done using a least squares approach [4.1] [4.4] [4.5], and is now described. The process has two stages; firstly the matrix equation relating the values for $\underline{F}$ to a polynomial $\underline{P}$, termed the Prony polynomial [4.6], is formed as

$$\begin{bmatrix} \underline{F}(U-1) \\ \underline{F}(U) \\ \vdots \\ \vdots \\ \underline{F}(N) \\ \underline{F}(N-1) \end{bmatrix} = \begin{bmatrix} \underline{F}(U-1) & \underline{F}(U-2) & \cdots & \underline{F}(1) & \underline{F}(0) \\ \underline{F}(U) & \underline{F}(U-1) & \cdots & \underline{F}(2) & \underline{F}(1) \\ \vdots & \vdots & \ddots & \vdots & \vdots \\ \vdots & \vdots & \iddots & \vdots & \vdots \\ \underline{F}(N) & \underline{F}(N-1) & \cdots & \underline{F}(N-U+1) & \underline{F}(N-U) \\ \underline{F}(N-1) & \underline{F}(N-2) & \cdots & \underline{F}(N-U) & \underline{F}(N-U-1) \end{bmatrix} \begin{bmatrix} \underline{P}(0) \\ \underline{P}(1) \\ \vdots \\ \vdots \\ \underline{P}(U-2) \\ \underline{P}(U-1) \end{bmatrix}. \tag{4.2}$$

The values for $\underline{P}$ are found using least squares [4.2], where N is the number of temporal samples in a single row of the time-reversal-mirror. A separate Prony series is required for each spatial row within each time-reversal-mirror. The values $\underline{P}(u)$ form the polynomial, $\sum_{u=0}^{U-1} \underline{P}(u)\varphi^u$. Equating the polynomial to zero, and solving for φ, gives the roots, which can be shown to equate to the values $\exp(\underline{\Lambda}(u))$ [4.5], therefore $\underline{\Lambda}$, the complex poles of Eqn.4.1, can be found from

$$\underline{\Lambda}(u) = \ln\left(\exp\left(\underline{\Lambda}(u)\right)\right). \tag{4.3}$$

Secondly, from the values of $\exp(\underline{\Lambda}(u))$ found in Eqn.4.3, a matrix equation relating $\underline{F}$ to the values $\underline{B}$ is formed as [4.5]

$$\begin{bmatrix} \underline{F}(0) \\ \underline{F}(1) \\ \vdots \\ \vdots \\ \underline{F}(N-2) \\ \underline{F}(N-1) \end{bmatrix} = \begin{bmatrix} \exp(\underline{\Lambda}(0))^0 & \exp(\underline{\Lambda}(1))^0 & \cdots & \exp(\underline{\Lambda}(U-1))^0 \\ \exp(\underline{\Lambda}(0))^1 & \exp(\underline{\Lambda}(1))^1 & \cdots & \exp(\underline{\Lambda}(U-1))^1 \\ \vdots & \vdots & \ddots & \vdots \\ \vdots & \vdots & \ddots & \vdots \\ \exp(\underline{\Lambda}(0))^{N-2} & \exp(\underline{\Lambda}(1))^{N-2} & \cdots & \exp(\underline{\Lambda}(U-1))^{N-2} \\ \exp(\underline{\Lambda}(0))^{N-1} & \exp(\underline{\Lambda}(1))^{N-1} & \cdots & \exp(\underline{\Lambda}(U-1))^{N-1} \end{bmatrix} \begin{bmatrix} \underline{B}(0) \\ \underline{B}(1) \\ \vdots \\ \vdots \\ \underline{B}(U-2) \\ \underline{B}(U-1) \end{bmatrix}. \quad (4.4)$$

Solving Eqn.4.4 for $\underline{B}$ is performed by re-expressing Eqn.4.4 in the form

$$\underline{F} = \underline{\underline{E}}\,\underline{B} \quad (4.5)$$

where $\underline{\underline{E}}$ is of dimensions $N \times U$, $\underline{B}$ is a vector of dimension U, and $\underline{F}$ is of dimension N. Multiplication of Eqn.4.5 by $\underline{\underline{E}}^T$, gives

$$\underline{\underline{E}}^T \underline{F} = \underline{\underline{E}}^T \underline{\underline{E}}\,\underline{B}, \quad (4.6)$$

rearranging Eqn.4.6 allows $\underline{B}$ to be evaluated as

$$\underline{B} = \left(\underline{\underline{E}}^T \underline{\underline{E}}\right)^{-1} \left(\underline{\underline{E}}^T \underline{F}\right). \quad (4.7)$$

Prony's method in this form can be used to temporally extrapolate the reverse stage of the time-reversal process without the need to compute the forward phase for the full number of temporal iterations. This reduces the time-reversal-mirrors size, and the simulation runtime.

4.1.1 Results

This section shows the impact of temporal truncation on the accuracy of a source reconstruction. In this case a moderate number of time steps are employed for the forward simulation and the time-reversal-mirror values that have been lost by truncating are predicted based upon the available values for each sample point. The reverse simulation runtime will then

exceed that of the forward simulation by the number of predicted time steps, where the prediction simply evaluates the Prony series for $k > N$. A 2D parallel plate waveguide laterally bounded by magnetic walls is shown in Figure 4-1, with two time-reversal-mirrors located at the input and output ports respectively.

$$\underline{\underline{{}_4V_{TRM}}}(y,k) = \underline{\underline{{}_kV_4^r}}(0,y) \tag{4.8a}$$

$$\underline{\underline{{}_2V_{TRM}}}(y,k) = \underline{\underline{{}_kV_2^r}}(X-1,y) \tag{4.8b}$$

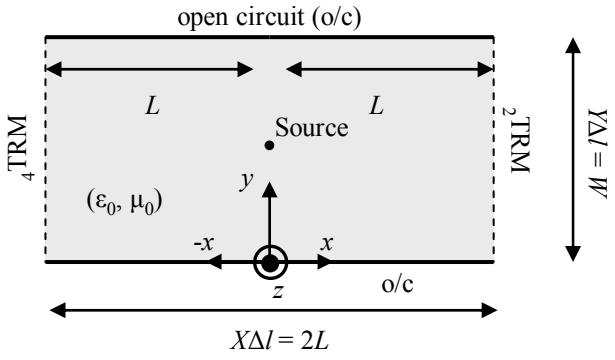

Figure 4-1 - 2D air-filled time-reversal-cavity, Δl is the spatial sampling, X and Y are the nodes in the longitudinal and transverse directions respectively.

The waveguide is defined and modelled using $Y = 151$, giving $\Delta l = 0.15\,\text{mm}$, $\Delta t = 3.57e-13\,\text{s}$, $X = Y = 151$, $L = W/2$ and $W = 22.86\,\text{mm}$. The number of temporal iterations are $N = 500$, $N = 1000$, $N = 10000$ and $N = 100000$. An impulsive source excites the cavity at the source location. The reconstructed source field E_z on the surface of the cavity, for the cases 500 and 10000 temporal iterations, is as shown in Figure 4-2a,b respectively, where a contour display with 5 levels is shown. Clearly simulation for fewer time steps results in increased spatial spreading of the reconstructed source and thus makes a notable contribution to inaccuracy.

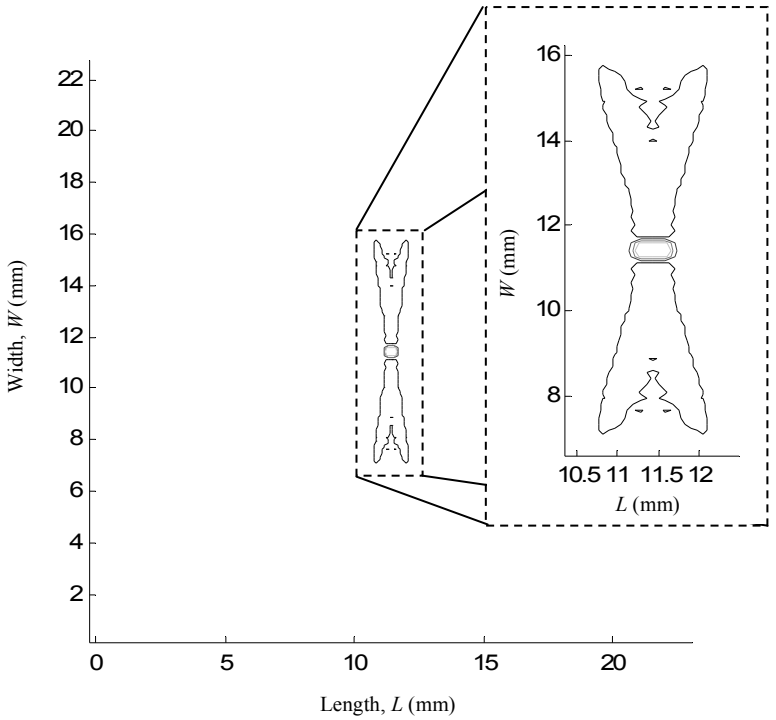

a)

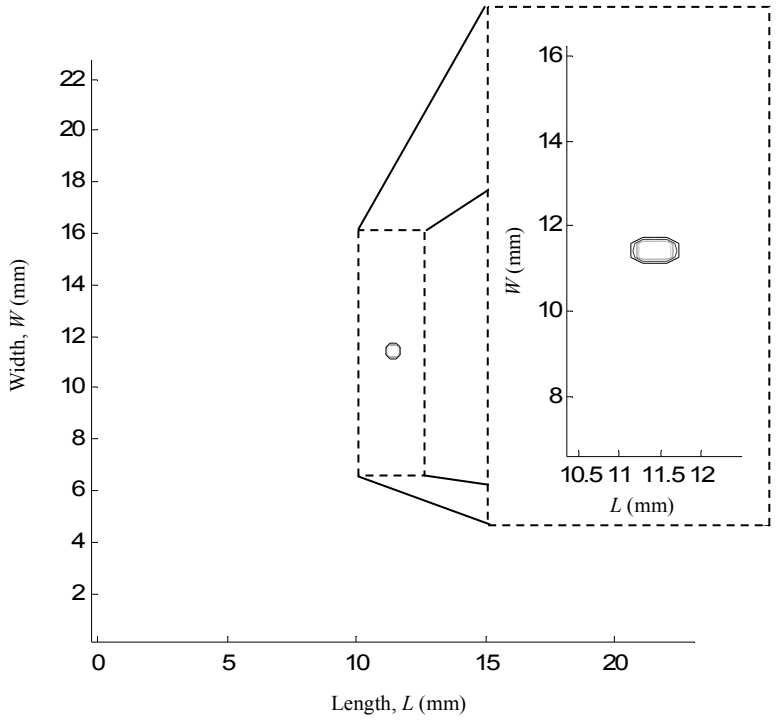

b)

Figure 4-2 - Time-reversed electric field with a) N = 500, and b) N = 10000. Δl = 0.15mm, Δt = 3.57e-13s, X = 151, Y = 151, L = W/2 and W = 22.86mm, a total of 5 contours are shown.

The electric field across the transverse direction at the source, $x = 0$ and $k = 0$ is shown in Figure 4-3, and compared to the original input source. It is seen, that for the shorter runtime significant accuracy has been lost, and that better source reconstruction is achieved for the longer runtimes.

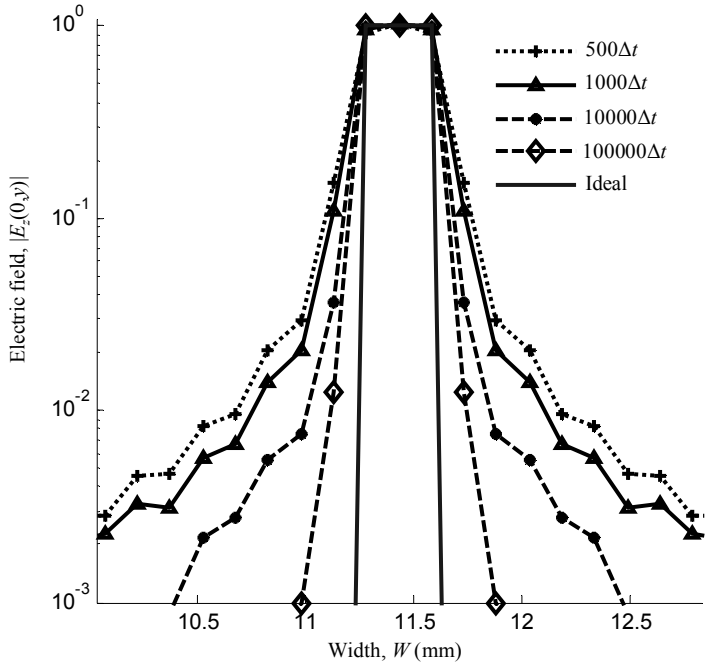

Figure 4-3 - Time-reversed electric field across width of waveguide at x = 0, for N = 500, N = 1000, N = 10000 and N = 100000. Δl = 0.15mm, Δt = 3.57e-13s, X = 151, Y = 151, L = W/2 and W = 22.86mm.

In many cases, long runtimes are not possible and a way of reducing this computational requirement is needed.

In practice, when using the Prony method for time-reversal it is not necessary to match a Prony series for the full number of temporal samples initially stored in the time-reversal-mirrors. The Prony series is required to extrapolate the transient field, and so should only be matched towards the end of the time-reversal-mirror data of the forward stage.

In order to measure the applicability of Prony's method for time-reversal, the example of Figure 4-1 is repeated in Figure 4-4a, where a Prony series

for each transverse sample point in the time-reversal-mirrors with $U = 18$ poles, was matched to the last 150 samples from forward simulations of $N = 500$, $N = 5000$ and $N = 7500$ and used to generate the remaining samples to reverse for $N = 10000$. The figure shows how the fidelity of the source reconstruction using the Prony series compares with the simply truncated cases. Clearly the Prony series offers a valuable improvement in accuracy and has reduced time-reversal-mirrors storage by 95%, 50% and 25% respectively. Unfortunately the number of poles required for the Prony series is largely problem dependant. Too few and a poor extrapolation is seen, too many and the least squares procedure becomes ill-conditioned [4.5]. For this particular example 18 poles was verified to be optimum. In Figure 4-4b the samples stored at $y = W/2$ in the time-reversal-mirror at time-steps $350 - 400$ for $N = 500$ are shown for comparison with the Prony extrapolated waveform using $U = 18$ poles, which shows the close match between the time-reversal-mirrors and the Prony extrapolated form for the known samples.

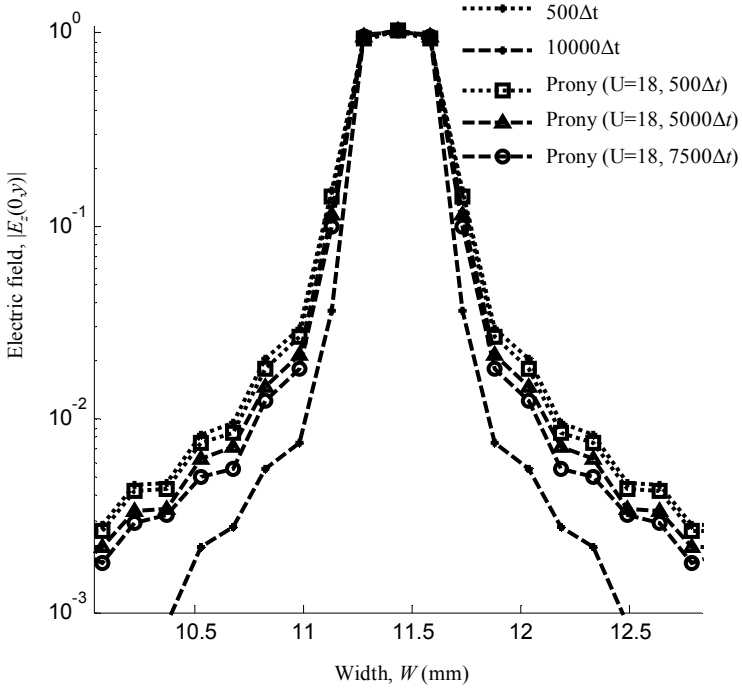

a)

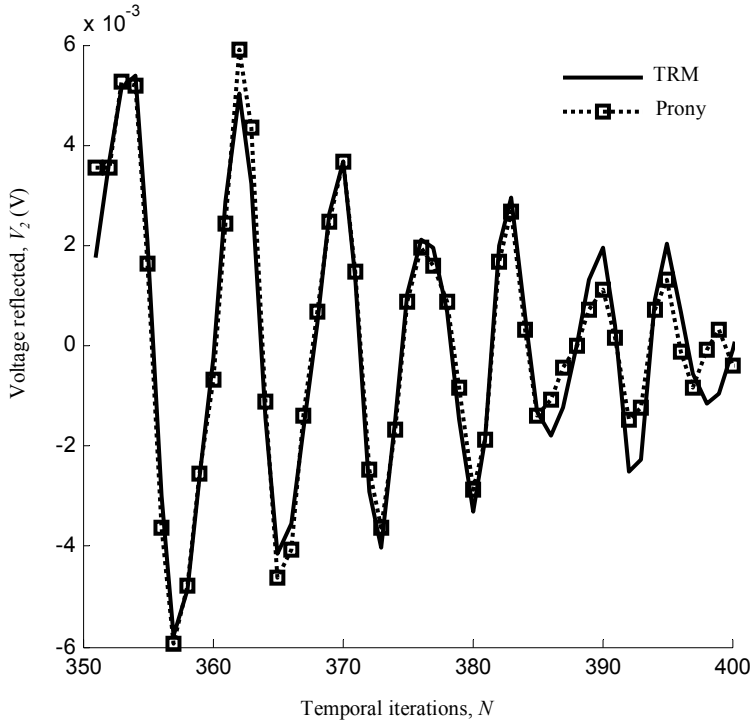

b)

Figure 4-4 - a) Time-reversed electric field across width of waveguide at x = 0. N = 500, N = 5000 and N = 7500 original samples, extrapolated to 10000 using Prony's method with 18 poles matched over last 150 samples, compared with the two original simulations of N = 500 and N = 10000. b) Prony series matched to data in time-reversal-mirror at y = $W/2$ at output port, samples 350-400.

4.1.1.1 Multiple Sources

Time-reversal recovery of two sources in relative proximity to one another further illustrates the loss of spatial resolution caused by truncation of the forward runtime. Two impulse sources at $x = 0$, are placed in the time-reversal-cavity of Figure 4-1, separated initially by a distance of S in y.

The separation distance after time-reversal is measured as the distance between the second moment of each source [4.3]. For the source in the lower half of the cavity, the second moment reads

$$M_2 = \sqrt{\sum_{y_1}^{y_2} \left(\underline{\underline{E_z}}(0, y) - \mu \right)^2} \tag{4.9}$$

where μ is the mean amplitude across the transverse region y_1 to y_2 (see Figure 4-6a overlay). This approach is used to reduce spurious measurements, resulting from poor resolution in the recovered field, as was seen in Figure 4-2 for a single source.

The initial source separation is $S = 65\Delta l = 1.65\,\text{mm}$, $\Delta l = 0.0253\,\text{mm}$, $\Delta t = 5.98e-14\,\text{s}$, $X = 901$ and $Y = 901$, where L and W are as previously defined. The increased spatial sampling is necessary to accurately measure the source separation. Figure 4-5 shows the change in the measured source separation with increasing simulation runtime, N. It is seen, with increasing runtime N, the time-reversal simulation is more accurate, and the measured source separation approaches the known separation.

A Prony extrapolation with 45 poles matched to the last 100 temporal samples in the time-reversal-mirrors and used to generate a further 1000 temporal iterations during the time-reversal is also shown for comparison in Figure 4-5. The Prony results are seen to reach the known separation for smaller N.

The merging of the two sources is shown in Figure 4-6a, which shows E_z for $N = 750$ time steps. In comparison, Figure 4-6b shows the electric field for $N = 4000$, illustrating the improved resolution. It is seen that, the application of time-reversal techniques using multiple sources is more sensitive to inaccuracies of time-reversal and requires finer spatial discretisation and longer runtimes.

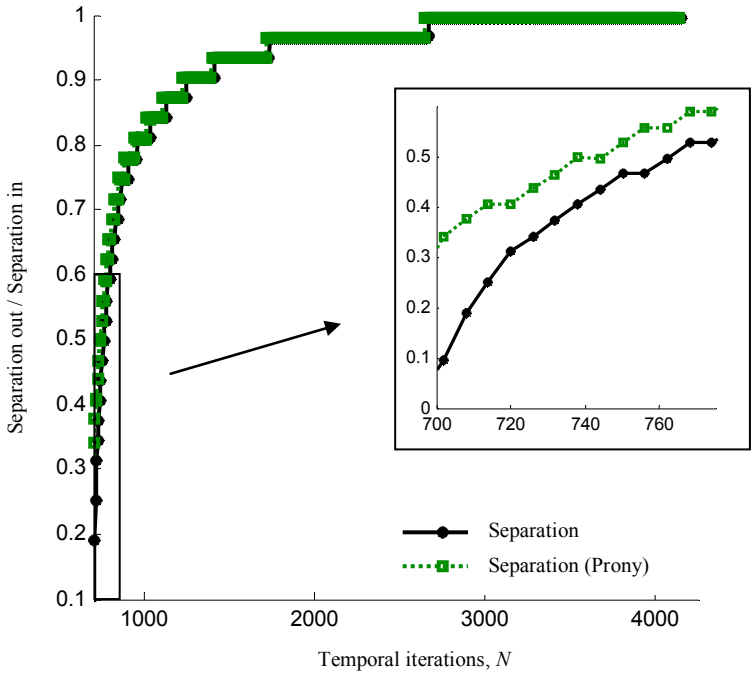

Figure 4-5 - Distance measured between two sources after time-reversal with respect to increasing temporal iterations in the model, Δl = 0.0253mm, Δt = 5.98e-14s, X = 901, Y = 901, L = W/2 and W = 22.86mm.

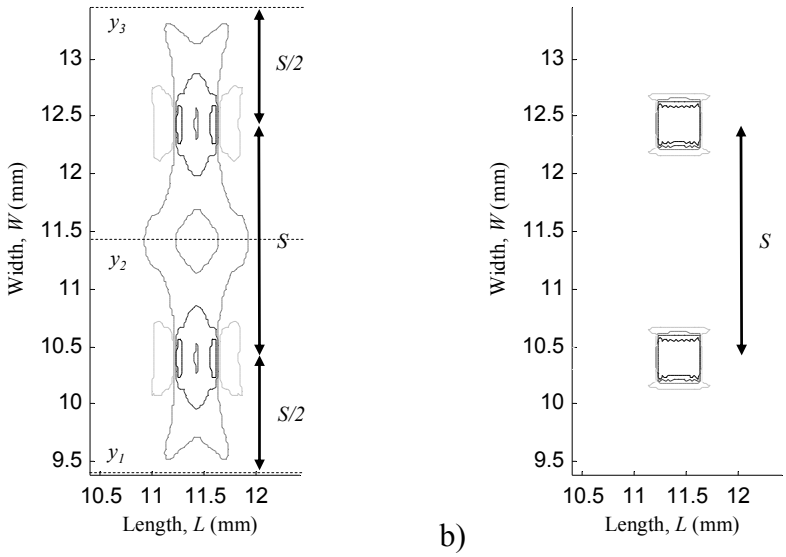

a) b)

Figure 4-6 - Reconstructed sources after time-reversal, a) N=750, b) N = 4000, 5 contour levels are shown. Δl = 0.0253mm, Δt = 5.98e-14s, X = 901, Y = 901, L = W/2 and W = 22.86mm.

Returning briefly to the example of the time-reversed impulse source of Figure 4-3, the measured half width of the source with respect to increasing temporal steps is shown in Figure 4-7. It is seen that even for considerably large runtimes, the measured half width does not converge to the known width of $3\Delta l = 0.45\,\text{mm}$. The remaining error can be attributed to the finite machine precision and evanescent field components. The next section assesses the impact of finite machine precision on time-reversal techniques both analytically and numerically.

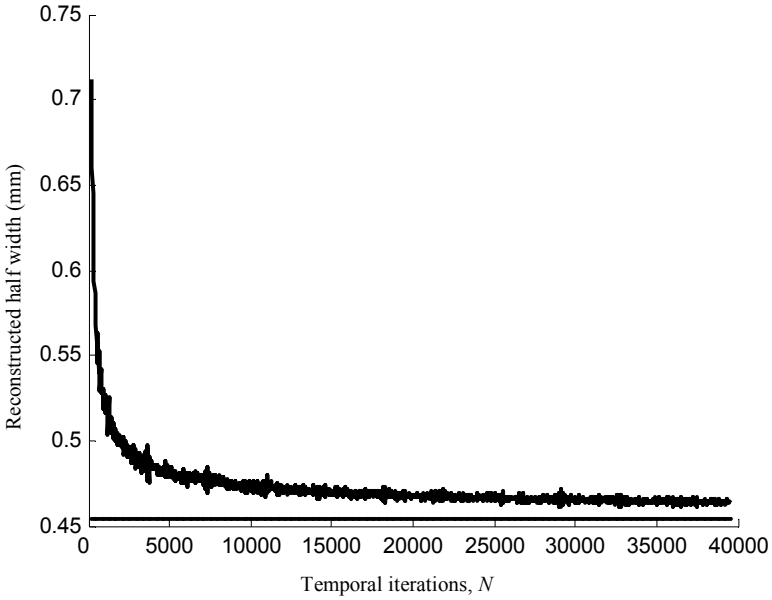

Figure 4-7 - Measured half width of recovered source after time-reversal with respect to increasing TLM simulation time. Δl = 0.15mm, Δt = 3.57e-13s, X = 151, Y = 151, L = W/2 and W = 22.86mm.

4.2 Evanescent Fields in Analytical and Numerical Time-Reversal

Evanescent fields occur in many component structures, including filters, impedance matching networks, antennas etc. A source excites a broad spectrum of both propagating and evanescent modes. On the other hand a numerical simulation has a limited machine precision available [4.7]. If the amplitude of the evanescent modes is below machine precision on arrival at

the time-reversal-mirrors then they will be lost for the purposes of time-reversal and subsequently cause loss of resolution in the reverse simulation.

For the waveguide example of Figure 4-1, the longitudinal distance at which the n th mode is lost can be calculated using Eqn.4.10.

$$L_n = \ln\left(10^{m/\gamma_n}\right), \tag{4.10}$$

which is found by equating the modal propagation term $\exp(-\gamma_n L_n)$, to the significant digit range of the simulation, 10^{-m}, where m is the number of significant digits stored, which can be single precision (7 digits) or double precision (14 digits). If the time-reversal-mirrors are placed such that $L > L_n$, the n th mode will be lost during the forward simulation, and is hence unrecoverable during the reverse stage.

This section analyses evanescent mode loss due to finite machine precision using analytical and numerical time-reversal.

4.2.1 Analytical Analysis of Evanescent Mode Loss

A theoretical investigation predicting the effect of evanescent modal loss on source reconstruction in time-reversal is examined first.

Generally, an impulse source excites a number of modes. The modal distribution of the n th mode propagating in a 2D waveguide in the x direction, with propagation constant, γ_n, can be expressed as

$$\underline{\underline{E_z}}(x, y, n) = A_n \cos\left(\left(y\Delta l + \Delta l/2\right)\frac{n\pi}{W}\right)\exp(-\gamma_n x\Delta l), \tag{4.11}$$

where the propagation constant is given as

$$\gamma_n = \sqrt{\left(\frac{n\pi}{W}\right)^2 - \omega^2 \mu\varepsilon}\,. \tag{4.12}$$

The propagation constant, is either imaginary or real, describing propagating, or, evanescent modes respectively. Substitution of Eqn.4.12 into Eqn.4.10 gives the distance at which the mode n is lost for time-reversal.

Using Eqn.4.11 it is possible to express the total field excited by an impulse in the cavity of Figure 4-1 as the summation of modes

$$\underline{\underline{E_z}}(x,y) = \sum_{n=0,2,4\ldots}^{Y-1} A_n \cos\left(\left(y\Delta l + \Delta l/2\right)\frac{n\pi}{W}\right)\exp(-\gamma_n x\Delta l) \tag{4.13}$$

where A_n are the input amplitudes of the modes n. Only even order modes are considered since the source is symmetric within the cavity, and open circuit boundary conditions are simulated. In this example the cavity medium is free-space, hence the propagation constant of Eqn.4.12 becomes

$$\gamma_n = \sqrt{\left(\frac{n\pi}{W}\right)^2 - \left(\frac{2\pi}{\lambda}\right)^2} \tag{4.14}$$

where λ will take the value for the dominant mode.

For small width sources, the amplitudes of the lower order modes are all of the same order of magnitude on the source plane. However the relative amplitude of the evanescent modes in respect to the dominant mode will rapidly decay, reaching machine precision at a distance L_n from the source plane. Therefore in practice the value of $A_n = 0$ and if this occurs before reaching the time-reversal-mirrors this mode is lost for the purpose of source reconstruction by reverse simulation.

Analytically the effect is demonstrated by truncating Eqn.4.13 to m significant figures at the distance L, i.e.

$$\underline{\underline{E_z}}(L,y)_m = \mathrm{trunc}_m\left(\sum_{n=0,2,4}^{Y-1} A_n \cos\left(\left(y\Delta l + \Delta l/2\right)\frac{n\pi}{W}\right)\exp(-\gamma_n L)\right), \tag{4.15}$$

and the evanescent modes with amplitudes below the machine precision will not be captured by the time-reversal-mirrors and are therefore lost.

For symmetric even order modes, direct application of the Cosine transform [4.8] will recover the modal amplitudes, A_n', of the field in the time-reversal-mirrors at L

$$A_n' = \begin{cases} \dfrac{\sum_{y=0}^{Y-1} \mathrm{trunc}_m\left(\underline{\underline{E_z}}(L,y)\right)\cos\left(\left(y\Delta l + \Delta l/2\right)\frac{n\pi}{W}\right)}{Y}, & n = 0, \\ \dfrac{\sum_{y=0}^{Y-1} \mathrm{trunc}_m\left(\underline{\underline{E_z}}(L,y)\right)\cos\left(\left(y\Delta l + \Delta l/2\right)\frac{n\pi}{W}\right)}{Y/2}, & n = 2,4,\ldots Y-1. \end{cases} \tag{4.16}$$

The value for A_n' is substituted into Eqn.4.13, with $x = 0$ and $y = Y/2$ giving E_z', the field at the source after the modes have been truncated at L.

The consequences of the effect are demonstrated in Figure 4-8 for the absolute normalised difference between E_z, the initial field amplitude, and E_z', the amplitude after the forced truncation is performed, using single (7 digit) and double (14 digit) precision. The transverse nodes were chosen as $Y = 15$, giving a total of 8 symmetric modes, and a spatial sampling in the transverse direction, $\Delta y = 1.52\,\mathrm{mm}$. The longitudinal sampling is $\Delta x = 0.5\,\mathrm{mm}$ and the width $W = 22.86\,\mathrm{mm}$.

The vertical lines show the distance a mode is predicted to be lost as calculated using Eqn.4.10 for single (grey solid) and double (diamonds) precision. It is seen a step in the measure occurs relatively close to where the evanescent mode is predicted to be lost. It initially appears that this is a very significant effect and that placing the time-reversal-mirrors too far from the source will completely undermine the approach.

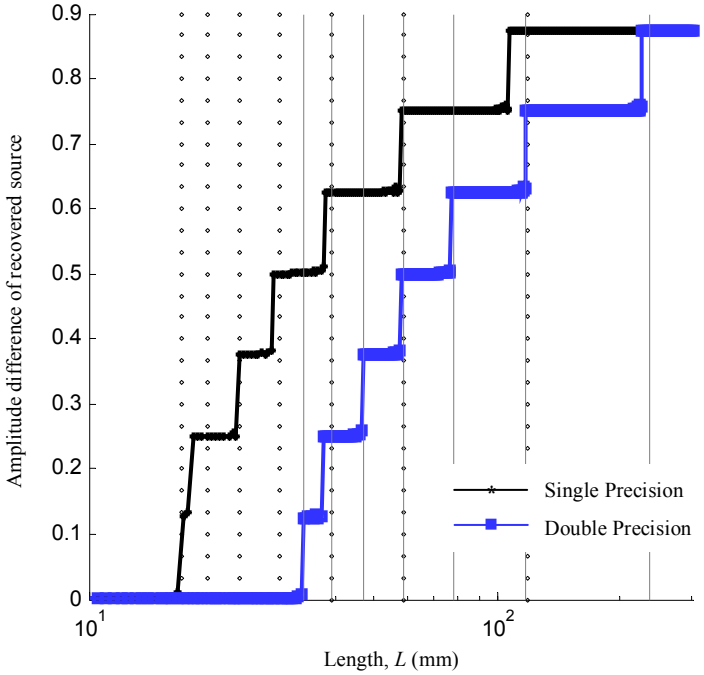

Figure 4-8 - Theoretical mode loss in 2D time-reversal-cavity for single and double precision, vertical lines show expected lengths at which a mode will be lost for single (grey solid) and double (diamonds) precision. Δy = 1.52mm, Δx = 0.5mm, Y = 15 and W = 22.86mm.

This problem is also present for non-guided structures. The same approach can be adapted to investigate the effect of modal loss in a general structure of an impulse source in free space. In Eqn.4.13, the transverse spatial dependence is replaced with the corresponding angular counterpart, and the longitudinal dependence by the corresponding Hankel function, giving

$$\underline{\underline{E_z}}(r,\theta) = \sum_{n=0,2,4...} A_n \exp(-jn\theta) H_n^{(2)}(k_0 r) \tag{4.17}$$

where r is the radial distance from the source and k_0 is the wave number. The field is now measured and artificially truncated cylindrically about the source, at increasing radius r. Figure 4-9 shows the normalised absolute difference between E_z, the initial field amplitude, and E_z', the amplitude after the forced truncation is performed, for varying radius, r. A total of 11 modes are shown up to a maximum radius of 95 m. Again, step like behaviour is seen as the radius increases and is explained by the fact that a particular mode is lost.

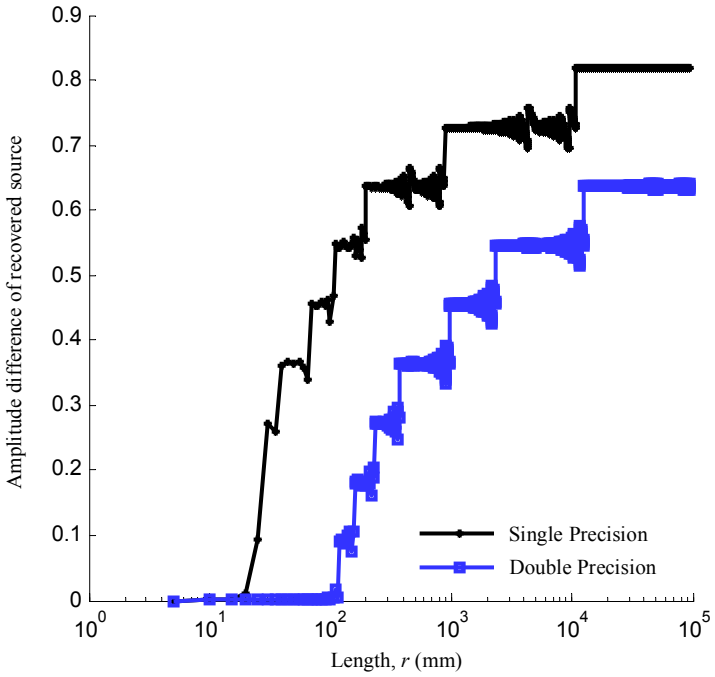

Figure 4-9 - Theoretical cylindrical mode loss example, Δ*l* = 0.5mm, 11 modes are modelled up to a maximum radius of 95m.

4.2.2 Comparison of Analytical and Numerical Time-Reversal of Evanescent Fields

The preceding discussion demonstrated analytically the impact of modal loss. The impulse source employed was a worse case scenario and in practice the importance of the evanescent modes may be less profound. To quantify this argument, a finite width source field distributed as a Gaussian function is now used.

A spatial Gaussian excitation across the transverse dimension of the cavity in Figure 4-1, similarly to the impulse source, will excite a number of propagating and evanescent modes [4.9]

$$\frac{1}{\sqrt{2\pi}\sigma_{in}}\exp\left(-\frac{\left((y\Delta l+\Delta l/2)-W/2\right)^2}{2\sigma_{in}{}^2}\right). \tag{4.18}$$

The number of physically significant evanescent modes is dependant upon the Gaussian spatial half-width, σ_{in}. In general, a spatial Gaussian distribution with a wider half-width has a narrower profile in the modal domain, and hence fewer evanescent modes are exited. Through this reasoning, a distribution that has lost some higher order modal information due to the machine precision will now have a greater half-width after time-reversal, σ_{out}. The smaller σ_{in}, the greater number of evanescent modes are excited which are consequently not captured by the time-reversal-mirrors, and the more substantial the spreading in the output distribution.

The analytical model is repeated using a spatial Gaussian distribution to excite a waveguide of fixed length $L = 20\,\text{mm}$. The modes lost from the Gaussian at L, are then artificially removed from the input Gaussian as done for the impulse source example, and measurement of the distribution half-width is made. In Figure 4-10 the result of σ_{out} with respect to σ_{in}, for

both single and double precision, where $\Delta l = 0.15\,\text{mm}$ and $W = 22.86\,\text{mm}$ is given. As expected, wide sources are reconstructed correctly, while narrow sources become broadened.

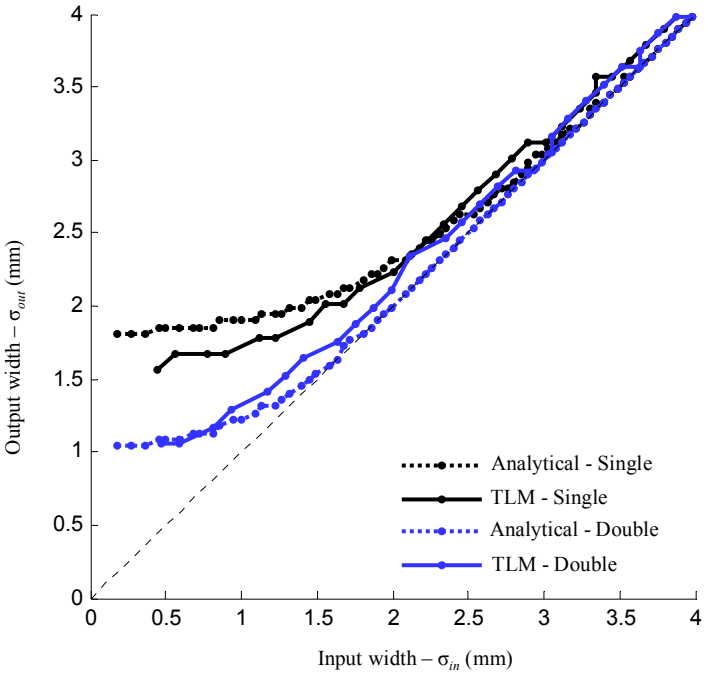

Figure 4-10 - Mode loss of Gaussian distribution predicted (analytical), and measured through time-reversal (TLM), σ_{out} with respect to σ_{in} for varying σ_{in}. Δl = 0.15mm, Δt = 3.57e-13s, X = 132, Y = 151, W = 22.86mm and L = 20mm.

The TLM simulations have been performed with $N = 4000$, $\Delta l = 0.15\,\text{mm}$, $\Delta t = 3.57e-13\,\text{s}$, $X = 132$, $Y = 151$, $W = 22.86\,\text{mm}$ and $L = 20\,\text{mm}$. The Gaussian input is defined identically to the analytical model in Eqn.4.18. The field stored in the time-reversal-mirrors is then time-reversed and re-injected for 4000 iterations, after which the half-width of the reconstructed Gaussian is measured and stored as σ_{out}. It can be seen that both analytical and numerical simulated wide sources are reconstructed more accurately than narrower sources. Very good agreement between the numerical TLM and analytical predicted results is seen.

4.3 Discussion of Lossy Materials

Although, time-reversal approaches are not strictly valid with lossy media as the time-invariance of the wave equation is broken, it is still possible to obtain useful results if the losses are small over the frequency range of interest. In [4.10] this was demonstrated for the example of a dielectric material with small losses using the finite-differences numerical procedure. The effect of losses in the forward simulation is compensated by introducing gain to reverse simulations. However, numerical time-reversal using lossy materials is hindered since the gain will often result in instability.

The effect of lossy materials in time-reversal is investigated using the Argand diagram [4.3]. The propagation constant for the 2D waveguide, Eqn.4.12, is analysed for the case when the waveguide of Figure 4-1 is filled with material with dielectric constant

$$\varepsilon = \varepsilon_0 \varepsilon_r \left(1 - j \frac{\sigma}{\omega \varepsilon_0 \varepsilon_r} \right) \tag{4.19}$$

where σ is the loss in S/m. Eqn.4.10 is rearranged to give

$$\gamma_m = \ln\left(10^{m/L}\right), \tag{4.20}$$

which allows a propagation constant to be determined, for a fixed cavity length and machine precision. This constant is the real component of the highest order mode recoverable during time-reversal with the given machine precision and cavity length.

The modal propagation constant of a mode in a lossy material is determined using Eqn.4.19 in Eqn.4.12. The cavity of Figure 4-1 is excited at 1GHz, the results of Figure 4-11 show the propagation constants for an example cavity of $L = 150\,\text{mm}$ and $W = 22.86\,\text{mm}$, for varying σ in the complex plane.

Higher indices correspond to higher order modes. The light dotted line shows the cut-off level assuming single precision and using Eqn.4.20, while the dark line shows the case for double precision. A mode to the left of the line is lost for the purposes of time-reversal. As the material loss increases, the propagation constants become complex quantities, with increasing decay rates, and more of the evanescent modes are lost as expected.

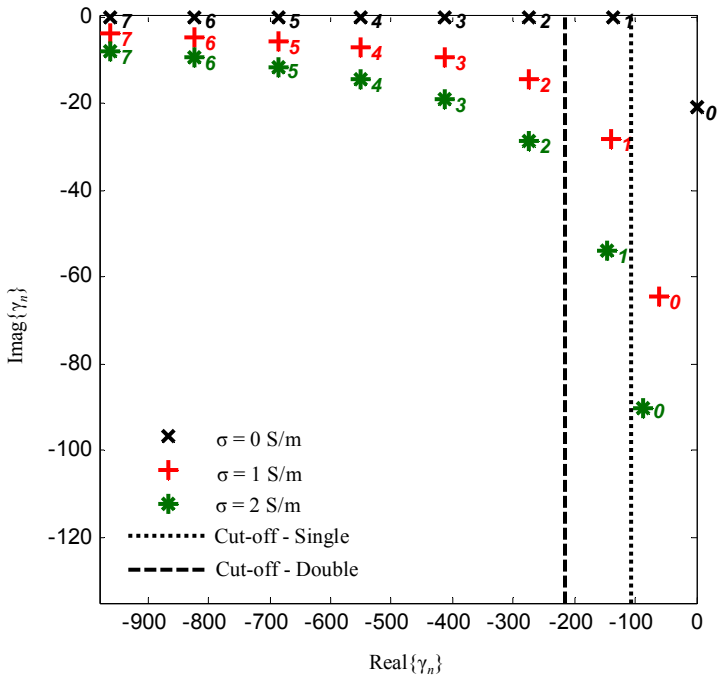

Figure 4-11 - Argand diagram showing propagation constants in cavity of length 150mm and width 22.86mm for varying loss, σ, in S/m. First 7 modes are shown (lowest to highest order).

The approach can also be used to analyse a wide variety of materials in time-reversal, for example frequency dependant materials. The case of human grey matter is of particular importance for biomedical applications [4.11]. As an example, Figure 4-12 shows the Argand diagram formed for human grey matter at 600 MHz ($\varepsilon_r = 54.72$, $\sigma = 0.819$ S/m), and 1.2 GHz ($\varepsilon_r = 51.57$, $\sigma = 1.08$ S/m) in a cavity of length $L = 150$ mm and width $W = 22.86$ mm. The cut-off levels for single and double precision are also

shown. It is seen that the increased frequency has the opposite effect of increasing the loss, and results in more modes being retained.

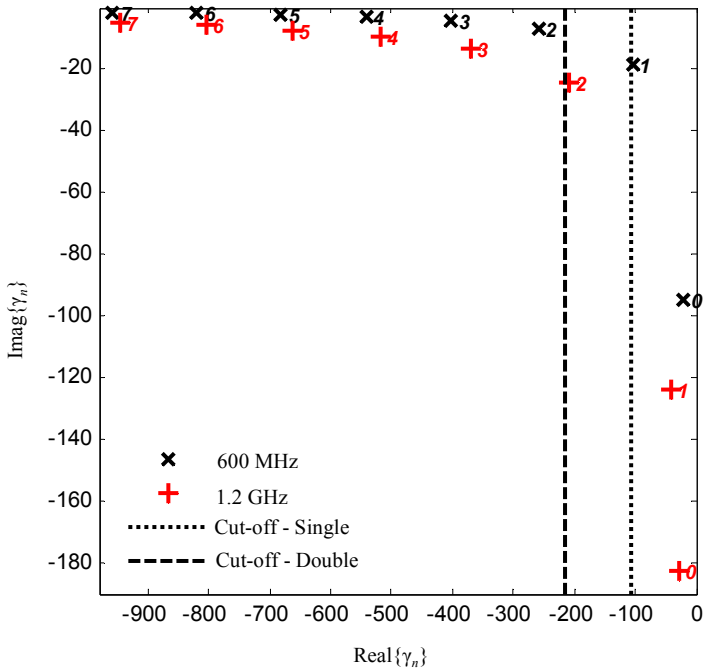

Figure 4-12 - Argand diagram of modal propagation constants for frequency dependant material of human grey matter, higher frequencies are better suited to time-reversal, L = 150mm and W = 22.86mm. First 7 modes are shown (lowest to highest order).

4.4 Conclusion

The objective of this chapter was twofold. First, the problem of temporal truncation in the time-reversal-cavity was analysed where it was shown the spatial spreading of the time-reversed source is a consequence of finite simulation time, and the Prony series was introduced to relax the computational and memory requirements by predicting the future behaviour of the discrete temporal waveform. The demonstration of the Prony method for the time-reversal of one and two sources was used as an example and time savings have been demonstrated.

Secondly, the modal content of the cavity was investigated. The effect of evanescent wave decay in a 2D parallel plate waveguide was used to examine the error in source reconstruction for the case of single and double machine precision, both analytically and numerically. Close agreement between analytical and numerical simulations is obtained. Finally, the effect of lossy materials was investigated, using an Argand diagram to predict the number of recoverable modes in time-reversal. It was shown that increasing the operating frequency has the opposite effect to increasing loss, thus minimising errors due to the presence of loss in the material.

4.5 References

[4.1] S. W. Park and Y. R. Kim, "Fitting Prony-Series Viscoelastic Models with Power-Law Presmoothing," *Journal of Materials in Civil Engineering*, vol. 13, pp. 26–32, January/February 2001.

[4.2] J. D. Wills, "Spectral Estimation for the Transmission Line Matrix Method," *IEEE Transactions on Microwave Theory and Techniques*, vol. 38, pp. 448–451, April 1990.

[4.3] E. Kreyszig, *Advanced Engineering Mathematics*. John Wiley & Sons Inc, New York, NY, 8th ed., 1998.

[4.4] K. W. Ko and R. Mittra, "A Combination of FD-TD and Prony's Methods for Analyzing Microwave Integrated Circuits," *IEEE Transactions on Microwave Theory and Techniques*, vol. 39, pp. 2176–2181, December 1991.

[4.5] J. Paul, *The Modelling of General Electromagnetic Materials in TLM*. PhD Thesis, University of Nottingham, 1998.

[4.6] A. J. Poggio, M. L. V. Blaricum, E. K. Miller, and R. Mittra, "Evaluation of a Processing Technique for Transient Data," *IEEE Transactions on Antennas and Propagation*, vol. 26, pp. 165–173, January 1978.

[4.7] W. Savitch, *Absolute C++*. Addison Wesley, Reading, MA, 2nd ed., 2006.

[4.8] W. H. Press, B. P. Flannery, S. A. Teukolsky, and W. T. Vetterling, *Numerical Recipes in C: The Art of Scientific Computing*. Cambridge University Press, Cambridge, 2nd ed., 1992.

[4.9] D. K. Cheng, *Field and Wave Electromagnetics*. Prentice-Hall, Reading, MA, 2nd ed., 1989.

[4.10] P. Kosmas and C. M. Rappaport, "Time Reversal With the FDTD Method for Microwave Breast Cancer Detection," *IEEE Transactions on Microwave Theory and Techniques*, vol. 53, pp. 2317–2323, July 2005.

[4.11] S. Gabriel, R. W. Lau, and C. Gabriel, "The Dielectric Properties of Biological Tissues: II. Measurements in the Frequency Range 10 Hz to 20 GHz," *Physics in Medicine and Biology*, vol. 41, pp. 2251–2269, November 1996. Online Resource: http://niremf.ifac.cnr.it/tissprop/htmlclie/htmlclie.htm.

5. Microwave Component Design using Time-Reversal

Automated optimisation techniques are often sought for the design of electromagnetic devices due to the increasing complexity and demanding performance requirements of modern systems. Time-reversal simulations are a physically based approach to this problem, alternating between forward-time simulations of trial designs and reverse-time simulations which re-inject a more desirable response of the system as an excitation in order to identify the component geometry that would produce it. This chapter introduces the method of time-reversal for microwave component design. The effect of damping of the iterative optimisation process is investigated. The concept of thresholds for accurate measurement of time-reversed recovered scatterer dimensions is introduced and the method is applied for the design examples of a microwave band pass filter, waveguide bend, and coupler.

5.1 Scatterer Reconstruction

In this section, the recovery of a metal scatterer within a time-reversal-cavity is investigated. The Lorentz reciprocity theorem, states "The relationship between source and resulting field is unchanged if source generation and measurement point are interchanged" [5.1]. As shown previously, the field measured at a boundary can be time-reversed to recover

the source location used to generate the field. In the case of component design, the time-reversal process is to recover the dimensions of scattering elements. The time-reversal process can be modified to perform this action as shown in [5.2]. Referring to the example of Figure 5-1, the source is termed $\vec{J}_i$, and a metal scatterer is placed as in the volume with induced source $\vec{J}_s$ on its boundary.

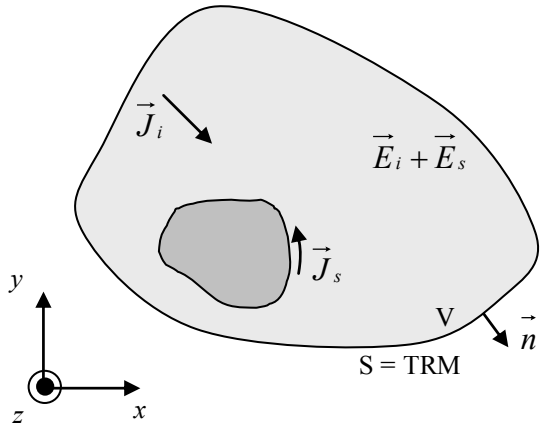

Figure 5-1 - Illustration of time-reversal-cavity with metal scatterer in volume. $\vec{J}_s$ is the induced source on the boundary of the scatterer.

The field measured at the time-reversal-mirror is $\vec{E}_i + \vec{E}_s$, the summation of the field generated by the input source, and the field from the scatterer. For component design, the field generated by the input source is not required. To remove this from the measured field, a second forward time simulation is performed, as in Figure 5-1, but with the scatterer removed, which is effectively the homogenous form of the problem space. The new situation is shown in Figure 5-2. $\vec{J}_2$ and $\vec{E}_2$ are the reverse source and field respectively.

In the time-reversal stage the scatterer is removed from the problem. Based on results of section 2.1.5, the time harmonic form of the induced source is

$$\vec{J}_s(t) = \vec{J}_s \exp(j\omega t) \tag{5.1}$$

and its reverse source is

$$\vec{J}_2(t) = \vec{J}_s(-t) = \vec{J}_s(t)\exp(-j2\omega t)\,. \tag{5.2}$$

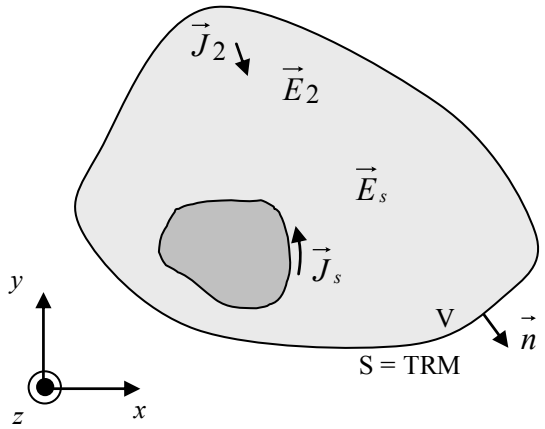

Figure 5-2 - Illustration of time-reversal-cavity with metal scatterer in volume, when homogenous form has been removed.

Substitution of Eqn.5.2 in the Lorentz reciprocity theorem, Eqn.2.22, gives

$$\oint_S \left(\vec{E}_s(t)\times\vec{H}_2(t) - \vec{E}_2(t)\times\vec{H}_s(t)\right)\cdot\vec{n}dS = \int_V \left(\vec{J}_s(t)\cdot\vec{E}_2(t) - \vec{J}_s(t)\exp(-j2\omega t)\cdot\vec{E}_s(t)\right)dV\,. \tag{5.3}$$

As before, the closed surface integral of the left hand side of Eqn.5.3 tends to zero as the radius of the surface tends to $+\infty$, hence

$$\int_V \left(\vec{J}_s(t)\cdot\vec{E}_2(t)\right)dV = \int_V \left(\vec{J}_s(t)\exp(-j2\omega t)\cdot\vec{E}_s(t)\right)dV\,, \tag{5.4}$$

from which it can be seen by comparing like terms, that the reverse field can be represented as

$$\vec{E}_2(t) = \vec{E}_s(t)\exp(-j2\omega t) = \vec{E}_s(-t)\,, \tag{5.5}$$

and hence $\vec{E}_2(t)$ is the time reversed form of the field generated by the scattered field from the induced source on the boundary of the scatterer.

5.1.1 Poynting Vector for Time-Reversal

As a result of the reverse simulation, new dimensions of a scatterer are determined. In the case of a metal scatterer, the field over the full simulation space is measured during time-reversal to determine the areas of minimal current density, which indicate the new locations of the scatterer boundaries. To perform this measurement the Poynting vector is used.

The absolute value of the Poynting vector is measured for each TLM node in the time-reversal-cavity during the reverse simulation, and the maximum value at each node over the full reverse time is then stored [5.3]. Since the Poynting vector will remain a minimum at nodes at metal boundaries, the resulting field map will contain minima for each boundary of the scatterer.

5.2 Time-Reversal for Component Design

This section will develop the method of time-reversal for component synthesis. The objective for time-reversal synthesis is to determine the dimensions of scattering elements to give a desired response. This process is demonstrated, building upon the early work of Forest and Hoefer [5.2] [5.3] and Sorrentino *et al*. [5.4] using the transmission-line modelling (TLM) method.

There are three distinct stages to the time-reversal design process. Firstly, a forward simulation of the complete structure, with known initial dimensions of the scattering element. This stage will be termed the inhomogeneous, or

particular solution. Figure 5-3 shows a general time-reversal-cavity with an arbitrary scatterer, the voltages stored in the mirror are

$$\underline{\underline{{}_1V_{TRM\,P}^{F}}}(x,k) = \underline{\underline{{}_kV_1^r}}(x,Y-1) \tag{5.6a}$$

$$\underline{\underline{{}_2V_{TRM\,P}^{F}}}(y,k) = \underline{\underline{{}_kV_2^r}}(X-1,y) \tag{5.6b}$$

$$\underline{\underline{{}_3V_{TRM\,P}^{F}}}(x,k) = \underline{\underline{{}_kV_3^r}}(x,0) \tag{5.6c}$$

$$\underline{\underline{{}_4V_{TRM\,P}^{F}}}(y,k) = \underline{\underline{{}_kV_4^r}}(0,y) \tag{5.6d}$$

where $\underline{\underline{{}_iV_{TRM\,P}^{F}}}$ is used to denote the forward particular solution time-reversal-mirror at port i of the TLM node next to the time-reversal-mirror. The particular solution holds the source excitation plus the field scattered from the scatterer.

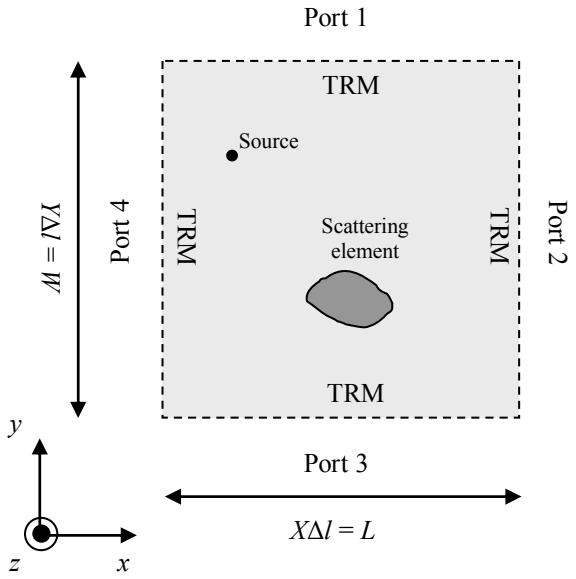

Figure 5-3 - Example time-reversal-cavity for time-reversal component design. An arbitrary scatter is shown.

In the next stage, the field in the time-reversal-mirrors is perturbed to better match a desired component response. In general, a complex difference

vector, $\underline{\hat{G}}$, is formed as the difference between the measured response, $\underline{g}$, and that desired, $\underline{g^d}$, as

$$\underline{\hat{G}} = \begin{cases} \underline{g^d} - \underline{g}, & \text{if within bandwidth,} \\ 0, & \text{otherwise.} \end{cases} \tag{5.7}$$

For microwave components, it is typical to analyse scattering parameters or S parameters in the frequency domain, and hence $\underline{g}$ in that sense will denote S parameters. Similarly $\underline{g}$ could denote coupling or directivity for a coupler.

Eqn.5.7 relates the desired response to that achieved with the current scatterer configuration. Application of the inverse Fourier transform to Eqn.5.7 recovers the complex difference in the time-domain, $\underline{G}(k)$. As an arbitrary scattered field distribution may not be physically realistic, it is necessary that the changes to the time-reversal-mirror equivalent sources are perturbational. The time-reversal-mirrors of the forward particular solution are then perturbed as

$$\underline{\underline{{}_{1,3}V_{TRM\,P}^{F}}}(x,k)' = (\alpha)\,\underline{\underline{{}_{1,3}V_{TRM\,P}^{F}}}(x,k) + (1-\alpha)\left(\underline{\underline{{}_{1,3}V_{TRM\,P}^{F}}}(x,k) - \underline{\phi}(x) \otimes |\,\underline{G_{1,3}}(k)\,|\right) \tag{5.8a}$$

$$\underline{\underline{{}_{2,4}V_{TRM\,P}^{F}}}(y,k)' = (\alpha)\,\underline{\underline{{}_{2,4}V_{TRM\,P}^{F}}}(y,k) + (1-\alpha)\left(\underline{\underline{{}_{2,4}V_{TRM\,P}^{F}}}(y,k) - \underline{\phi}(y) \otimes |\,\underline{G_{2,4}}(k)\,|\right) \tag{5.8b}$$

where α is a damping factor used to control the convergence of the process, a through analysis of which is given in the next section, and $\underline{\phi}$ is the modal distribution of the dominant mode. For the example of a 2D parallel plate

metal waveguide with transverse cross section in y the modal distribution for the dominant mode is [5.5]

$$\underline{\phi}(y) = \sin\left(\left(y\Delta l + \Delta l / 2 \right) \frac{\pi}{W} \right) \tag{5.9}$$

where Δl is the spatial sampling, and the TLM nodes are placed with an offset of $\Delta l / 2$ from the boundary.

In the next stage the contribution of the source is removed from the time-reversal-mirrors. This is done by performing a forward simulation without the scatterer, giving the homogenous solution, termed $\underline{\underline{{}_{i}V_{TRM\,H}^{F}}}$. The reverse mirrors are obtained as

$$\underline{\underline{{}_{1,3}V_{TRM}^{R}}}(x,k) = \underline{\underline{{}_{1,3}V_{TRM\,P}^{F}}}(x,k)' - \underline{\underline{{}_{1,3}V_{TRM\,H}^{F}}}(x,k), \tag{5.10a}$$

$$\underline{\underline{{}_{2,4}V_{TRM}^{R}}}(y,k) = \underline{\underline{{}_{2,4}V_{TRM\,P}^{F}}}(y,k)' - \underline{\underline{{}_{2,4}V_{TRM\,H}^{F}}}(y,k). \tag{5.10b}$$

In the final stage the resulting time-reversal-mirrors are re-injected into the problem space for time $k = N-1, N-2, ...0$.

The particular, homogenous and reverse simulations are applied iteratively, until convergence to the desired component response is achieved, and hence the correct scatterer dimensions are found.

The method described in section 5.1 for recovery of the boundary of the scatterers is then implemented during the reverse simulation. The Poynting vector is simplified if the shunt TLM node for transverse magnetic polarisation is used

$$\begin{aligned}\vec{P} &= \vec{E} \times \vec{H} \\ &= \begin{vmatrix} \vec{a}_x & \vec{a}_y & \vec{a}_z \\ 0 & 0 & E_z \\ H_x & H_y & 0 \end{vmatrix} = -\vec{a}_x E_z H_y + \vec{a}_y E_z H_x .\end{aligned} \tag{5.11}$$

where H_x, H_y and E_z are as defined in Chapter three.

In order to measure the scatterer dimensions from the absolute of Eqn.5.11 it is necessary to apply a threshold to the Poynting vector to distinguish metal from the background medium of the time-reversal-cavity, this is the discussion of the next section.

5.3 Threshold and Damping Selection

As discussed above and in [5.2] the boundary of the perturbed septum is defined by the locus of nulls in the maximum Poynting vector observed during the reverse simulation. However, as true nulls are never actually generated a threshold value must be used. This section investigates the use of applied thresholds, to measure the scatterer dimensions from the recovered Poynting vector, and the application of damping through the term α in Eqn.5.8, of the difference vector, $\underline{G}(k)$, to the accuracy of the convergence of the design process.

The choice of threshold and damping values is largely dependant upon a given component. This section will demonstrate two simple examples, which are suitable to investigate the threshold and damping selection, while maintaining an acceptable simulation runtime.

The general time-reversal-cavity of Figure 5-3 is simplified by the inclusion of short circuit boundary conditions in the place of time-reversal-mirrors 1 and 3, see Figure 5-4. The structure is a 2D parallel plate waveguide. The scatterer is placed as a metal septum, creating a high pass filter [5.3].

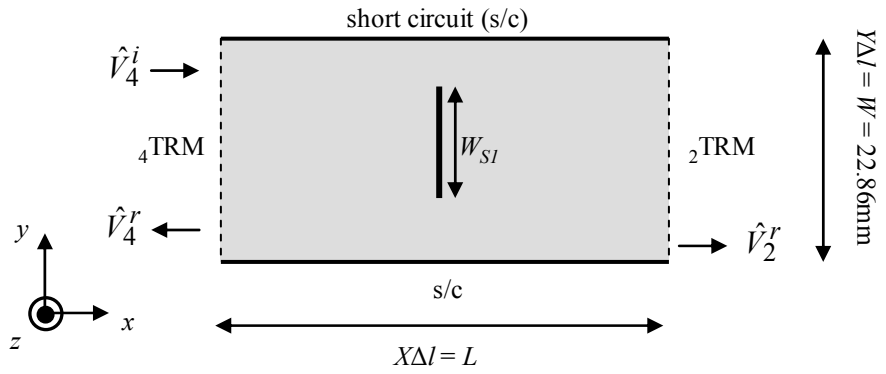

Figure 5-4 - X-band microwave high pass filter formed from inductive scatterer in electric waveguide.

The optimisation of the single scatterer of Figure 5-4 will be investigated with a view to developing a general method of selecting threshold and damping values for structures with more degrees of freedom.

For simplicity the desired response is measured from a TLM simulation of Figure 5-4 with the septum width fixed at known width W_{S1}^d. In a practical application, the desired response would be given as a pre-specification. The desired S_{11} and S_{21} are measured from the TLM model using the discrete Sine transform [5.6]

$$\underline{S_{11}^d} = \frac{FFT\left(\sum_{y=0}^{Y-1}\sin\left[(y\Delta l + \Delta l/2)\pi/W\right]_k\underline{V_4^r}(y)\right)}{FFT\left(\sum_{y=0}^{Y-1}\sin\left[(y\Delta l + \Delta l/2)\pi/W\right]_k\underline{V_4^i}(y)\right)} = \frac{{}_k\underline{\hat{V}_4^r}}{{}_k\underline{\hat{V}_4^i}}, \tag{5.12a}$$

$$\underline{S_{21}^d} = \frac{FFT\left(\sum_{y=0}^{Y-1}\sin\left[(y\Delta l + \Delta l/2)\pi/W\right]_k\underline{V_2^r}(y)\right)}{FFT\left(\sum_{y=0}^{Y-1}\sin\left[(y\Delta l + \Delta l/2)\pi/W\right]_k\underline{V_4^i}(y)\right)} = \frac{{}_k\underline{\hat{V}_2^r}}{{}_k\underline{\hat{V}_4^i}}. \tag{5.12b}$$

The complex difference vector for the time-reversal-mirrors at the input and output ports respectively, is

$$\underline{\hat{G}_4} = \begin{cases} \underline{S_{11}^d} - \underline{S_{11}}, & \text{if within bandwidth,} \\ 0, & \text{otherwise,} \end{cases} \tag{5.13a}$$

$$\underline{\hat{G}_2} = \begin{cases} \underline{S_{21}^d} - \underline{S_{21}}, & \text{if within bandwidth,} \\ 0, & \text{otherwise.} \end{cases} \tag{5.13b}$$

After a single time-reversal step, the value of the maximum of the absolute magnitude of the Poynting vector, measured using Eqn.5.11 during reversal, is extracted at the septa location. This vector is then scaled so that all values are between 0 and 1, and stored in a column vector of size Y.

The time-reversal optimisation of the septum width starts with the initial widths of the septum as $W_{S1} = 61\Delta l = 10.33$ mm, the width of the waveguide is $W = 22.86$ mm, with transverse nodes $Y = 135$. Spatial and temporal steps are $\Delta l = 0.169$ mm and $\Delta t = 3.99e-13$ s respectively. The waveguide length of $L = 5.25$ mm is modelled with $X = 31$ nodes. A total of $N = 8192$ temporal samples are used. The optimisation bandwidth is $7-14$ GHz.

The filter is excited at the input port with a spatial sinusoid of period $2W$

$$\underline{{}_0V_4^i}(y,0) = \sin\left(\left(y\Delta l + \Delta l/2\right)\frac{\pi}{W}\right). \tag{5.14}$$

For maximum damping $\alpha = 1$, the Poynting vector is as shown in Figure 5-5a and the transverse field distribution across the septa is as shown in Figure 5-5b. The recovered field contains the minima in the place of the septum as expected, but also large oscillations either side.

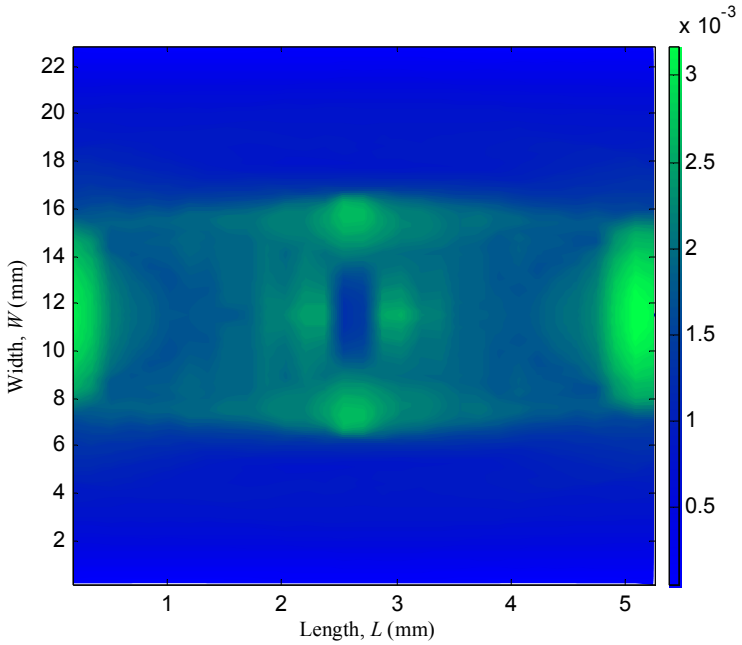

a)

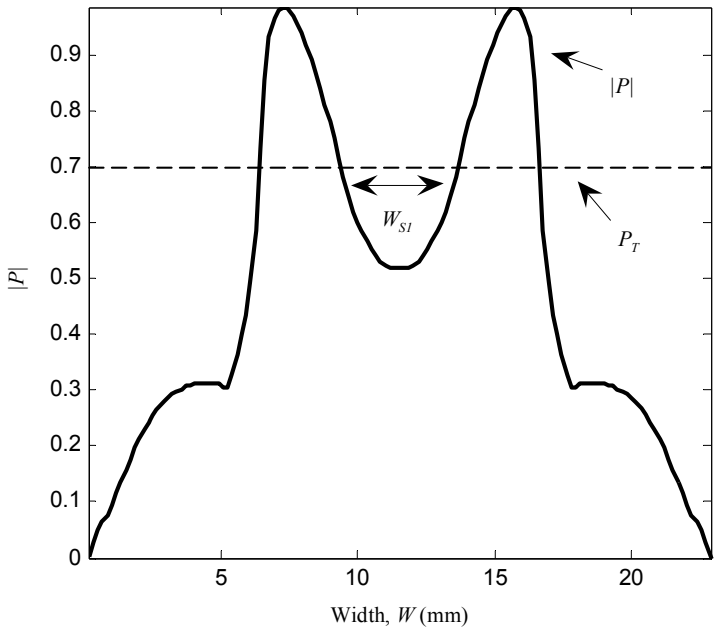

b)

Figure 5-5 - a) Resulting field plot found by storing maximum of Poynting vector during time-reversal for single septum in waveguide, 91 contour levels are shown, b) transverse cross section at septum scaled to unity, P_T shown as example, Δl = 0.169mm, Δt = 3.99e-13s, X = 31, Y = 135, L = 5.25mm, W = 22.86mm and N = 8129.

With maximum damping, no perturbation is applied, and the measured width from Figure 5-5b should match the input width. It is seen, only when the threshold, $P_T = 1$, is the correct width measured. In more complex components noise in the recovered Poynting vector is often created, due to resonance between scatterers [5.2]. This noise inhibits the measurement of the scatterer dimensions. In the work performed during this thesis, the thresholds are not fixed at 1. In Figure 5-5b the example $P_T = 0.7$ is shown, whereby the width is measured between the inner two crossings of the threshold with the Poynting vector.

To solve the problem of inaccurate convergence when $P_T < 1$, a measurement of the width, from a time-reversal simulation with maximum damping, is measured first, termed the control width. A percentage increase or decrease of the septum width from the perturbed model in comparison to the control, is then used to adjust the known input width before the next iteration of the design procedure. Using κ to symbolise the time-reversal design iteration

$$\kappa+1 W_{S1} = \left(\frac{\kappa W_{S1_{Perturbed}}}{\kappa W_{S1_{Control}}} \right) \kappa W_{S1} \,. \tag{5.15}$$

The initial S parameters, with $W_{S1} = 61\Delta l = 10.33$ mm, against those desired from a septa width of $W_{S1}{}^{d} = 27\Delta l = 4.57$ mm are shown in Figure 5-6. The desired width was chosen arbitrarily to represent an example of a high pass filter characteristic.

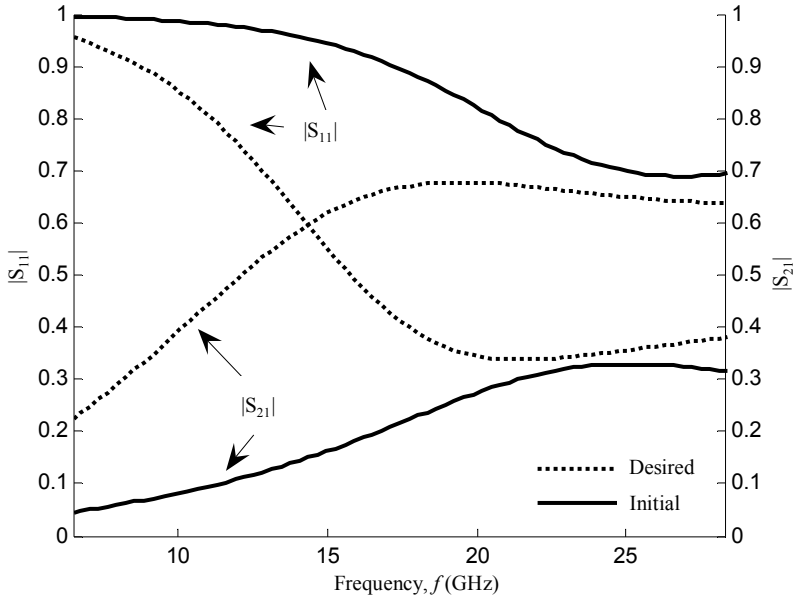

Figure 5-6 - S parameters for dominant mode of X-band high pass filter formed from inductive element in WR90 waveguide, Δl = 0.169mm, Δt = 3.99e-13s, X = 31, Y = 135, L = 5.25mm, W = 22.86mm and N = 8192.

The time-reversal design starting from $W_{S1} = 61\Delta l$ mm, performed for each value of P_T and α, where a total of 20 steps between 0 and 1 is used for each, results in the contour plot of Figure 5-7. The number of time-reversal iterations, N_{TR}, until convergence to the desired S parameters is shown by the height of the contour.

In the case of $P_T < 0.5$ and $\alpha < 0.3$, no convergence was found. The lighter areas are those with optimal convergence of $N_{TR} = 2$ time-reversal iterations. It can be seen that optimum convergence is found when $0.5 < P_T < 0.9$ and $0.3 < \alpha < 0.6$. Outside this area, convergence may take longer, as in the case of $\alpha > 0.6$. The contour plot requires the computation of 400 time-reversal simulations (20 values of P_T by 20 values of α), which takes approximately 3.5 days on an AMD Athlon 2 GHz processor with 128 KB L1 cache, 1 MB L2 cache, 200 MHz Bus and 2 GB of RAM.

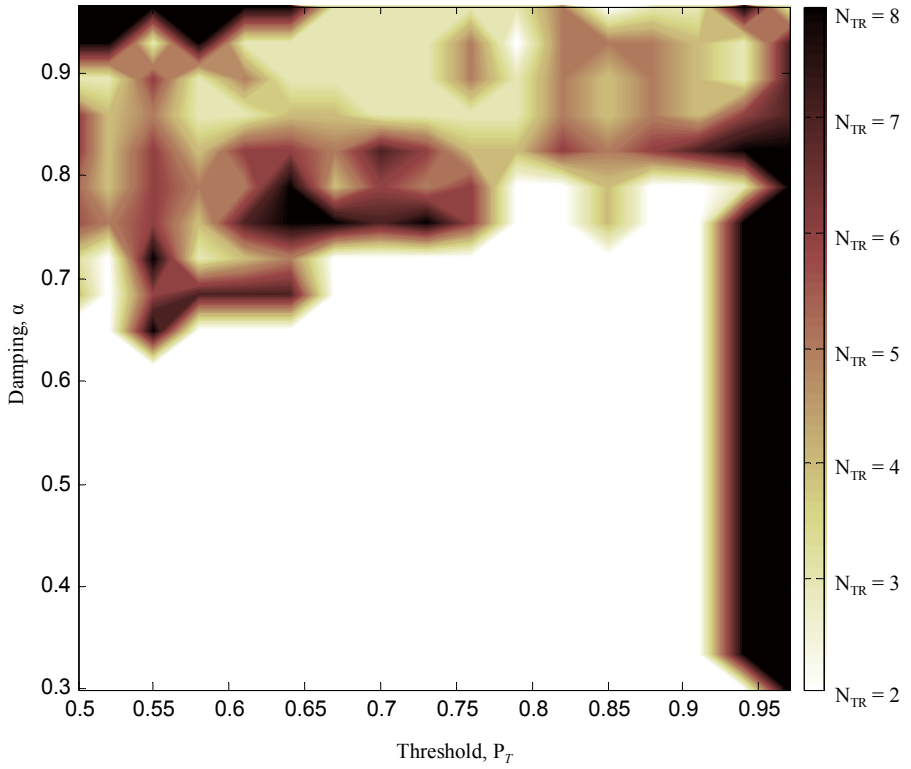

Figure 5-7 - Contour plot displaying P_T with respect to α, for time-reversal optimisation of single septum. Contour levels show iterations until convergence, with white being optimal. For $P_T < 0.5$ and $\alpha < 0.3$ no convergence is found. Δl = 0.169mm, Δt = 3.99e-13s, X = 31, Y = 135, L = 5.25mm, W = 22.86mm and N = 8129. There are 20×20 points in the plot, with 71 contour levels.

In general, a high pass filter can be formed using a wide variety of metal obstacles in the transverse dimension of the waveguide, for example, screws, posts or irises [5.7]. In Figure 5-8, a high pass filter is formed using a metal iris. Again, a known achievable solution, with $W_{S1}^{d} = 67\Delta l = 12.25\,\text{mm}$ was arbitrarily chosen as the desired solution, while $W_{S1} = 27\Delta l = 4.94\,\text{mm}$ was used as the initial starting iris width. For this model the sampling was $\Delta l = 0.183\,\text{mm}$, $\Delta t = 4.31e-13\,\text{s}$, $X = 51$, $Y = 125$, $L = 9.33\,\text{mm}$, $W = 22.86\,\text{mm}$ and $N = 16384$. The optimisation bandwidth remains the same.

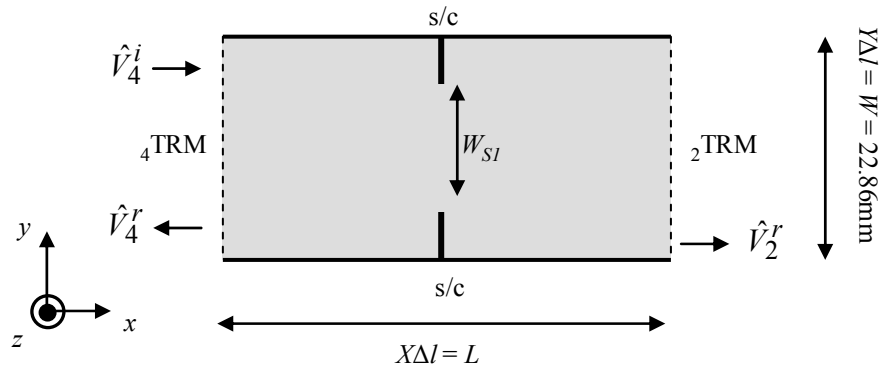

Figure 5-8 - X-band microwave high pass filter formed from inductive scatterer (iris) in metal waveguide.

In Figure 5-9, a contour plot is shown illustrating the iterations until convergence for each selection of the damping and threshold values. For $\alpha < 0.5$ and $P_T < 0.65$ no convergence was found. It is seen that the optimum convergence is when $0.7 < P_T < 0.75$ and $0.65 < \alpha < 0.75$.

It is impractical to perform a full analysis of the threshold and damping of more complex components due to the runtimes involved. The two examples above have shown the contour plot is reasonably well behaved and optimal convergence is confined to a single area.

For the examples of this thesis a simple trial and error approach, starting from $\alpha = 0$ and increasing incrementally, varying the threshold values at each increment of α until stable accurate convergence is found is sufficient. In the majority of examples, there is more than one free variable, and hence the thresholds are termed T_1, T_2, T_3, etc.

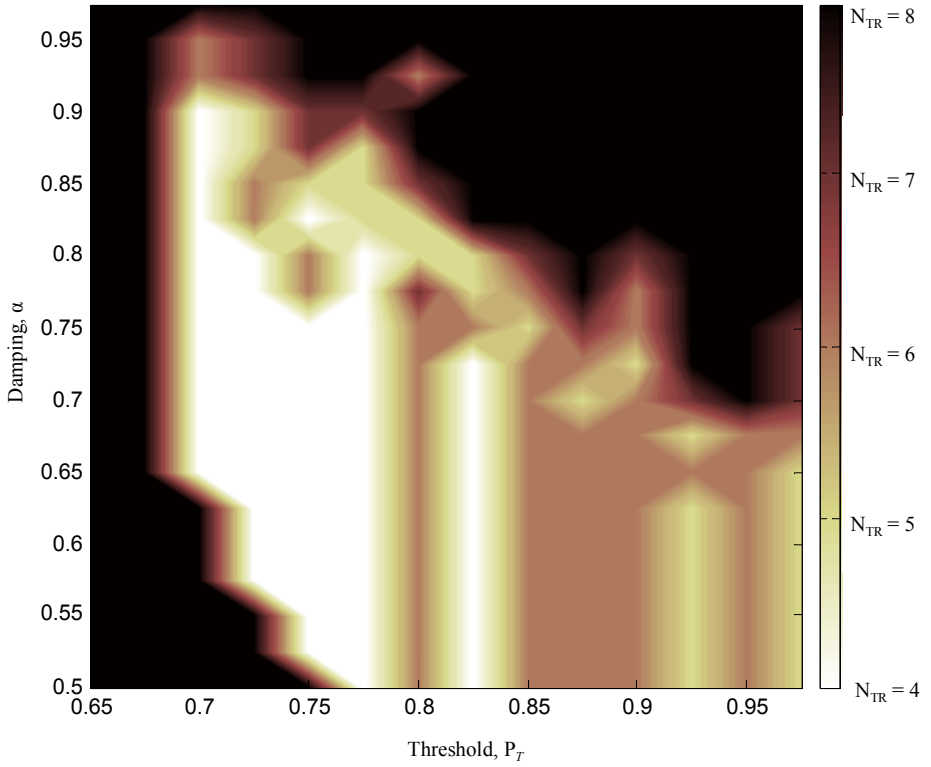

Figure 5-9 - Contour plot displaying P_T with respect to α, for time-reversal optimisation of single iris. Contour levels show iterations until convergence, with white being optimal. For $P_T < 0.65$ and $\alpha < 0.5$ no convergence is found. Δl = 0.183mm, Δt = 4.31e-13s, X = 51, Y = 125, L = 9.33mm, W = 22.86mm and N = 16384. There are 20×20 points in the plot, with 71 contour levels.

5.4 Spatial Resolution

For any simulation of a physical component the accuracy of the result is dependant upon the accuracy of the model. Ideally the spatial sampling should be large enough to give an acceptable runtime, but small enough for accurate results. In numerical models, the simulation is usually defined by the choice of both Δl and Δt. In a TLM model, Δt is dependant upon Δl and hence the investigation of the effect of the spatial resolution on the convergence of the time-reversal design process is necessary.

The high pass microwave filter defined by Figure 5-4, was initially designed using 135 spatial nodes across the transverse width. This gave a spatial sampling of approximately one node every 0.169 mm. In order to investigate the effect of the numerical spatial sampling upon the convergence of the time-reversal design, the example of Figure 5-4 is repeated in Figure 5-10, with the spatial resolution reduced by a factor of 2. In this case $Y = 67$, $\Delta l = 0.34$ mm, $\Delta t = 8.05e-13$ s, $X = 15$, and the initial value for $W_{S1} = 31\Delta l$ mm, with desired of $W_{S1}^{d} = 13\Delta l$ mm. The reduced spatial sampling is necessary, since increasing the spatial resolution will make the repeated time-reversal simulations intractable.

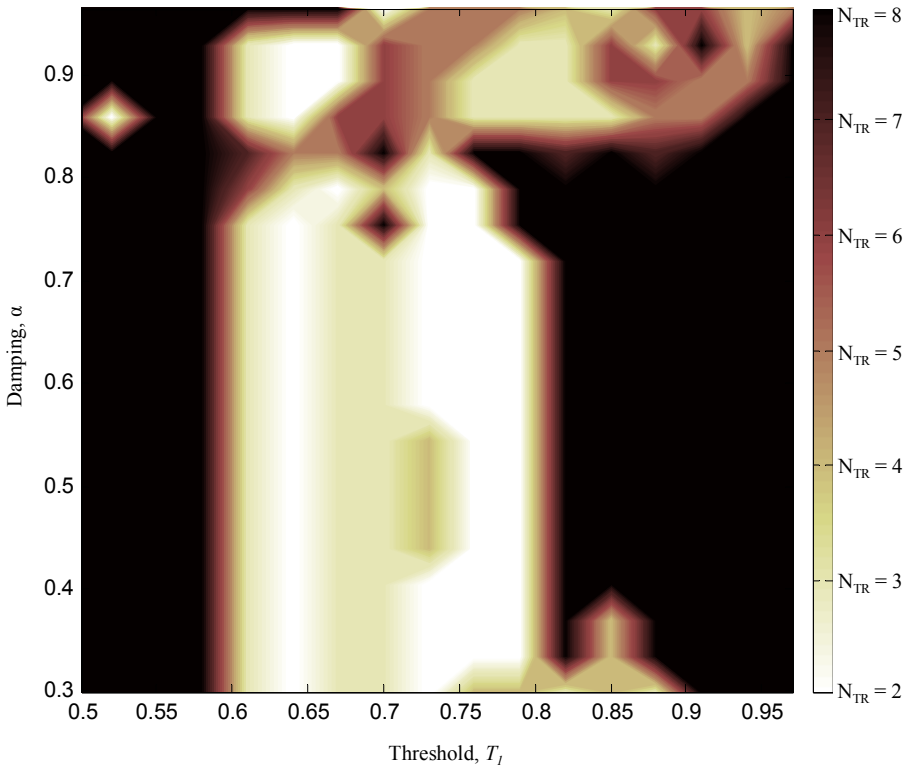

Figure 5-10 - Contour plot displaying T_1 with respect to α, for time-reversal optimisation of single septum. Δl = 0.34mm, Δt = 8.05e-13s, X = 15, Y = 67, L = 5.12mm, W = 22.86mm and N = 8129. There are 20×20 points in the plot, with 71 contour levels.

Comparing results from Figure 5-10 and Figure 5-7, it is seen that reducing the spatial resolution of the numerical model also reduces the area of optimal convergence for the time-reversal, yet the optimal iterations until convergence are unchanged.

The high pass filter formed by the metal iris in Figure 5-8, is similarly repeated, with the spatial sampling reduced by a factor of 2 giving $Y = 63$ and $\Delta l = 0.36$. The corresponding values are $\Delta t = 8.56e-13\,\text{s}$, $X = 25$, $L = 9.07\,\text{mm}$, $W = 22.86\,\text{mm}$ and $N = 16384$. $W_{S1} = 13\Delta l\,\text{mm}$ initially and $W_{S1}^{d} = 33\Delta l\,\text{mm}$. The effect of varying the threshold and damping at the coarser resolution is given in Figure 5-11, again showing reduced area of optimal time-reversal convergence compared with Figure 5-9.

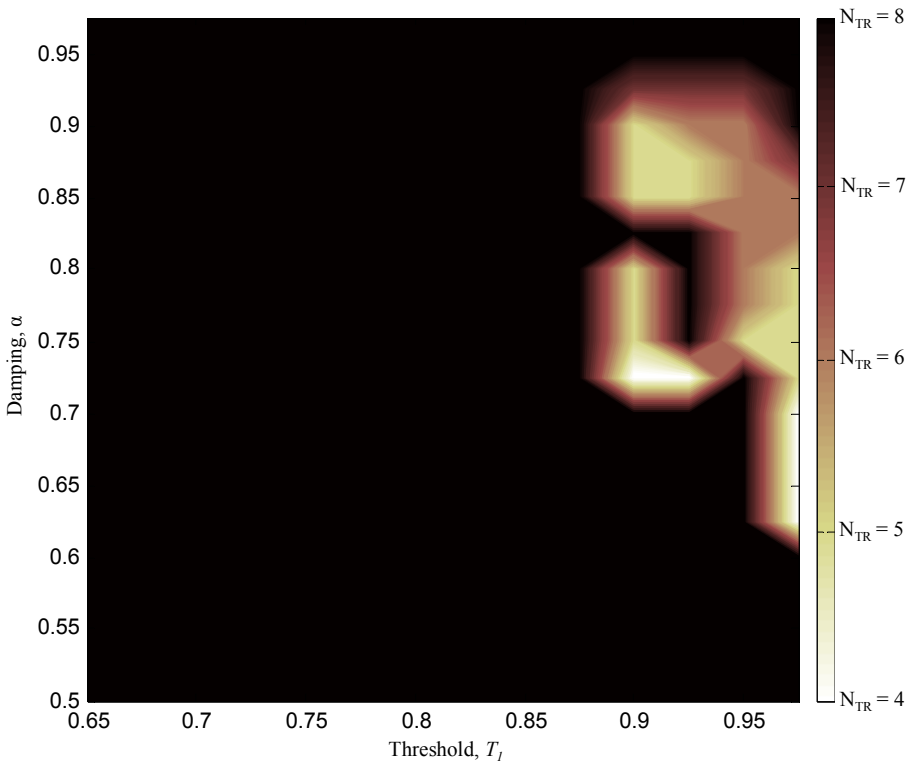

Figure 5-11 - Contour plot displaying T_1 with respect to α, for time-reversal optimisation of single iris, at reduced spatial sampling of Δl = 0.36mm, Δt = 8.56e-13s, X = 25, Y = 63, L = 9.07mm, W = 22.86mm and N = 16384. There are 20×20 points in the plot, with 71 contour levels.

The reduced area of optimal convergence in both examples can be explained by the fact that larger Δl will sample fewer transverse modes of the waveguide, and thus result in errors in the time-reversal. In Figure 5-11 the optimum threshold value has increased, indicating there is less noise in the Poynting vector, which is expected if fewer modes are present. In both figures it is seen the optimum convergence rate, $N_{TR} = 2$ and $N_{TR} = 4$ respectively, is unchanged by the level of spatial sampling.

5.5 Case Studies

Previous sections introduced the concept of component design using the time-reversal method, and performed an analysis of the effect of thresholds and damping with the time-reversal procedure on simple devices. This section will introduce four case study examples, two microwave filters, a waveguide bend, and a coupler.

5.5.1 2nd Order Septa Filter

This section optimises a band pass microwave filter using the time-reversal method, in order to demonstrate the ability of time-reversal to converge to a desired response. The circuit equivalence of the filter is used to produce a desired set of S parameters, which are then used as input parameters to time-reversal to determine physical dimensions of optimised scatterers.

In Figure 5-12 a 2D band pass filter formed from two metal septa spaced a quarter of a wavelength in the longitudinal direction of a metal parallel plate waveguide is shown. A practical filter would require five or more septa to achieve a narrow pass band, typically of around 1GHz, and return loss of around $40-50$ dB. However, the second order example is used to minimise the runtime and memory of the simulation.

The S parameters are optimised within the single mode of operation of the WR90 waveguide. Operating within the single mode region means the corresponding Maxwell's equations are comparable to the Telegraphers equations [5.8] and the single mode transmission-line circuit equivalence of Figure 5-13 can be used to generate a set of desired S parameters. This equivalence holds, providing the septa are infinitely thin in the longitudinal direction, x. The waveguide has a cut-off frequency of

$$f_c = \frac{v}{2W} \tag{5.16}$$

where v is the speed of light in free space. For the WR90 waveguide of Figure 5-12, $W = 22.86\,\text{mm}$ and the cut-off occurs at $6.56\,\text{GHz}$.

This example is synonymous with a 3D parallel plate waveguide, with uniform field in z. Only transverse magnetic (TM) modes are modelled. The width of each septum in the transverse direction determines its inductance [5.7].

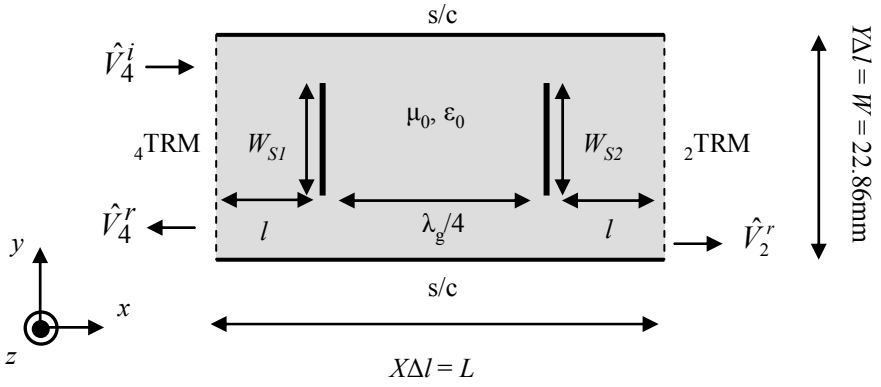

Figure 5-12 - 2nd order X-band microwave band pass filter formed from two inductive septa in WR90 X-band waveguide, W = 22.86mm. $\hat{\mathbf{V}}^{\mathbf{r}}$ and $\hat{\mathbf{V}}^{\mathbf{i}}$ are the Fourier transform of the reflected and incident temporal voltage vectors onto the time-reversal-mirrors.

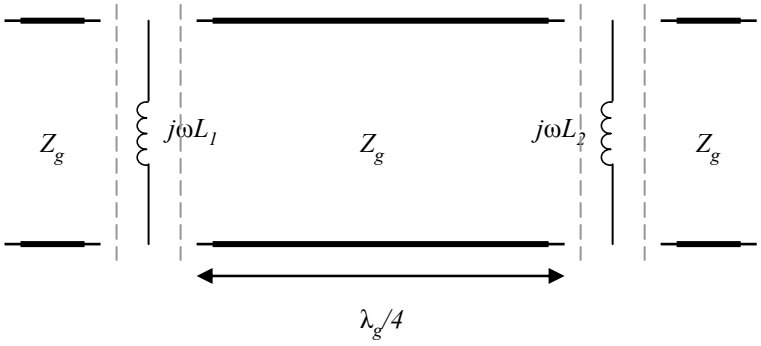

Figure 5-13 - Transmission-line circuit equivalence of the microwave filter in Figure 5-12, L_1 = 2.7nH, L_2 = 2.85nH.

From Figure 5-13 the transmission-line equivalence is used to generate the desired S_{11}^d and S_{21}^d, where septa are modelled using shunt inductances. The desired S parameters of the band pass filter are obtained analytically using the ABCD matrix formulation. The resulting ABCD matrix of the filter is found as a cascade of individual ABCD matrices for transmission-lines and shunt inductances, i.e.

$$\begin{bmatrix} \underline{A}(\beta) & \underline{B}(\beta) \\ \underline{C}(\beta) & \underline{D}(\beta) \end{bmatrix} = \begin{bmatrix} \cos(\beta l) & jZ_g \sin(\beta l) \\ j\sin(\beta l)/Z_g & \cos(\beta l) \end{bmatrix} \begin{bmatrix} 1 & 0 \\ 1/(j\omega L_1) & 1 \end{bmatrix} \begin{bmatrix} \cos(\beta\lambda_g/4) & jZ_g \sin(\beta\lambda_g/4) \\ j\sin(\beta\lambda_g/4)/Z_g & \cos(\beta\lambda_g/4) \end{bmatrix} \begin{bmatrix} 1 & 0 \\ 1/(j\omega L_2) & 1 \end{bmatrix} \begin{bmatrix} \cos(\beta l) & jZ_g \sin(\beta l) \\ j\sin(\beta l)/Z_g & \cos(\beta l) \end{bmatrix} \quad (5.17)$$

where $l = (L - \lambda_g/4)/2$, $Z_g = Z_0/\sqrt{1 - f_c^{\,2}/f^2}$, $Z_0 = \sqrt{\mu_0/\varepsilon_0}$, $\beta = 2\pi/\lambda_f$, were $\lambda_f = \lambda/\sqrt{1 - f_c^{\,2}/f^2}$ and $\lambda_g = \lambda/\sqrt{1 - f_c^{\,2}/f_r^{\,2}}$. f_r is the centre frequency of the filter.

The desired S_{11}^d and S_{21}^d parameters are found from the ABCD matrix as [5.9]

$$\underline{S_{11}^d} = \frac{\underline{A} + \underline{B}/Z_g - Z_g\underline{C} - \underline{D}}{\underline{A} + \underline{B}/Z_g + Z_g\underline{C} + \underline{D}}, \tag{5.18a}$$

$$\underline{S_{21}^d} = \frac{2}{\underline{A} + \underline{B}/Z_g + Z_g\underline{C} + \underline{D}}. \tag{5.18b}$$

The S parameters from the forward TLM simulation are obtained using Eqns.5.12a,b, i.e.,

$$\underline{S_{11}} = \frac{FFT\left(\sum_{y=0}^{Y-1}\sin\left[\left(y\Delta l + \Delta l/2\right)\pi/W\right]{}_k\underline{V_4^r}(y)\right)}{FFT\left(\sum_{y=0}^{Y-1}\sin\left[\left(y\Delta l + \Delta l/2\right)\pi/W\right]{}_k\underline{V_4^i}(y)\right)} = \frac{{}_k\underline{\hat{V}_4^r}}{{}_k\underline{\hat{V}_4^i}}, \tag{5.19a}$$

$$\underline{S_{21}} = \frac{FFT\left(\sum_{y=0}^{Y-1}\sin\left[\left(y\Delta l + \Delta l/2\right)\pi/W\right]{}_k\underline{V_2^r}(y)\right)}{FFT\left(\sum_{y=0}^{Y-1}\sin\left[\left(y\Delta l + \Delta l/2\right)\pi/W\right]{}_k\underline{V_4^i}(y)\right)} = \frac{{}_k\underline{\hat{V}_2^r}}{{}_k\underline{\hat{V}_4^i}}. \tag{5.19b}$$

Desired S parameters are obtained for $L_1 = 2.7\,\text{nH}$ and $L_2 = 2.85\,\text{nH}$. These values were chosen since they are known to be comparable with the inductance possible from the elements within a WR90 waveguide [5.7]. The symmetric spatial sinusoidal excitation with period two times the waveguide width is applied at the input port of the microwave filter, as in Eqn.5.14. Initial septa widths are set to $3\Delta l = 0.89\,\text{mm}$ each. The TLM simulation parameters are $\Delta l = 0.297\,\text{mm}$, $\Delta t = 7e-13\,\text{s}$, $X = 67$, $Y = 77$, $L = 19.89\,\text{mm}$, $W = 22.86\,\text{mm}$, $N = 16384$, $T_1 = 0.15$, $T_2 = 0.6$ and the damping, $\alpha = 0.93$. The centre frequency of the filter is $f_r = 12.5\,\text{GHz}$.

Figure 5-14 shows the S parameters converging to the desired S parameters at four separate iterations of the time-reversal procedure. The initial septa widths of $W_{S1} = W_{S2} = 3\Delta l = 0.89\,\text{mm}$ produce a poor approximation to the target performance, which is then optimised. It is seen the first few time-reversal optimisation steps produce the most improvement in performance which is practically valuable for large problems that may preclude more than a few iterations.

An exact match to the desired parameters is not expected since the inductance of each septum is not a fixed value but changes with frequency [5.7], a factor that is not accounted for in the analytical model of Figure 5-13.

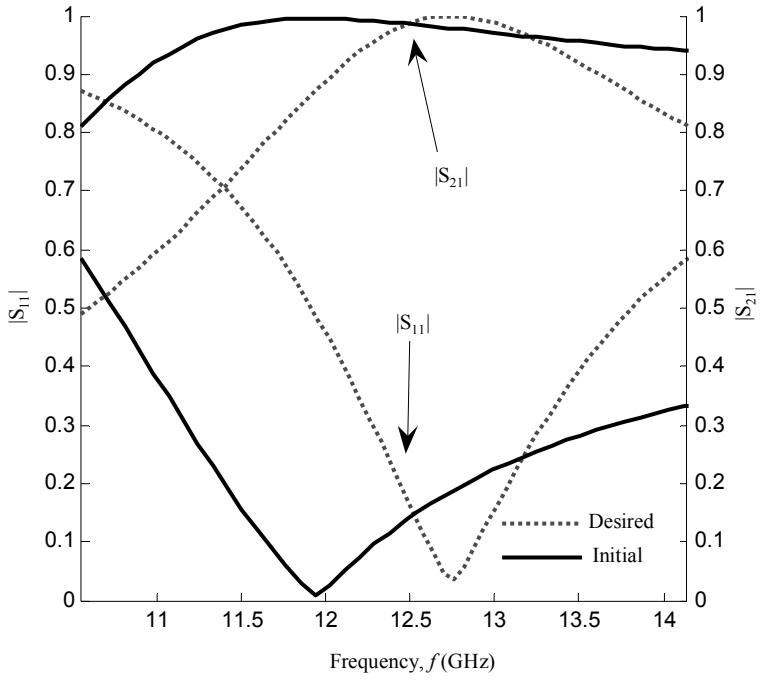

a)

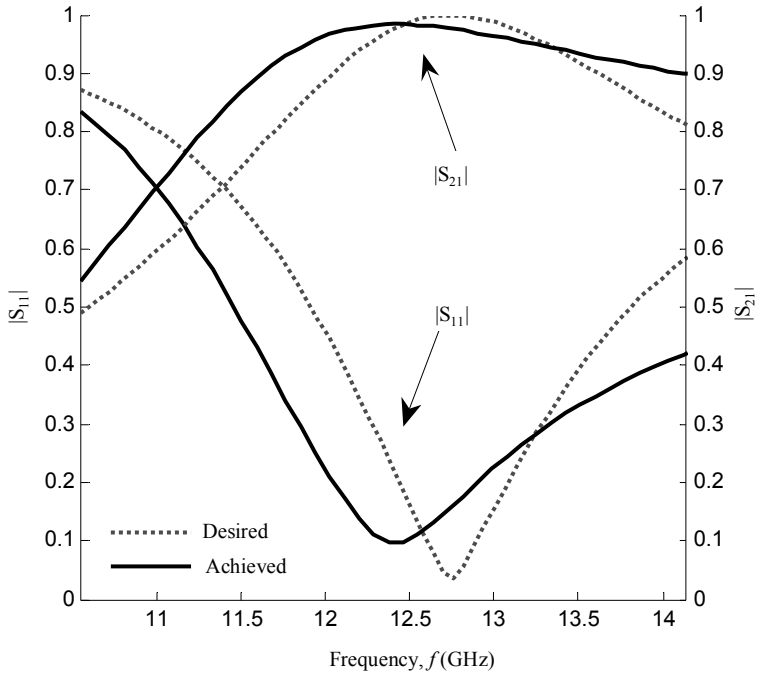
|S21|
|S11|
|S11|
|S21|
Desired
Achieved
Frequency, f (GHz)

b)

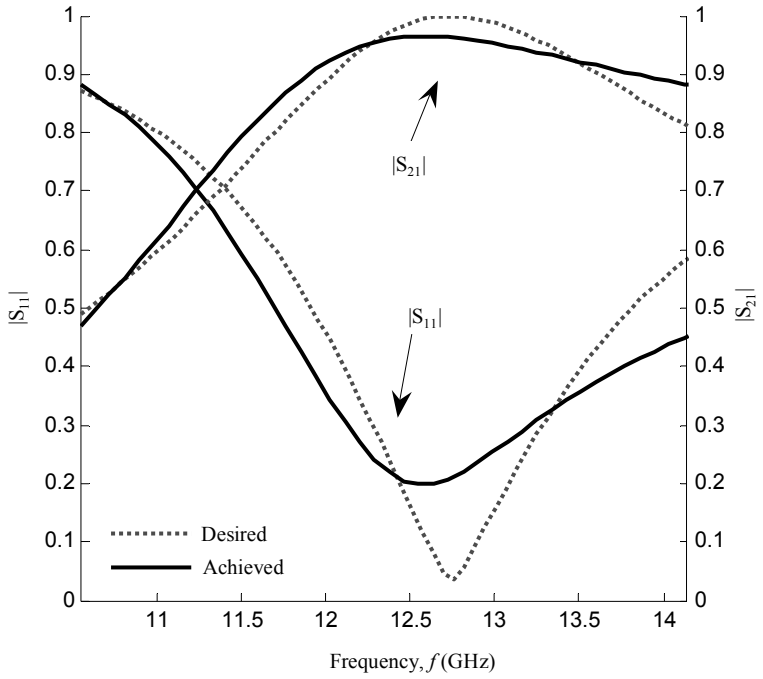
|S21|
|S11|
|S11|
|S21|
Desired
Achieved
Frequency, f (GHz)

c)

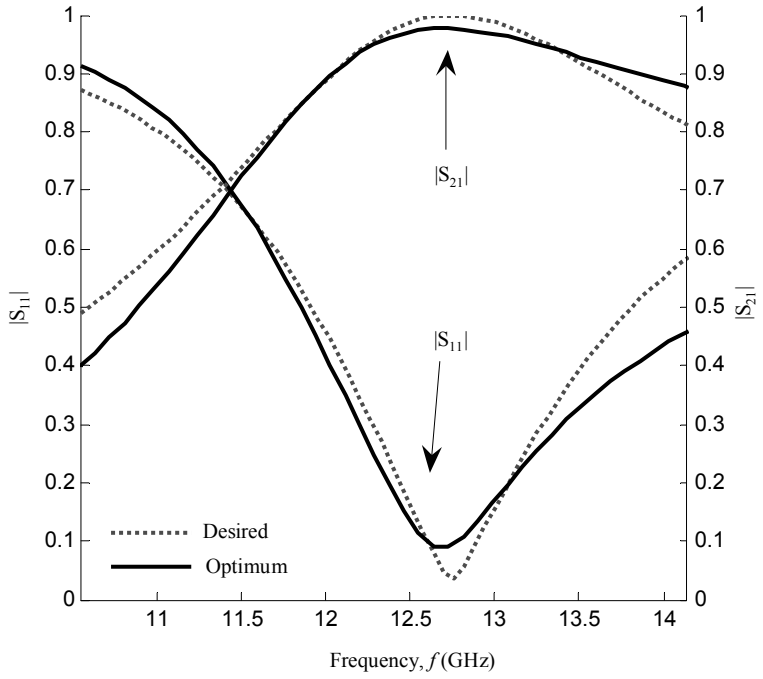

d)

Figure 5-14 - S parameters of 2nd order microwave band pass septa filter optimised using time-reversal, a) initial configuration, b) iteration 3, c) iteration 7, d) configuration at iteration 8. Δl = 0.297mm, Δt = 7e-13s, X = 67, Y = 77, L = 19.89mm, W = 22.86, N = 16384, optimised septa widths from Eqn.5.15 are W_{S1} = 1.96mm and W_{S2} = 2.55mm, snapped to TLM nodes W_{S1} = 7Δl = 2.08mm and W_{S2} = 9Δl = 2.67mm

To determine when optimal convergence is reached the scalar figure of merit of Eqn.5.20 is introduced as

$$FoM = \frac{\sum^{N_{BW}} \left| \underline{S}_{11}^{d} - \underline{S}_{11} \right| + \left| \underline{S}_{21}^{d} - \underline{S}_{21} \right|}{2N_{BW}} \tag{5.20}$$

where N_{BW} is the number of sample points in the bandwidth the filter is optimised within.

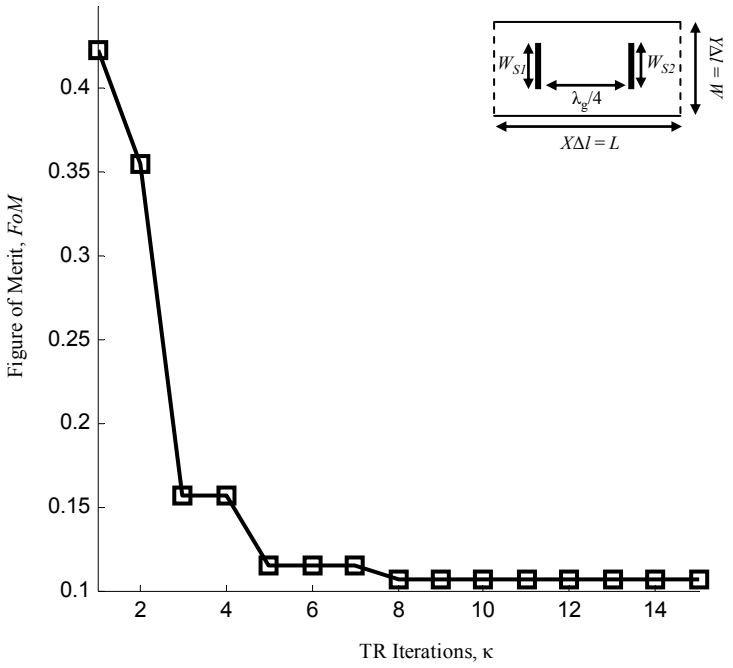

Figure 5-15 - Convergence of time-reversal design process of 2nd order band pass septa filter, Δl = 0.297mm, Δt = 7e-13s, X = 67, Y = 77, L = 19.89mm, W = 22.86mm, N = 16384, optimised septa widths from Eqn.5.15 are W_{S1} = 1.96mm and W_{S2} = 2.55mm, snapped to TLM nodes $W_{S1} = 7\Delta l$ = 2.08mm and $W_{S2} = 9\Delta l$ = 2.67mm from initial configuration of $W_{S1} = W_{S2}$ = 0.89mm.

Application of Eqn.5.20 to the filter example is given in Figure 5-15, which shows the convergence of the FoM with respect to the number of time-reversal iterations and a monotonic improvement is observed for the first 8 iterations after which no further improvement is seen. The flat sections in the graph are explained by the use of Eqn.5.15, since the updated septum widths are snapped to the nearest node when simulated in the TLM. Optimal septa widths using Eqn.5.15 are found to be $W_{S1} = 1.96\,\text{mm}$ and $W_{S2} = 2.55\,\text{mm}$, resulting in $7\Delta l$ and $9\Delta l$ respectively, when snapped to odd TLM nodes to keep the structure symmetric.

5.5.2 2nd Order Iris Filter

The design of a microwave band pass filter was demonstrated in the previous section where metal septa were placed to create shunt inductance.

In general, any metal obstacle perpendicular to the direction of propagation will act as a shunt inductance [5.7]. In this example a band pass filter is designed using time-reversal, where the shunt inductance is created through the use of two irises as shown by Figure 5-16.

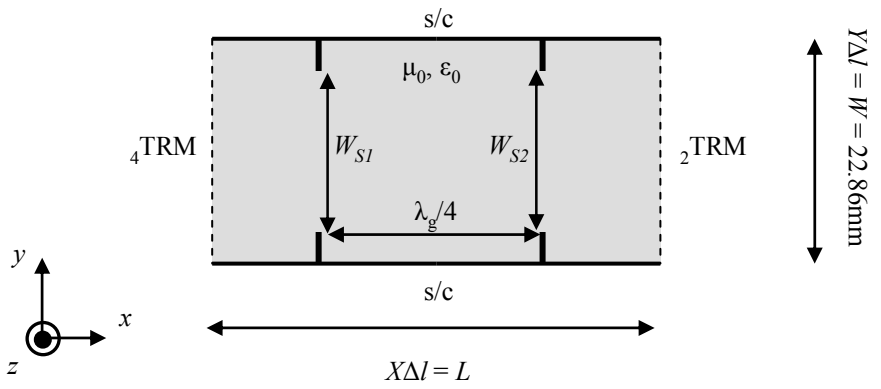

Figure 5-16 - 2nd order X-band microwave band pass filter formed from two inductive irises spaced a quarter of a wavelength in the longitudinal direction.

The need to keep the irises infinitely thin in the longitudinal plane (x-direction) arises again, so as to compare the measured response from the microwave filter with the equivalent passive circuit of Figure 5-13. In this case the principle design methodology of the septa filter is followed, with the exception the desired values for L_1 and L_2 are now $2.75\,\text{nH}$ and $2.45\,\text{nH}$ respectively. These values were chosen so as to demonstrate the time-reversal procedure optimising to smaller measured parameters.

The source excitation is the spatial sinusoid of period $2W$. The TLM simulation parameters are $\Delta l = 0.199\,\text{mm}$, $\Delta t = 4.69e-13\,\text{s}$, $X = 100$, $Y = 115$, $L = 19.9\,\text{mm}$, $W = 22.86\,\text{mm}$ and $N = 16384$. The threshold and damping values are $T_1 = 0.85$, $T_2 = 0.83$ and $\alpha = 0.96$. The initial widths between the segments of each iris are $W_{S1} = W_{S2} = 61\Delta l = 12.13\,\text{mm}$. The S_{11} and S_{21} output of the filter is measured using Eqn.5.19 and shown in Figure 5-17 against the desired response computed using Eqn.5.18.

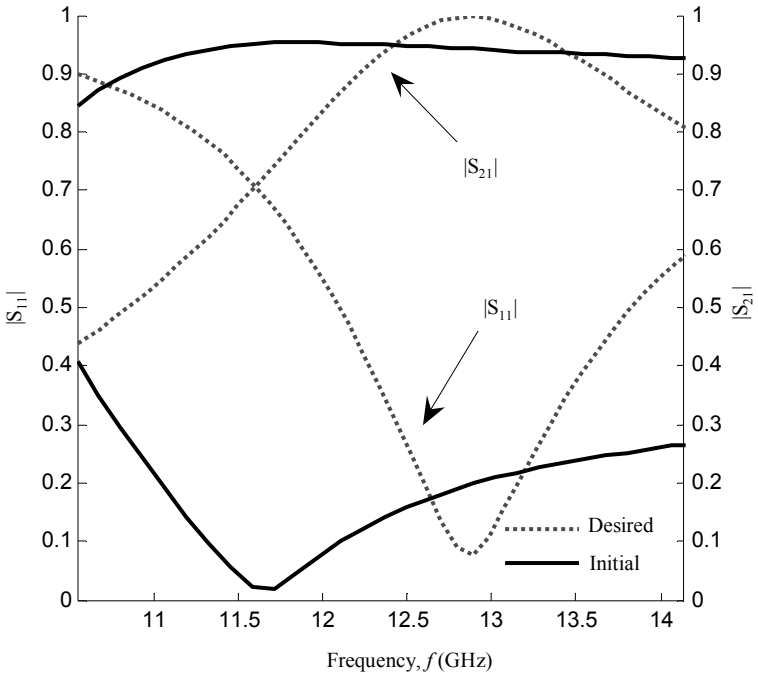

Figure 5-17 - S parameters of 2nd order microwave band pass iris filter at start of time-reversal procedure. Δl = 0.199mm, Δt = 4.69e-13s, X = 100, Y = 115, L = 19.9mm, W = 22.86mm, N = 16384, iris spaces were $W_{S1} = W_{S2}$ = 12.13mm.

The filter is optimised within the frequency band $10-14$ GHz, for the single mode of operation. The waveguide dimensions were WR90, where $W = 22.86$ mm, the cut-off frequency of 6.56 GHz remains unchanged.

The time-reversal design of the problem proceeds in Figure 5-18 showing the optimised S parameters at iterations 4, 5 and 9 of the time-reversal design.

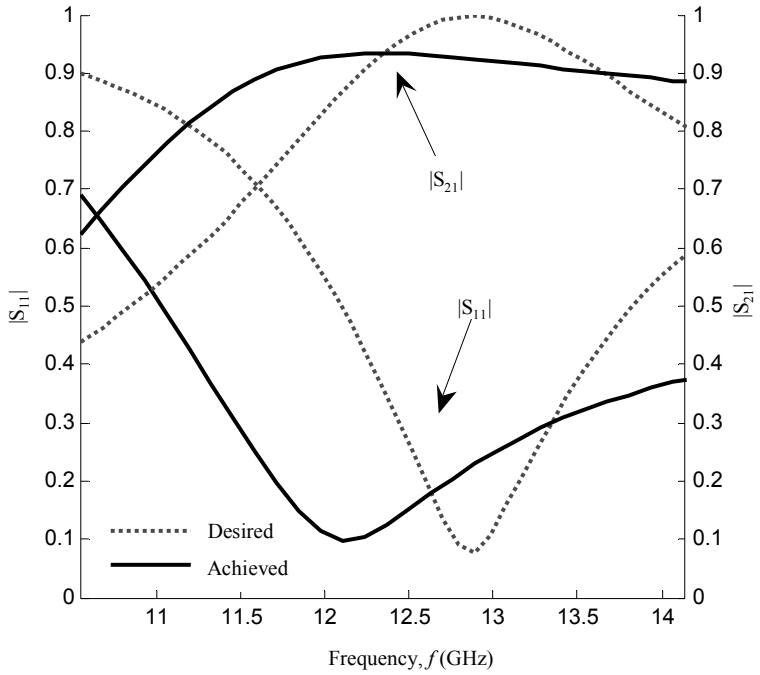
|S21|
|S11|
|S11|
|S21|
Desired
Achieved
Frequency, f (GHz)

a)

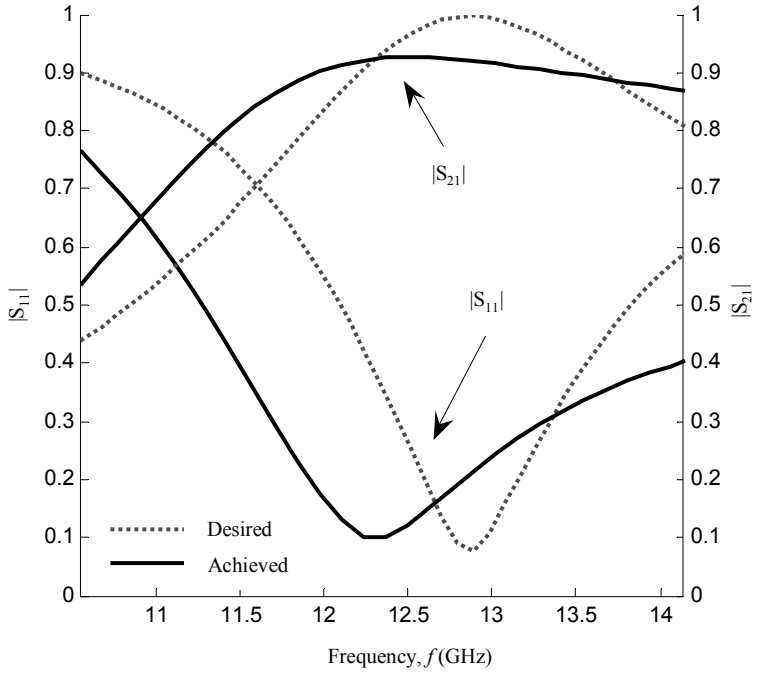
|S21|
|S11|
|S11|
|S21|
Desired
Achieved
Frequency, f (GHz)

b)

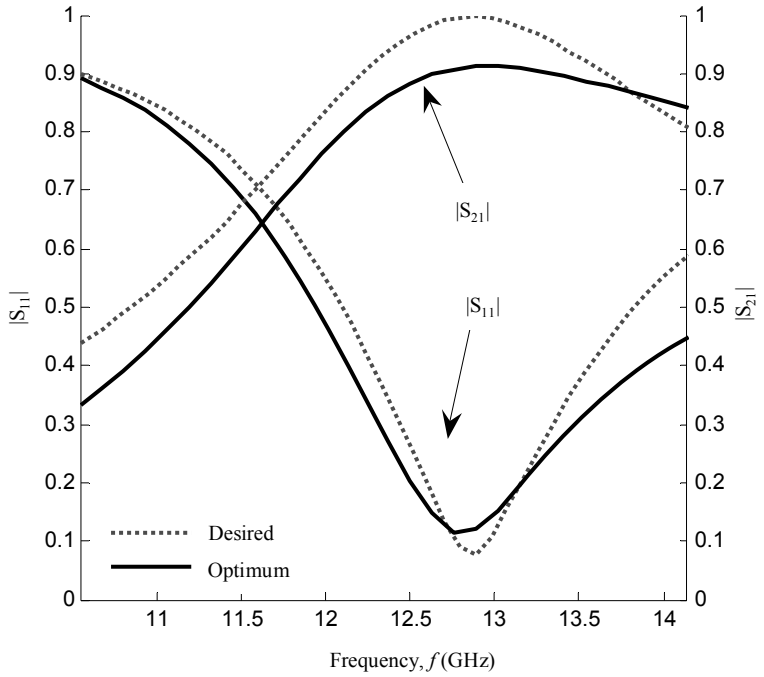

c)

Figure 5-18 - S parameters of 2nd order band pass iris filter optimised using time-reversal, a) iteration 4, b) iteration 5, c) optimised at iteration 9. Δl = 0.199mm, Δt = 4.69e-13s, X = 100, Y = 115, L = 19.9mm, W = 22.86mm, N = 16384, optimised irises from Eqn.5.15 are W_{S1} = 9.2mm and W_{S2} = 9.61mm, snapped to TLM nodes $W_{S1} = 47\Delta l$ = 9.34mm and $W_{S2} = 49\Delta l$ = 9.74mm.

Figure 5-19 shows the figure of merit, FoM, with respect to time-reversal iterations, κ. The optimised dimensions of the irises using Eqn.5.15 were $W_{S1} = 9.2\,\text{mm}$ and $W_{S2} = 9.61\,\text{mm}$, snapped to TLM nodes $W_{S1} = 47\Delta l = 9.34\,\text{mm}$ and $W_{S2} = 49\Delta l = 9.74\,\text{mm}$.

While time intensive, for this example it is simple to verify the time-reversal process has found the optimum solution by measuring FoM for each combination of W_{S1} and W_{S2}, in steps of the spatial sampling, Δl, for separate forward TLM simulations. In Figure 5-20 a contour plot is displayed, which shows the minimum is at $W_{S1} = 47\Delta l = 9.34\,\text{mm}$ and $W_{S2} = 49\Delta l = 9.74\,\text{mm}$, as found by the time-reversal.

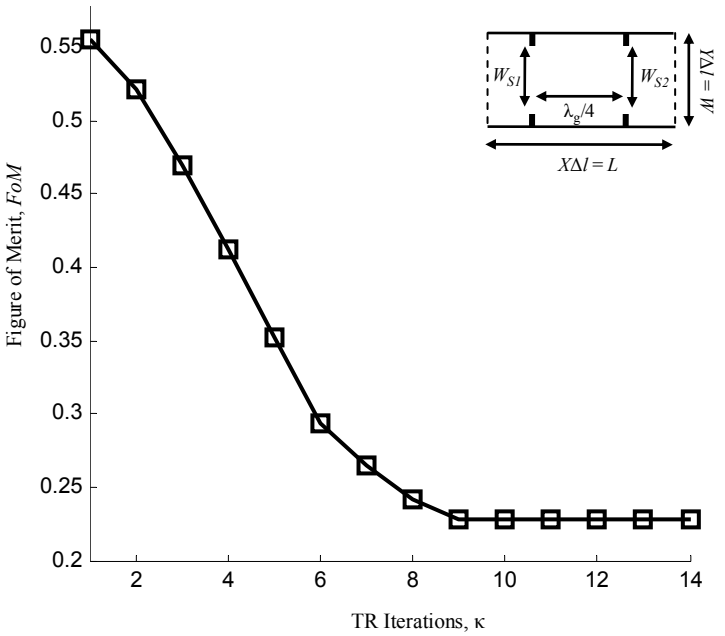

Figure 5-19 - Convergence of time-reversal design process of 2nd order band pass iris filter, Δl = 0.199mm, Δt = 4.69e-13s, X = 100, Y = 115, L = 19.9mm, W = 22.86mm, N = 16384, optimised iris spaces from Eqn.5.15 are W_{S1} = 9.2mm and W_{S2} = 9.61mm, snapped to TLM nodes $W_{S1} = 47\Delta l$ = 9.34mm and $W_{S2} = 49\Delta l$ = 9.74mm, from initial configuration of $W_{S1} = W_{S2}$ = 12.13mm.

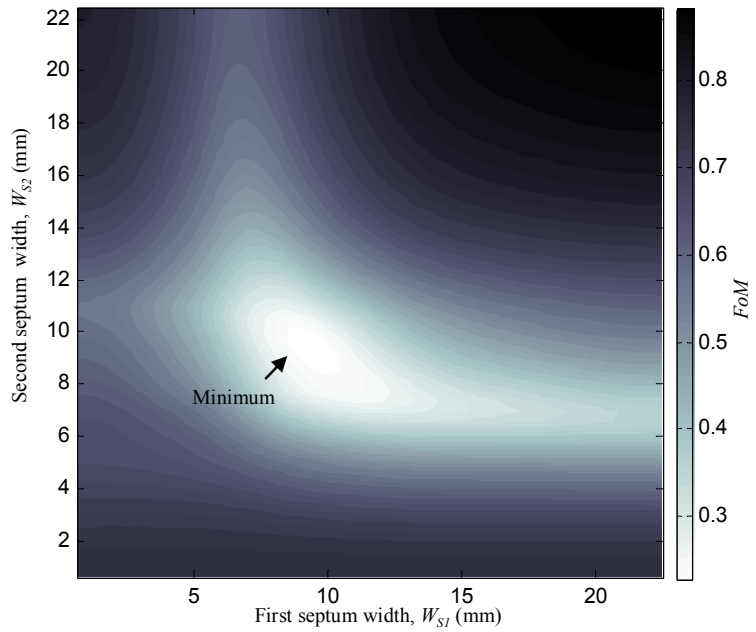

Figure 5-20 - Contour plot of *FoM* for W_{S1} with respect to W_{S2} for iris band pass filter, minimum is at $W_{S1} = 47\Delta l$ = 9.34mm and $W_{S2} = 49\Delta l$ = 9.74mm. Δl = 0.199mm, Δt = 4.69e-13s, X = 100, Y = 115, L = 19.9mm, W = 22.86mm, N = 16384. A total of 45 contours are shown.

5.5.3 90° Waveguide Bend

Waveguide systems, when deployed in large scale projects, often require the need to connect at angles due to obstructing external obstacles. One common waveguide interface occurs when two guides of matching dimensions are connected at right angles to one another [5.10] [5.11].

To minimise the return loss and maximise the throughput, the addition of a tuning post is often used [5.12] [5.13]. A tuning post placed within the bend of Figure 5-21 will excite a number of evanescent modes [5.7] which create a store of magnetic energy, and hence the post acts as an inductive obstacle. The required placement/size/shape of this post to minimise the return loss and maximise the throughput is often achieved through experience, analytical methods, or trial and error [5.13] [5.14].

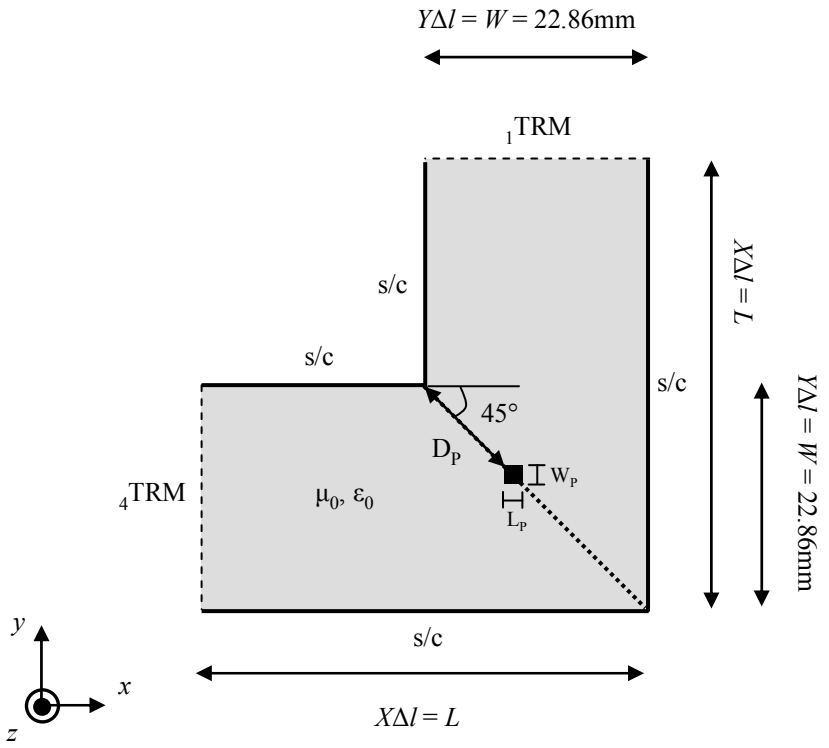

Figure 5-21 - 90° WR90 waveguide bend, tuning post moves along D_P to minimise return loss at the input port.

For simplicity, in the model designed here, the post position is of primary concern, and so the post is made rectangular and of fixed width and length, $W_P = L_P$. An analysis of the cost of fixing the size is performed after the time-reversal design is completed. The post is constrained to move along the main diagonal, shown by the dotted line in Figure 5-21.

The design objective of the time-reversal is to determine the optimum displacement D_P at which the post should be placed to minimise the return loss at the input port, given only a 'best-guess' initial position. The output time-reversal-mirror captures the TLM voltages reflected from port 1 of the neighbouring TLM node, and is of the same size as the input time-reversal-mirror at port 4.

The design criteria are specified for the bend in the bandwidth of $6.8 - 8.8\,\text{GHz}$ and with a centre frequency of $7.8\,\text{GHz}$.

$$\underline{S_{11}^d} = \begin{cases} 0, & \text{if within bandwidth,} \\ \textit{undefined}, & \text{otherwise,} \end{cases} \tag{5.21a}$$

$$\underline{S_{21}^d} = \begin{cases} 1, & \text{if within bandwidth,} \\ \textit{undefined}, & \text{otherwise.} \end{cases} \tag{5.21b}$$

Although the microwave model cannot reach these values, it is informative to design for the best possible case. The figure of merit is the return loss

$$FoM = 20\log_{10}\left|\underline{S_{11}}(f_d)\right| \tag{5.22}$$

where f_d is the desired centre of the frequency band the bend is designed within. The source excitation is a spatial sinusoid at the input port of period $2W$. The simulation variables are $\Delta l = 0.18\,\text{mm}$, $\Delta t = 4.31e-13\,\text{s}$, $X = 220$, $Y = 125$, $L = 40.23\,\text{mm}$, $W = 22.86\,\text{mm}$ and $N = 16384$. The initial position of the post is $D_P = 15.26\,\text{mm}$. The post width and length are

fixed to $W_P = L_P = 30\Delta l = 5.5\,\text{mm}$, The threshold and damping values are, $T_1 = 0.89$ and $\alpha = 0.9$. In Figure 5-22 four stages of the return loss are shown.

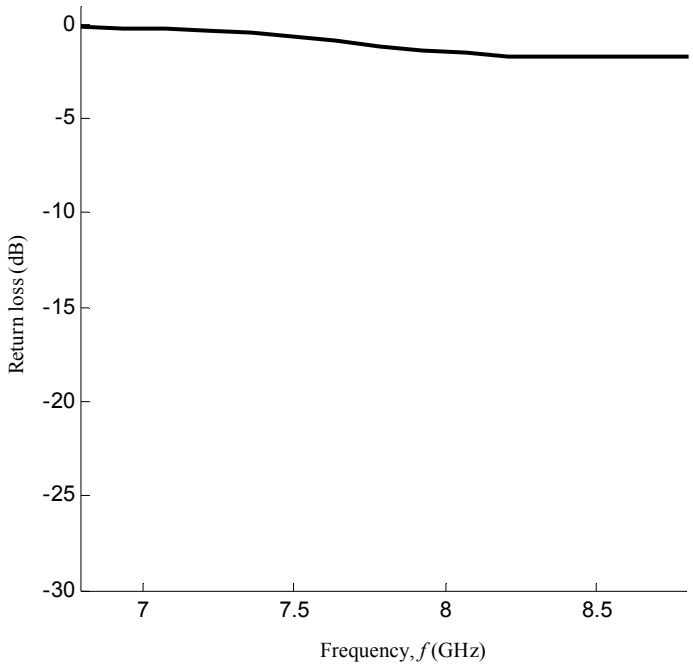

a)

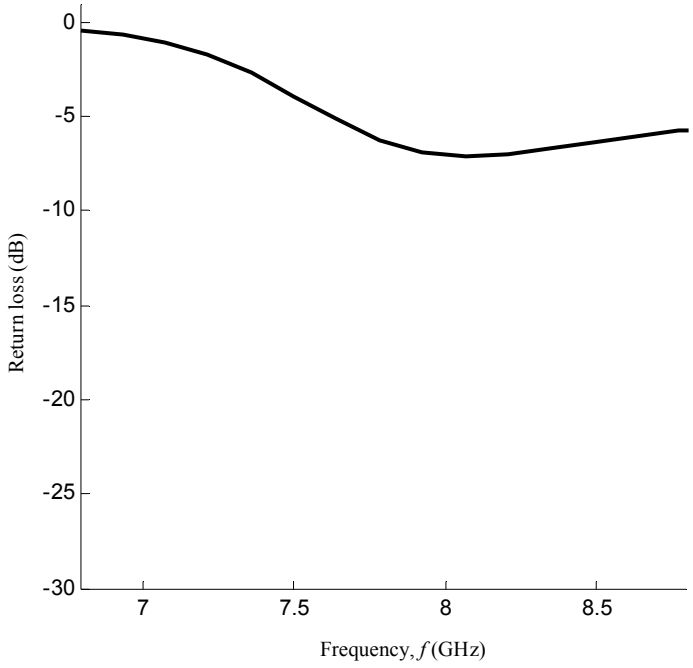

b)

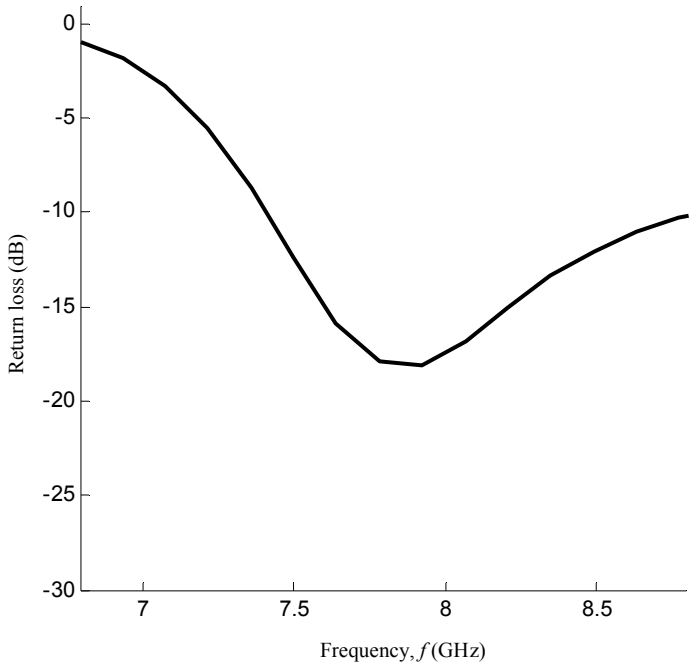

c)

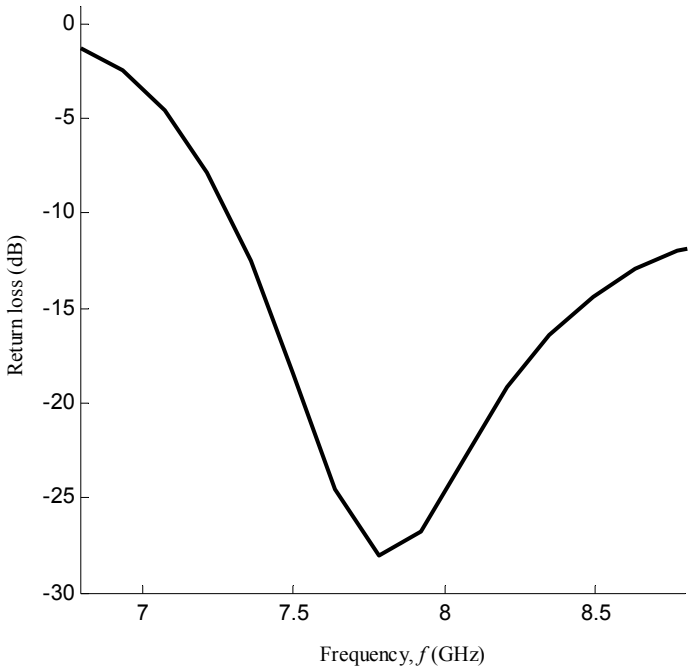

d)

Figure 5-22 - Return loss of 90° waveguide bend design optimised using time-reversal, a) initial, b) iteration 7, c) iteration 11, d) optimised at iteration 13. Δl = 0.18mm, Δt = 4.31e-13s, X = 220, Y = 125, L = 40.23mm, W = 22.86mm and N = 16384. Optimised displacement D_P = 20.43mm from initial D_P = 15.26mm.

Figure 5-23 shows the return loss at the centre frequency ($7.8\,\text{GHz}$) with respect to time-reversal iterations, the time-reversal algorithm was stopped when the return loss remained a minimum, and the final optimised diagonal displacement calculated from the final position of the post in TLM nodes was $D_P = 20.43\,\text{mm}$. The optimised return loss is seen to improve from $-1.12\,\text{dB}$ to $-28.07\,\text{dB}$, resulting in a throughput increase of 12% to over 96% of the input signal transmitted through the bend. A complex bend using multiple tuning posts typically achieves a return loss of around $30-35\,\text{dB}$, and hence the single post example is quite good. Tapered bends [5.11], using varying angles of taper, can reduce the return loss to around $50\,\text{dB}$, but they are not discussed further here.

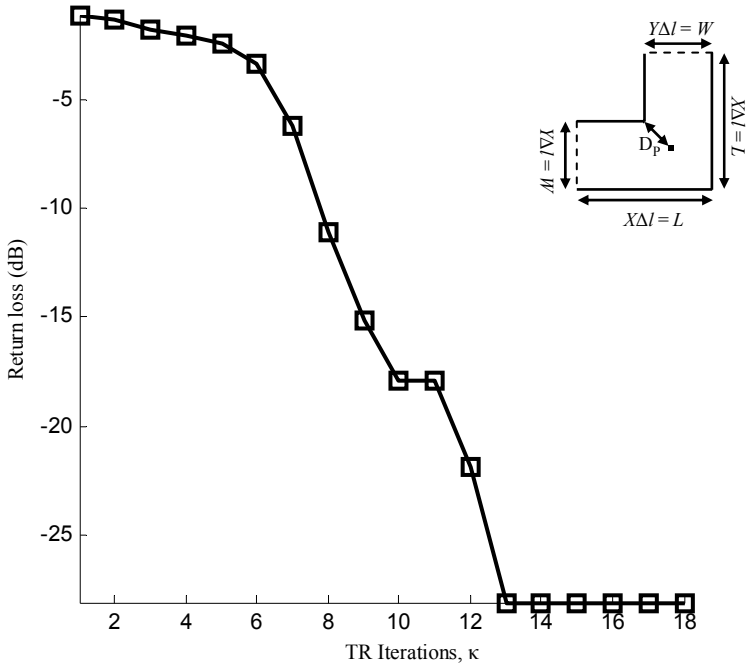

Figure 5-23 - Convergence of time-reversal design of 90° waveguide bend. Δl = 0.18mm, Δt = 4.31e-13s, X = 220, Y = 125, L = 40.23mm, W = 22.86mm and N = 16384. Optimised displacement D_P = 20.43mm from initial D_P = 15.26mm.

For the time-reversal design the post width and length were fixed at $5.5\,\text{mm}$. This is often the case when waveguide components are manufactured, since varying the post size increases the complexity of the manufacturing process. It is informative to investigate the effect changing the post size has on the

return loss. Eqn.5.23 compares the return loss for a post of size $W_P \times L_P$ to a post of size $(W_P + \Delta l) \times (L_P + \Delta l)$, and is used to compute the sensitivity in the return loss of the bend for varying post dimensions, where $W_P = L_P$

$$\underline{Sens}(W_P) = 1 - 10^{\frac{-\left|\left|_{(W_P, L_P)} \underline{S_{11}}_{dB}(f_d)\right| - \left|_{(W_P+\Delta l, L_P+\Delta l)} \underline{S_{11}}_{dB}(f_d)\right|}{20}} \tag{5.23}$$

f_d is fixed at the desired centre frequency of $7.8\,\text{GHz}$.

In Figure 5-24 an analysis of the sensitivity of the return loss to the post size is made, when the top left of the post was fixed at $D_P = 16.81\,\text{mm}$ and the post area varied. The throughput varies by less than $1.5\,\%$ at $\pm 1.5\,\text{mm}$ from the post size chosen for the time-reversal design. It is seen the post location is of more importance than its size.

Further, since only a single variable (the post displacement) is optimised, it is possible to analyse the effect the initial post displacement has upon the convergence of the time-reversal design process. In Figure 5-25 the total time-reversal iterations are shown against the initial post displacement. It is seen that the further the post is from its optimal position, the greater the number of time-reversal iterations are required for convergence.

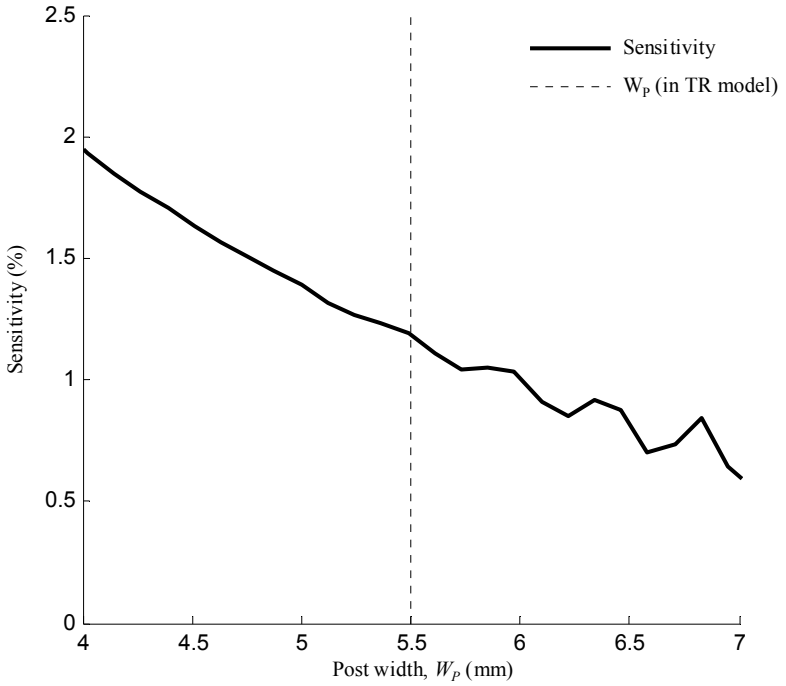

Figure 5-24 - Sensitivity analysis of varying tuning post size in 90° waveguide bend. Δl = 0.061mm, Δt = 1.44e-13s, X = 470, Y = 375, D_P = 16.81mm, other parameters are the same as Figure 5-23.

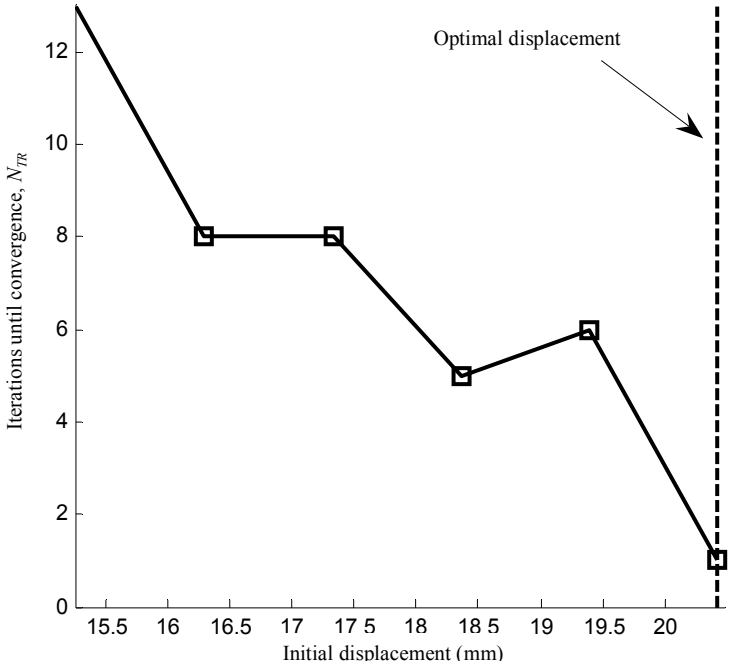

Figure 5-25 - Time-reversal design iterations with respect to initial post displacement for the 90° waveguide bend matching section. Δl = 0.18mm, Δt = 4.31e-13s, X = 220, Y = 125, L = 40.23mm, W = 22.86mm and N = 16384.

5.5.4 Directional Coupler

5.5.4.1 Theory

A directional coupler is a four port waveguide device used to couple an input signal from one waveguide into another [5.1]. In Figure 5-26 a two hole directional coupler for the WR90 waveguide is shown. The device ports are characterised by their operation. Port C is the coupled port, since a field incident at port A will couple to it. Port B is known as the through port, while port D is the isolated port. In an ideal directional coupler the isolated port will receive zero power.

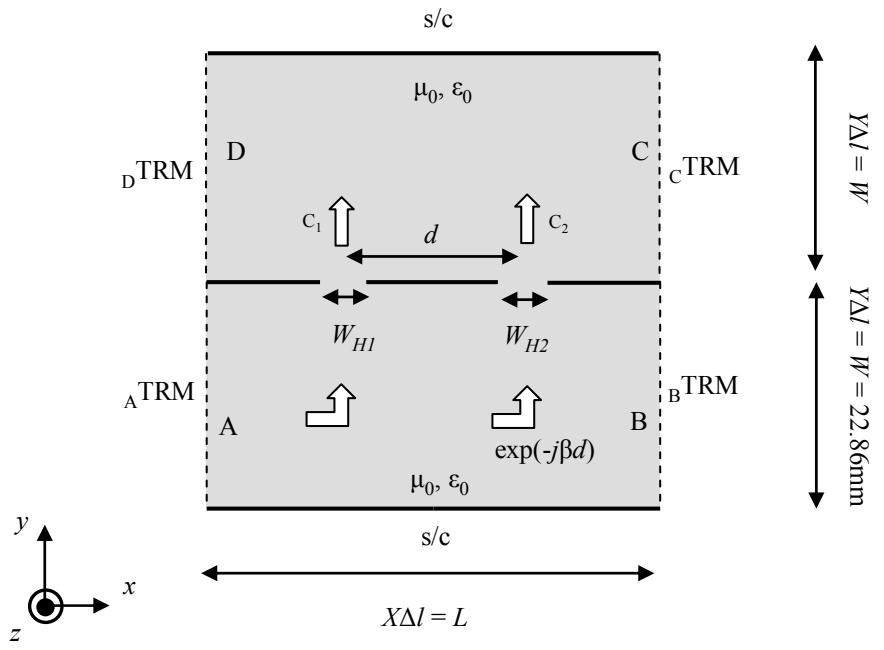

Figure 5-26 - Standard microwave two-hole directional coupler for WR90 wave guiding system.

The coupling of any waveguide coupler is achieved due to cancellation and superposition of field components. The coupler structure is engineered so the field components through hole 1 and 2 travelling forward will add in phase, while those through hole 1 and 2 travelling to port D will cancel, isolating port D, while splitting the input signal between ports B and C

[5.7]. In Figure 5-26 the reference plane is taken as the centre of hole 1, and it is seen the field at hole 2 has travelled a distance of d, the bold arrows are used to denote coupling coefficients through holes 1 and 2. Hence the forward field, at port C is

$$\begin{aligned}\vec{E}_C &= C_1 \exp(-j\beta d) + C_2 \exp(-j\beta d) \\ &= \exp(-j\beta d)(C_1 + C_2).\end{aligned} \tag{5.24}$$

The backward field through hole 2 travels a total distance of $2d$ to return to hole 1. d forward in the lower waveguide and d backward (out of phase) in the upper waveguide, hence the field D is

$$\begin{aligned}\vec{E}_D &= \left(C_1 \exp(-j\beta 0) + C_2 \exp(-2j\beta d)\right) \\ &= \left(C_1 + C_2 \exp(-2j\beta d)\right).\end{aligned} \tag{5.25}$$

Assuming $W_{H1} = W_{H2}$, then $C_1 = C_2$ and Eqns.5.24-5.25 simplify to read

$$\vec{E}_C = 2C_1 \exp(-j\beta d), \tag{5.26a}$$

$$\vec{E}_D = C_1\left(1 + \exp(-2j\beta d)\right). \tag{5.26b}$$

If $2\beta d = n\pi$, where n is an odd integer, $\vec{E}_D = 0$, and hence port D of the coupler is isolated. Rearranging and substituting $\beta = 2\pi/\lambda_g$ into the above requirement, gives for the hole separation

$$d = n\pi/(2\beta) = n\lambda_g/4. \tag{5.27}$$

The minimum separation between the holes, d, is for $n = 1$, a quarter of a guide wavelength.

The coupling and directivity of a directional coupler in decibels for the coupler in Figure 5-26 is defined as [5.7]

$$\underline{C} = 10\log_{10}\left(\frac{\underline{\underline{P_A}}(f)}{\underline{P_C}(f)}\right), \tag{5.28a}$$

$$\underline{D} = 10\log_{10}\left(\frac{\underline{\underline{P_C}}(f)}{\underline{P_D}(f)}\right), \tag{5.28b}$$

where P_A denotes power at the input port, P_C denotes power at the coupled port and P_D denotes the power at the isolated port.

In the TLM simulation, the coupling and directivity are computed efficiently using

$$\underline{C} = 10\log_{10}\left(\frac{\underline{\underline{\hat{V}_A}}(f)^2/Z_0}{\underline{\hat{V}_C}(f)^2/Z_0}\right) = 20\log_{10}\left(\frac{\underline{\underline{\hat{V}_A}}(f)}{\underline{\hat{V}_C}(f)}\right), \tag{5.29a}$$

$$\underline{D} = 20\log_{10}\left(\frac{\underline{\underline{\hat{V}_C}}(f)}{\underline{\hat{V}_D}(f)}\right), \tag{5.29b}$$

where the ^ operator denotes the Fourier transform of the time domain voltages and $Z_0 = 1$ using normalised TLM nodes.

5.5.4.2 Time-Reversal Design Process

The time-reversal design objective is to determine the hole widths W_{H1} and W_{H2} subject to an optimal coupling, the hole separation is fixed at $\lambda_g/4$, where λ_g is the wavelength of the desired frequency in the waveguide. It is seen in Figure 5-26 a total of four mirrors are required. The time-reversal-mirror at port A is formed as

$$\underline{\underline{{}_{A}V_{TRM\,P,H}^{F,\,R}}} = \underline{\underline{{}_{4}V_{TRM\,P,H}^{F,\,R}}}(y,k), \tag{5.30a}$$

where $y = 0...Y-1$. Similarly,

$$\underline{\underline{{}_{D}V_{TRM\,P,H}^{F,\,R}}} = \underline{\underline{{}_{4}V_{TRM\,P,H}^{F,\,R}}}(y,k), \tag{5.30b}$$

where $y = Y...2Y$. For the case of the time-reversal-mirrors at ports B and C, it is seen

$$\underline{\underline{{}_{B}V_{TRM\,P,H}^{F,\,R}}} = \underline{\underline{{}_{2}V_{TRM\,P,H}^{F,\,R}}}(y,k), \quad \text{where } y = 0...Y-1, \tag{5.30c}$$

$$\underline{\underline{{}_{C}V_{TRM\,P,H}^{F,\,R}}} = \underline{\underline{{}_{2}V_{TRM\,P,H}^{F,\,R}}}(y,k), \quad \text{where } y = Y...2Y. \tag{5.30d}$$

The same design process as section 5.2 is followed, but with a few alterations that will now be described. Until now the time-reversal process has been demonstrated on purely two port systems, where both time-reversal-mirrors are perturbed. In this model, only the coupling and directivity are perturbed.

As an example, the desired coupling is fixed at 20 dB or 10 %. This is a typical application when the coupler is used to split a high powered signal for measurement via a low powered device [5.1]. The difference equation in the bandwidth $8-10$ GHz now reads

$$\underline{\hat{G}_2} = \begin{cases} \underline{C^d} - \underline{C}, & \text{if within bandwidth,} \\ 0, & \text{otherwise,} \end{cases} \tag{5.31a}$$

$$\underline{\hat{G}_4} = \begin{cases} \underline{D^d} - \underline{D}, & \text{if within bandwidth,} \\ 0, & \text{otherwise.} \end{cases} \tag{5.31b}$$

Port D is desired isolated and in the simulation $40\,\text{dB}$ was used, or 1%, which is practically acceptable [5.15]. In this model, the hole widths are optimised. Better directivity, of around $40-50\,\text{dB}$ over a wider bandwidth, typically $3-4\,\text{GHz}$, can be achieved by using a higher order design; however, the second order design is demonstrated to allow the same model to be used in further development of the time-reversal in subsequent chapters.

The time-reversal design process begins with initial hole widths of $W_{H1}=3\Delta l=0.6\,\text{mm}$ and $W_{H2}=5\Delta l=0.99\,\text{mm}$. It is known [5.1], for the backward and forward field components to cancel, W_{H1} should equate to W_{H2}. This restraint is not forced upon the time-reversal design process, as it is more interesting to illustrate whether the time-reversal determines this. TLM simulation parameters are $\Delta l=0.199\,\text{mm}$, $\Delta t=4.69e-13\,\text{s}$, $Y=115$, $W=22.86\,\text{mm}$ and $N=16384$. The threshold and damping values were, $T_1=0.05$, $T_2=0.42$ and $\alpha=0.91$. The input excitation of the spatial sinusoid of period $2W$ is applied at port A. In Figure 5-27 three variations of the coupling and directivity are shown for the time-reversal design iterations, 4, 7 and 11 respectively. When optimised, W_{H1} and W_{H2} were found to be $5.73\,\text{mm}$ each using Eqn.5.15, giving a TLM simulation with $W_{H1}=W_{H2}=29\Delta l=5.76\,\text{mm}$. The desired directivity of $40\,\text{dB}$ is not achieved, as is expected since only two holes are used, yet it is informative to design for the best possible case.

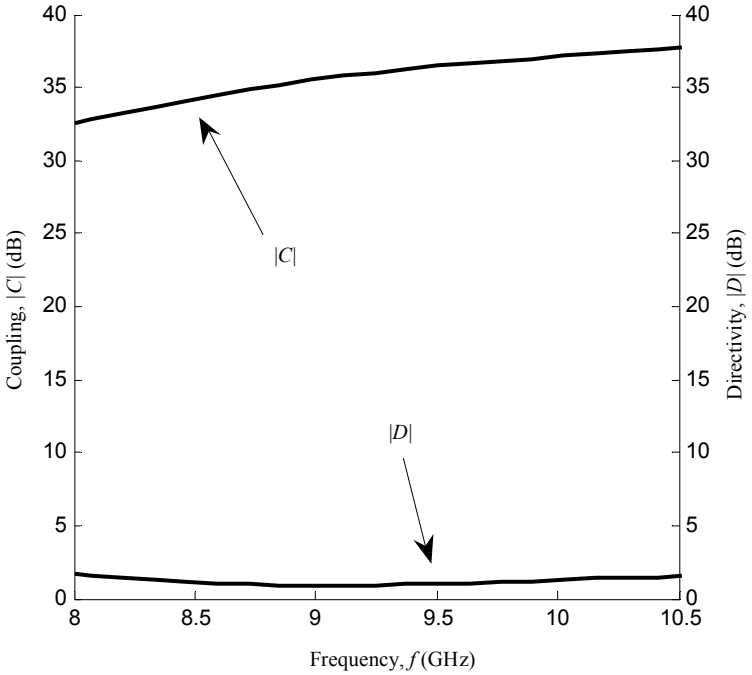
40
35
30
25
20
15
10
5
0
8
8.5
9
9.5
10
10.5
Coupling, |C| (dB)
Directivity, |D| (dB)
|C|
|D|
Frequency, f (GHz)

a)

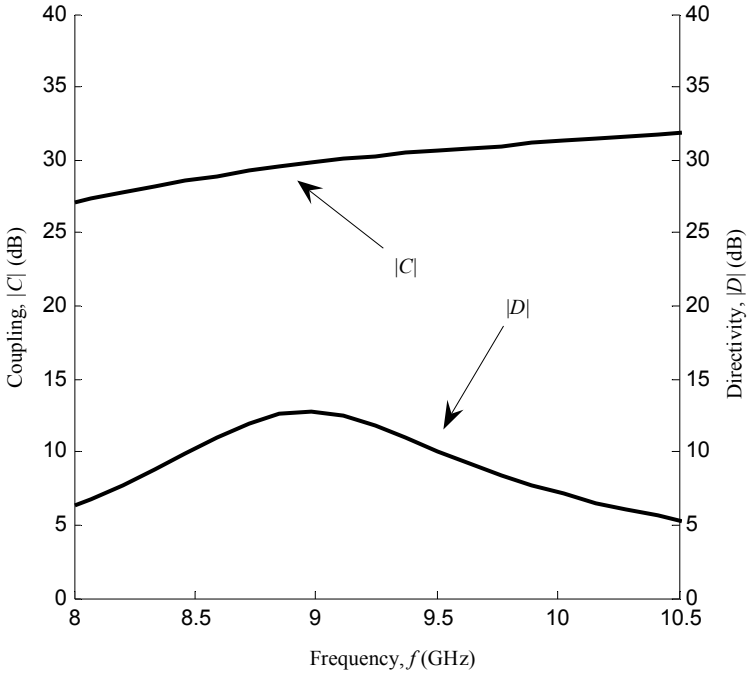
40
35
30
25
20
15
10
5
0
8
8.5
9
9.5
10
10.5
Coupling, |C| (dB)
Directivity, |D| (dB)
|C|
|D|
Frequency, f (GHz)

b)

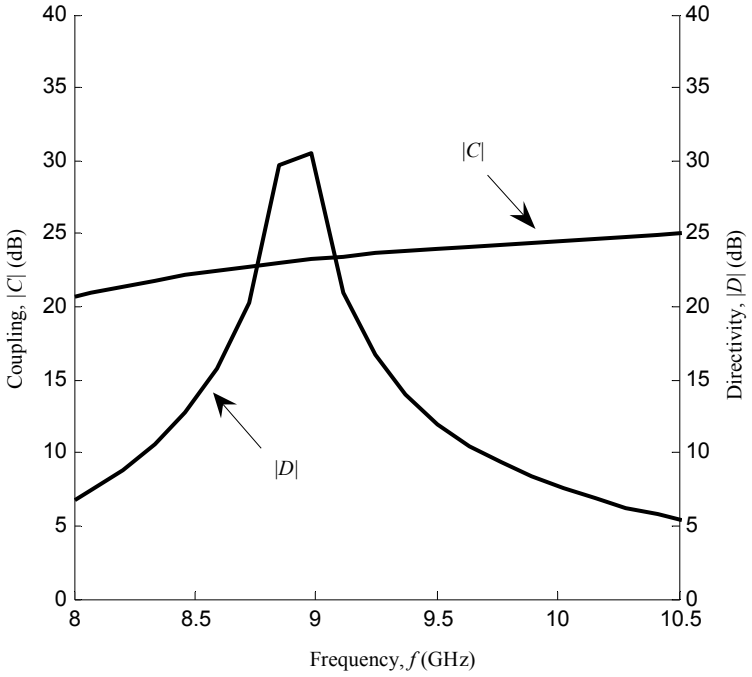

c)

Figure 5-27 - Coupling and directivity of directional coupler, time-reversal iteration a) κ = 4, b) κ = 7 and c) optimised, κ = 11. Δ*l* = 0.199mm, Δ*t* = 4.69e-13s, Y = 115, W = 22.86mm and N = 16384. Initially W_{H1} = 0.6mm and W_{H2} = 0.99mm. Optimised $W_{H1,2}$ = 5.73mm using Eqn.5.15, snapped to TLM nodes the optimised holes are $W_{H1,2}$ = 29Δ*l* = 5.76mm.

In Figure 5-28 the measured hole widths at each design iteration are shown, from which it is seen the time-reversal design has found the optimum solution at iteration 11.

To complete the analysis, Figure 5-29 shows the coupling and directivity against time-reversal iteration number, κ at the centre of the bandwidth 9 GHz.

From Figure 5-28 and Figure 5-29 it is seen that the time-reversal design process continues to attempt optimisation due to the high design specification and the results oscillate around the optimum solution. This behaviour is a problem specific phenomenon that was not seen for the two filters or the bend design.

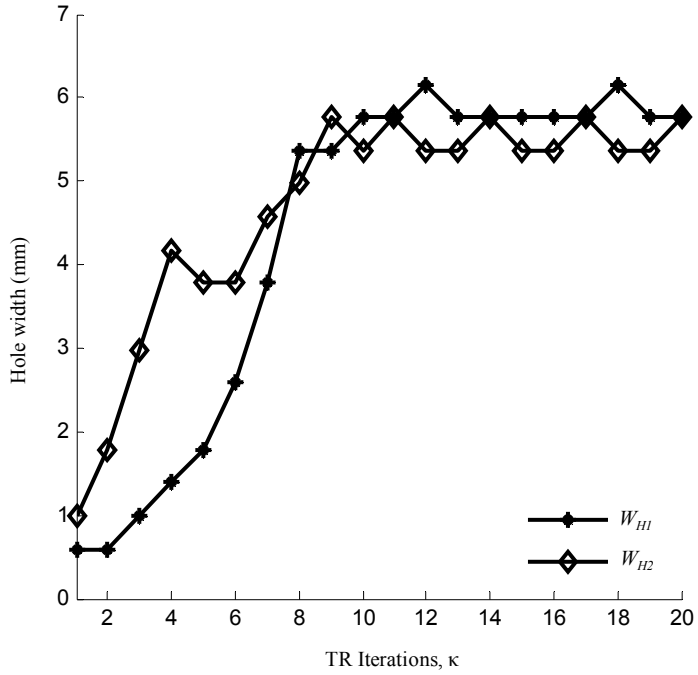

Figure 5-28 - Measured hole widths of two-hole coupler during time-reversal design, optimum is found at κ = 11, and again at κ = 14, 17, 20. Δ*l* = 0.199mm, Δ*t* = 4.69e-13s, Y = 115, W = 22.86mm and N = 16384.

To further investigate the oscillation, Figure 5-30 shows the coupling and directivity when the spatial discretisation is achieved using a finer mesh with $\Delta l = 0.09\,\text{mm}$. The finer sampling removes the oscillation, at the expense of more than doubling the runtime. The optimal solution is found to be $W_{H1} = W_{H2} = 5.45\,\text{mm}$.

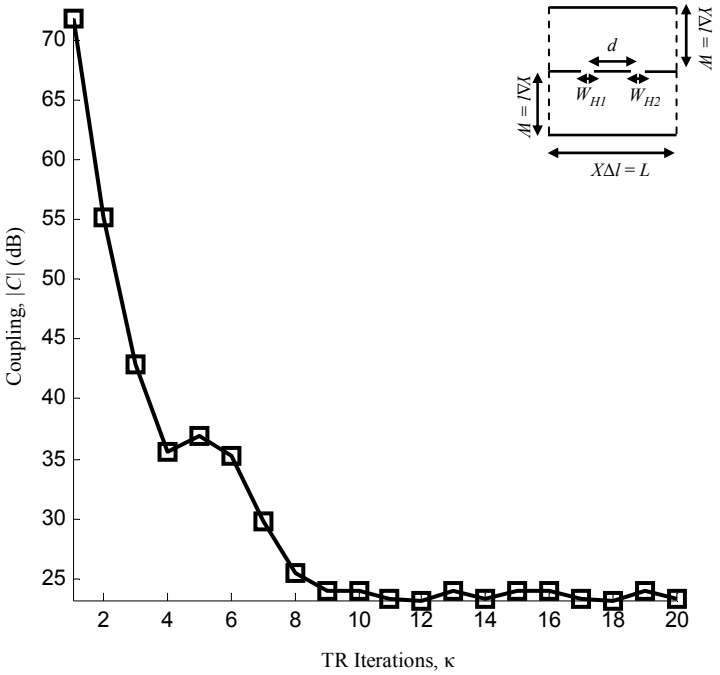

a)

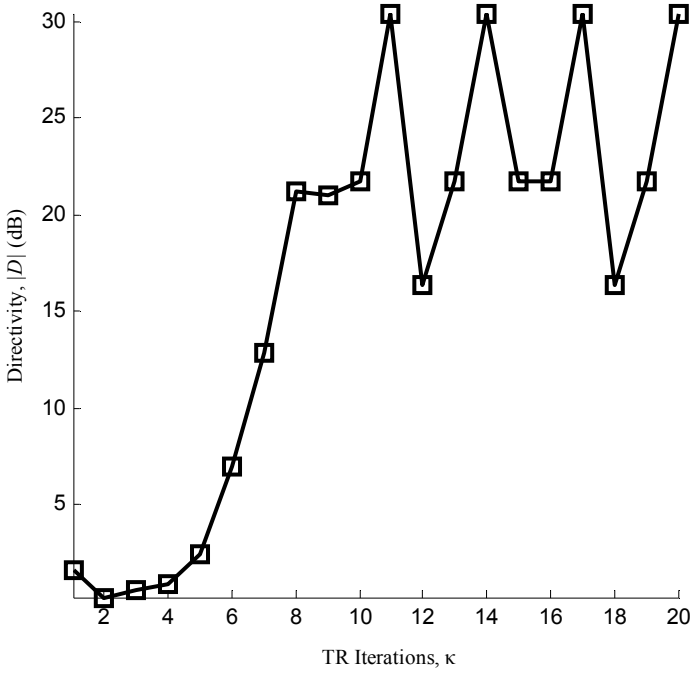

b)

Figure 5-29 - Convergence of time-reversal design procedure of directional coupler design, a) coupling, b) directivity. Δl = 0.199mm, Δt = 4.69e-13s, Y = 115, W = 22.86mm and N = 16384. Initially W_{H1} = 0.6mm and W_{H2} = 0.99mm. Optimised $W_{H1,2}$ = 5.73mm using Eqn.5.15, snapped to TLM nodes the optimised holes are $W_{H1,2} = 29\Delta l$ = 5.76mm.

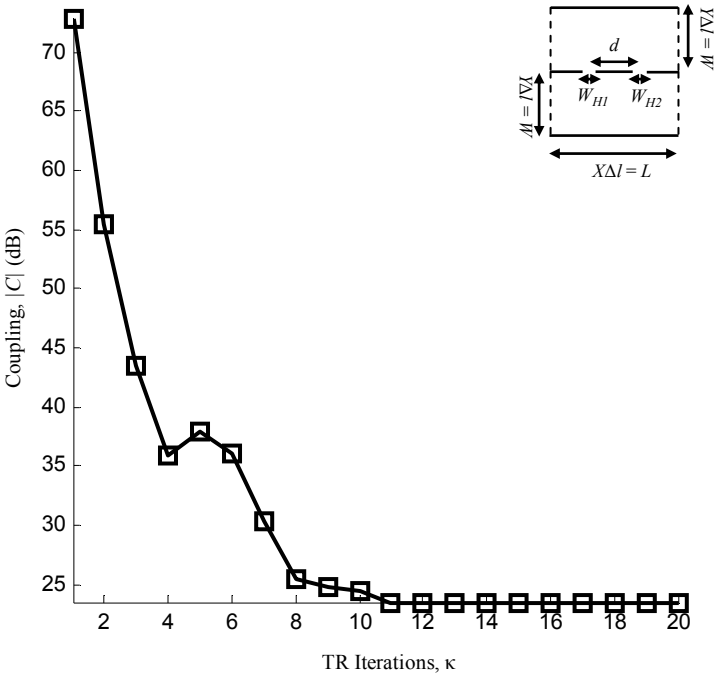

a)

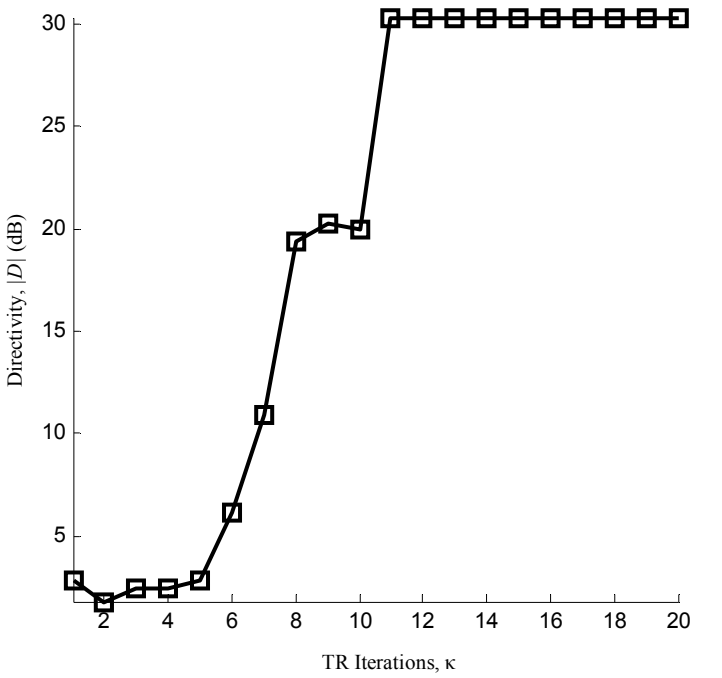

b)

Figure 5-30 - Convergence of time-reversal design procedure of directional coupler design using finer level of spatial sampling, a) coupling, b) directivity. Δl = 0.09mm, Δt = 2.15e-13s, Y = 251, W = 22.86mm and N = 16384.

5.6 Conclusion

The chapter began by reviewing the method of time-reversal design at microwave frequencies. This was then extended to the case of multiple design iterates, and the choice of threshold and damping values for use within the procedure was investigated. Four example case studies were introduced, two filters, a waveguide bend, and a directional coupler. The chapter has demonstrated the use of time-reversal for wide band system design, and shown how the method is derived for waveguide component optimisation.

The need for four time-reversal-mirrors for the coupler design is seen to double the memory required by the time-reversal design algorithm. The next chapter investigates techniques for reducing the memory required for time-reversal component design optimisation.

5.7 References

[5.1] D. M. Pozar, *Microwave Engineering*. John Wiley & Sons Inc, New York, NY, 3rd ed., 2007.

[5.2] M. Forest and W. J. R. Hoefer, "A Novel Synthesis Technique for Conducting Scatterers Using TLM Time Reversal," *IEEE Transactions on Microwave Theory and Techniques*, vol. 43, pp. 1371–1378, June 1995.

[5.3] M. Forest and W. J. R. Hoefer, "TLM Synthesis of Microwave Structures Using Time Reversal," pp. 779–782, IEEE Microwave Theory and Techniques Symposium Digest, Albuquerque, NM, USA, 1-5 June 1992.

[5.4] R. Sorrentino, P. P. So, and W. J. R. Hoefer, "Numerical Microwave Synthesis by Inversion of the TLM Process," pp. 1273–1277, 21st European Microwave Conference Digest, Stuttgart, Germany, 4-6 October 1991.

[5.5] D. K. Cheng, *Field and Wave Electromagnetics*. Prentice-Hall, Reading, MA, 2nd ed., 1989.

[5.6] E. Kreyszig, *Advanced Engineering Mathematics*. John Wiley & Sons Inc, New York, NY, 8th ed., 1998.

[5.7] R. E. Collin, *Foundations for Microwave Engineering*. John Wiley & Sons Inc, New York, NY, 2nd ed., 2001.

[5.8] D. de Cogan, W. J. O'Connor, and S. Pulko, *Transmission Line Matrix (TLM) in Computational Mechanics*. CRC Press, London, 2005.

[5.9] R. Ludwig and P. Bretchko, *RF Circuit Design Theory and Applications*. Prentice-Hall, Upper Saddle River, NJ, 2000.

[5.10] S. Amari and J. Bornemann, "Modelling of Propagation and Scattering in Waveguide Bends," pp. 1–4, 30th European Microwave Conference, Paris, France, 4-6 October 2000.

[5.11] R. Coccioli, M. Mongiardo, G. Pelosi, and R. Ravanelli, "Design of Matched Bends in Rectangular Waveguides by Finite Element Method," *International Journal of Microwave and Millimeter-Wave Computer-Aided Engineering*, vol. 6, pp. 391–398, November 1996.

[5.12] R. E. Collin, *Field Theory of Guided Waves*. John Wiley & Sons Inc, New York, NY, 2nd ed., 1990.

[5.13] R. Elio and E. B. El-Sharawy, "Reducing Losses in Dielectric Waveguide Discontinuities," *IEEE Transactions on Microwave Theory and Techniques*, vol. 46, pp. 1045–1054, August 1998.

[5.14] M. Mongiardo, A. Morino, and T. Rozzi, "Analysis and Design of Wide-Band Matched Waveguide Bends Including Discontinuities," pp. 983–986, IEEE Microwave Theory and Techniques Symposium Digest, Orlando, FL, USA, 16-20 May 1995.

[5.15] Flann Microwave, Online: http://www.flann.com/Products_Home/Couplers/couplers.html, Retrieved: 20/08/2009.

6. Interpolation and Modal Filtering

Time-reversal simulation using the conventional numerical algorithm provides the basis for a simple component optimisation procedure. However, the computational requirements of the approach can become excessive, requiring the recording of complete field time histories on a surface surrounding the problem space. It was seen, for the final case study of the directional coupler of the previous chapter, the memory requirements of the time-reversal process doubled, due to the need for four time-reversal-mirrors. In general, the memory requirements depend on the number of ports and the number of time steps in the simulation and can easily become intractable.

In this chapter the Prony method presented in Chapter four is used for the design optimisation and as a way of reducing the number of temporal iterations required by the transmission-line modelling (TLM) method.

Temporal, spatial and modal filtering methods are employed to reduce the computational resources demanded by the time-reversal process. The example case studies of the band pass filter, waveguide bend and coupler are used to quantify the balance between computational efficiency gains and final design quality.

6.1 Prony's Method

In this section Prony's method introduced in Chapter four is applied to the design process to temporally extrapolate the time-reversal-mirror samples, reducing the memory requirements of the full time-reversal design method.

The particular and homogenous solutions are both computed for the reduced time $N - N_P$, after which the perturbation is performed. The reverse stage is computed for the full time N, using a Prony series with U poles to extrapolate the additional N_P time steps.

6.1.1 Results

In order to measure the application of Prony's method to time-reversal design, the second order septum filter first designed in Chapter five is repeated, with the exception, the initial forward particular and homogenous models are performed for the reduced time $N = 8192$. The TLM parameters are the same as chapter five, where $\Delta l = 0.297\,\text{mm}$, $\Delta t = 7e-13\,\text{s}$, $X = 67$, $Y = 77$, $L = 19.85\,\text{mm}$, $W = 22.86\,\text{mm}$, and $W_{S1} = W_{S2} = 0.89\,\text{mm}$ initially. A Prony series with $U = 100$ poles matched over the last 2000 samples, is then used to extrapolate a further $N_P = 8192$ reverse time samples, giving the combined total of 16384. In Figure 6-1a the convergence of the time-reversal design process using the scalar figure of merit is shown for the bandwidth $10-14\,\text{GHz}$. The TLM time-reversal algorithm with Prony converges to the same solution of septa widths as in the classical time-reversal optimisation in Chapter five, however the figure of merit is different to Chapter five, due to the reduced runtime of the forward particular solution, and hence the reduced number of sample points in the measure. Figure 6-1b shows the optimised S parameters.

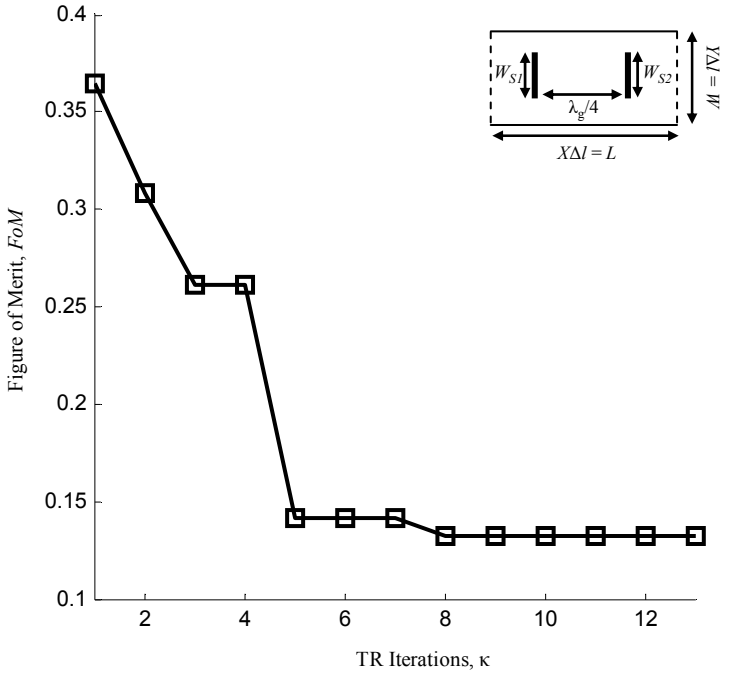

a)

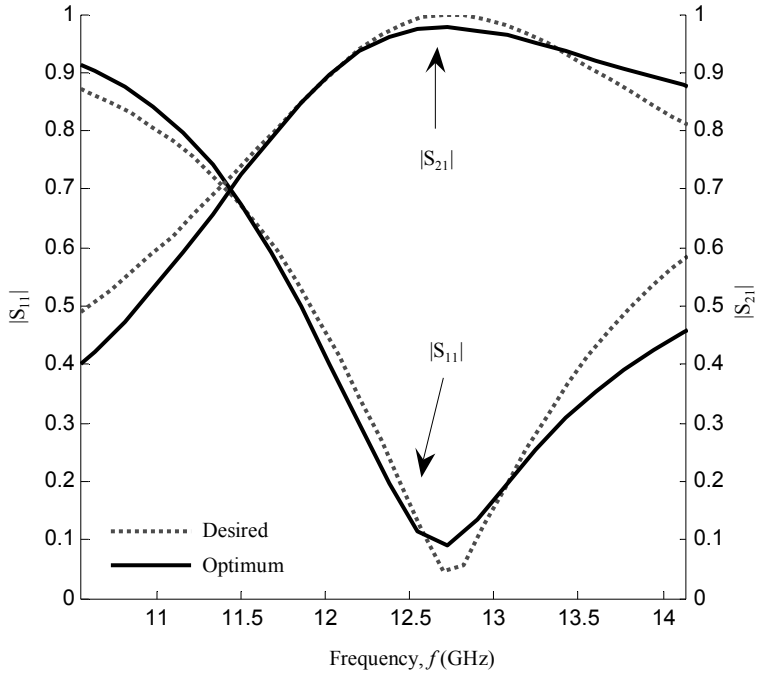

b)

Figure 6-1 - a) Convergence of time-reversal design process of 2nd order band pass septa filter, using Prony's method to extrapolate half of the reverse temporal iterations, b) optimised S parameters. Δl = 0.297mm, Δt = 7e-13s, X = 67, Y = 77, L = 19.89mm, W = 22.86mm.

While successful in reducing the memory and runtime requirements of the time-reversal procedure, the number of poles in the Prony series is dependant upon the source, time-reversal-cavity and component designed. An alternative approach to the one presented is to perform the Prony extrapolation on the forward data before the perturbation is applied; this however had no noticeable differences. A general method for memory reduction that is applicable for a wider range of components is now demonstrated.

6.2 Temporal and Spatial Linear Interpolation

As discussed in Chapter five, the perturbation of the reverse scattered field before the reverse simulation, causes a loss of resolution of the scattering object. The key issue is whether the quantity of recorded data can be reduced in order to save memory without causing significant loss of resolution. In this section, the methods of temporal and spatial linear interpolation applied to the time-reversal-mirrors are investigated.

Linear interpolation is used to estimate unknown samples of a discrete ordered data set. For the purpose of time-reversal, the time-reversal-mirrors will only save a proportion of the forward time data, interpolating the unknown samples as the weighted average of the neighbouring stored values. In temporal interpolation every k th temporal sample is stored. For example, if 50% of the time-reversal-mirrors are stored then 1 in every 2 temporal samples are stored, see Figure 6-2a. If 80% of the time-reversal-mirrors are stored then 4 in 5 samples are stored etc. In this manner, to ensure that the interpolation is equally spaced in the time-reversal-mirrors, storing more than 50% of the time-reversal-mirrors means storing $N-1$ in every N samples, while below 50% requires storage of 1 in every N samples, interpolating those samples not stored.

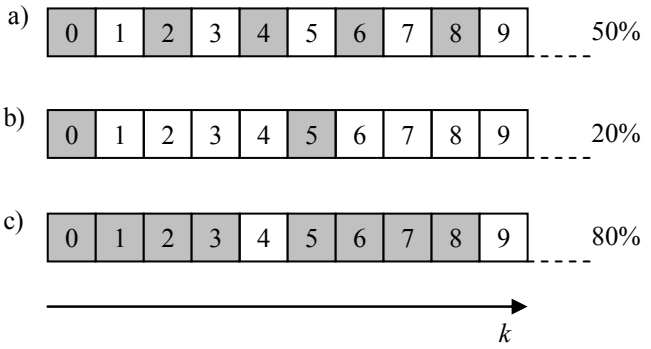

Figure 6-2 - Illustration of linear temporal interpolation. Grey boxes are samples stored, while white are interpolated as the weighted average of the nearest stored neighbour.

Spatial linear interpolation is similarly applied, with the exception the interpolation is applied to the spatial index of the time-reversal-mirror.

The method of spatial or temporal linear interpolation is seen to reduce the memory requirements of the time-reversal-mirrors, from $X \times N$ to $X \times N / N_{TRM}$ or $Y \times N$ to $Y \times N / N_{TRM}$, where N_{TRM} is the level of interpolation. Both spatial and temporal interpolations are problem independent, in that they are applied to the time-reversal-mirrors, with no knowledge of the component structure.

6.3 Modal Decomposition

In many cases, a more appropriate representation of the scattered fields for the purposes of complexity reduction is a local modal decomposition. With modal filtering only a simple time varying scalar amplitude for each physically significant mode present in the far field need be stored rather than a full time varying vector of spatial samples across the waveguide.

As an example, for a 2D parallel metal plate waveguide with Y transverse nodes, there are $N_M = Y - 1$ possible modes. If a symmetric spatial sinusoid excites the waveguide as in the previous examples of Chapter five, only a

limited number of these modes will actually exist [6.1]. The symmetric source is known to excite only odd symmetric order modes, and hence $N_M = (Y-1)/2$, where Y is odd

$$\underline{V}(y) = \sin\left(\left(y\Delta l + \Delta l/2\right)\frac{\pi}{W}\right). \tag{6.1}$$

Assuming the symmetric excitation of Eqn.6.1, the transverse modal distribution within the waveguide using TLM shunt nodes is expressed as

$$\underline{V}(y) = \sum_{n=0}^{N_M-1} A_n \sin\left(\left(y\Delta l + \Delta l/2\right)\frac{(2n+1)\pi}{W}\right) \tag{6.2}$$

where A_n is the amplitude of the mode $2n+1$, and n ranges from 0 to $N_M - 1$. Multiplication of Eqn.6.2 by the spatial sinusoid over one half period W, and summation over the spatial domain, y and the modal domain, n, gives

$$\begin{aligned}\sum_{n=0}^{N_M-1}\sum_{y=0}^{Y-1}\underline{V}(y)\sin\left(\left(y\Delta l + \Delta l/2\right)\frac{(2n+1)\pi}{W}\right) = \\ \sum_{n=0}^{N_M-1} A_n \sum_{y=0}^{Y-1}\sin^2\left(\left(y\Delta l + \Delta l/2\right)\frac{(2n+1)\pi}{W}\right).\end{aligned} \tag{6.3}$$

As $\Delta l \to 0$, the summation of the squared spatial sinusoid will tend to $Y/2$ for all n, since a symmetric excitation is assumed. Eqn.6.3 becomes

$$\sum_{n=0}^{N_M-1}\sum_{y=0}^{Y-1}\underline{V}(y)\sin\left(\left(y\Delta l + \Delta l/2\right)\frac{(2n+1)\pi}{W}\right) = Y/2\sum_{n=0}^{N_M-1} A_n\ . \tag{6.4}$$

Rearranging, it is seen the modal amplitudes of Eqn.6.2 are

$$\sum_{n=0}^{N_M-1} A_n = \frac{\sum_{n=0}^{N_M-1}\sum_{y=0}^{Y-1} \underline{V}(y)\sin\left(\left(y\Delta l + \Delta l/2\right)\frac{(2n+1)\pi}{W}\right)}{Y/2}. \tag{6.5}$$

Hence for a single mode, Eqn.6.5 is written as

$$A_n = \frac{\sum_{y=0}^{Y-1} \underline{V}(y)\sin\left(\left(y\Delta l + \Delta l/2\right)\frac{(2n+1)\pi}{W}\right)}{Y/2} \tag{6.6}$$

where n in the range 0 to $N_M - 1$ denotes the modes 1,3,5,...$Y-2$ (odd symmetric). The time-reversal design procedure remains unchanged, with the exception that the reverse time-reversal-mirror update equation, is now, in modal form

$$\underline{\underline{V_{TRM}}}^{R}(n,k) = \underline{\underline{V_{TRM\,P}}}^{F}(n,k)' - \underline{\underline{V_{TRM\,H}}}^{F}(n,k). \tag{6.7}$$

The modal decomposition method is possible, providing the modal content of a device is known.

6.4 Case Studies

In this section, the case studies introduced and designed using time-reversal in Chapter five, are analysed for the temporal and spatial linear interpolation, and modal decomposition memory reduction methods. The TLM parameters are the same as those given in Chapter five.

6.4.1 2nd Order Septa Filter

The microwave band pass filter formed from the network of two metal septa in a WR90 waveguide of width $W = 22.86\,\text{mm}$, was designed using time-reversal in the previous chapter.

6.4.1.1 Temporal and Spatial Linear Interpolation

For each interpolation level, a time-reversal design simulation is performed, beginning with the initial septa widths, and optimising to the desired response. In Figure 6-3a a comparison of the figure of merit of the final solution, and the number of time-reversal iterations until convergence is shown, using temporal linear interpolation. The left vertical axis shows the number of time-reversal iterations until convergence is reached; the right shows the figure of merit of the final solution found. The extent of filtering is expressed as the percentage of the full data set recorded and is shown as the horizontal axis.

Comparison of Figure 6-3a to Figure 5-15 shows the optimal solution is found when $100\,\%$ of the time-reversal-mirrors are stored as expected. Interpolation to approximately $88\,\%$ is seen to be possible without changing the final solution, at the expense of requiring further time-reversal iterations. If less than $88\,\%$ of the time-reversal-mirrors are stored, the interpolation causes erratic suboptimal convergence.

In Figure 6-4a the septa widths with respect to the level of temporal interpolation are shown. As an example of a poor design, the widths of the septum when $33\,\%$ (1 in 3 samples) of the time-reversal-mirrors were stored are seen to be $W_{S1} = 1.48\,\text{mm}$ and $W_{S2} = 0.89\,\text{mm}$, compared to the optimal solution in TLM nodes of $W_{S1} = 7\Delta l = 2.08\,\text{mm}$ and $W_{S2} = 9\Delta l = 2.67\,\text{mm}$, these are largely inaccurate.

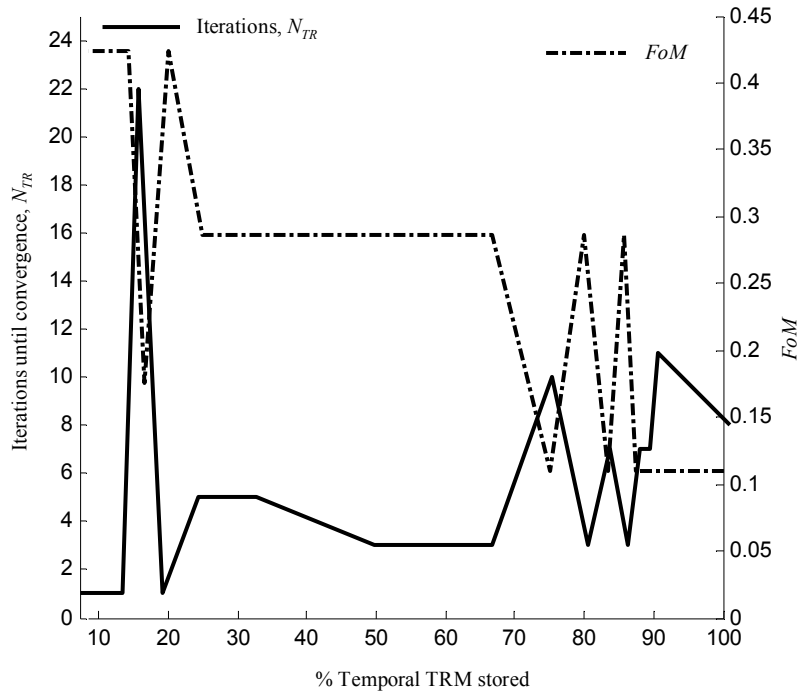

a)

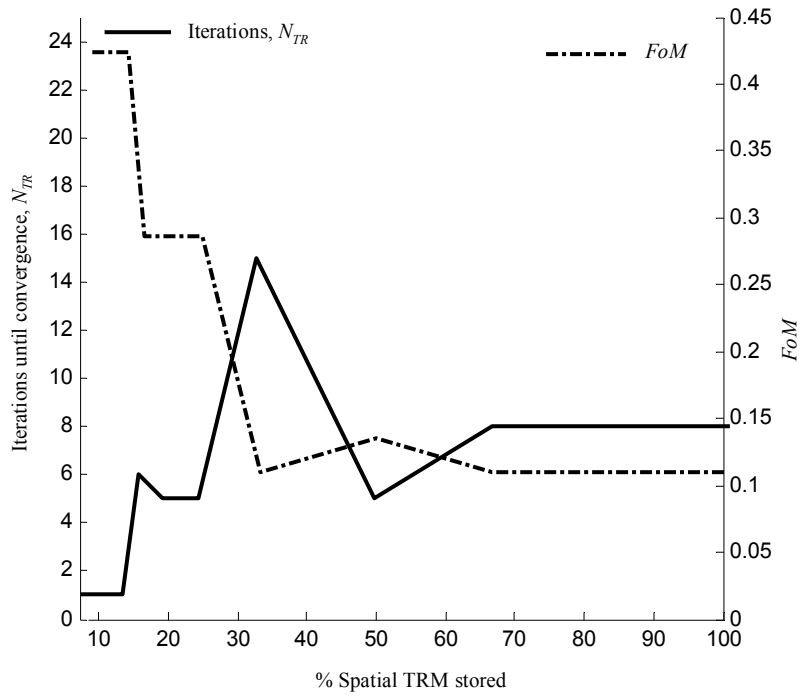

b)

Figure 6-3 - a) Temporal interpolation applied at time-reversal-mirrors for septa microwave band pass filter, b) spatial interpolation. TLM parameters are as in Chapter five.

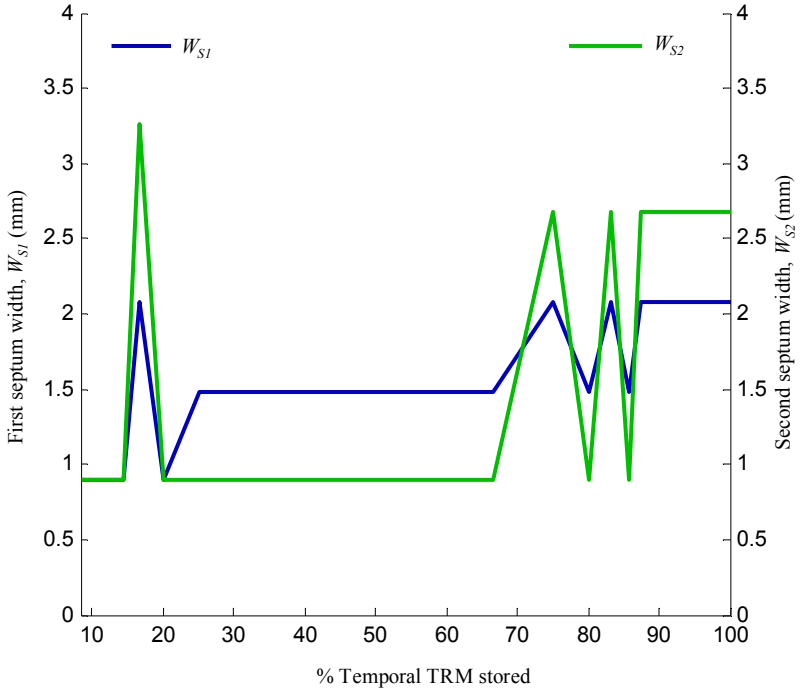

a)

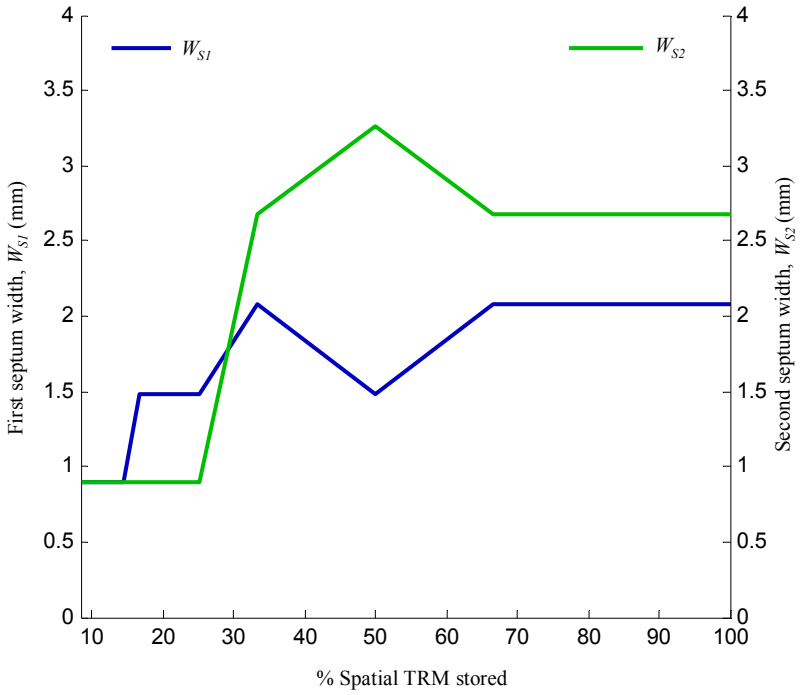

b)

Figure 6-4 - Septa widths for: a) temporal interpolation applied at time-reversal-mirrors for septa microwave band pass filter, b) spatial interpolation. TLM parameters are as in Chapter five.

In Figure 6-3b the interpolation of spatial data is shown, where the figure of merit has converged to an approximate minimum to 33% of the time-reversal-mirrors stored. In Figure 6-4b the septa widths are shown, where it is seen the second septum is affected the most by the spatial interpolation. The result of using less memory is an increase in time-reversal iterations, which increase to 15 at 33%. The multiple simulations take many days to complete, which was the reason for choosing a second order filter, practical filters require many septa and achieve return losses of around $40-50$ dB in the pass band, yet are computationally expensive to simulate.

For comparison with Chapter five, the time-reversal design convergence when 80% of the spatial time-reversal-mirrors are stored is shown in Figure 6-5.

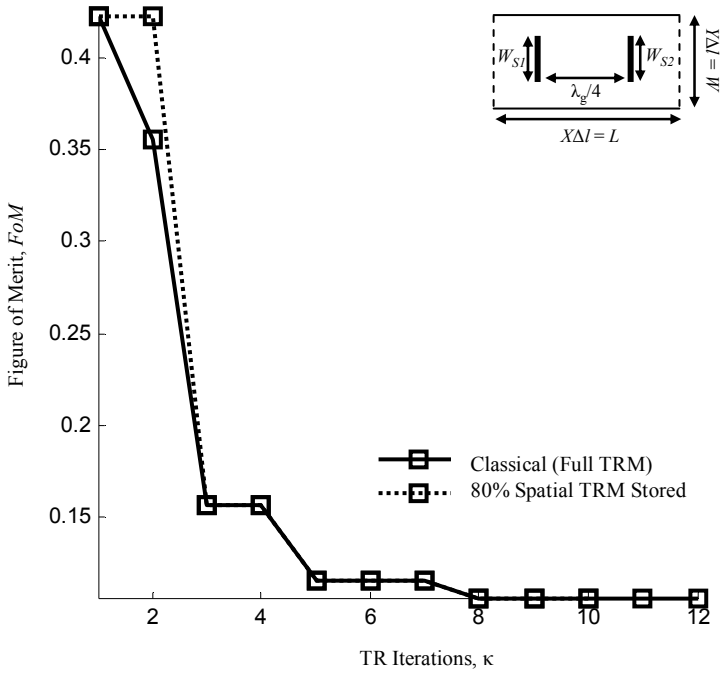

Figure 6-5 - Convergence of time-reversal design process of 2nd order band pass septa filter, storing 80% of spatial time-reversal-mirrors. TLM parameters are as in Chapter five.

From Figure 6-5 it is seen the interpolation has caused the time-reversal to take longer to converge in the initial first few design steps, after these, the interpolation achieves the same result as found when storing the full time-reversal-mirrors.

6.4.1.2 Modal Decomposition

The method of modal decomposition from Eqn.6.6, is expressed in the form for the input and output ports respectively of the filter as

$$\underline{M_4}(n,k) = \frac{\sum_{y=0}^{Y-1} \underline{\underline{{}_kV_4^r}}(0,y)\sin\left(\left(y\Delta l + \Delta l/2\right)\frac{(2n+1)\pi}{W}\right)}{Y/2} \tag{6.8a}$$

$$\underline{M_2}(n,k) = \frac{\sum_{y=0}^{Y-1} \underline{\underline{{}_kV_2^r}}(X-1,y)\sin\left(\left(y\Delta l + \Delta l/2\right)\frac{(2n+1)\pi}{W}\right)}{Y/2} \tag{6.8b}$$

where the matrix $\underline{M_{4,2}}$ is an N_M by N store of the modal amplitudes. The time-reversal design is repeated, for increasing modes stored. The numerical parameters are the same as before.

In Figure 6-6 the number of design iterations required for convergence and the FoM of the optimized solution for the band pass filter example is shown, ranging from $2.6\,\%$ (only the dominant lowest order mode is stored) to $100\,\%$ (all higher order evanescent modes stored).

It is seen the number of time-reversal iterations until convergence is reached changes with the number of stored modes, and stabilized when more than $80\,\%$ of the modes were stored. For this small test example, this is a sizeable memory saving of $1946\,\mathrm{KB}$.

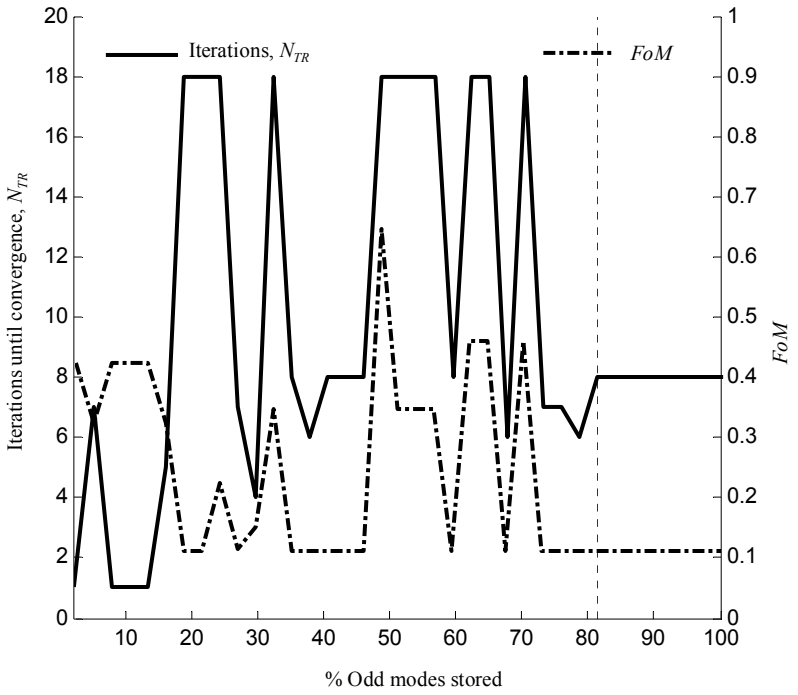

Figure 6-6 - Modal decomposition applied at time-reversal-mirrors for septa microwave band pass filter. Iterations until convergence and *FoM* of optimised solution with respect to percentage of odd modal amplitudes stored. TLM parameters are as in Chapter five.

6.4.2 2nd Order Iris Filter

The band pass filter created through the use of inductive irises was designed using time-reversal in Chapter five. In this section, the results for the three memory reduction methods applied to this example are demonstrated.

6.4.2.1 Temporal and Spatial Linear Interpolation

The temporal interpolation is applied identically to the septa filter. A separate time-reversal simulation is computed for each level of interpolation, and the results are given in Figure 6-7a. In Figure 6-8a the iris widths are shown. For this example it is seen the temporal interpolation is ineffective.

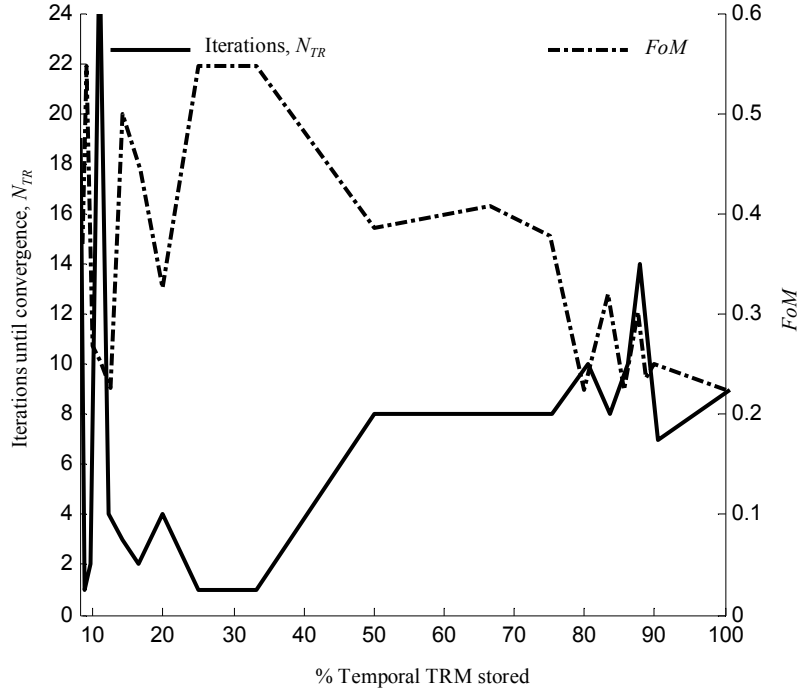

a)

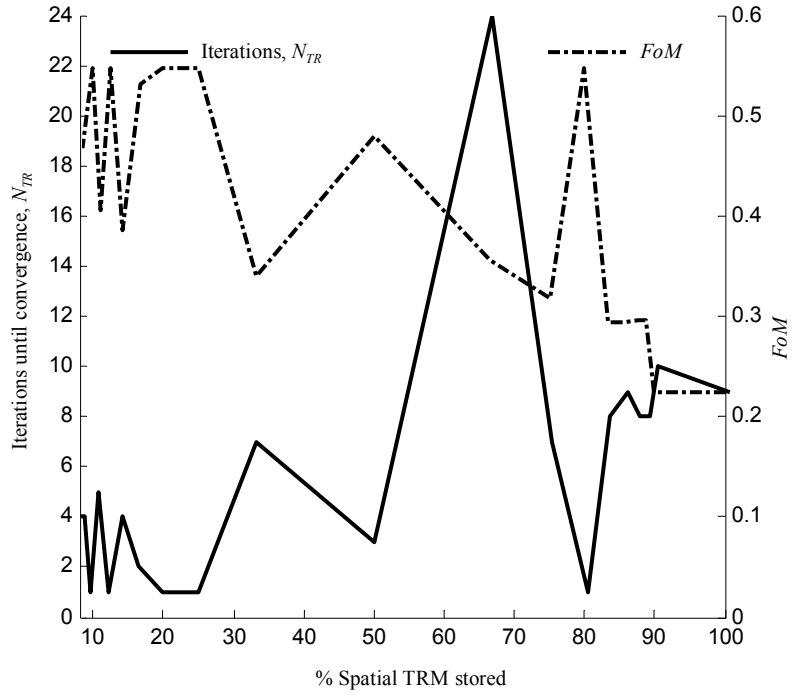

b)

Figure 6-7 - a) Temporal interpolation applied at time-reversal-mirrors in example of microwave iris band pass filter, b) spatial interpolation. TLM parameters are as in Chapter five.

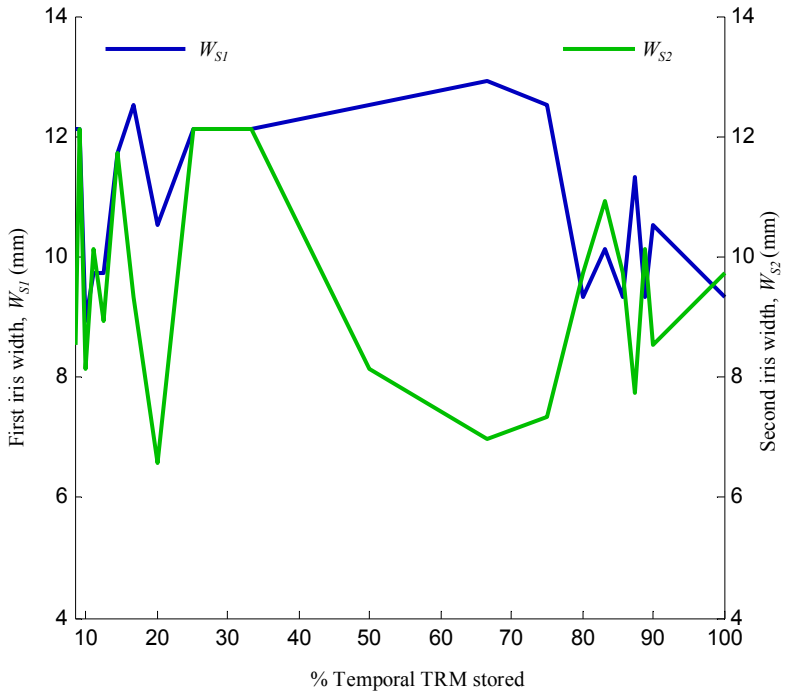

a)

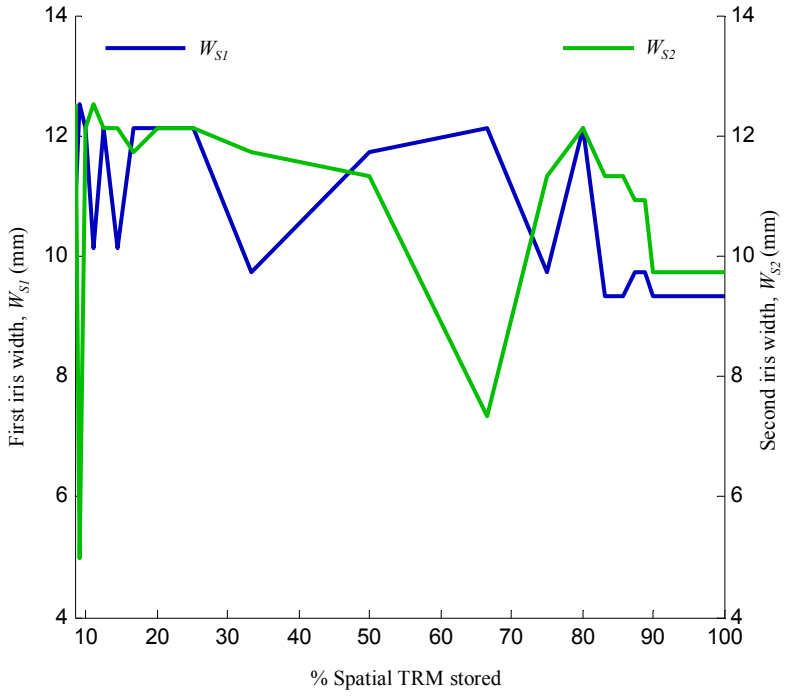

b)

Figure 6-8 - Iris widths for: a) temporal interpolation applied at time-reversal-mirrors in example of microwave iris band pass filter, b) spatial interpolation. TLM parameters are as in Chapter five.

In Figure 6-7b and Figure 6-8b the result of spatial interpolation of the iris filter is shown. Similarly to the septa filter, the spatial interpolation outperforms the temporal, and results in a memory reduction of approximately 10 %, further reductions result in suboptimal solutions.

6.4.2.2 Modal Decomposition

In this section the modal decomposition method is applied. Similarly, since the design uses the symmetric excitation of Eqn.6.1, only odd modes are stored. A separate time-reversal design is performed for increasing number of odd modes stored, and the results of Figure 6-9 are found. The optimum percentage of stored modes is approximately 85 %, a memory reduction of 2189 KB.

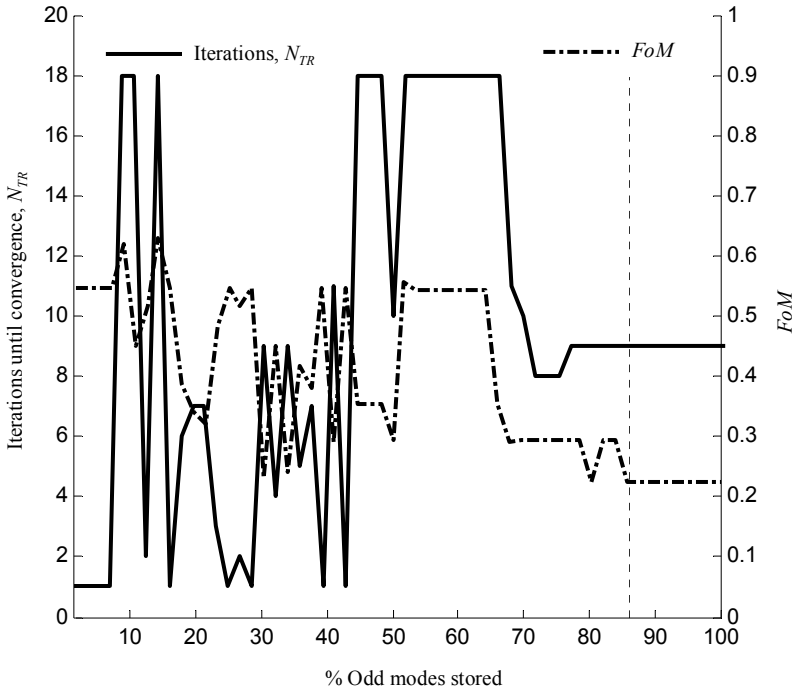

Figure 6-9 - Modal decomposition applied at time-reversal-mirrors in example of microwave iris band pass filter. Iterations until convergence and *FoM* of optimised solution with respect to percentage of odd modal amplitudes stored. TLM parameters are as in Chapter five.

It is seen in Figure 6-9, the convergence was erratic until approximately $50\,\%$ of the odd modes were stored, at which point the simulation becomes stable and then after approximately $65\,\%$, begins to converge, reaching the optimum solution when $85\,\%$ or more odd modes were stored.

To investigate this effect further, the optimised S parameters when time-reversal design is performed with 40 and 56 ($N_M - 1$) odd modes stored, is shown in Figure 6-10a,b respectively. These correspond to $70\,\%$ and $100\,\%$ of the odd modes. When 40 modes were stored the optimised iris widths in TLM nodes were $W_{S1} = 9.34\,\text{mm}$, and $W_{S2} = 11.73\,\text{mm}$, in comparison, the optimal widths are $W_{S1} = 9.34\,\text{mm}$ and $W_{S2} = 9.74\,\text{mm}$, which shows the reduced modes stored has impacted the convergence of the second iris, resulting in the suboptimal S parameters of Figure 6-10a.

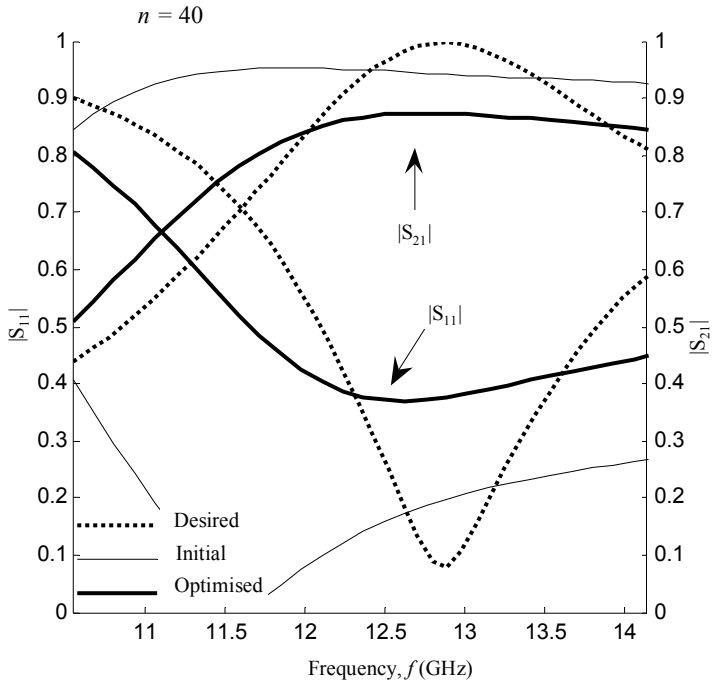

a)

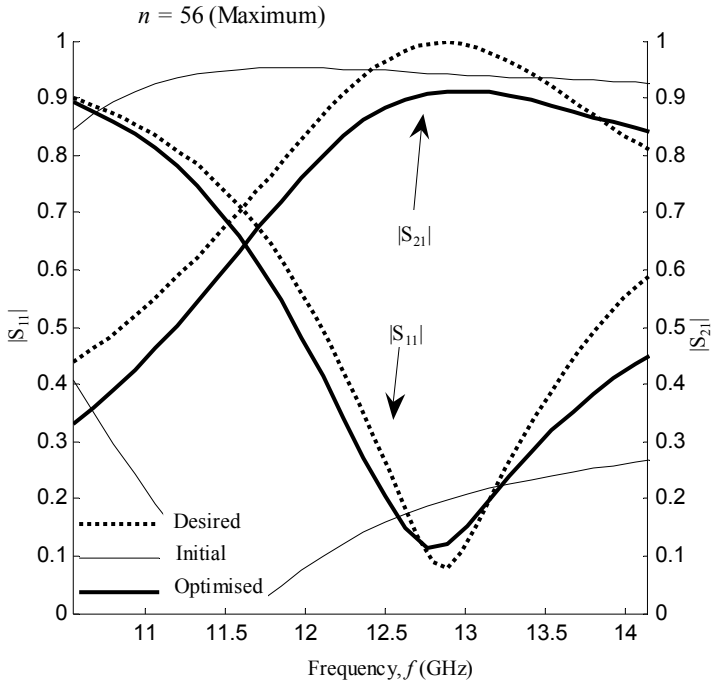

b)

Figure 6-10 - Initial, optimised and desired S parameters for iris filter when a) 40 modes were stored and b) 56, TLM parameters are as in Chapter five.

6.4.3 90° Waveguide Bend

The waveguide bend example of the optimisation of the tuning post is now investigated with the application of the memory reduction methods.

6.4.3.1 Temporal and Spatial Linear Interpolation

The temporal interpolation applied for the time-reversal design of the bend results in Figure 6-11a and Figure 6-12a for the return loss and post displacement respectively. It is seen, as more temporal samples are interpolated (as the percentage reduces), the return loss of the design increases. A direct correlation between increased iterations and optimised solution is seen. In general, the iterations increase as more of the time-reversal-mirror is stored, and a better design is found. As discussed earlier, complex bends using multiple posts can achieve return losses of around $30-35\,\mathrm{dB}$. With this in mind, the single tuning post model for interpolation of $90-95\,\%$ is acceptable since only a single post has been used.

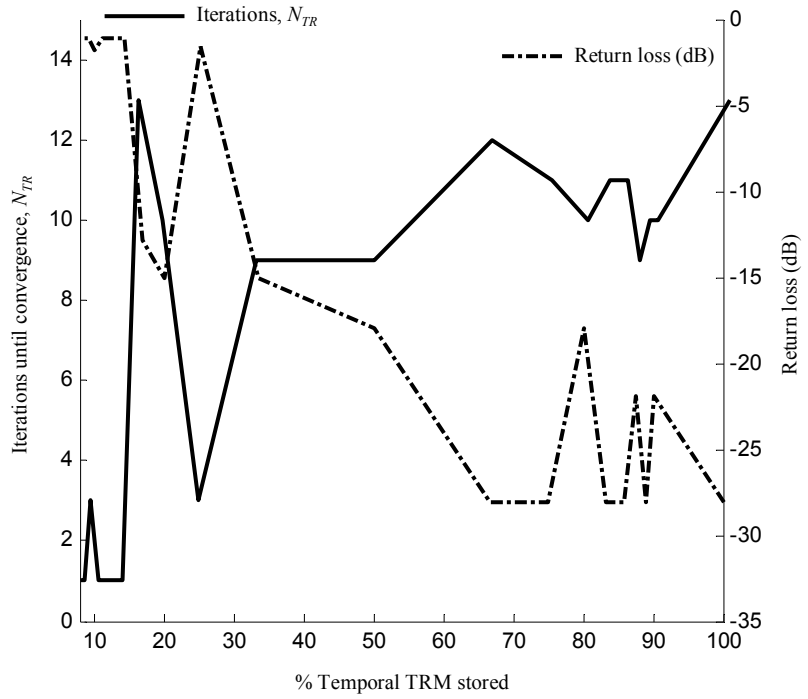

a)

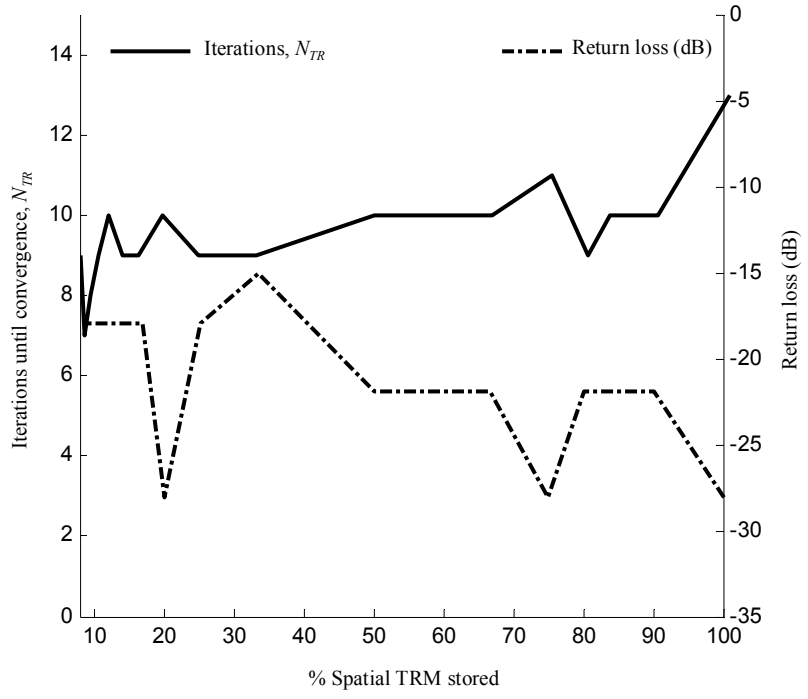

b)

Figure 6-11 - a) Temporal interpolation applied at time-reversal-mirrors in example of 90º waveguide bend, b) spatial interpolation. TLM parameters are as in Chapter five.

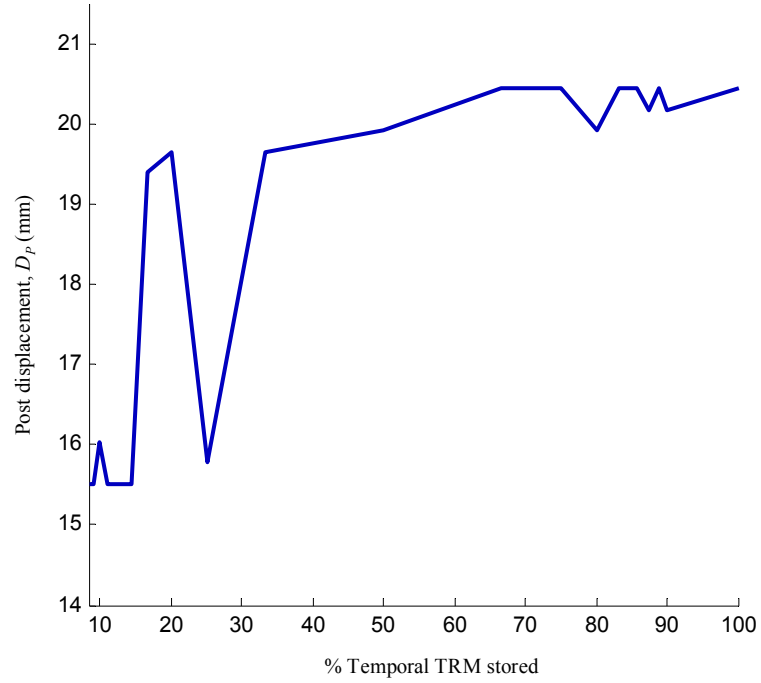

a)

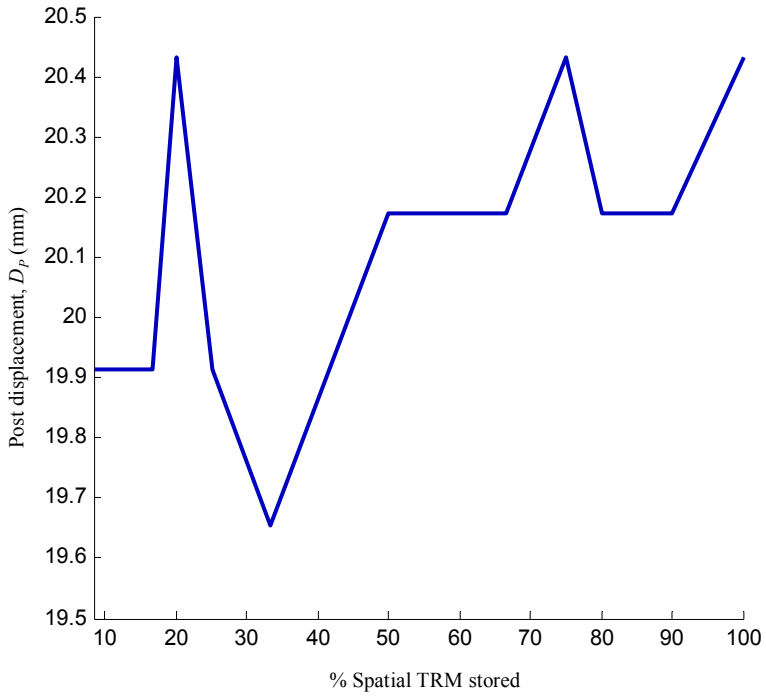

b)

Figure 6-12 - Post displacement for: a) temporal interpolation applied at time-reversal-mirrors in example of 90º waveguide bend, b) spatial interpolation. TLM parameters are as in Chapter five.

In Figure 6-11b the application of the spatial interpolation to the bend design is shown. In this case it is seen the return loss varies between approximately -15 to -28 dB, and only when around 75% or 100% of the time-reversal-mirrors are stored, is the optimum design found. In Figure 6-12b the post displacement with respect to the level of spatial interpolation is shown, where it is seen again, small changes in the displacement have a large impact on the return loss.

6.4.3.2 Modal Decomposition

In this section, the application of the modal decomposition to the bend is demonstrated. The modal decomposition for the filter models, shown in Eqn.6.8 now reads

$$\underline{M_4}(n,k) = \frac{\sum_{y=0}^{Y-1} \underline{\underline{{}_kV_4^r}}(0,y)\sin\left(\left(y\Delta l + \Delta l/2\right)\frac{(2n+1)\pi}{W}\right)}{Y/2} \tag{6.9a}$$

$$\underline{M_1}(n,k) = \frac{\sum_{x=0}^{Y-1} \underline{\underline{{}_kV_1^r}}((X-Y)+x, y=X-1)\sin\left(\left(x\Delta l + \Delta l/2\right)\frac{(2n+1)\pi}{W}\right)}{Y/2} \tag{6.9b}$$

where $(X-Y)$ is the spatial offset in x for the time-reversal-mirror at the output port.

The results of the modal decomposition, applied at the time-reversal-mirrors, using Eqns.6.9 for increasing percentage of odd modes stored, is shown in Figure 6-13. As before, a separate time-reversal design simulation is performed for each level of modal amplitudes stored. In Figure 6-13 it is seen, the convergence remains steady when approximately 70% of the odd modes were stored, a memory reduction of 4762 KB.

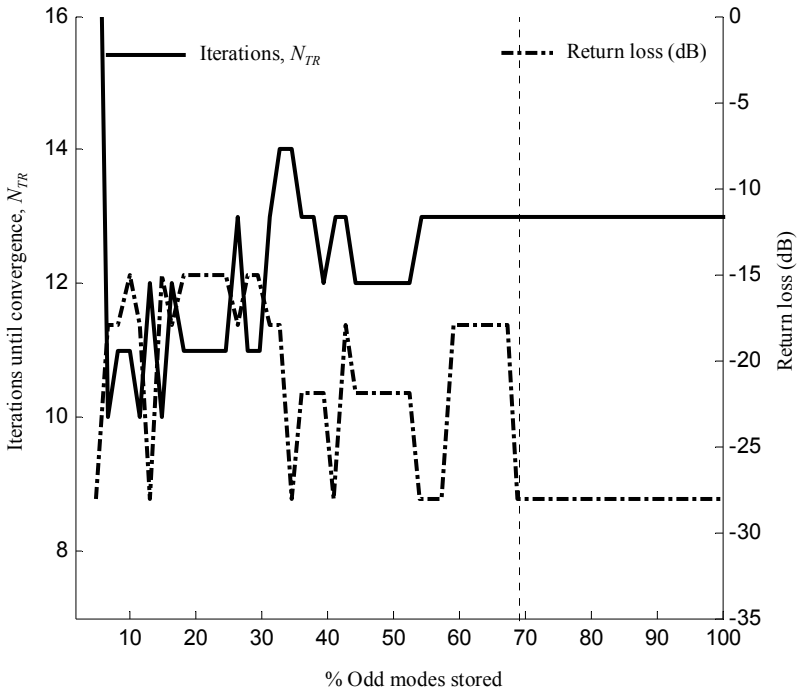

Figure 6-13 - Modal decomposition applied at time-reversal-mirrors in example of 90º waveguide bend. Iterations until convergence and return loss of optimised solution with respect to percentage of odd modal amplitudes stored. TLM parameters are as in Chapter five.

6.4.4 Directional Coupler

The directional coupler example requires four time-reversal-mirrors. This doubles the memory required in comparison to the previous devices shown. Due to the need to repeat the simulation at varying levels of interpolation, the coarser model, with $\Delta l = 0.199$ mm from Chapter five is used.

6.4.4.1 Temporal and Spatial Linear Interpolation

The time-reversal-mirrors of the coupler are treated individually for application of the interpolation. For temporal interpolation, the coupling is as shown in Figure 6-14a, while Figure 6-14b shows the directivity. The coupling is seen to be largely unaffected by interpolation above 20 %; however the directivity, which defines the isolation of port D, only remains optimal when 90 % or more of the time-reversal-mirrors are stored.

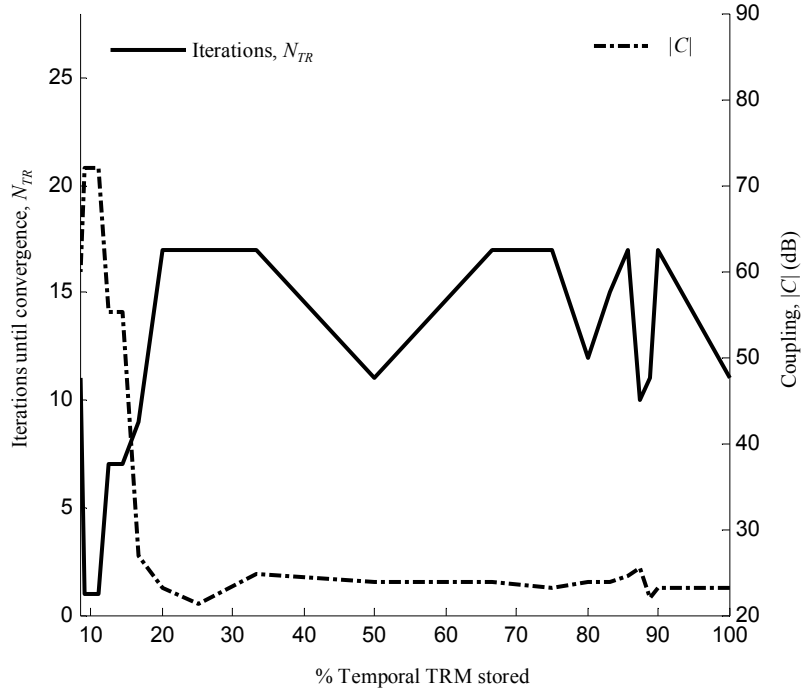

a)

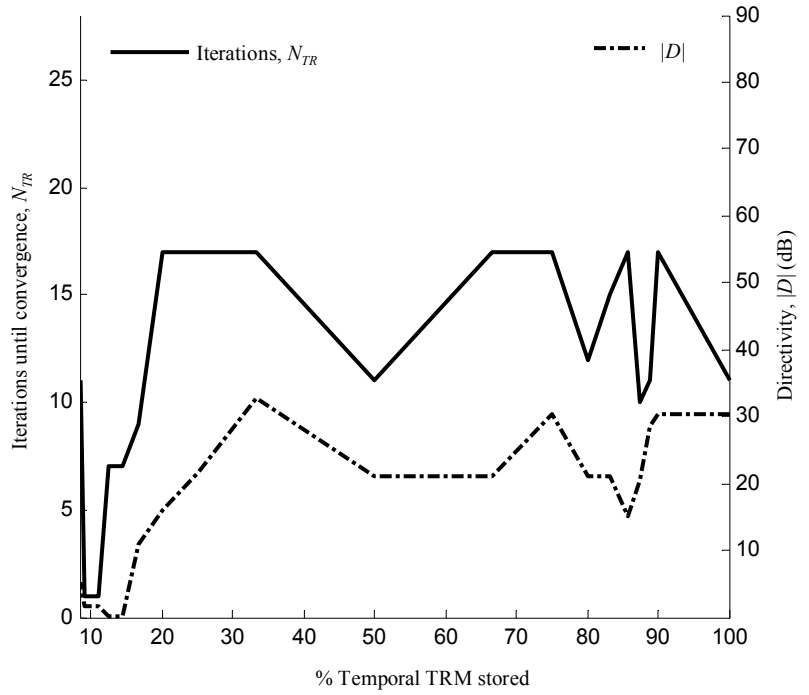

b)

Figure 6-14 - Temporal interpolation applied at time-reversal-mirrors in example of directional coupler, a) coupling, b) directivity. TLM parameters are as in the coarser model of Chapter five.

In Figure 6-15a the hole widths of the coupler with respect to the temporal interpolation is shown. It is seen the hole widths reach the optimal solution of $W_{H1} = W_{H2} = 29\Delta l = 5.76\,\text{mm}$ when $90\,\%$ or more of the time-reversal-mirrors are stored.

Similarly, spatial interpolation applied at the time-reversal-mirrors of ports A through D, is shown for the hole widths in Figure 6-15b and the coupling and directivity in Figure 6-16a,b, respectively. Again, the coupling appears largely unaffected by the use of interpolation; however the directivity is hindered considerably.

A directivity of $20\,\text{dB}$ at $90\,\%$ interpolation, shows more power is lost to the isolated port, than is coupled. A practical coupler would need a directivity of at least $30\,\text{dB}$, and hence the spatial interpolation is ineffective for this example.

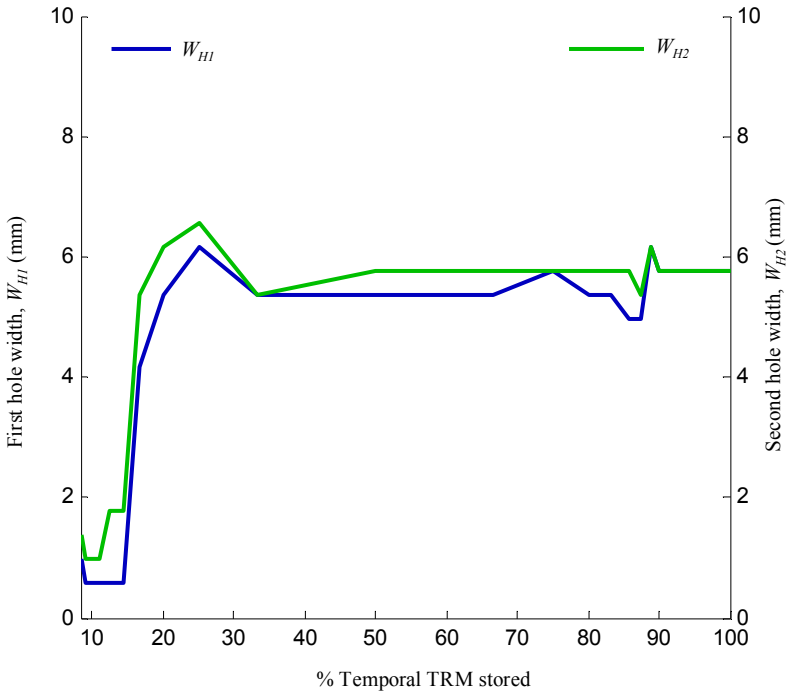

a)

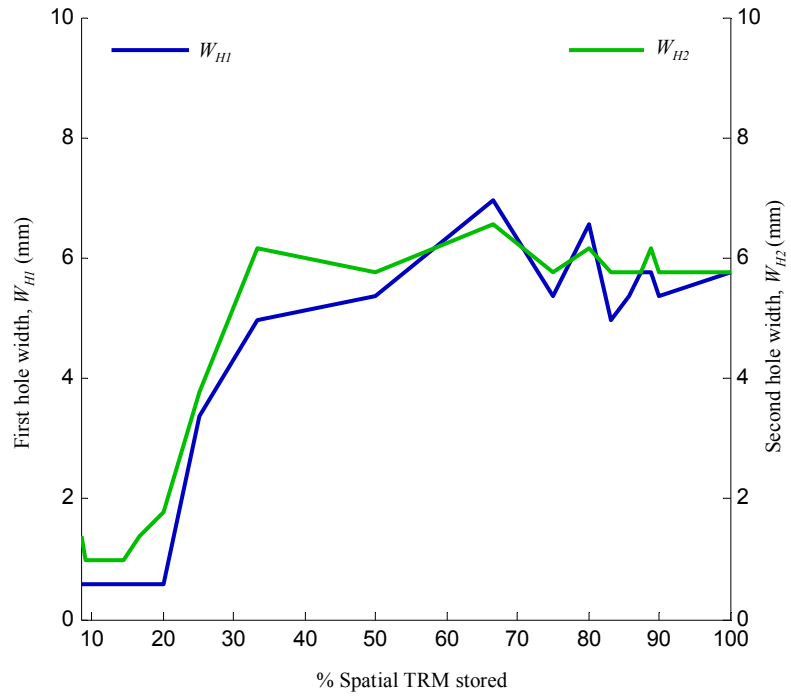

b)

Figure 6-15 - Hole widths for: a) temporal interpolation applied at time-reversal-mirrors in example of directional coupler, b) spatial interpolation. TLM parameters are as in the coarser model of Chapter five.

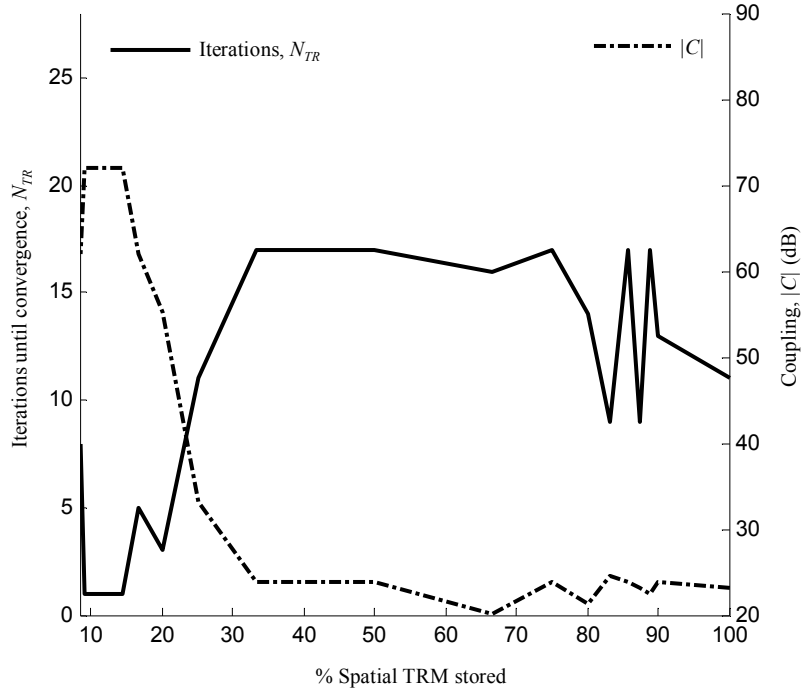

a)

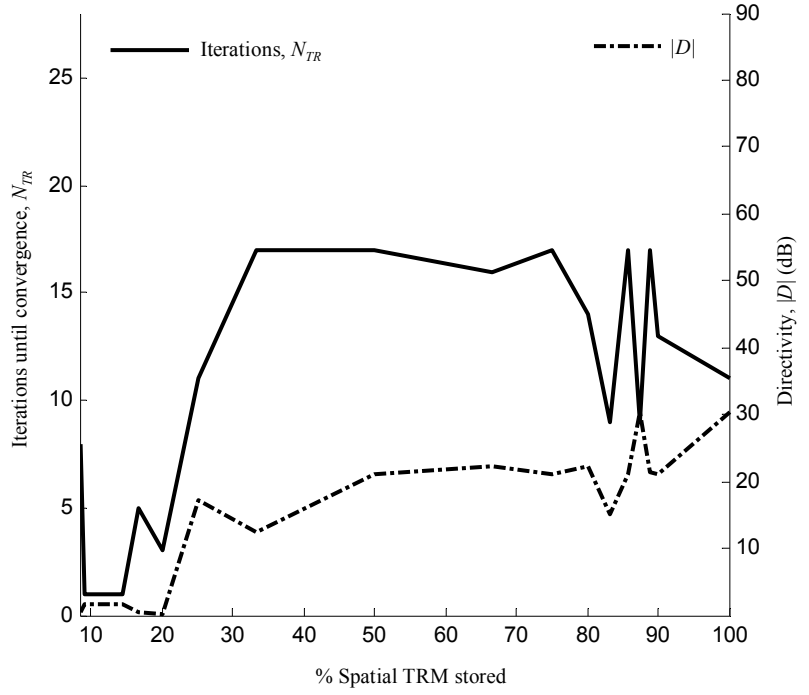

b)

Figure 6-16 - Spatial interpolation applied at time-reversal-mirrors in example of directional coupler, a) coupling, b) directivity. TLM parameters are as in the coarser model of Chapter five.

6.4.4.2 Modal Decomposition

The modal decomposition of Eqns.6.8 now read

$$\underline{M_A}(n,k) = \frac{\sum_{y=0}^{Y-1} \underline{\underline{{}_kV_4^r}}(0,y)\sin\left(\left(y\Delta l + \Delta l/2\right)\frac{(2n+1)\pi}{W}\right)}{Y/2}, \tag{6.10a}$$

$$\underline{M_B}(n,k) = \frac{\sum_{y=0}^{Y-1} \underline{\underline{{}_kV_2^r}}(X-1,y)\sin\left(\left(y\Delta l + \Delta l/2\right)\frac{(2n+1)\pi}{W}\right)}{Y/2}, \tag{6.10b}$$

$$\underline{M_C}(n,k) = \frac{\sum_{y=0}^{Y-1} \underline{\underline{{}_kV_2^r}}(X-1,Y+y)\sin\left(\left(y\Delta l + \Delta l/2\right)\frac{(2n+1)\pi}{W}\right)}{Y/2}, \tag{6.10c}$$

$$\underline{M_D}(n,k) = \frac{\sum_{y=0}^{Y-1} \underline{\underline{{}_kV_4^r}}(0,Y+y)\sin\left(\left(y\Delta l + \Delta l/2\right)\frac{(2n+1)\pi}{W}\right)}{Y/2}. \tag{6.10d}$$

Using Eqns.6.10, the modal decomposition method is applied upon the four ports of the coupler, and results in Figure 6-17. The time-reversal design iterations until convergence and the coupling with respect to the percentage of odd modes stored is shown in Figure 6-17a. In comparison, the directivity is given in Figure 6-17b. It is seen that providing approximately $60\,\%$ or more of the odd modes are stored, the time-reversal iterations to convergence are $N_{TR} = 11$ or $N_{TR} = 12$ and the optimal solution is found. It is likely the fluctuation of the iterations can be removed by increasing the spatial sampling of the model, as was seen in Chapter five, yet this would greatly increase the computational demand of the repeated simulations.

This problem requires approximately $29184\,\mathrm{KB}$ to store the four time-reversal-mirrors using standard modal time-reversal. Hence, a $40\,\%$ reduction ($11674\,\mathrm{KB}$) is a considerable memory saving.

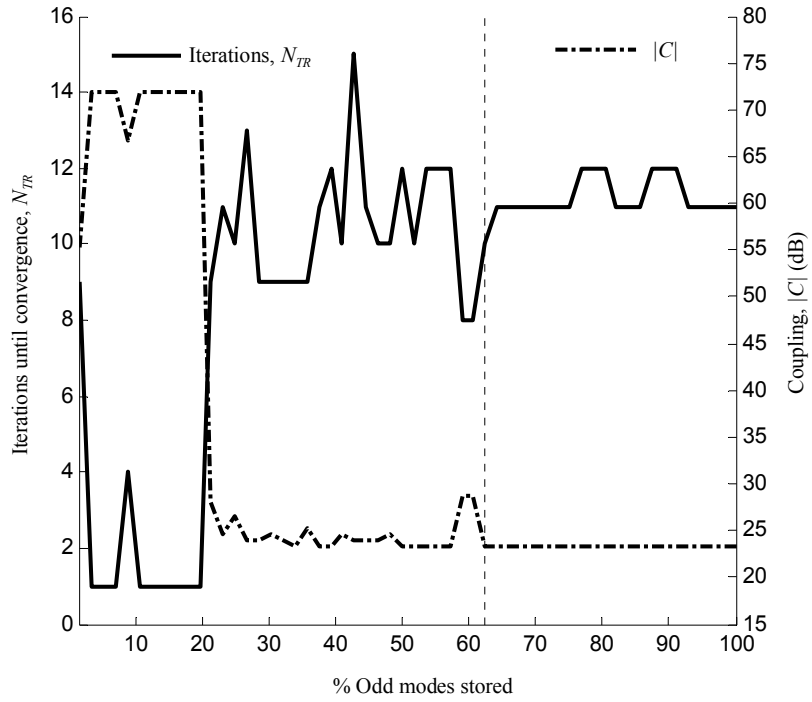

a)

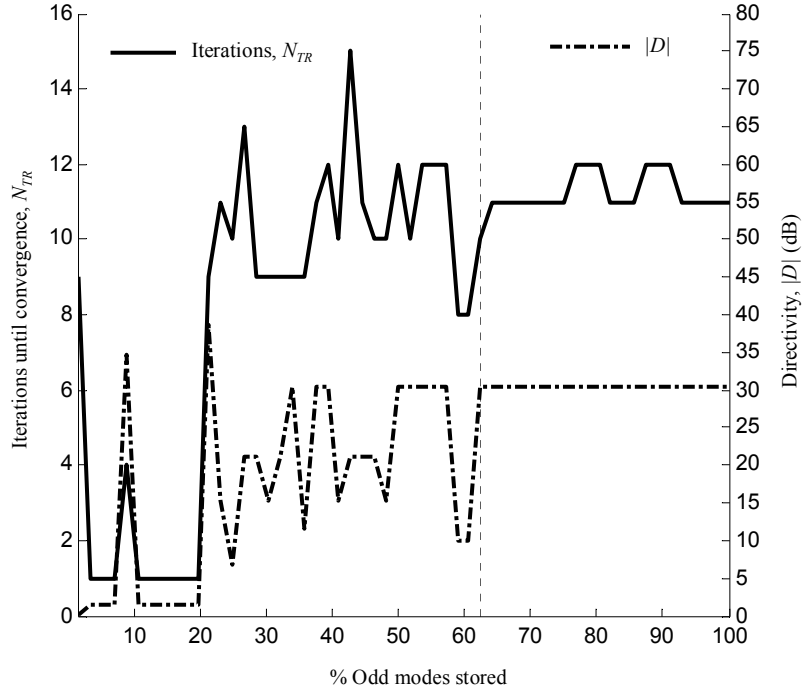

b)

Figure 6-17 - Modal decomposition applied at time-reversal-mirrors of directional coupler. a) Iterations until convergence, and coupling of optimised solution with respect to percentage of odd modal amplitudes stored, b) directivity. TLM parameters are as in the coarser model of Chapter five.

6.5 Conclusion

Time-reversal as a technique for microwave component design has notable computational requirements. In this chapter a number of approaches have been introduced to ameliorate this problem without compromising the performance of the iterative optimisation process.

The two microwave band pass filters, waveguide bend, and directional coupler examples designed using the standard time-reversal procedure of the previous chapter, were redesigned with the application of the memory reduction methods.

Linear interpolation, both in the spatial and temporal domains has been used to reduce the memory required. The performance with the majority of design models is acceptable above 90% of the stored time-reversal-mirrors; however the degree to which they are applied is largely problem specific, erratic, and typically results in degradation of the final design. A direct correlation between optimised solution and design iterations is seen, where in general, fewer design steps results in a poor solution.

The modal decomposition method converged to the optimum solution in all test designs, with at least a reduction of 15% of the odd modes stored, although it is seen for the bend and coupler models $30-37\%$ reductions were possible.

6.6 References

[6.1] R. E. Collin, *Foundations for Microwave Engineering*. John Wiley & Sons Inc, New York, NY, 2nd ed., 2001.

7. Convergence Acceleration

The most obvious disadvantage of the time-reversal design method is the need for multiple time domain simulations which are inherently computationally intensive and therefore it is critically important to maximize the convergence rate of the iterations. In this chapter the physically based time-reversal iterations are accelerated using both stationary and non-stationary linear acceleration methods. Krylov subspace methods which provide a valuable improvement in computational efficiency are considered, and the design examples of the filters, waveguide bend and coupler are demonstrated using the acceleration methods.

A number of symbols used previously in the thesis, are used here in the context of the derivation of the acceleration methods and do not represent the same quantities.

7.1 Time-Reversal and Iterative Acceleration

The need for solutions of large systems of linear equations has become common place in modern engineering applications. Before the popularity of iterative methods, direct solvers were common place. These were typically designed for a single structure, and although fast, had limited application. The use of numerical iterative solvers became more popular with the ease of access to computing resources, and have been gaining popularity in many areas of scientific computing [7.1].

The idea examined here stems from the fact that each time-reversal optimisation iteration is analogous to a steepest descent minimization step: only the most recent state of the design is explicitly used to determine the next search direction. Therefore, it is proposed that acceleration methods classically employed to significantly improve the convergence rates of algebraic minimisation problems will provide the same advantages if adapted to time-reversal optimisation.

A typical application of an iterative linear solver will act upon the equation

$$\underline{\underline{A}}\,\underline{x} = \underline{b} \tag{7.1}$$

where $\underline{\underline{A}}$ is a $N \times N$ matrix, $\underline{b}$ is a $N \times 1$ vector of desired values and $\underline{x}$ is the $N \times 1$ vector to be found.

In Figure 7-1 a block illustration of the iterative time-reversal design process using acceleration is shown. The simulation begins with the input of the constant primary excitation, a forward simulation is performed, and the S parameters measured, the solution is subtracted from the desired solution, to give the difference vector, $\hat{G}$. The subscript κ denotes the time-reversal iteration. The reverse simulation proceeds and the scatterer dimensions are measured as before. The distinction of the accelerated time-reversal is in how the excitation for the reverse simulation is updated. The matrix operator $\underline{\underline{A}}$ is introduced, and can be thought of as the process of (a) performing the reverse time simulation, (b) the extraction of the scatterer geometry, (c) performing a forward simulation with this geometry excited by the primary source and (d) measurement of the scattering parameters.

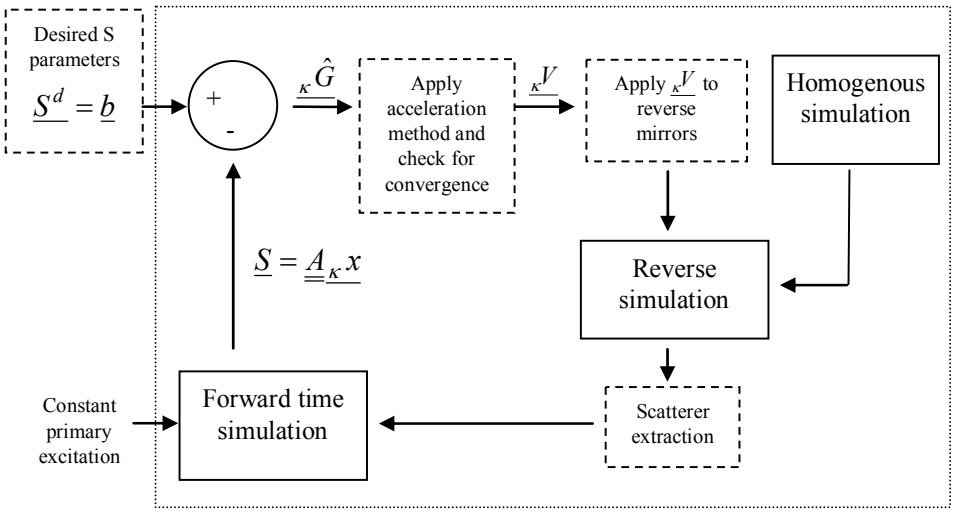

Figure 7-1 - Schematic illustration of time-reversal design process using linear acceleration.

It is clear that $\underline{\underline{A}}$ is actually non-linear, however it is proposed that it can be treated as sufficiently linear with respect to the small perturbations to $\underline{x}$ to permit application of the established acceleration methods.

The perturbation applied to the time-reversal-mirror when S parameters are optimised, can be expressed as a difference vector in the form $\underline{\hat{G}}$. In terms of iterative solver mathematics, the vector at the input (TLM port 4) and the output (TLM port 2)

$$\underline{\hat{G}_4} = \begin{cases} \underline{S_{11}^d} - \underline{S_{11}}, & \text{if within bandwidth,} \\ 0, & \text{otherwise,} \end{cases} \tag{7.2a}$$

$$\underline{\hat{G}_2} = \begin{cases} \underline{S_{21}^d} - \underline{S_{21}}, & \text{if within bandwidth,} \\ 0, & \text{otherwise,} \end{cases} \tag{7.2b}$$

is usually referred to as the residual, and is a measure of error. The residual of Eqn.7.1 is expressed as

$$\underline{r} = \underline{b} - \underline{\underline{A}}\underline{x}. \tag{7.3}$$

The S parameters are calculated from the Fourier transform of the temporal voltages incident and reflected upon the time-reversal-mirrors at the input and the output, as defined in Chapter five

$$\underline{\underline{S_{(1,2)1}}}(f) = \frac{\underline{\hat{V}_{4,2}^{r}}(f)}{\underline{\hat{V}_{4}^{i}}(f)}. \tag{7.4}$$

With this in mind it is straightforward to represent the time-reversal process in the matrix form as

$$\underline{\hat{G}} = \underline{b} - \underline{\underline{A}}\underline{x}, \tag{7.5}$$

where $\underline{b}$ is a $N \times 1$ vector representing the desired S parameters, x is a $N \times 1$ vector of reflected voltages on the time-reversal-mirrors and $\underline{\underline{A}}$ is the diagonal $N \times N$ matrix representing $1/\underline{\hat{V}_4^i}$, the incident voltages at the input.

The matrix $\underline{\underline{A}}$ is easily invertible. However, inversion of $\underline{\underline{A}}$ directly to find $\underline{x}$ is not useful for time-reversal, since $\underline{x}$ may not necessarily correspond to a physical component structure when found in this manner. Instead $\underline{x}$ is optimised iteratively, constraining to a given device.

It is widely known that the solution of large systems of linear equations can be accelerated using either stationary point methods, such as successive over relaxation (SOR) [7.1], or non-stationary or Krylov subspace methods [7.2] such as conjugate gradients (CG) and generalized minimal residual (GMRES).

7.2 Successive Over Relaxation

The method of SOR is among the most commonly used stationary point methods, and is assumed to originate from the early work of Southwell [7.3]. In general, iterative methods that can be expressed in the form

$$\underline{x}_{\kappa+1} = \underline{\underline{M}}\,\underline{x}_{\kappa} + \underline{c} \tag{7.6}$$

where $\underline{\underline{M}}$ and $\underline{c}$ are independent of the time-reversal iteration κ, and are broadly classed as stationary point, since they optimise the vector $\underline{x}$ using the same parameters at each time-reversal iteration, κ. SOR accelerates convergence by introducing the stationary point ω. The update equation for the SOR method is [7.1]

$$\underline{x}_{\kappa+1} = \underline{\underline{M}}_{\omega}\,\underline{x}_{\kappa} + \underline{c}_{\omega} \tag{7.7}$$

where ω in this context is used to denote the SOR point variable in the range $0 < \omega < 2$. $\underline{\underline{M}}_{\omega}$ and $\underline{c}_{\omega}$ are defined as

$$\underline{\underline{M}}_{\omega} = (\underline{\underline{D}} - \omega\underline{\underline{L}})^{-1}\left((1-\omega)\underline{\underline{D}} + \omega\underline{\underline{U}}\right) \tag{7.8}$$

$$\underline{c}_{\omega} = \omega(\underline{\underline{D}} - \omega\underline{\underline{L}})^{-1}\underline{b} \tag{7.9}$$

where $\underline{\underline{D}}$, $\underline{\underline{U}}$, $\underline{\underline{L}}$ are the diagonal, upper triangular and lower triangular matrices of $\underline{\underline{A}}$ respectively.

In the context of time-reversal, it can be seen from Eqns.7.8-7.9 that $\underline{\underline{M}}_{\omega}$ and $\underline{c}_{\omega}$ are independent of the time-reversal iteration κ as desired. Since $\underline{\underline{A}}$ is a diagonal matrix $\underline{\underline{U}} = \underline{\underline{L}} = \underline{\underline{0}}$, this simplifies Eqns.7.8-7.9

$$\underline{\underline{M_\omega}} = \underline{\underline{D}}^{-1}\left((1-\omega)\underline{\underline{D}}\right) = (1-\omega), \tag{7.10}$$

$$\underline{c_\omega} = \omega \underline{\underline{D}}^{-1}\underline{b}. \tag{7.11}$$

Substitution of Eqns.7.10-7.11 into Eqn.7.7 gives

$$\underline{{}_{\kappa+1}x} = (1-\omega)\underline{{}_{\kappa}x} + \omega\underline{\underline{D}}^{-1}\underline{b}. \tag{7.12}$$

Substitution of Eqn.7.12 into Eqn.7.2 with the use of Eqn.7.4 gives

$$\underline{{}_{\kappa}\hat{G}_{SOR}}(f) = \begin{cases} \underline{S^d}(f) - \dfrac{\underline{\underline{{}_{\kappa+1}x}}(f)}{\underline{\hat{V}_4^i}(f)}, & \text{if within bandwidth,} \\ 0, & \text{otherwise.} \end{cases} \tag{7.13}$$

Eqn.7.13 is expanded and simplified to give

$$\begin{aligned} \underline{{}_{\kappa}\hat{G}_{SOR}}(f) &= \begin{cases} \underline{S^d}(f) - \dfrac{(1-\omega)\underline{{}_{\kappa}x}(f) + \omega\underline{\underline{D}}^{-1}(f,f)\underline{b}(f)}{\underline{\hat{V}_4^i}(f)}, \\ 0, \end{cases} \\ \underline{{}_{\kappa}\hat{G}_{SOR}} &= \begin{cases} \underline{S^d} - \left((1-\omega)\underline{S} + \omega\underline{S^d}\right), \\ 0, \end{cases} \\ &= \begin{cases} (1-\omega)\left(\underline{S^d} - \underline{S}\right), & \text{if within bandwidth,} \\ 0, & \text{otherwise.} \end{cases} \end{aligned} \tag{7.14}$$

Eqn.7.14 is the final form of the SOR as applied to microwave time-reversal, and it can be seen that the method results in the use of one extra variable, ω, applied to the difference vector, $\underline{\hat{G}}$ during the perturbation phase of the time-reversal process. The resulting time-reversal-mirror perturbation at time-reversal iteration κ is

$$\underline{\underline{V_{TRM\,P}}}^{F}(y,k)' = (\alpha)\underline{\underline{V_{TRM\,P}}}^{F}(y,k) + (1-\alpha)\left(\underline{\underline{V_{TRM\,P}}}^{F}(y,k) - \underline{\phi}(y) \otimes |\, {}_{\kappa}\underline{G_{SOR}}(k)\,|\right) \tag{7.15}$$

where $\underline{G_{SOR}}$ is the inverse Fourier transform of $\hat{G}_{SOR}$ from Eqn.7.14.

The choice for ω is selected within the range $0 < \omega < 2$ [7.1], however due to the application of SOR in Eqn.7.15, $\omega > 1$ is redundant. In general terms, the optimum choice for ω is problem specific. The application of ω will also result in a different field plot formed from the maximum of the Poynting vector during reversal, and hence the optimum damping and threshold values for a simulation will not necessarily match those used for the classical time-reversal. In the examples of this thesis, the SOR variable, ω, was varied incrementally at each choice of time-reversal damping, α, similarly to how the optimum thresholds are determined.

7.3 Conjugate Gradients

Stationary point methods can progress towards the optimum solution in directions already explored by previous iterations and this behaviour creates redundancy in the technique [7.4].

An alternative to the SOR approach is to ensure that the residual vectors ${}_{\kappa}\underline{r}$ from successive iterations are orthogonal to one another. This is non-stationary acceleration and is the basis of Krylov subspace linear solvers such as the conjugate gradient (CG) method [7.2] [7.5]. Using the orthogonal residual vectors to construct search directions, ensures the iterative procedure does not take a step in the same direction as a previous iteration. The CG method is used to orthogonalise the vector ${}_{\kappa}\underline{x}$ for the reverse time simulation.

Krylov subspace methods in general, of which CG is an example, project the solution, $\underline{x}$, onto the set of vectors $\{\underline{b}, \underline{\underline{A}}\underline{b}, \underline{\underline{A}}^2\underline{b}, ...\}$, where $\underline{b}$ is the solution being sought, and $\underline{\underline{A}}$ is the matrix operation, in a manner so as to minimize $\underline{b} - \underline{\underline{A}}\underline{x}$.

A vector, ${}_{\kappa}\underline{d}$ termed the search direction, is taken from the subspace [7.5]

$$\underline{\underline{D}} = \left\{ {}_0\underline{r}, \underline{\underline{A}}\,{}_0\underline{r}, \underline{\underline{A}}^2\,{}_0\underline{r}, \underline{\underline{A}}^3\,{}_0\underline{r} ... \right\}. \tag{7.16}$$

The subspace shown in Eqn.7.16 is known as a Krylov subspace, and is formed from the repeated application of the matrix $\underline{\underline{A}}$ to the residual. This is the foundation of the CG Krylov subspace method. Eqn.7.16 requires only the previous search vector to determine the new search direction, and hence storage of the full subspace $\underline{\underline{D}}$ is not required.

The full derivation of CG is voluminous, and not necessary for this work, details can be found in [7.1], [7.5] and [7.6]. The CG algorithm summarises as

$${}_{\kappa+1}\underline{x} = {}_{\kappa}\underline{x} + {}_{\kappa}\alpha\,{}_{\kappa}\underline{d}\,, \tag{7.17a}$$

$$\begin{aligned} {}_{\kappa+1}\underline{r} &= {}_{\kappa}\underline{r} - {}_{\kappa}\alpha\,\underline{\underline{A}}\,{}_{\kappa}\underline{d} \\ &= \underline{b} - \underline{\underline{A}}\,{}_{\kappa}\underline{x}, \end{aligned} \tag{7.17b}$$

$${}_{\kappa+1}\underline{d} = {}_{\kappa+1}\underline{r} - {}_{\kappa+1}\beta(\kappa)\,{}_{\kappa}\underline{d}\,, \tag{7.17c}$$

where

$${}_{\kappa}\alpha = \frac{{}_{\kappa}\underline{r}^T\,{}_{\kappa}\underline{r}}{{}_{\kappa}\underline{d}^T\,\underline{\underline{A}}\,{}_{\kappa}\underline{d}}\,, \tag{7.17d}$$

and

$$_{\kappa+1}\beta(\kappa) = -\frac{\underline{_{\kappa+1}r}^{T}\,\underline{_{\kappa+1}r}}{\underline{_{\kappa}r}^{T}\,\underline{_{\kappa}r}}. \tag{7.17e}$$

At $\kappa = 0$, $\underline{_0 r}$ and $\underline{_0 d}$ are set to

$$\underline{_0 d} = \underline{_0 r} = \underline{b} - \underline{\underline{A}}\,\underline{_0 x} \tag{7.17f}$$

for initial estimate $\underline{_0 x}$.

For the purposes of time-reversal, the CG method of Eqns.7.17 is applied to the vector $\underline{_\kappa x}$, for the input and output ports at time-reversal iteration, κ, from the forward particular solution. The resulting vector $\underline{_{\kappa+1} x}$ is used for computation of the inverse simulation, through the difference vector $\underline{\hat{G}}$.

It can be seen the time-reversal process of forward and reverse simulations, can be thought of as computations at times, κ and $\kappa+1$, respectively, where the next forward and reverse simulations are iterations $\kappa+1$ and $\kappa+2$. Hence the first forward particular simulation (with scattering elements in place) is computing $\underline{_0 x}$ for use in Eqns.7.17 to orthogonalise for the reverse simulation.

7.4 Generalised Minimal Residual

In section 7.3, the solution to the matrix equation $\underline{\underline{A}}\,\underline{x} = \underline{b}$, was accelerated using CG to determine orthogonal search directions, which is a form of Gram-Schmidt conjugation [7.4]. An alternative approach is to minimise the norm of the residual, $\underline{r}$ in the Krylov subspace [7.4]. This is the methodology for the generalised minimal residual (GMRES) technique.

In GMRES, a modification of the Gram-Schmidt process, termed the Arnoldi Gram-Schmidt method [7.1] is used to derive the orthogonal basis vectors for the search directions. The Arnoldi method forces Gram-Schmidt orthgonalisation upon the search directions, by removing all components that are not orthogonal to previous search directions, the vectors $\underline{_{\kappa}d}$ then form a Krylov subspace. This can be thought of as an explicit algorithm, in comparison to CG which is implicit.

In GMRES acceleration all previous search directions are needed to perform the orthogonalisation. It is necessary to introduce further notation. The subspace formed from the union of vectors $\underline{_{\kappa}d}$, will be termed $\underline{\underline{_{\kappa}D}}$, where the subscript is now used to denote the number of vectors stored in the subspace $\underline{\underline{D}}$, of dimensions $N \times \kappa$.

Before GMRES is introduced, it is first necessary to define the upper Hessenberg matrix $\underline{\underline{H}}$ [7.7] [7.8], as an $N_{TR} - 1 \times N_{TR}$ matrix with zeros below the first sub diagonal. By use of the Arnoldi Gram-Schmidt procedure the GMRES algorithm is given as [7.4]

$$\underline{_0 d} = \underline{_0 r} / \left\| \underline{_0 r} \right\|_2 \tag{7.18a}$$

$$\underline{\underline{H}}(a,b) = 0 \ \textbf{for} \ 0 \le a \le N_{TR} - 1, \ 0 \le b \le N_{TR} \tag{7.18b}$$

for $\kappa = 0,1,...N_{TR} - 1$

$$\underline{_{\kappa}w} = \underline{\underline{A}}\,\underline{_{\kappa}d} \tag{7.18c}$$

for $a = 0,1,2...\kappa$

$$\underline{\underline{H}}(\kappa,a) = \underline{_{\kappa}w}^T \, \underline{_a d} \tag{7.18d}$$

$$\underline{_{\kappa}w} = \underline{_{\kappa}w} - \underline{\underline{H}}(\kappa,a)\,\underline{_a d} \tag{7.18e}$$

end for

$$\underline{\underline{H}}(\kappa,\kappa+1) = \left\| {}_{\kappa}\underline{w} \right\|_2 \tag{7.18f}$$

if $\underline{\underline{H}}(\kappa,\kappa+1) = 0$ **end** (7.18g)

$${}_{\kappa+1}\underline{d} = {}_{\kappa}\underline{w} / \underline{\underline{H}}(\kappa,\kappa+1) \tag{7.18h}$$

find ${}_{\kappa}\underline{y}$ **such that** $\min\left(\left\| \left\| {}_{0}\underline{r} \right\|_2 \underline{\rho}_0 - \underline{\underline{\underline{\underline{H}}}}_{\kappa,\kappa+1} {}_{\kappa}\underline{y} \right\|_2 \right)$ (7.18m)

$${}_{\kappa}\underline{x} = {}_{0}\underline{x} + \underline{\underline{\underline{D}}}_{\kappa} {}_{\kappa}\underline{y} \tag{7.18n}$$

end for

where $\underline{\rho_0}^T = \{1,0,0,....0\}$ and is of dimension $\kappa+1$.

Eqns.7.18c-h are the Arnoldi Gram-Schmidt procedure. It is seen ${}_{\kappa}\underline{w}$ is a temporary vector, formed from the Arnoldi vector at κ multiplied by $\underline{\underline{A}}$, orthogonalised to all previous Arnoldi vectors, and hence becomes ${}_{\kappa+1}\underline{d}$. The Arnoldi method forces Gram-Schmidt orthgonalisation upon the unit vectors ${}_{\kappa}\underline{d}$, by removing from ${}_{\kappa}\underline{w}$ all components that are not orthogonal to previous ${}_{\kappa}\underline{d}$, hence ${}_{\kappa}\underline{w} / \left\| {}_{\kappa}\underline{w} \right\|_2$ is orthogonal to all previous ${}_{\kappa}\underline{d}$, and the vectors ${}_{\kappa}\underline{d}$, form a Krylov subspace.

The algorithm breaks down at Eqn.7.18g if $\left\| {}_{\kappa}\underline{w} \right\|_2$ becomes zero, this will only happen if the residual is zero, and hence is sometimes termed a lucky breakdown [7.1].

In the case of time-reversal, ${}_{\kappa}\underline{y}$ from Eqn.7.18m is required to update ${}_{\kappa}\underline{x}$ in Eqn.7.18n to perform the reverse simulation. The Hessenberg matrix has zeros below the first sub diagonal; it is this property that allows efficient computation of ${}_{\kappa}\underline{y}$. A method known as QR decomposition [7.9] is first performed to express the Hessenberg matrix as $\underline{\underline{H}} = \underline{\underline{Q}}\,\underline{\underline{R}}$, where $\underline{\underline{Q}}$ is

orthogonal of dimensions $\kappa+1\times\kappa$, and $\underline{\underline{R}}$ is upper triangular and of dimensions $\kappa\times\kappa$.

The matrix $\underline{\underline{Q}}$ is formed from the orthognalised column-wise vectors of $\underline{\underline{H}}$,

$$\underline{\underline{Q}}=\left[\frac{\underline{{}_0h}}{\left\|\underline{{}_0h}\right\|_2},\frac{\underline{{}_1h}}{\left\|\underline{{}_1h}\right\|_2},\frac{\underline{{}_2h}}{\left\|\underline{{}_2h}\right\|_2},\ldots\frac{\underline{{}_\kappa h}}{\left\|\underline{{}_\kappa h}\right\|_2}\right], \tag{7.19}$$

where the $\underline{{}_ih}$ are column vectors of dimension $\kappa+1$, calculated as

$$\underline{{}_ih}=\begin{cases}\underline{\underline{H}}(i,.), & i=0,\\ \underline{\underline{H}}(i,.)-\sum_{a=0}^{i-1}\left(\frac{\left\langle\underline{\underline{H}}(i,.),\underline{{}_ah}\right\rangle}{\left(\left\|\underline{{}_ah}\right\|_2\right)^2}\underline{{}_ah}\right), & i>0.\end{cases} \tag{7.20}$$

$\underline{\underline{H}}(i,.)$ are the column vectors from $\underline{\underline{H}}$ and $\langle,\rangle$ is the inner product defined for two general vectors as $\left\langle\underline{h_1},\underline{h_2}\right\rangle=\left(\underline{h_2}*\right)^T\underline{h_1}$. Since $\underline{\underline{Q}}^T\underline{\underline{Q}}=\underline{\underline{I}}$ [7.9], the matrix $\underline{\underline{R}}$ is calculated as

$$\underline{\underline{R}}(a,b)=\underline{\underline{Q}}^T\underline{\underline{H}}=\left\langle\underline{\underline{H}}(a,.),\frac{\underline{{}_bh}}{\left\|\underline{{}_bh}\right\|_2}\right\rangle \tag{7.21}$$

where $a=0...\kappa$ and $b=0...\kappa$.

The matrix $\underline{\underline{R}}$ is upper triangular since the inner product is 0 for $a<b$ [7.9]. The problem of finding $\underline{{}_\kappa y}$ such that Eqn.7.18m is a minimum can

now be re-expressed using the $\underline{\underline{Q}}\underline{\underline{R}}$ decomposition of $\underline{\underline{H}}$, hence Eqn.7.18m becomes

$$\begin{aligned} &\min\left(\left\|\underline{\underline{0}}r\right\|_2 \underline{\rho_0} - \underline{\underline{Q}}\underline{\underline{R}}_{\kappa}\underline{y}\right\|_2\Big) \\ &\min\left(\left\|\underline{\underline{Q}}^T\left\|\underline{\underline{0}}r\right\|_2 \underline{\rho_0} - \underline{\underline{R}}_{\kappa}\underline{y}\right\|_2\right). \end{aligned} \tag{7.22}$$

Assigning, a new vector $\underline{\chi} = \underline{\underline{Q}}^T \left\|\underline{\underline{0}}r\right\|_2 \underline{\rho_0}$ the problem is reduced to finding the solution to Eqn.7.23.

$$\underline{\chi} = \underline{\underline{R}}_{\kappa}\underline{y}. \tag{7.23}$$

Reverse Gaussian elimination is then used to solve for $\underline{\kappa y}$.

$$\underline{\kappa y}(i) = \begin{cases} \dfrac{\underline{\chi}(i)}{\underline{\underline{R}}(i,i)}, & i = \kappa, \\ \dfrac{\underline{\chi}(i) - \sum_{a=i+1}^{\kappa} \underline{\underline{R}}(a,i)\,\underline{\kappa y}(a)}{\underline{\underline{R}}(i,i)}, & i = \kappa-1, \kappa-2, \ldots 0. \end{cases} \tag{7.24}$$

It is important to note, the GMRES method requires storage of the full Krylov subspace, $\underline{\underline{D}}$, a problem that is not encountered when using CG. In practice this memory is negligible in comparison to the size of the time-reversal-mirrors. If memory is a problem, a restarted version of GMRES can be used, where the procedure is stopped at κ, and restarted with step κ becoming step zero [7.4]. For the purposes of time-reversal, restarted GMRES will not be needed since the optimum solution is generally found before the dimensions of $\underline{\underline{D}}$ become a problem. Further details of GMRES can be found in [7.1].

7.5 Case Studies

The case studies of the previous chapters are now demonstrated, with the application of the three linear acceleration methods. The TLM parameters and initial and desired optimisation criteria are the same as those used in Chapter five.

7.5.1 2nd Order Septa Filter

The microwave filter created by the cascaded network of two metal septa in the WR90 waveguide was designed using the classical time-reversal design process in Chapter five. In this section, the acceleration methods of SOR, CG and GMRES are applied to the filter and compared with the classical solution.

7.5.1.1 Stationary Point Acceleration

In section 7.2, the SOR method applied to the optimisation of S parameters results in Eqn.7.15. In Figure 7-2 the figure of merit, FoM, against iteration number for different values of ω is shown. Three selected values of ω are given, where it is seen, optimal convergence is found for $0.54 \le \omega \le 0.58$, (within this range the results do not change). The SOR has converged to the optimum solution with a reduction of 2 time-reversal design steps. This is the maximum possible acceleration using SOR, as other values for ω produce slower convergence. It is intuitive the value of ω is dependant upon the damping, α, and hence the threshold and damping values were, $T_1 = 0.15$, $T_2 = 0.6$ and $\alpha = 0.82$. These were found by incrementally increasing the value of α, and varying T_1, T_2 and ω until optimal convergence was found, as described in Chapter five for the un-accelerated case. In this case the optimal widths using Eqn.5.15 were found to be $W_{S1} = 1.99$ mm and $W_{S2} = 2.65$ mm.

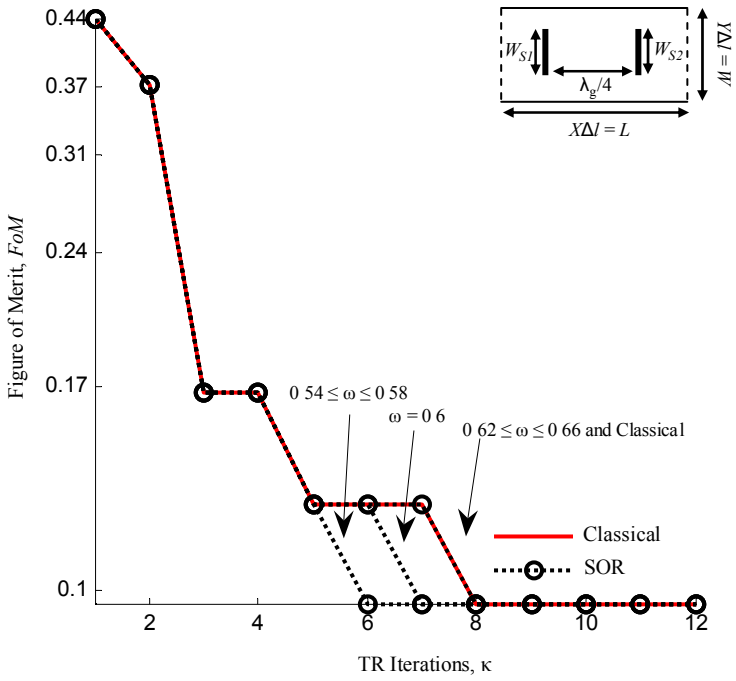

Figure 7-2 - Convergence of the classical time-reversal design process of 2nd order band pass septa filter in comparison to SOR, Δl = 0.297mm, Δt = 7e-13s, X = 67, Y = 77, L = 19.9mm, W = 22.86mm and N = 16384, optimised septa widths for SOR were W_{S1} = 1.99mm and W_{S2} = 2.65mm from initial configuration of $W_{S1} = W_{S2}$ = 0.89mm.

7.5.1.2 Non-Stationary Acceleration

Application of the CG and GMRES process for design of the septa filter produces the convergence rate shown in Figure 7-3, in comparison to the SOR and classical solutions. The simulation is stopped when FoM remains a minimum. A maximum acceleration of 50% is observed for CG. The optimum threshold and damping values were found to be $T_1 = 0.71$, $T_2 = 0.61$ and $\alpha = 0.77$. The threshold and damping values for GMRES were found to be $T_1 = 0.65$, $T_2 = 0.63$ and $\alpha = 0.8$. In this example, a saving of 50% is approximately an hour on the AMD Athlon $2\,\text{GHz}$ single threaded processor.

The CG method when implemented upon a linear problem is known to reach the optimum solution in exactly m steps [7.1], where m is the dimensionality of the problem, and ignoring floating point rounding errors. However, the time-reversal optimisation of the septa widths is non-linear, so a true orthogonal path will not be seen. In Figure 7-4 the contour levels indicate the figure of merit of the solution using the corresponding septa widths. The path taken by CG, GMRES and SOR in comparison to the classical time-reversal procedure is shown, were it is seen, CG reaches the optimum septum dimensions in fewer steps. Optimised septa widths for CG were $W_{S1} = 1.97\,\text{mm}$ and $W_{S2} = 2.5\,\text{mm}$, and GMRES were $W_{S1} = 2.14\,\text{mm}$ and $W_{S2} = 2.43\,\text{mm}$. In comparison, the classical solution finds $W_{S1} = 1.96\,\text{mm}$ and $W_{S2} = 2.55\,\text{mm}$, and SOR optimises to $W_{S1} = 1.99\,\text{mm}$ and $W_{S2} = 2.65\,\text{mm}$. These solutions are not in multiples of the TLM nodes, since the initial septa width is iteratively optimised, based upon the percentage difference in the perturbed time-reversal, to the control time-reversal, as stated in Chapter five, Eqn.5.15. These widths are snapped to the nearest TLM node in the simulation, of $W_{S1} = 7\Delta l = 2.08\,\text{mm}$ and $W_{S2} = 9\Delta l = 2.67\,\text{mm}$.

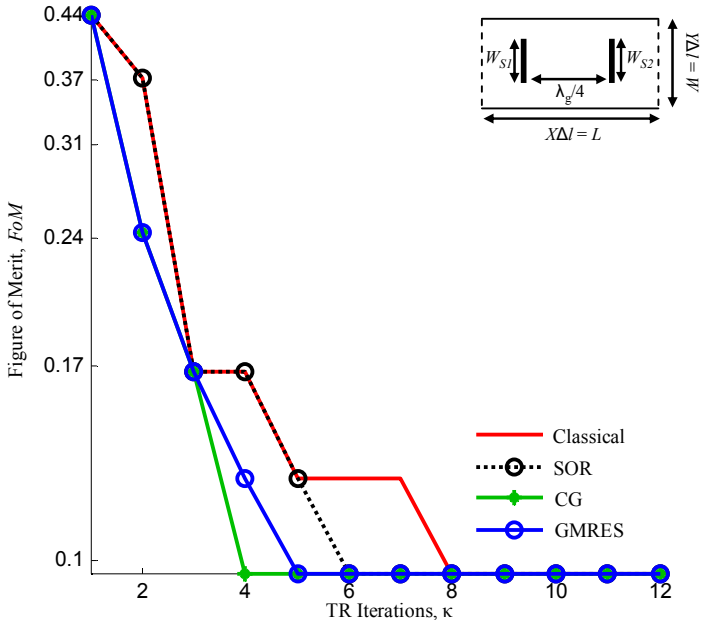

Figure 7-3 - Convergence of classical time-reversal design process of 2nd order band pass septa filter in comparison to SOR, CG and GMRES, Δl = 0.297mm, Δt = 7e-13s, X = 67, Y = 77, L = 19.9mm, W = 22.86mm and N = 16384.

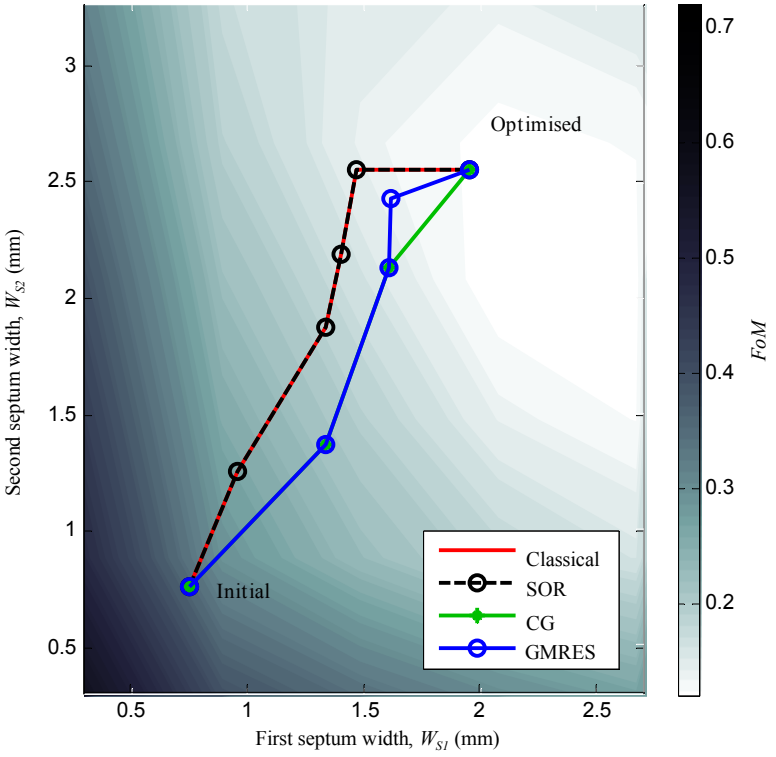

Figure 7-4 - Path to solution of GMRES and CG in comparison to the classical time-reversal design process and SOR with ω = 0.54 of 2nd order band pass septa filter, Δl = 0.297mm, Δt = 7e-13s, X = 67, Y = 77, L = 19.9mm, W = 22.86mm and N = 16384, plot contains 101 contours.

7.5.2 2nd Order Iris Filter

This section will compare the acceleration methods on the example of the microwave band pass filter formed from two irises. Figure 7-5 shows the convergence of all three methods and also shows the result obtained using the classical time-reversal.

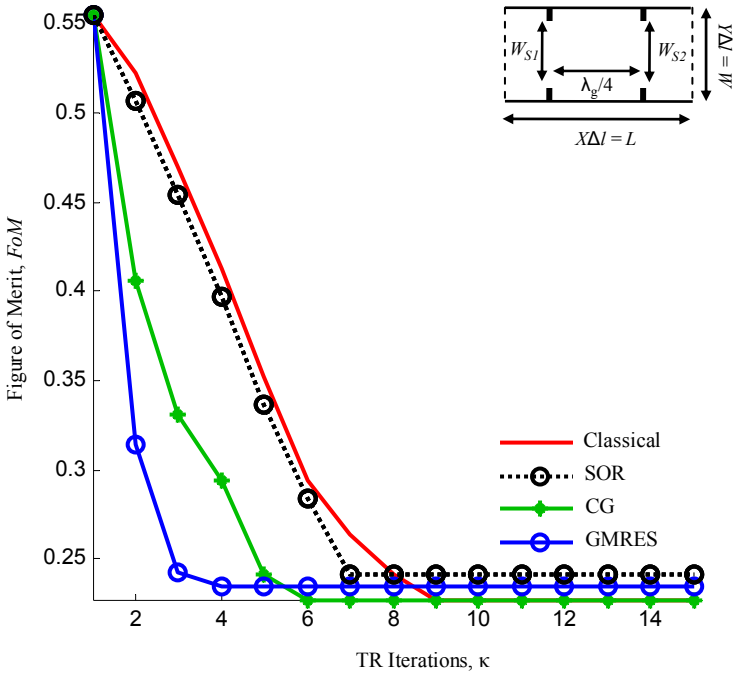

Figure 7-5 - Convergence of the classical time-reversal design process of 2nd order band pass iris filter in comparison to SOR, CG and GMRES, Δl = 0.199mm, Δt = 4.69e-13s, X = 100, Y = 115, L = 19.9mm, W = 22.86mm and N = 16384. Optimised iris widths for SOR were W_{S1} = 9.61mm and W_{S2} = 9.9mm, for CG were W_{S1} = 9.26mm and W_{S2} = 9.72mm and for GMRES were W_{S1} = 8.45mm and W_{S2} = 9.72mm.

In classical time-reversal, convergence to the optimal solution of $W_{S1} = 9.2\,\text{mm}$ and $W_{S2} = 9.61\,\text{mm}$ was found in 9 iterations as shown in Chapter five. The threshold and damping values for SOR are $T_1 = 0.84$, $T_2 = 0.87$ and $\alpha = 0.89$. Optimal convergence is found when the SOR parameter is in the range $0.24 \le \omega \le 0.3$. The parameters for CG are

$T_1 = 0.71$, $T_2 = 0.26$, $\alpha = 0.77$ and GMRES parameters are $T_1 = 0.69$, $T_2 = 0.26$ and $\alpha = 0.75$. Optimised iris widths for SOR were $W_{S1} = 9.61\,\text{mm}$ and $W_{S2} = 9.9\,\text{mm}$, for CG were $W_{S1} = 9.26\,\text{mm}$ and $W_{S2} = 9.72\,\text{mm}$ and for GMRES were $W_{S1} = 8.45\,\text{mm}$ and $W_{S2} = 9.72\,\text{mm}$. In this case, when snapped to the nearest TLM nodes, both the classical and CG result in $W_{S1} = 47\Delta l = 9.34\,\text{mm}$ and $W_{S2} = 49\Delta l = 9.74\,\text{mm}$. SOR results in $W_{S1} = 49\Delta l = 9.74\,\text{mm}$ and $W_{S2} = 49\Delta l = 9.74\,\text{mm}$, while GMRES results in $W_{S1} = 43\Delta l = 8.55\,\text{mm}$ and $W_{S2} = 49\Delta l = 9.74\,\text{mm}$.

Figure 7-5 shows that the CG method is optimal, and converges within 6 iterations, a runtime reduction of 30 % or approximately 1.5 hours, using the 2 GHz processor.

GMRES converges in fewer iterations, but is sub-optimal. The optimised S parameters of SOR, CG and GMRES are shown in Figure 7-6. Both SOR and GMRES are non-optimal in comparison to those found by CG, which are the same as those found by the classical time-reversal design of Chapter five. The reason for this is due to the presence of higher order modes between the waveguide wall and irises, creating noise in the recovered Poynting vector of this design. The problem of noise in the Poynting vector was also noted in [7.10].

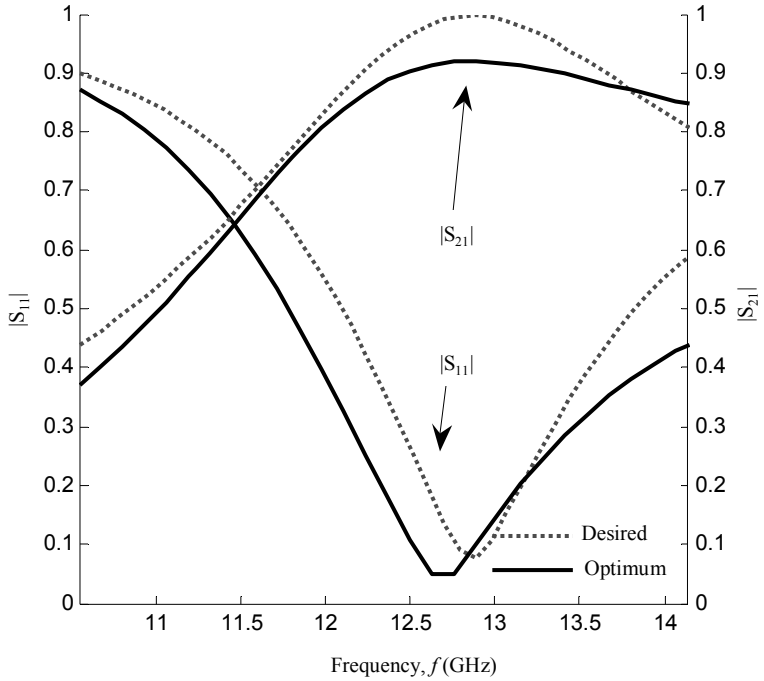
|S11|
|S21|
|S21|
|S11|
Desired
Optimum
Frequency, f (GHz)

a)

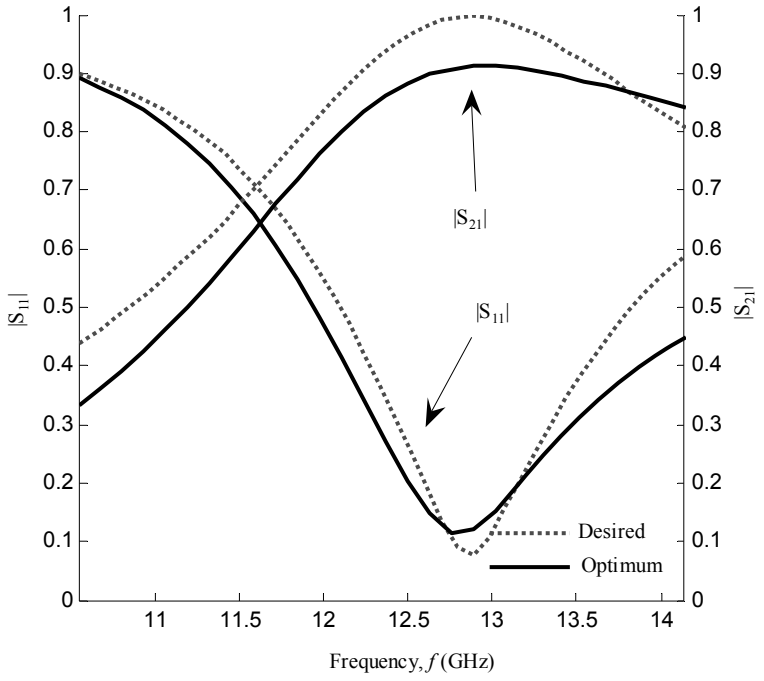
|S11|
|S21|
|S21|
|S11|
Desired
Optimum
Frequency, f (GHz)

b)

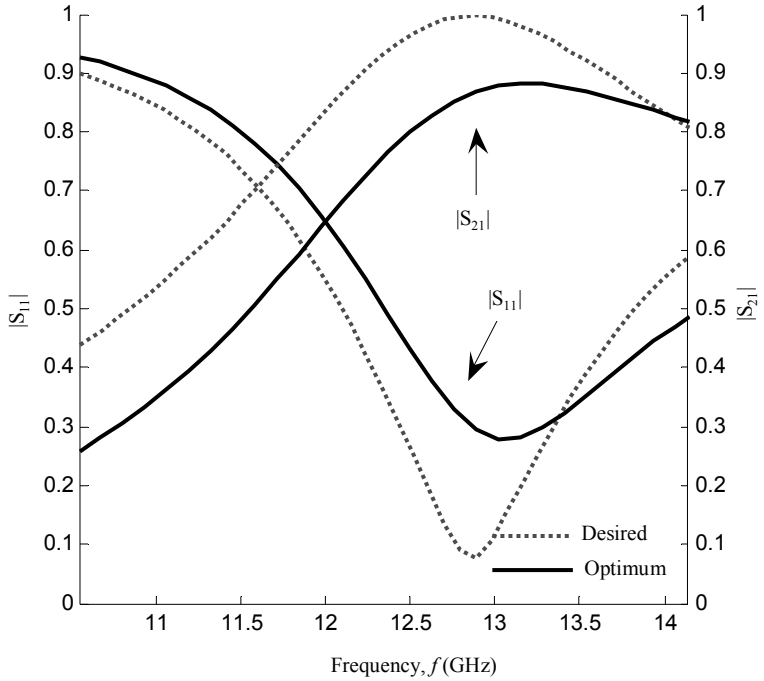

c)

Figure 7-6 - S parameters of 2nd order microwave band pass iris filter optimised using a) SOR, b) CG and c) GMRES. Δ*l* = 0.199mm, Δ*t* = 4.69e-13s, X = 100, Y = 115, L = 19.9mm, W = 22.86mm and N = 16384.

7.5.3 90° Waveguide Bend

The waveguide bend designed in Chapter five, was shown to reduce the return loss in a 90º bend by suitable placement of a tuning post. The three acceleration methods of SOR, CG and GMRES are now demonstrated.

The threshold and damping values for SOR are $T_1 = 0.95$ and $\alpha = 0.85$. For CG and GMRES the threshold and damping values are $T_1 = 0.95$, $\alpha = 0.91$, $T_1 = 0.95$ and $\alpha = 0.9$, respectively. Figure 7-7 shows the convergence of the accelerated schemes, using the optimal range for the ω parameter of $0.65 \le \omega \le 0.66$. All techniques reduce the number of iterations to converge to the optimal solution in comparison to the classical time-reversal. The three acceleration methods find identical optimal post displacement to the classical time-reversal of Chapter five resulting in a diagonal displacement calculated as $D_P = 20.43\,\text{mm}$.

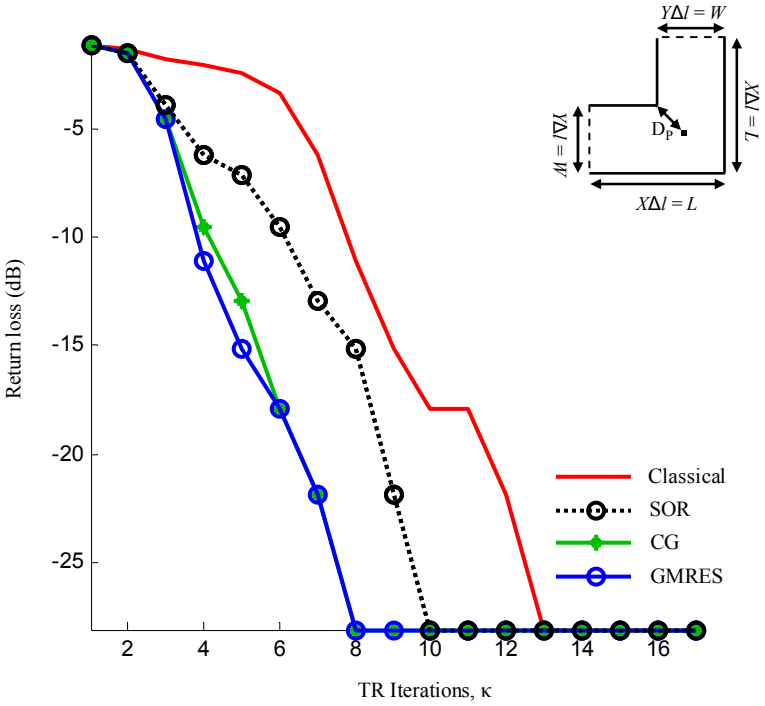

Figure 7-7 - Convergence of the classical time-reversal design process of 90° waveguide bend matching section in comparison to SOR, CG and GMRES, Δl = 0.18mm, Δt = 4.31e-13s, X = 220, Y = 125, L = 40.23mm, W = 22.86mm and N = 16384.

The computational resources required, both in terms of run time and memory, for most practical problems will be heavily dominated by the time domain simulations. SOR introduces virtually no additional overhead compared with the basic time-reversal and reduces the overall run time by approximately 25 %. GMRES and CG provide a further reduction in run times of up to 40 %, corresponding to up to 3 hours on the single threaded 2 GHz processor.

In Chapter five, it was seen the initial post displacement affects the convergence of the time-reversal design process. The analysis is repeated in Figure 7-8, with the inclusion of the linear acceleration methods. It is seen, the acceleration is of more value when the initial post displacement is further from the optimal solution.

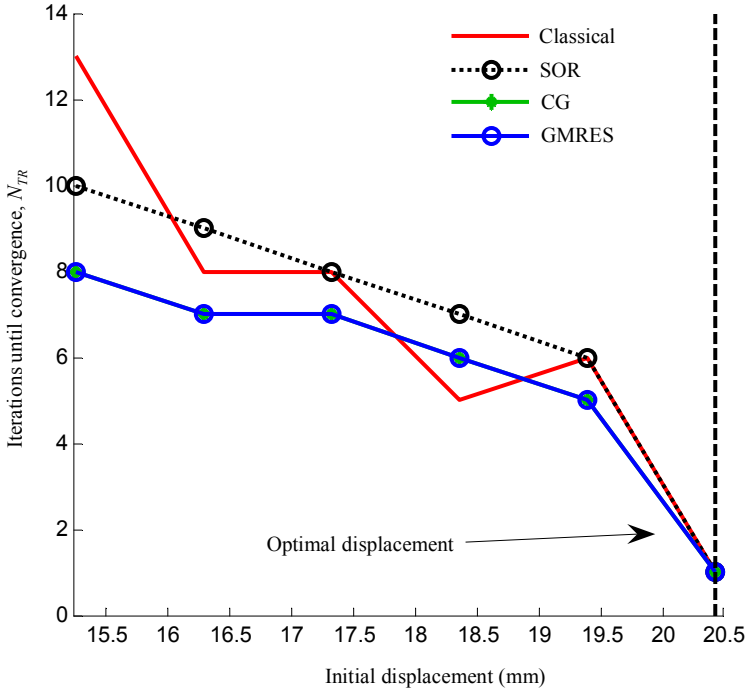

Figure 7-8 - Time-reversal design iterations with respect to initial post displacement for the 90° waveguide bend matching section, comparison of SOR, CG and GMRES acceleration methods. Δl = 0.18mm, Δt = 4.31e-13s, X = 220, Y = 125, L = 40.23mm, W = 22.86mm and N = 16384.

7.5.4 Directional Coupler

The design of the directional coupler using linear acceleration methods is more involved. It was shown in Chapter five that

$$\underline{C} = 20\log_{10}\left(\frac{\underline{\hat{V}_A}(f)}{\underline{\hat{V}_C}(f)}\right), \tag{7.25a}$$

$$\underline{D} = 20\log_{10}\left(\frac{\underline{\hat{V}_C}(f)}{\underline{\hat{V}_D}(f)}\right). \tag{7.25b}$$

It is seen from Eqn.7.25b, that the directivity is not directly in the form $\underline{\underline{A}}\,\underline{x} = \underline{b}$, since both $\underline{\hat{V}_C}$ and $\underline{\hat{V}_D}$ depend upon κ, the time-reversal iteration, and hence direct application of the linear solvers is not possible.

For a directional coupler, it is possible to express a further quantity, the isolation, as the leakage of current from the input port (port A) to the isolated port (port D) [7.11], in this manner

$$\underline{I} = 20\log_{10}\left(\frac{\hat{\underline{\underline{V}}}_A(f)}{\hat{\underline{V}}_D(f)}\right). \tag{7.26}$$

It is seen from Eqn.7.25a and Eqn.7.26 that

$$\underline{I} - \underline{C} = 20\log_{10}\left(\frac{\hat{\underline{\underline{V}}}_A(f)}{\hat{\underline{V}}_D(f)}\right) - 20\log_{10}\left(\frac{\hat{\underline{\underline{V}}}_A(f)}{\hat{\underline{V}}_C(f)}\right) = \underline{D} \tag{7.27}$$

and hence perturbation to the desired isolation at port D, will result in convergence to the desired directivity of the coupler. Rearranging Eqn.7.25a it is seen

$$\begin{aligned} &\log_{10}\left(\frac{\hat{\underline{\underline{V}}}_A(f)}{\hat{\underline{V}}_C(f)}\right) = \frac{\underline{\underline{C}}(f)}{20}, \\ &\underbrace{\hat{\underline{\underline{V}}}_A(f)}_{\underline{\underline{A}}}\underbrace{\left(1/\hat{\underline{V}}_C(f)\right)}_{\underline{x}} = \underbrace{10^{\frac{\underline{\underline{C}}(f)}{20}}}_{\underline{b}=\underline{C}^d} \end{aligned} \tag{7.28}$$

where $\underline{\underline{A}}$ is the diagonal matrix formed from the elements of $\hat{\underline{V}}_A$. Similarly for Eqn.7.26

$$\hat{\underline{\underline{V}}}_A(f)\left(\frac{1}{\hat{\underline{V}}_D(f)}\right) = 10^{\frac{\underline{\underline{I}}(f)}{20}}. \tag{7.29}$$

From Eqns.7.28-7.29, the directional coupler parameters are now expressed in the correct form. In this manner, the difference vector $\underline{G}$ used for the time-reversal design process is expressed using the isolation as

$$\underline{\hat{G}_C} = \begin{cases} \underline{C^d} - \underline{C}, & \text{if within bandwidth,} \\ 0, & \text{otherwise,} \end{cases} \tag{7.30a}$$

$$\underline{\hat{G}_D} = \begin{cases} \underline{I^d} - \underline{I}, & \text{if within bandwidth,} \\ 0, & \text{otherwise.} \end{cases} \tag{7.30b}$$

where

$$\underline{I^d} = \underline{D^d} + \underline{C^d}, \tag{7.31}$$

and the desired coupling/isolation are as per the right hand side of Eqns.7.28-7.29.

The threshold and damping values for SOR are $T_1 = 0.05$, $T_2 = 0.4$ and $\alpha = 0.93$. The optimal convergence was found when $0.8 \le \omega \le 0.98$. For CG, $T_1 = 0.04$, $T_2 = 0.42$, $\alpha = 0.98$ and for GMRES, $T_1 = 0.01$, $T_2 = 0.47$ and $\alpha = 0.96$. The convergence rate of all three methods, in comparison to the classical time-reversal design process is shown in Figure 7-9a,b,c for the coupling, directivity and isolation respectively. The isolation for the initial design is good, since the holes are small. This gradually becomes worse as the hole sizes increase and more power reaches ports C and D, until the optimum solution is found, at which point the field superposition travelling backwards cancels and the isolation improves.

The optimum solution depends on the method used, SOR finds $W_{H1} = W_{H2} = 5.37$ mm, snapped to TLM nodes this is $27\Delta l$, in comparison the classical solution finds $29\Delta l$. CG finds $W_{H1} = W_{H2} = 5.56$ mm, in TLM

nodes this is $27\Delta l$, while GMRES finds $W_{H1} = W_{H2} = 6.16\,\text{mm}$, or $31\Delta l$. The graphs have been truncated after the optimum solution is found for ease of illustration. CG results in the best convergence, with a runtime reduction of 27 %, or 4 hours on the 2 GHz processor.

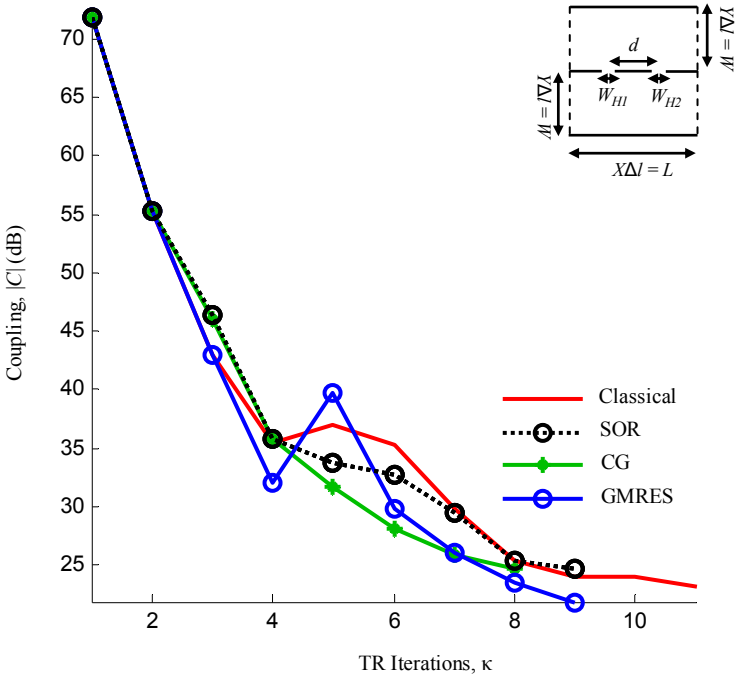

a)

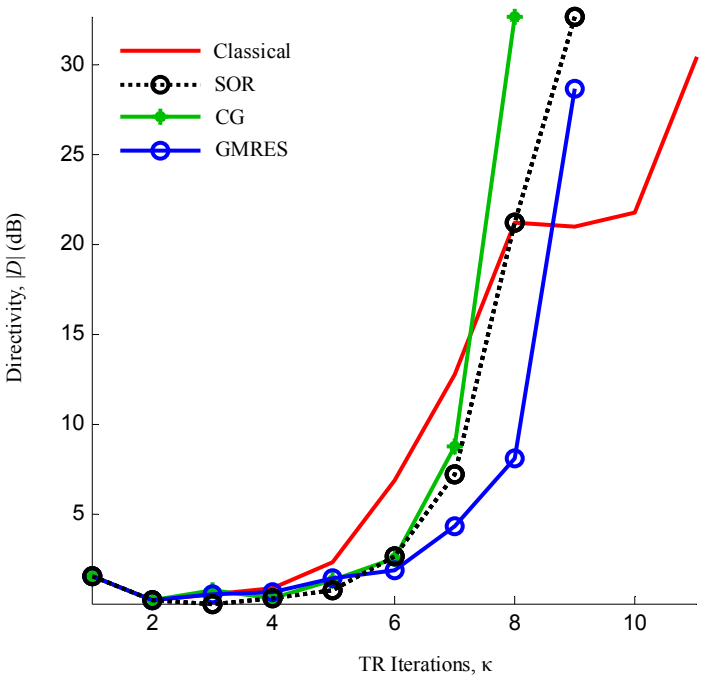

b)

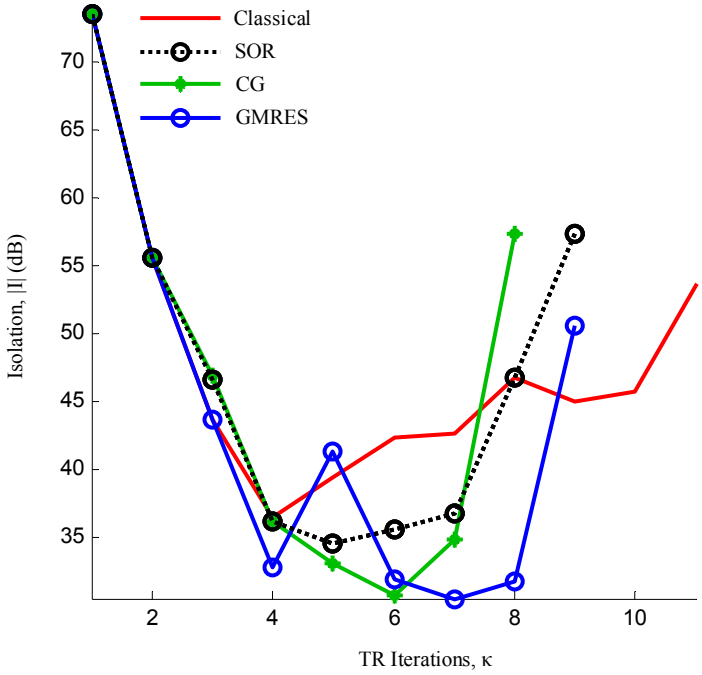

c)

Figure 7-9 - Convergence of the classical time-reversal design of directional coupler, in comparison to SOR, CG and GMRES, a) coupling, b) directivity and c) isolation. Δl = 0.199mm, Δt = 4.69e-13s, Y = 115, W = 22.86mm and N = 16384.

7.6 Conclusion

The chapter has demonstrated the derivation and application of stationary and non-stationary large matrix linear solvers to the time-reversal design algorithm. The method of SOR was seen to reduce the iterative design steps required to reach optimal convergence with virtually zero additional overhead or complexity in the time-reversal process. Unfortunately the optimum choice for the SOR point ω is problem dependant, and hence in return for accelerated time-reversal convergence, the setup stage of the time-reversal process increases in complexity. For the majority of the case studies there was a single region within which the SOR variable optimised the convergence.

The Krylov subspace methods of CG and GMRES were then demonstrated, and although slightly more complex, were seen to further accelerate the convergence of the algorithm, in some examples reaching convergence 50% faster than the original time-reversal design algorithm. The results from CG and GMRES are sufficiently close to not suggest a preference.

It was seen, reduction in overall runtime is primarily obtained from a more rapid initial convergence, which is advantageous as in larger scale problems available computing restrictions may only permit a few iterations to be undertaken to fine tune a design. The next chapter looks at the problems of time-reversal design when used for larger components.

7.7 References

[7.1] Y. Saad, *Iterative Methods for Sparse Linear Systems*. Society for Industrial and Applied Mathematics (SIAM), Philadelphia, PA, 2nd ed., 2003.

[7.2] M. R. Hestenes and E. Stiefel, "Methods of Conjugate Gradients for Solving Linear Systems," *Journal of Research of the National Bureau of Standards*, vol. 49, pp. 409–436, December 1952.

[7.3] R. Southwell, *Relaxation Methods in Theoretical Physics*. Clarendon Press, Oxford, 1946.

[7.4] R. Barrett, M. Berry, T. F. Chan, J. Demmel, J. Donato, J. Dongarra, V. Eijkhout, R. Pozo, C. Romine, and H. V. der Vorst, *Templates for the Solution of Linear Systems: Building Blocks for Iterative Methods*. Society for Industrial and Applied Mathematics (SIAM), Philadelphia, PA, 2nd ed., 1994.

[7.5] J. R. Shewchuk, "An Introduction to the Conjugate Gradient Method Without the Agonizing Pain," School of computer Science, Carnegie Mellon University, Pittsburgh, PA 15213, August 1994. Available online at: http://www.cs.cmu.edu/ jrs/jrspapers.html, Retrieved: 12/02/2009.

[7.6] L. Smith, *Linear Algebra*. Springer, New York, NY, 3rd ed., 1998.

[7.7] K. Hessenberg, “Treatment of Linear Eigenvalue Problems Using the Hamilton-Cayley Equation,” *Bericht der Reihe Numerische Verfahren*, pp. 1+36, July 1940.

[7.8] W. H. Press, B. P. Flannery, S. A. Teukolsky, and W. T. Vetterling, *Numerical Recipes in C: The Art of Scientific Computing*. Cambridge University Press, Cambridge, 2nd ed., 1992.

[7.9] E. Kreyszig, *Advanced Engineering Mathematics*. John Wiley & Sons Inc, New York, NY, 8th ed., 1998.

[7.10] M. Forest and W. J. R. Hoefer, “A Novel Synthesis Technique for Conducting Scatterers Using TLM Time Reversal,” *IEEE Transactions on Microwave Theory and Techniques*, vol. 43, pp. 1371–1378, June 1995.

[7.11] D. M. Pozar, *Microwave Engineering*. John Wiley & Sons Inc, New York, NY, 3rd ed., 2007.

8. Internal Time-Reversal-Mirrors

The loss of modal content for source reconstruction was seen to impact the spatial resolution of the reconstructed source in Chapter four. Loss of spatial resolution due to evanescent mode decay in the presence of finite machine precision restricts the scope for optimising large complex devices. In terms of scatterer reconstruction, the loss in spatial resolution will hinder the measurement of the device parameters, and hence introduce errors or prevent the time-reversal process from converging to the optimum design. This problem will worsen as the time-reversal-mirrors are placed further from the scatterer(s) to be optimised, which will become necessary as more complicated structures are designed.

If the full modal content of the structure is known, it is possible to capture the higher order evanescent modes before they have decayed at the bounding time-reversal-mirrors. The next section covers the basic theory needed to express the field within a simple waveguide in terms of its modal content; the following section will then develop a novel method to capture the higher order modal content for time-reversal, which will be demonstrated on two additional band pass filter sample designs.

8.1 Evanescent Fields and Time-Reversal

A single odd symmetric mode of an electric field propagating in a 2D metal waveguide in x, see Figure 8-1, can be expressed through the Sine form as

$$\underline{\underline{E_z}}(x,y,n) = \underline{M}(n)\sin\left(\left(y\Delta l + \Delta l/2\right)\frac{(2n+1)\pi}{W}\right)\exp(-\gamma_n x\Delta l) \tag{8.1}$$

where $n = 0,1,...N_{M1}-1$, $\underline{M}$ is a vector of dimension N_{M1} of the modal amplitudes, and N_{M1} is the total number of modes in the waveguide, $(Y-1)/2$ assuming a symmetric excitation.

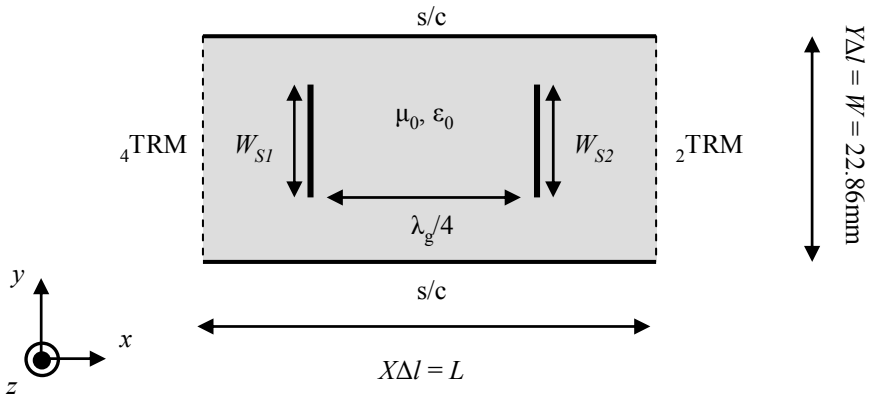

Figure 8-1 - 2nd order X-band microwave band pass filter formed from two inductive septa in WR90 waveguide.

From Eqn.8.1, the total field at longitudinal length $x\Delta l$ in the waveguide of Figure 8-1 can be expressed as a summation of modes in the form

$$\begin{aligned}\underline{\underline{E_z}}(x,y) &= \sum_{n=0}^{N_{M1}-1}\underline{\underline{E_z}}(x,y,n) \\ &= \sum_{n=0}^{N_{M1}-1}\underline{M}(n)\sin\left(\left(y\Delta l + \Delta l/2\right)\frac{(2n+1)\pi}{W}\right)\exp(-\gamma_n x\Delta l).\end{aligned} \tag{8.2}$$

$\underline{M}(n)$ at the time-reversal-mirrors is calculated from the voltage reflected from the ports of the transmission-line model (TLM) nodes neighbouring the time-reversal-mirrors, as

$$\underline{M}(n) = \frac{\sum_{y=0}^{Y-1} \sin\left(\left(y\Delta l + \Delta l/2 \right) \frac{(2n+1)\pi}{W} \right) \underline{V^r}}{Y/2}. \tag{8.3}$$

The bounding time-reversal-mirrors in Figure 8-1 store N_{M1} modes. However, the evanescent modes are known to be lost. The primary effect of such modal loss is a reduction in the spatial resolution of the model which leads to non-optimal designs and slow rates of convergence. Increasing the number of significant digits in the simulation is not a practically viable option.

Eqn.8.3 is also valid within the waveguide structure. To ensure that the evanescent modes are captured before they have decayed below machine precision, it is proposed that additional pairs of time-reversal-mirrors are placed within the problem space, located in close proximity to each of the scattering elements, these mirrors are termed internal-time-reversal-mirrors. The development of internal-time-reversal-mirrors will now be shown.

8.1.1 Internal Time-Reversal-Mirrors

At the internal-time-reversal-mirrors, the amplitudes of the majority of the evanescent modes are evaluated and stored. Moreover, these modes are then removed from the field radiating into the remainder of the simulation space which is necessary to ensure that they will not be recorded again by any of the other time-reversal-mirrors. At the original outer time-reversal-mirrors only the fundamental and remaining $N_{M2} - 1$ lower order mode amplitudes now need to be evaluated and stored. The rest are evanescent and are captured at the internal-time-reversal-mirrors. This is analogous to the distinction between local and accessible modes made in classical mode matching analysis of waveguide problems [8.1]. This process is shown visually in Figure 8-2. A 3D sketch is used to clarify the argument, but a 2D model is used in the example results.

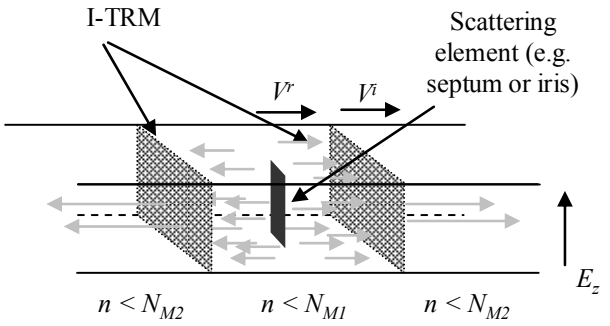

Figure 8-2 - Schematic presentation illustrating evanescent modes incident upon internal-time-reversal-mirrors (I-TRM). The mirrors remove evanescent modes stored.

Using Eqn.8.3 to measure the modal amplitude at port 2 of a node with an internal-time-reversal-mirror capturing a field propagating in $+x$, the TLM connection process [8.2] becomes

$$\underline{\underline{{}_{k+1}V_4^i}}(x+1,y) = \underline{\underline{{}_{k}V_2^r}}(x,y) - \sum_{n=N_{M2},\ldots}^{N_{M1}-1} \left\{ \underline{M_2}(n) \sin\left(\left(y\Delta l + \Delta l/2 \right) \frac{(2n+1)\pi}{W} \right) \right\} \tag{8.4}$$

where the modes $2N_{M2}+1$, … $2(N_{M1}-1)+1$, have been removed from the field reflected from node (x,y) connecting to the neighbouring node, $(x+1,y)$.

Eqn.8.4 is similarly derived for a field propagating in $-x$, by substituting $\underline{\underline{V_2^i}}(x-1,y)$ for $\underline{\underline{V_4^i}}(x+1,y)$, $\underline{\underline{V_4^r}}(x,y)$ for $\underline{\underline{V_2^r}}(x,y)$ and $\underline{M_4}(n)$ for $\underline{M_2}(n)$.

The internal-time-reversal-mirrors allow storage of the higher order field components [8.3], which would have been lost before reaching the bounding time-reversal-mirrors. It is intuitive the removal of evanescent modes when stored within the internal-time-reversal-mirrors during the forward stage of the design process has no effect on the measured S parameters, since by definition the evanescent modes are outside the bandwidth the device is to be designed within. This also means the internal-time-reversal-mirrors do not require perturbation, and hence the reverse time-reversal-mirror for an internal-time-reversal-mirror is simply

$$\underline{\underline{V_{ITRM}}}^{R}(n,k) = \underline{\underline{V_{ITRM\,P}}}^{F}(n,k) - \underline{\underline{V_{ITRM\,H}}}^{F}(n,k), \tag{8.5}$$

where the index $n = N_{M2},...N_{M1} - 1$. The bounding time-reversal-mirrors are hence

$$\underline{\underline{V_{TRM}}}^{R}(n,k) = \underline{\underline{V_{TRM\,P}}}^{F}(n,k)' - \underline{\underline{V_{TRM\,H}}}^{F}(n,k), \tag{8.6}$$

where the index $n = 0,1,...N_{M2} - 1$, and the $'$ symbolises the perturbation has been performed for these modes. In practice, with the case studies of this thesis it is only necessary to perturb the dominant mode.

N_{M2} is chosen such that all evanescent modes that will have significantly decayed at the bounding time-reversal-mirrors are now stored at the internal-time-reversal-mirrors. The demonstration problem of Figure 8-1 is shown in Figure 8-3 with two internal-time-reversal-mirrors surrounding each septum. The distance at which each internal-time-reversal-mirror is placed from its corresponding septum is determined by Eqn.8.7, for the highest order mode excited using the odd symmetric excitation $2(N_{M1} - 1) + 1 = Y - 2$

$$L_{M1} = \ln\left(10^{m/\gamma_{N_{M1}}}\right). \tag{8.7}$$

$\gamma_{N_{M1}}$ is the modal propagation constant defined as

$$\gamma_{N_{M1}} = \sqrt{\left(\frac{(2n+1)\pi}{W}\right)^2 - \left(\frac{2\pi}{\lambda_g}\right)^2} \tag{8.8}$$

where $n = N_{M1} - 1$.

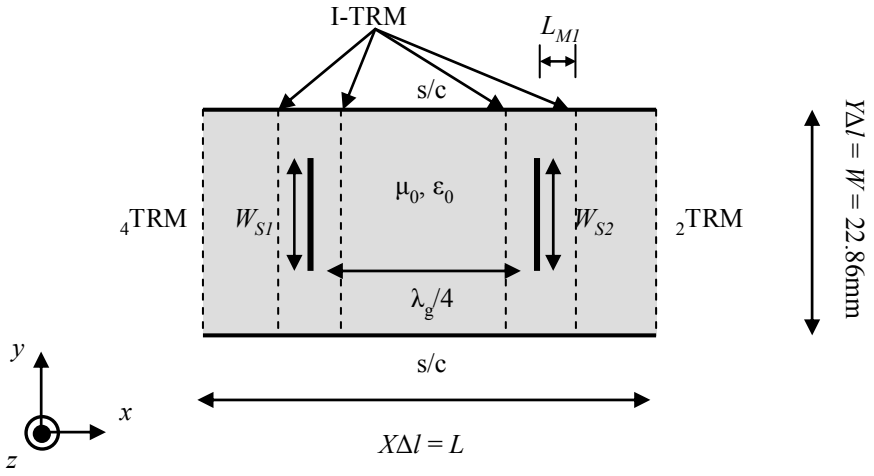

Figure 8-3 - 2nd order X-band microwave band pass filter with internal-time-reversal-mirrors (I-TRM) used to capture higher order evanescent modes decaying from each septa.

Since,

$$\lambda_g = \frac{v}{\sqrt{{f_r}^2 - {f_c}^2}}, \tag{8.9}$$

using Eqn.8.8 and Eqn.8.9

$$\gamma_n = \sqrt{\left(\frac{(2n+1)\pi}{W}\right)^2 - \left(\frac{2\pi}{v}\sqrt{{f_r}^2 - {f_c}^2}\right)^2} \,. \tag{8.10}$$

Substitution of Eqn.8.10 into Eqn.8.7, with the values, $n = N_{M1} - 1$ (where $N_{M1} = (Y-1)/2$) giving the highest order mode supported by the waveguide, $f_c = 6.56\,\text{GHz}$, $f_r = 12.5\,\text{GHz}$, $W = 22.86\,\text{mm}$, $m = -7$ and noting the $\sqrt{2}$ factor for 2D TLM, gives $L_{M1} = 1.5\,\text{mm}$, which is short enough to retain the highest order mode with 7 significant digits of accuracy (single precision). The bounding time-reversal-mirrors hold the 12 lower order modes (6 as only odd modes are excited and stored), known to propagate the distance $L/2$ with 7 significant digits of accuracy, while the internal-time-reversal-mirrors store the remaining higher order modes.

In order to investigate the improved accuracy using internal-time-reversal-mirrors, the maximum of the Poynting vector during time-reversal for a single iterate of the time-reversal design process of the second order septa filter is measured using classical time-reversal, and then with the internal-time-reversal-mirrors in Figure 8-4a,b. The TLM parameters were the same as Chapter five.

It is noticeable, the septa in Figure 8-4b with the internal-time-reversal-mirrors have a much greater resolution than those in Figure 8-4a using only the classical time-reversal-mirrors.

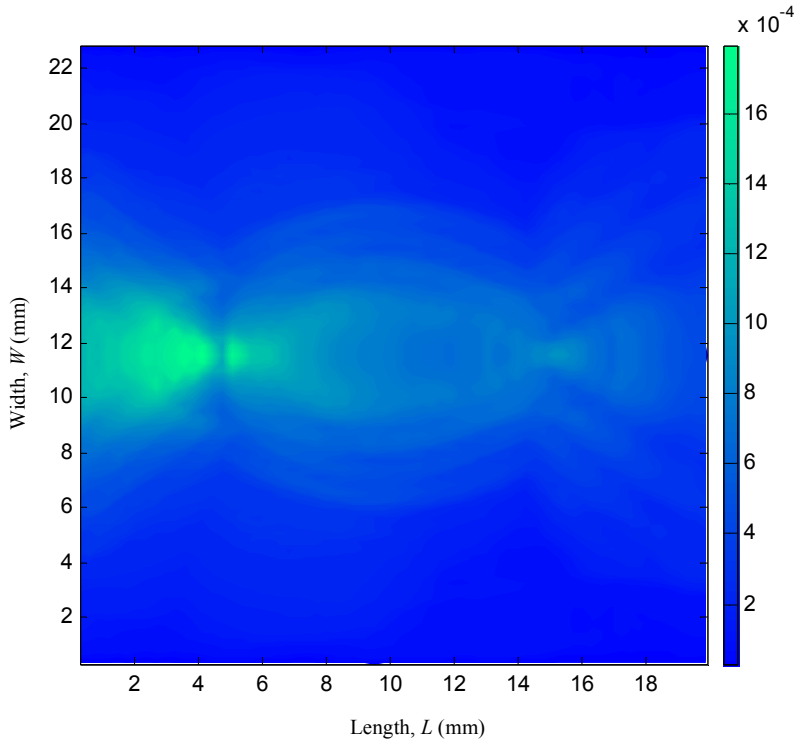

a)

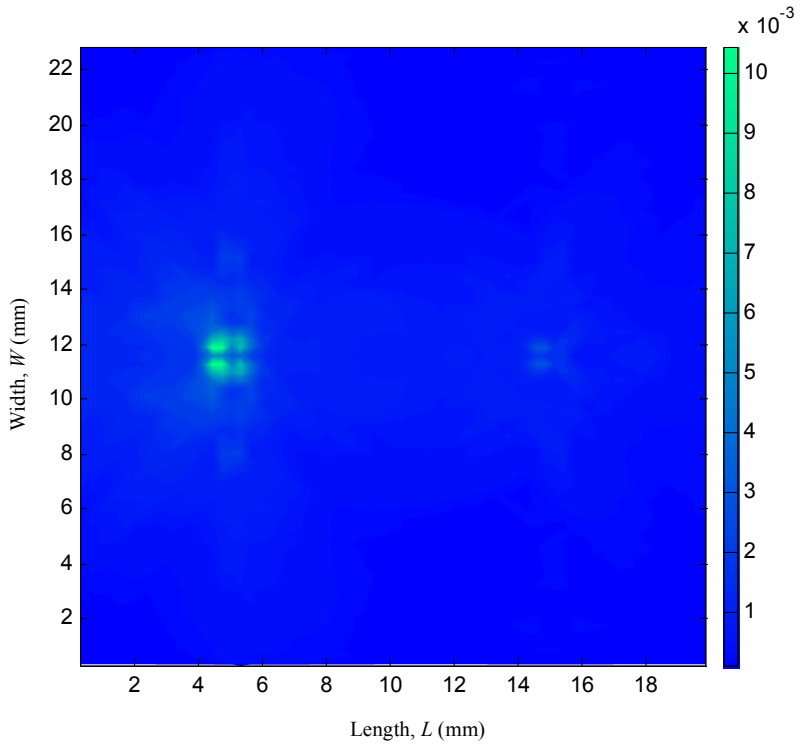

b)

Figure 8-4 - Maximum of Poynting vector during time-reversal of a) Figure 8-1 (without internal-mirrors) and b) Figure 8-3 (with internal-mirrors). Δl = 0.297mm, Δt = 7e-13s, X = 67, Y = 77, L = 19.89mm, W = 22.86mm, N = 16384 and $W_{S1} = W_{S2}$ = 0.89mm. A total of 91 contours are shown.

8.2 Case Studies

This section will analyse how the increased spatial resolution achieved using internal-time-reversal-mirrors, affects the convergence rate of the design process, and then introduce two further examples. The first, a higher order filter, and the second, an example of a band pass filter, with an optimum solution that is known to be able to be matched perfectly in the TLM model. Both examples are then designed using the acceleration methods of Chapter seven [8.4] and internal-time-reversal-mirrors, to determine the acceleration when the full set of evanescent modes are retained.

8.2.1 2nd Order Filter

In Figure 8-4 it is seen the time-reversal recovery of a scatter surrounded by two internal mirrors retains a significantly higher proportion of the evanescent modes for reversal, and hence is able to reconstruct the scatterers with a higher degree of spatial resolution than is possible using only the classical mirrors. Hence the thresholds and damping that gave the best convergence for the conventional time-reversal design process of the filter, will not give the best convergence when internal-time-reversal-mirrors are used. With internal-time-reversal-mirrors, $T_1 = 0.34$, $T_2 = 0.6$ and $\alpha = 0.93$. It is seen, in comparison with the values from the classical time-reversal using only external time-reversal-mirrors of Chapter five where $T_1 = 0.15$, $T_2 = 0.62$ and $\alpha = 0.93$, the thresholds for both septa have changed considerably. Observation of Figure 8-4 verifies this, since the resolution around the septa has improved.

The extent to which the increase in modal information affects the convergence rate of the time-reversal design process is shown in Figure 8-5. For comparison, results using just the classical time-reversal-mirrors at the ends of the filter are also shown. In this case, it is apparent that both curves converge, but that the use of internal-time-reversal-mirrors require one less

iteration. This small gain is not without value given that even one pair of forward-reverse time domain simulations may actually involve a significant calculation effort for large problems. Therefore for this example, the loss of evanescent mode data reaching the external time-reversal-mirrors does not seriously hamper the design process.

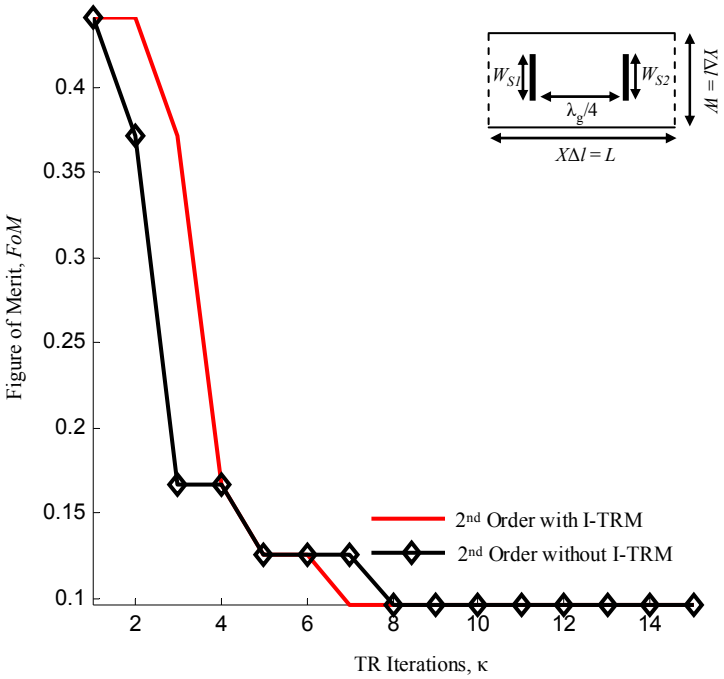

Figure 8-5 - Convergence of time-reversal design process of 2nd order band pass septa filter with and without internal mirrors (I-TRM), Δl = 0.297mm, Δt = 7e-13s, X = 67, Y = 77, L = 19.89mm, W = 22.86mm, N = 16384, optimised septa widths were W_{S1} = 1.96mm and W_{S2} = 2.55mm, in TLM nodes $W_{S1} = 7\Delta l$ = 2.08mm and $W_{S2} = 9\Delta l$ = 2.67mm from initial configuration of $W_{S1} = W_{S2}$ = 0.89mm.

8.2.2 3rd Order Filter

This case study will increase the complexity of the filter, by the inclusion of additional metal septa, see Figure 8-6. Higher order filters are desirable since the bandwidth selected is narrower, and the return loss (S_{11}) decreases further in the pass band. The increased order of the filter makes the design unsolvable using the conventional time-reversal process, since the middle

septum is now too far from the external bounding time-reversal-mirrors to be recovered with acceptable spatial resolution.

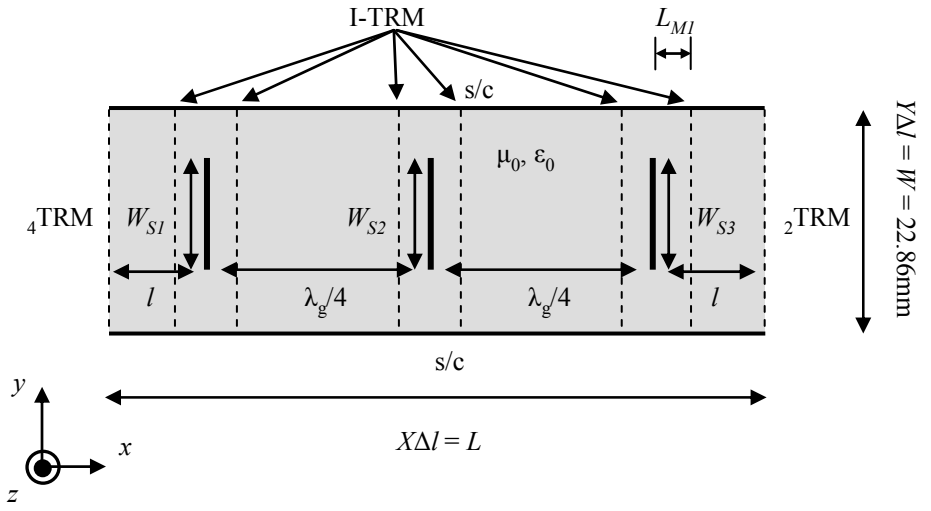

Figure 8-6 - 3rd order X-band microwave band pass filter formed from three inductive septa in WR90 waveguide. Internal-time-reversal-mirrors (I-TRM) are placed around each septum to capture evanescent modes.

The extrapolation of the desired ABCD matrix from the second order to a third order design following the procedure in Chapter five is [8.5]

$$\begin{bmatrix} \underline{A}(\beta) & \underline{B}(\beta) \\ \underline{C}(\beta) & \underline{D}(\beta) \end{bmatrix} = \begin{bmatrix} \cos(\beta l) & jZ_g \sin(\beta l) \\ j\sin(\beta l)/Z_g & \cos(\beta l) \end{bmatrix} \begin{bmatrix} 1 & 0 \\ 1/(j\omega L_1) & 1 \end{bmatrix} \begin{bmatrix} \cos(\beta\lambda_g/4) & jZ_g \sin(\beta\lambda_g/4) \\ j\sin(\beta\lambda_g/4)/Z_g & \cos(\beta\lambda_g/4) \end{bmatrix} \begin{bmatrix} 1 & 0 \\ 1/(j\omega L_2) & 1 \end{bmatrix} \begin{bmatrix} \cos(\beta\lambda_g/4) & jZ_g \sin(\beta\lambda_g/4) \\ j\sin(\beta\lambda_g/4)/Z_g & \cos(\beta\lambda_g/4) \end{bmatrix} \begin{bmatrix} 1 & 0 \\ 1/(j\omega L_3) & 1 \end{bmatrix} \begin{bmatrix} \cos(\beta l) & jZ_g \sin(\beta l) \\ j\sin(\beta l)/Z_g & \cos(\beta l) \end{bmatrix} \tag{8.11}$$

where $l = (L - 2(\lambda_g/4))/2$, and λ_g, Z_g and β are as previously defined.

$\underline{S_{11}^d}$ and $\underline{S_{21}^d}$ are calculated using the ABCD to S matrix transform given in Chapter five. Six internal-time-reversal-mirrors were spaced $L_{M1} = 1.5\,\text{mm}$ from the septa, as shown in Figure 8-6. The bounding time-reversal-mirrors successfully store the lower 4 odd symmetric order modes, known to propagate the distance $L/2$ with 7 significant digits of accuracy, while the internal-time-reversal-mirrors store the remaining higher order modes.

The values for the desired inductances in Eqn.8.11 were set at $1.95\,\text{nH}$, $1.55\,\text{nH}$ and $1.7\,\text{nH}$ respectively. These values were chosen to give the desired pass band shown in Figure 8-7. For a practical application, many more septa, typically five or more are required, to achieve a return loss of around $40-50\,\text{dB}$ in the pass band. This is not done here since the time-reversal simulation will be heavily time and memory intensive, and the analysis of the internal mirrors is the primary interest of this chapter.

The symmetric spatial sinusoid of period two times the waveguide width excites the filter at the input port. The filter is optimised within the frequency bandwidth $10-14\,\text{GHz}$. The TLM parameters are $\Delta l = 0.297\,\text{mm}$, $\Delta t = 7e-13\,\text{s}$, $X = 101$, $Y = 77$, $L = 29.99\,\text{mm}$, $W = 22.86\,\text{mm}$ and $N = 16384$. The threshold and damping values for classical time-reversal with internal-time-reversal-mirrors are $T_1 = 0.06$, $T_2 = 0.31$, $T_3 = 0.28$ and $\alpha = 0.97$. The threshold and damping values for classical time-reversal with only the external mirrors are $T_1 = 0.02$, $T_2 = 0.2$, $T_3 = 0.28$ and $\alpha = 0.97$. The initial S parameters of the model, for septa widths of $W_{S1} = 3\Delta l = 0.89\,\text{mm}$, $W_{S2} = 23\Delta l = 6.83\,\text{mm}$, and $W_{S3} = 23\Delta l = 6.83\,\text{mm}$ are also shown in Figure 8-7.

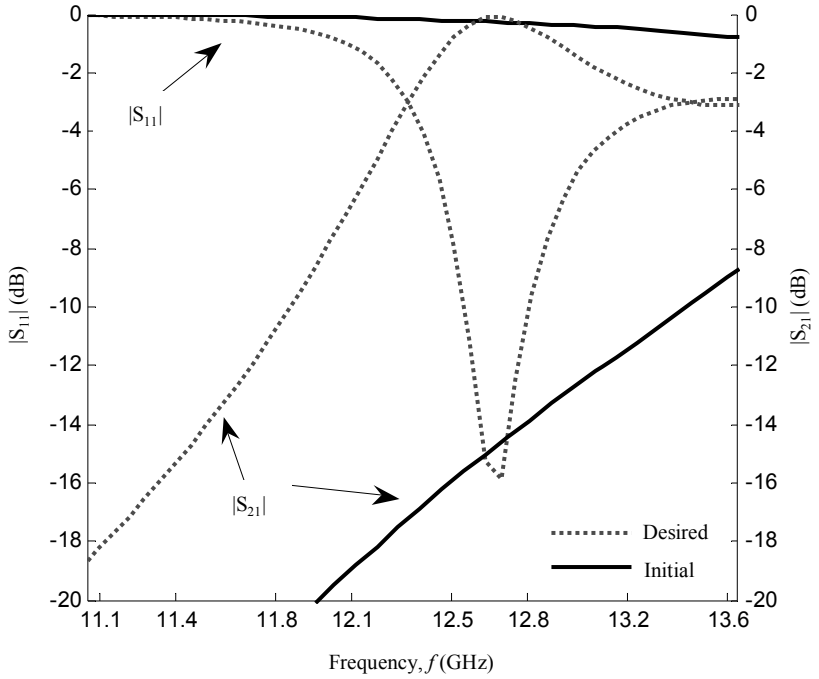

Figure 8-7 - S parameters in dB of 3rd order microwave band pass septa filter, desired with respect to initial. Δl = 0.297mm, Δt = 7e-13s, X = 101, Y = 77, L = 29.99mm, W = 22.86mm and N = 16384, W_{S1} = 0.89mm, W_{S2} = 6.83mm, and W_{S3} = 6.83mm.

In Figure 8-8 the convergence rate of the time-reversal design process is shown. It is seen that with the standard time-reversal approach the algorithm begins to converge, but since evanescent modes are lost, the time-reversal subsequently diverges. The time-reversal with internal mirrors is seen to converge after 24 iterations. The final optimised septa widths were, $W_{S1} = 4.82\,\text{mm}$, $W_{S2} = 3.96\,\text{mm}$ and $W_{S3} = 4.75\,\text{mm}$.

In Figure 8-9 four iterations of the time-reversal design process of the third order filter are shown after 6, 10, 15 and 24 iterations. An exact match to the desired S parameters is not expected, due to the fluctuation of inductance with frequency in the microwave model that is not accounted for in the transmission-line equivalence [8.6].

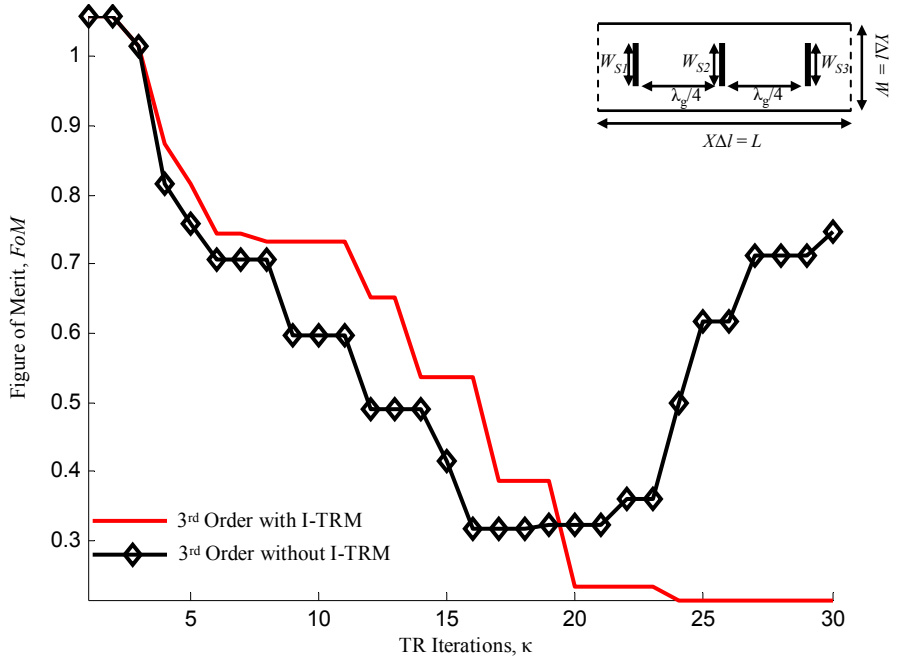

Figure 8-8 - Convergence of time-reversal design process of 3rd order band pass filter with and without internal mirrors, Δl = 0.297mm, Δt = 7e-13s, X = 101, Y = 77, L = 29.99mm, W = 22.86mm and N = 16384. Optimised septa widths for the internal-mirror (I-TRM) time-reversal were W_{S1} = 4.82mm, W_{S2} = 3.96mm and W_{S3} = 4.75mm, from initial configuration of W_{S1} = 0.89mm, W_{S2} = 6.83mm, and W_{S3} = 6.83mm.

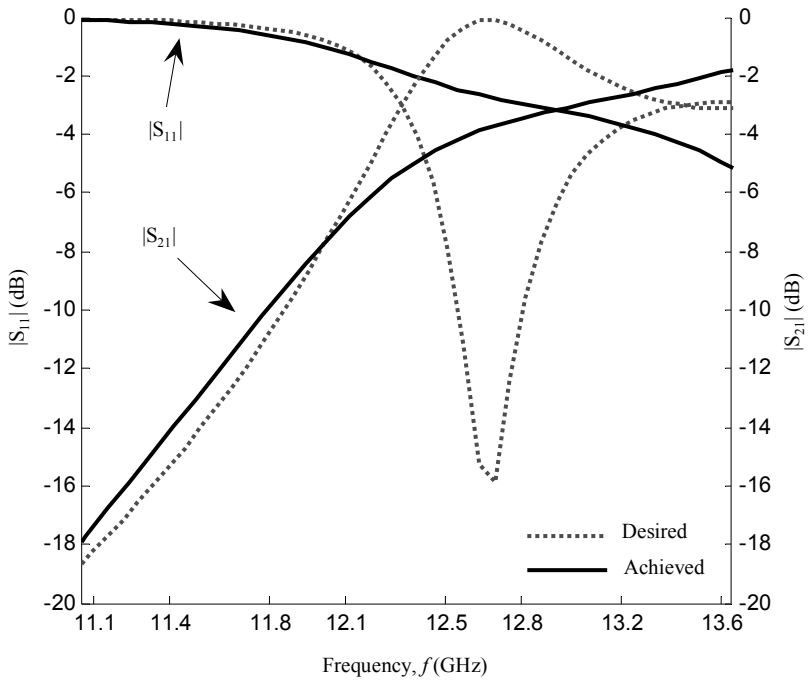

a)

b)

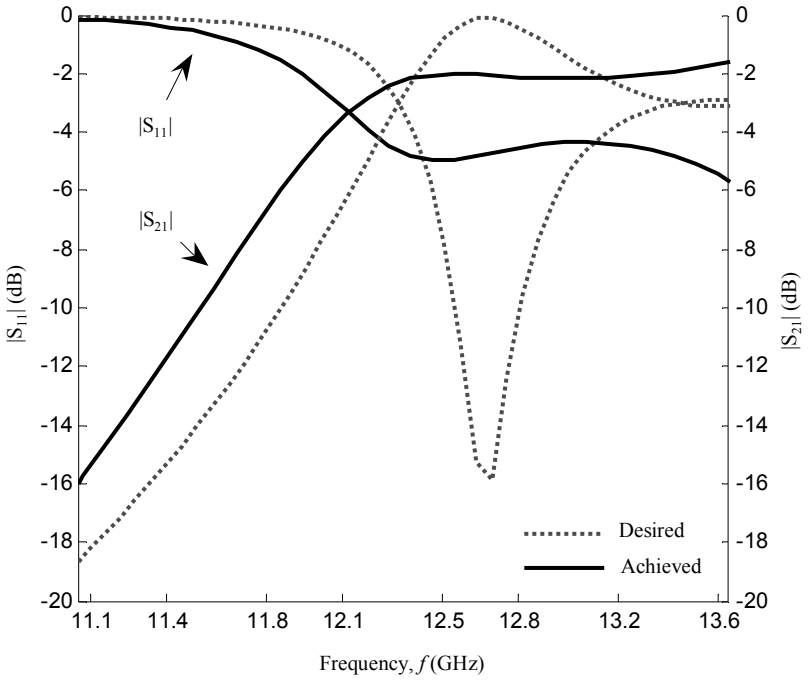
|S11|
|S21|
|S11| (dB)
|S21| (dB)
Desired
Achieved
Frequency, f (GHz)
0
-2
-4
-6
-8
-10
-12
-14
-16
-18
-20
11.1
11.4
11.8
12.1
12.5
12.8
13.2
13.6

c)

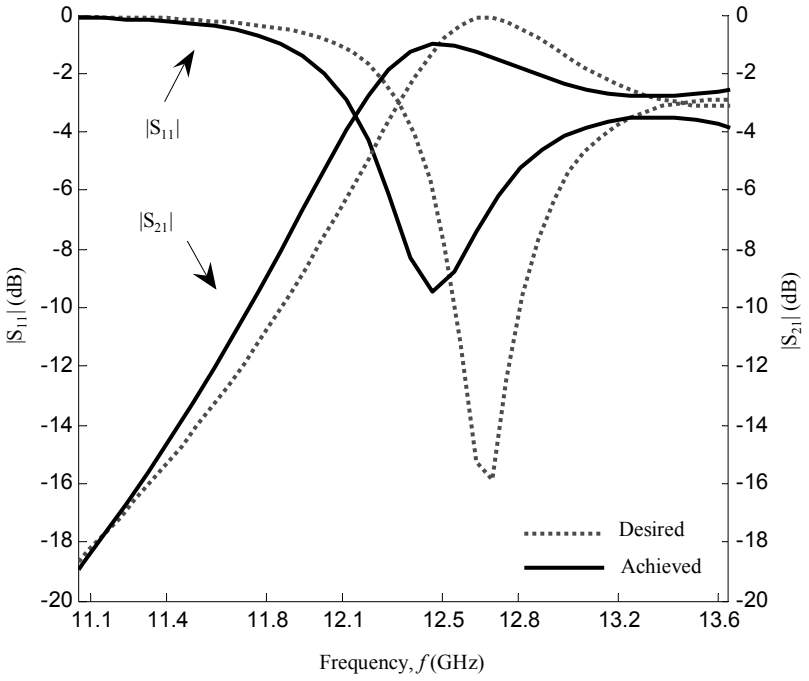
|S11|
|S21|
|S11| (dB)
|S21| (dB)
Desired
Achieved
Frequency, f (GHz)
0
-2
-4
-6
-8
-10
-12
-14
-16
-18
-20
11.1
11.4
11.8
12.1
12.5
12.8
13.2
13.6

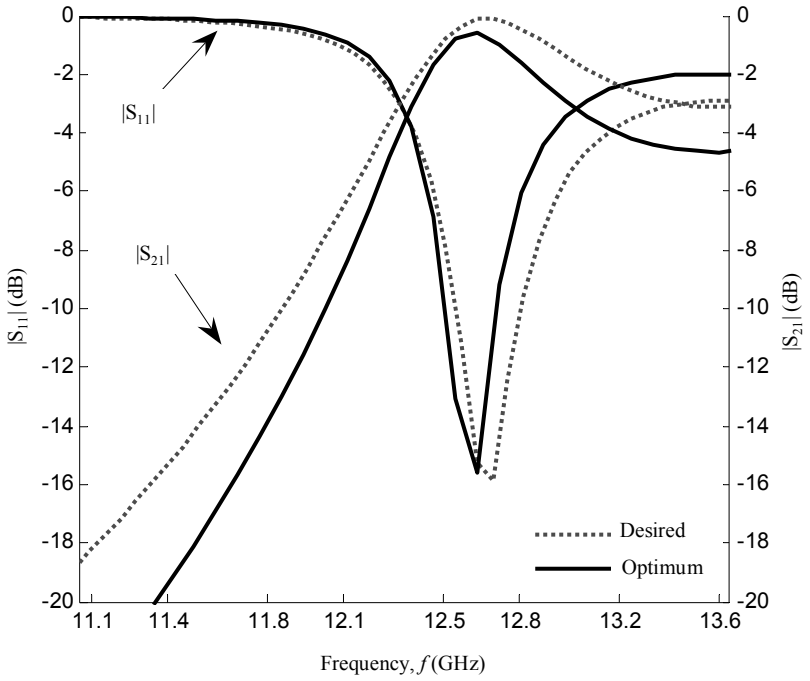

d)

Figure 8-9 - S parameters of 3rd order microwave band pass septa filter optimised using time-reversal, a) κ = 6, b) κ = 10, c) κ = 15, d) final configuration at κ = 24. Δ*l* = 0.297mm, Δ*t* = 7e-13s, X = 101, Y = 77, L = 29.99mm, W = 22.86mm and N = 16384, optimised septa widths were W_{S1} = 4.82mm, W_{S2} = 3.96mm and W_{S3} = 4.75mm.

Figure 8-10 shows the convergence rate of all three acceleration methods when applied to the perturbation of the external time-reversal-mirrors of the third order filter. The minimum of the FoM was the stopping criteria. The threshold and damping values for SOR were $T_1 = 0.06$, $T_2 = 0.31$, $T_3 = 0.28$, $\alpha = 0.97$, with $\omega = 0.2$, for CG, $T_1 = 0.05$, $T_2 = 0.8$, $T_3 = 0.11$, $\alpha = 0.96$ and for GMRES, $T_1 = 0.05$, $T_2 = 0.27$, $T_3 = 0.29$ and $\alpha = 0.95$. It is seen the CG and GMRES achieve the best result, obtaining acceptable convergence within 14-15 iterations. For SOR the optimised septa widths in odd TLM nodes were $W_{S1} = 4.76 = 17\Delta l$ mm, $W_{S2} = 4.62 = 15\Delta l$ mm, $W_{S3} = 4.75 = 15\Delta l$ mm, for CG, $W_{S1} = 4.8 = 17\Delta l$ mm, $W_{S2} = 4.29 = 13\Delta l$ mm, $W_{S3} = 4.66 = 15\Delta l$ mm and for GMRES, $W_{S1} = 4.45 = 15\Delta l$ mm, $W_{S2} = 4.93 = 13\Delta l$ mm, $W_{S3} = 4.09 = 13\Delta l$ mm. The

GMRES solution is the best, finding an optimal solution in 14 time-reversal iterations or 42 % of the full runtime. For this model computed using an AMD Athlon 2 GHz processor, the reduction in runtime is approximately 5.5 hours.

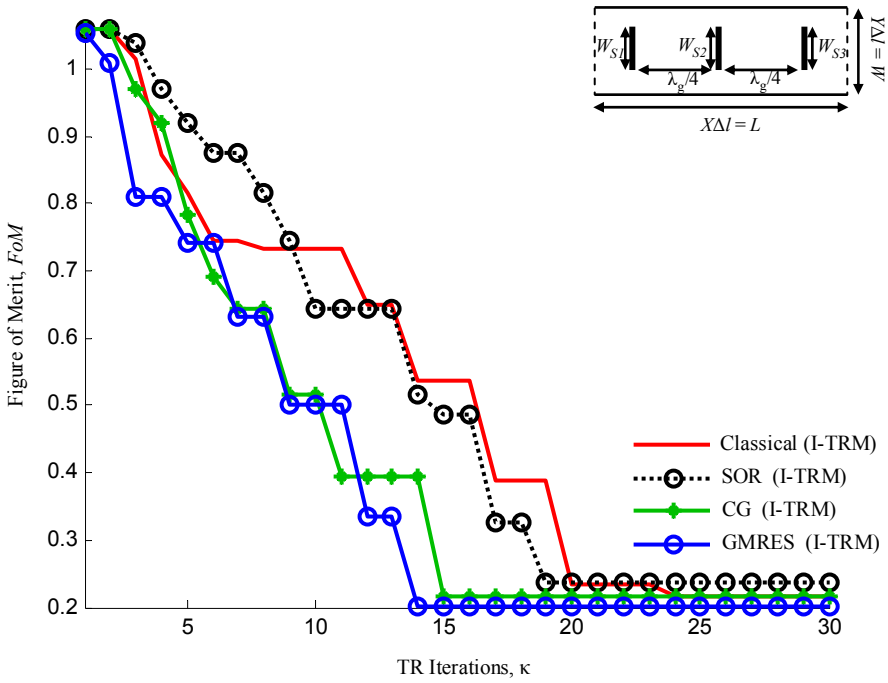

Figure 8-10 - Convergence of time-reversal design process of 3rd order band pass septa filter using internal mirrors (I-TRM), SOR, CG and GMRES are compared with the classical time-reversal. Δl = 0.297mm, Δt = 7e-13s, X = 101, Y = 77, L = 29.99mm, W = 22.86mm and N = 16384.

8.2.3 2nd Order Iris Filter with Known Solution

The example case studies for time-reversal design have been optimising using best case solutions. This subsection will introduce a new model, where known achievable S parameters are set as the desired solution.

The second order iris filter first used in Chapter five is known to be equivalent to the transmission-line representation of the septa filter, used to generate the desired S parameters. An alternative formation to generate a set

of desired S parameters, is achieved through measuring $\underline{S_{11}}$ and $\underline{S_{21}}$ from a desired configuration of iris widths. The iris widths are then set to their initial values, and the time-reversal optimisation applied to find the optimal widths. This approach, while not very practical for true component design, provides a known 'zero error' perfect solution for the time-reversal design process to be evaluated with.

In Figure 8-11 the schematic for the iris filter is shown, where the lightly shaded irises show the optimal widths of $W_{S1}^{d} = 47\Delta l = 9.34\,\text{mm}$ and $W_{S2}^{d} = 49\Delta l = 9.74\,\text{mm}$ (not to scale). The TLM parameters are $\Delta l = 0.199\,\text{mm}$, $\Delta t = 4.69e-13\,\text{s}$, $X = 100$, $Y = 115$, $L = 19.88\,\text{mm}$, $W = 22.86\,\text{mm}$ and $N = 16384$. The initial widths were $W_{S1} = W_{S2} = 61\Delta l = 12.13\,\text{mm}$ (shown as the dark irises) and generate the S parameters shown in Figure 8-12, where the desired S parameters are shown for comparison. A symmetric spatial sinusoid with period two times the waveguide width excites the filter at the input port. The optimisation bandwidth is $10-14\,\text{GHz}$. The internal-time-reversal-mirrors are placed identically as for the second order septa filter, where $L_{M1} = 1.5\,\text{mm}$, and the external bounding time-reversal-mirrors store the 12 lower order modes (or the 6 odd modes known to have been excited), while the internal-time-reversal-mirrors store the remaining higher order odd modes. The threshold and damping values for the classical time-reversal are $T_1 = 0.85$, $T_2 = 0.83$, $\alpha = 0.93$ for SOR, $T_1 = 0.85$, $T_2 = 0.83$, $\alpha = 0.8$, with $0.58 \le \omega \le 0.6$ for CG, $T_1 = 0.27$, $T_2 = 0.23$, $\alpha = 0.98$ and for GMRES, $T_1 = 0.51$, $T_2 = 0.72$ and $\alpha = 0.89$.

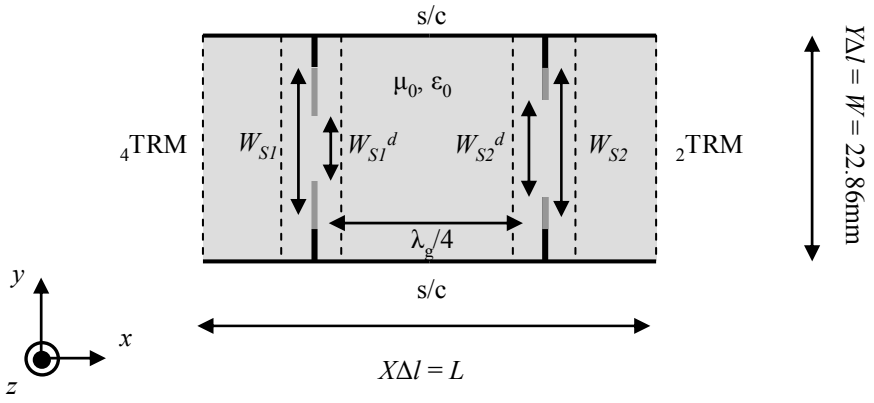

Figure 8-11 - 2nd order X-band microwave band pass filter formed from two inductive irises in WR90 waveguide. W_{S1} = W_{S2} = 61Δ*l* at start, optimised widths are W_{S1}^{d} = 47Δ*l* and W_{S2}^{d} = 49Δ*l* allowing a perfect solution to be found.

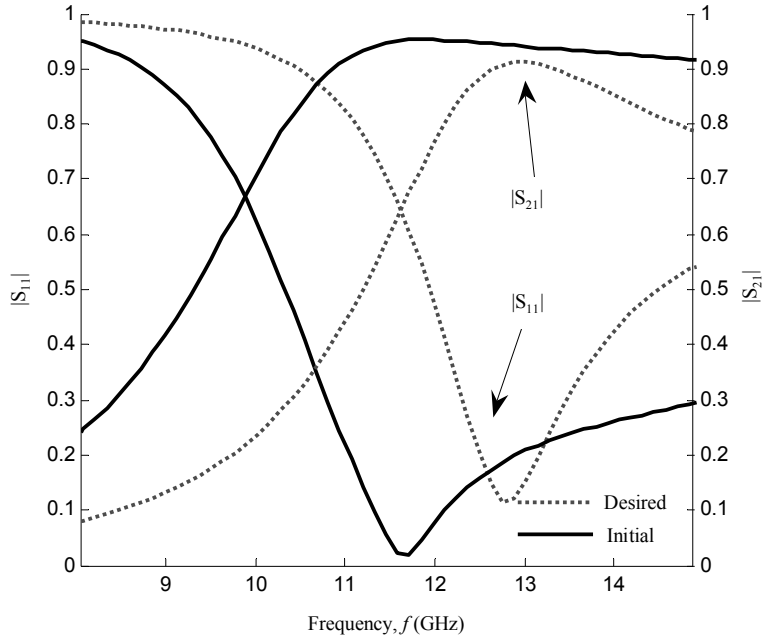

Figure 8-12 - S parameters of 2nd order microwave band pass iris filter, Δ*l* = 0.199mm, Δ*t* = 4.69e-13s, X = 100, Y = 115, L = 19.88mm, W = 22.86mm and N = 16384.

The convergence rate of Figure 8-13 is observed, where the SOR, GMRES and CG solutions are also shown. The potential of the Krylov subspace solvers (CG and GMRES) with time-reversal is now seen, where a reduction of over 30% of the runtime is observed, or around 3 hours on the 2 GHz processor.

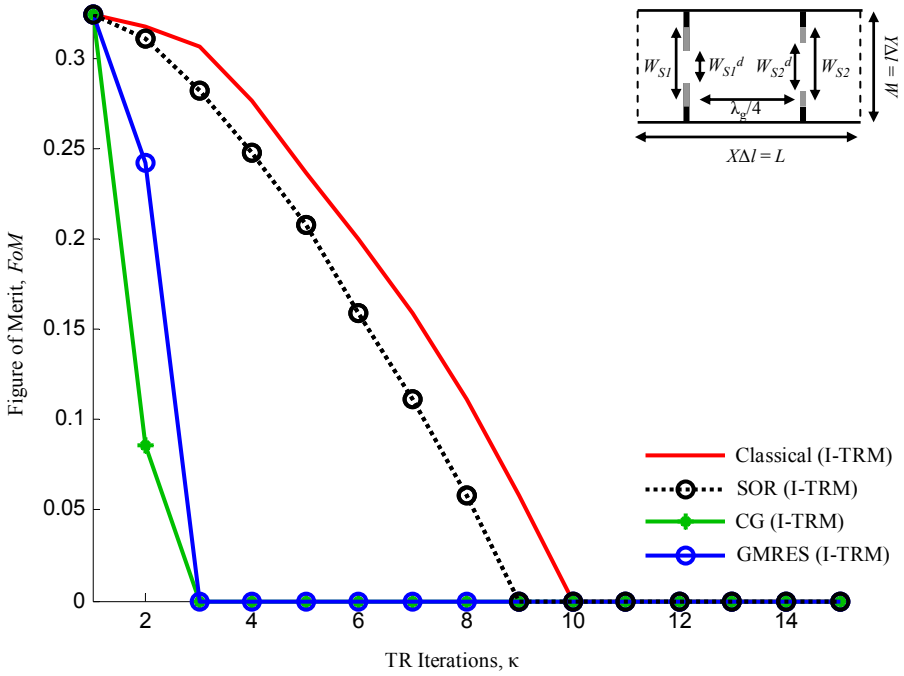

Figure 8-13 - Convergence of time-reversal design process of 2nd order band pass iris filter with known 'perfect' solution using internal mirrors (I-TRM), SOR, CG and GMRES are compared. Δl = 0.199mm, Δt = 4.69e-13s, X = 100, Y = 115, L = 19.88mm, W = 22.86mm and N = 16384.

8.3 Conclusion

The inherent mode filtering caused by finite machine precision seriously undermines the fidelity of the time-reversal design. This chapter has introduced internal-time-reversal-mirrors as a novel solution to this problem to ensure that all physically significant modes are captured correctly. This introduces a valuable degree of robustness into the design process. A third order filter was then designed, which was previously not possible using only

external time-reversal-mirrors. Finally, a filter with a known reachable 'zero-error' optimal solution was designed, and it was shown, the linear acceleration methods of the previous chapter improve performance further when a perfect design configuration exists. It was shown that the internal-time-reversal-mirrors not only offer improvements to the convergence rate but are imperative for achieving convergence for the more complex structure.

8.4 References

[8.1] T. E. Rozzi, "Network Analysis of Strongly Coupled Transverse Apertures in Waveguides," *International Journal of Circuit Theory and Applications*, vol. 1, pp. 161–179, 1973.

[8.2] C. Christopoulos, *The Transmission-line Modeling Method: TLM*. John Wiley & Sons/IEEE Publications, New York, NY, 1995.

[8.3] D. K. Cheng, *Field and Wave Electromagnetics*. Prentice-Hall, Reading, MA, 2nd ed., 1989.

[8.4] Y. Saad, *Iterative Methods for Sparse Linear Systems*. Society for Industrial and Applied Mathematics (SIAM), Philadelphia, PA, 2nd ed., 2003.

[8.5] R. Ludwig and P. Bretchko, *RF Circuit Design Theory and Applications*. Prentice-Hall, Upper Saddle River, NJ, 2000.

[8.6] R. E. Collin, *Foundations for Microwave Engineering*. John Wiley & Sons Inc, New York, NY, 2nd ed., 2001.

9. 3D Time-Reversal

For a number of physical components, modelling in 2D only is not suitable. This chapter demonstrates the expansion of the 2D time-reversal algorithm to 3D. The transmission-line modelling (TLM) symmetrical condensed node (SCN), as covered in Chapter three, is used. A 3D microwave filter analogous to the 2D band pass filter is demonstrated. A dipole antenna is then introduced, and the development of the time-reversal algorithm is shown.

9.1 Introduction to 3D Time-Reversal

In Chapter three, the derivation of the symmetrical condensed node (SCN) for the numerical simulation of an electromagnetic field was given. In comparison to the 2D shunt node, there is now the additional field components E_x, E_y, and H_z. To simulate the additional components, each propagation direction in the node contains two voltages. The SCN is repeated in Figure 9-1 for ease. In addition a time-reversal-mirror has been placed upon ports 1 and 5. In Figure 9-1 it is seen, for full 3D time-reversal, 12 time-reversal-mirrors are required.

Throughout the chapter, the time-reversal-mirrors will use the same numbering as the SCN, for example

$$\underline{\underline{{}_1V_{TRM}}}^{F}(x,y,k) = \underline{\underline{{}_kV_1^r}}(x,y,0)\,, \tag{9.1a}$$

$$\underline{\underline{{}_2V_{TRM}}}^{F}(x,z,k) = \underline{\underline{{}_kV_2^r}}(x,Y-1,z)\,, \tag{9.1b}$$

$$\underline{\underline{{}_3V_{TRM}}}^{F}(y,z,k) = \underline{\underline{{}_kV_3^r}}(0,y,z)\,, \tag{9.1c}$$

etc.

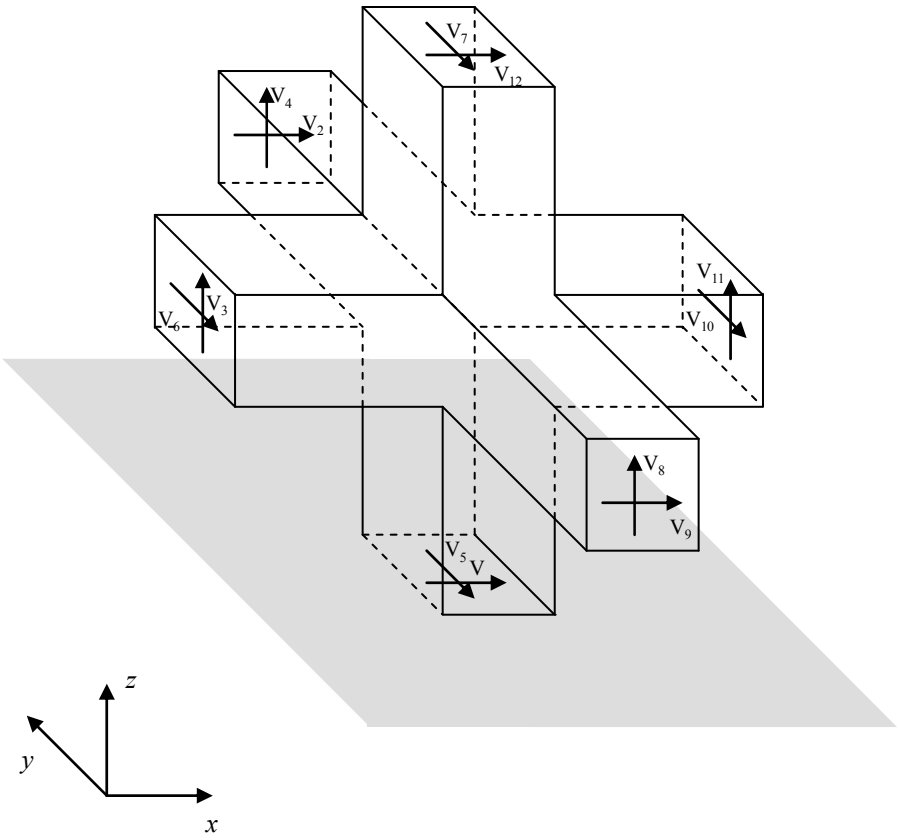

Figure 9-1 - 3D transmission-line model symmetrical condensed node, with the addition of a time-reversal-mirror upon ports 1 and 5.

In reverse, the time-reversal-mirrors become line sources as in the 2D case, and hence the incident voltages upon the transmission-line modelling (TLM) nodes bounding with the time-reversal-mirrors are

$$\underline{\underline{{}_kV_1^i}}(x,y,0) = \underline{\underline{{}_1V_{TRM}{}^F}}(x,y,k), \tag{9.2a}$$

$$\underline{\underline{{}_kV_2^i}}(x,Y-1,z) = \underline{\underline{{}_2V_{TRM}{}^F}}(x,z,k), \tag{9.2b}$$

$$\underline{\underline{{}_kV_3^i}}(0,y,z) = \underline{\underline{{}_3V_{TRM}{}^F}}(y,z,k), \tag{9.2c}$$

etc.

The general time-reversal algorithm for 2D component design is formed identically for 3D, with the exception that the time-reversal-mirrors perturbation, homogenous removal, and reverse equations are now 3D matrices. For the example of port 1 of the SCN, the time-reversal-mirror perturbation is

$$\begin{aligned}\underline{\underline{{}_1V_{TRM\,P}{}^F}}(x,y,k)' = {} & (\alpha)\underline{\underline{{}_1V_{TRM\,P}{}^F}}(x,y,k) + \\ & (1-\alpha)\left(\underline{\underline{{}_1V_{TRM\,P}{}^F}}(x,y,k) - \underline{\underline{\phi}}(x,y)\otimes|\underline{G_1}(k)|\right),\end{aligned} \tag{9.3}$$

and the reverse time-reversal-mirror is constructed as

$$\underline{\underline{{}_1V_{TRM}{}^R}}(x,y,k) = \underline{\underline{{}_1V_{TRM\,P}{}^F}}(x,y,k)' - \underline{\underline{{}_1V_{TRM\,H}{}^F}}(x,y,k). \tag{9.4}$$

The next section introduces the thin wire formulation for the TLM SCN, which will be used to model the dipole antenna.

9.2 Thin Wire in the SCN

The accurate modelling of a thin wire using TLM is possible in three ways. The first is to define a short circuit boundary between two nodes. While simple, this is of limited use at high frequencies, due to the need for extremely fine meshing. The two remaining methods either place the wire between the nodes [9.1], or within the node [9.2], using a combination of empirical values and numerical analysis. For simplicity and accuracy, the

wire between nodes is the simplest to implement upon the SCN already shown and will now be demonstrated.

In Figure 9-2 the thin wire is placed vertically between nodes $(x-1, y, z)$ and (x, y, z) using the form described in [9.1] [9.3] [9.4]. It is seen the wire will couple to port 11 of node $(x-1, y, z)$ and port 3 of node (x, y, z) of the neighbouring SCN. This form allows coupling of the wire with the orthogonal electric field component.

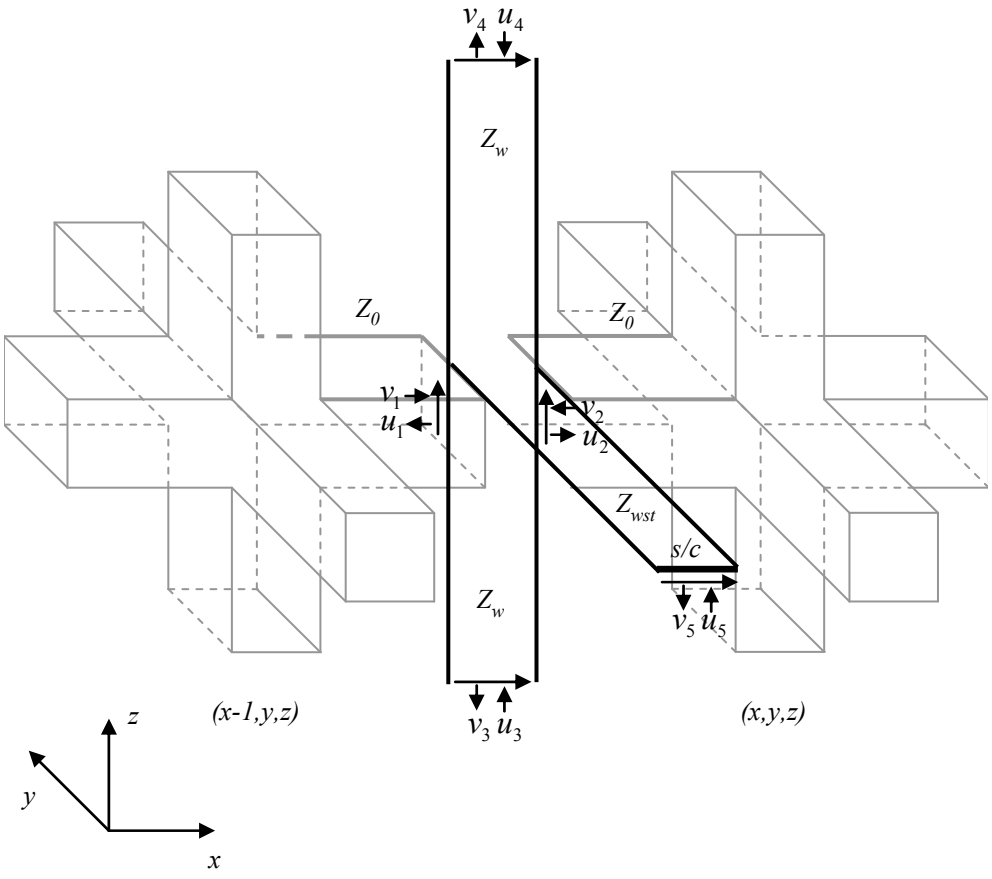

Figure 9-2 - Two 3D TLM SCN with thin wire formulation between nodes. The wire has impedance Z_w and stub impedance Z_{wst}.

To simulate propagation with the wire, the connection between ports 3 and 11 of the neighbouring SCN is modified to allow the connected voltages to

scatter and connect to the wire. The scatter/connect process for the wire embeds a 2D scattering within the 3D TLM connection routine. Using the notation of Figure 9-2, the nodal scattering is defined as

$$\begin{bmatrix} \underline{v}_1(z) \\ \underline{v}_2(z) \\ \underline{v}_3(z) \\ \underline{v}_4(z) \\ \underline{v}_5(z) \end{bmatrix} = \underline{\underline{S}} \begin{bmatrix} \underline{u}_1(z) \\ \underline{u}_2(z) \\ \underline{u}_3(z) \\ \underline{u}_4(z) \\ \underline{u}_5(z) \end{bmatrix} \tag{9.5}$$

where $\underline{u}_{1,2}(z)$ and $\underline{v}_{1,2}(z)$ are the SCN incident and reflected voltages upon ports 11 and 3 of nodes $(x-1, y, z)$ and (x, y, z) respectively,

$$\underline{u}_1(z) = \underline{\underline{V}}_{11}^{i}(x-1, y, z), \tag{9.6a}$$

$$\underline{u}_2(z) = \underline{\underline{V}}_{3}^{i}(x, y, z), \tag{9.6b}$$

$$\underline{\underline{V}}_{11}^{r}(x-1, y, z) = \underline{v}_1(z), \tag{9.6c}$$

$$\underline{\underline{V}}_{3}^{r}(x, y, z) = \underline{v}_2(z). \tag{9.6d}$$

The scattering matrix is defined similarly to the 5-port TLM node, and can be shown to be [9.3]

$$\underline{\underline{S}} = \frac{1}{Z_{ad}} \begin{bmatrix} -Z_0 & 2(Z_{wst}+2Z_w) & 2Z_0 & -2Z_0 & 2Z_0 \\ 2(Z_{wst}+2Z_w) & -Z_0 & 2Z_0 & -2Z_0 & 2Z_0 \\ 2Z_w & 2Z_w & Z_0+2Z_{wst} & 4Z_w & -4Z_w \\ -2Z_w & -2Z_w & 4Z_w & Z_0+2Z_{wst} & 4Z_w \\ 2Z_{wst} & 2Z_{wst} & -4Z_{wst} & 4Z_{wst} & Z_0-2Z_{wst}+4Z_w \end{bmatrix} \tag{9.7}$$

where $Z_{ad} = Z_0 + 2Z_{wst} + 4Z_w$. $Z_w = \dfrac{\Delta t}{C}$ and $Z_{wst} = 2\left(\dfrac{L}{\Delta t} - \dfrac{\Delta t}{C}\right)$ and are the wire impedance, and wire stub impedance respectively.

It is seen from Eqn.9.7, the scattering matrix satisfies the property $\underline{\underline{S}} = \underline{\underline{S}}^{-1}$ required for time-reversal. This may prove useful for designs with wires that remain in place during reversal.

The values for the capacitance, C and the inductance, L per unit length of the wire are defined as [9.2]

$$C = \frac{2\pi\varepsilon}{\ln\left(\frac{0.4\Delta l}{r}\right)}\Delta l \tag{9.8a}$$

$$L = \frac{\mu}{2\pi}\ln\left(\frac{0.15\Delta l}{r}\right)\Delta l \tag{9.8b}$$

where 0.4 and 0.15 are empirical values based upon numerical experimentation [9.2] and r is the radius of the wire.

The connection procedure for the wire is defined as

$$\underline{u_3}(z) = \underline{v_4}(z-1) \tag{9.9a}$$

$$\underline{u_4}(z) = \underline{v_3}(z+1) \tag{9.9b}$$

$$\underline{u_5}(z) = -\underline{v_5}(z) \tag{9.9c}$$

where $\underline{u_{1,2}}$ and $\underline{v_{1,2}}$ are connected through the SCN connection process.

This completes the coverage of the thin wire formulation between the SCN, more details can be found in [9.2] and [9.4].

9.3 Case Studies

In this section, two components are demonstrated and designed using the 3D time-reversal algorithm. The band pass waveguide filter of Chapter five and

a linear dipole are designed using time-reversal in 3D. The dipole antenna illustrates the time-reversal design process with free space radiating components.

9.3.1 WR90 Waveguide Band Pass Filter

In Figure 9-3 the band pass filter formed through two inductive septa is shown. The infinitely thin septa act as shunt inductances, just as in the 2D version, and so the passive circuit equivalence of Chapter five is used.

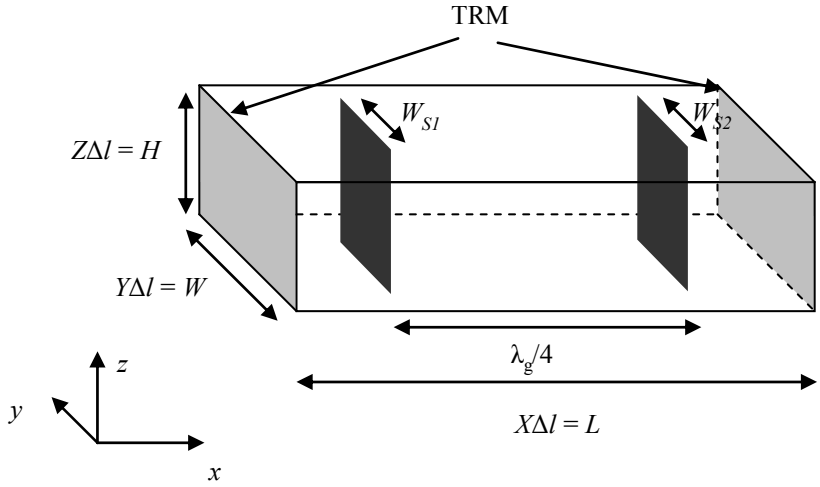

Figure 9-3 - 2nd order WR90 waveguide band pass filter in 3D.

The waveguide boundaries are short circuit, where the input and output ports are defined as time-reversal-mirrors. The lowest order mode is the TM_{10} mode ($E_x = 0$), giving a cut-off at

$$f_c = \frac{v}{2}\sqrt{\left(\frac{n}{W}\right)^2 + \left(\frac{m}{H}\right)^2} = \frac{v}{2W}. \tag{9.10}$$

The input port is excited for the dominant TM_{10} mode via a symmetric spatial sinusoid of period $2W$,

$$\begin{aligned} \underline{\underline{{}_0V_3^i}}(0,y,z) &= \sin\left(\left(y\Delta l+\Delta l/2\right)\frac{n\pi}{W}\right)\cos\left(\left(z\Delta l+\Delta l/2\right)\frac{m\pi}{W}\right) \\ &= \sin\left(\left(y\Delta l+\Delta l/2\right)\frac{\pi}{W}\right), \qquad n=1,m=0 \end{aligned} \tag{9.11}$$

where it is seen from the corresponding scattering matrix of the SCN in Chapter three, only the field components for the TM_{10} mode are excited, E_z, H_x and H_y.

Since only the TM_{10} mode is excited, port 6 and 10 remain zero throughout the simulation, hence only two 3D time-reversal-mirrors are required to store the reflected voltages at ports 3 and 11.

The scattering parameters are now measured from the ports of the 3D waveguide. The electric field can be expressed as the summation of modes

$$\underline{\underline{E_z}}(0,y,z) = \sum_{n=1,3,5}^{N_n}\sum_{m=0,1,3}^{N_m} A_{nm}\sin\left(\frac{n\pi(y\Delta l+\Delta l/2)}{W}\right)\cos\left(\frac{m\pi(z\Delta l+\Delta l/2)}{H}\right) \tag{9.12}$$

where N_n and N_m take the values $Y-2$ and $Z-2$ respectively (assuming odd symmetric modes).

Expressing $\underline{\underline{E_z}}(0,y,z)$ as $\underline{\underline{E_z}}(y,z)$ for simplicity, multiplying both sides of Eqn.9.12 by $\sin\left(\frac{n\pi(y\Delta l+\Delta l/2)}{W}\right)\cos\left(\frac{m\pi(z\Delta l+\Delta l/2)}{H}\right)$ and summing over the spatial and modal domains gives

$$\begin{aligned}\sum_{n=1}^{N_n}\sum_{m=0}^{N_m}\sum_{y=0}^{Y-1}\sum_{z=0}^{Z-1}\underline{\underline{E_z}}(y,z)\sin\left(\frac{n\pi(y\Delta l+\Delta l/2)}{W}\right)\cos\left(\frac{m\pi(z\Delta l+\Delta l/2)}{H}\right)\\ =\sum_{n=1}^{N_n}\sum_{m=0}^{N_m}\sum_{y=0}^{Y-1}\sum_{z=0}^{Z-1}A_{nm}\sin^2\left(\frac{n\pi(y\Delta l+\Delta l/2)}{W}\right)\cos^2\left(\frac{m\pi(z\Delta l+\Delta l/2)}{H}\right)\\ =\sum_{n=1}^{N_n}\sum_{m=0}^{N_m}A_{nm}\sum_{y=0}^{Y-1}\sin^2\left(\frac{n\pi(y\Delta l+\Delta l/2)}{W}\right)\sum_{z=0}^{Z-1}\cos^2\left(\frac{m\pi(z\Delta l+\Delta l/2)}{H}\right).\end{aligned} \tag{9.13}$$

Setting $n=1,\ m=0$ and expressing Eqn.9.13 for the single TM_{10} mode gives

$$\begin{aligned}\sum_{y=0}^{Y-1}\sum_{z=0}^{Z-1}\underline{\underline{E_z}}(y,z)\sin\left(\frac{\pi(y\Delta l+\Delta l/2)}{W}\right)\\ =A_{10}\sum_{y=0}^{Y-1}\sin^2\left(\frac{\pi(y\Delta l+\Delta l/2)}{W}\right)\sum_{z=0}^{Z-1}1.\end{aligned} \tag{9.14}$$

Rearranging and noting the summation of the square of the Sine over one half period for the odd symmetric order modes is $Y/2$, yields

$$A_{10}=\frac{\sum_{y=0}^{Y-1}\sum_{z=0}^{Z-1}\underline{\underline{E_z}}(y,z)\sin\left(\frac{\pi(y\Delta l+\Delta l/2)}{W}\right)}{(Y/2)Z}. \tag{9.15}$$

It is seen from Eqn.9.15, the S parameters for the dominant mode can be calculated from the TLM simulation as

$$\underline{S_{11}}=\frac{FFT\left(\sum_{y=0}^{Y-1}\sum_{z=0}^{Z-1}\underline{\underline{{}_kV_3^r}}(0,y,z)\sin\left[(y\Delta l+\Delta l/2)\pi/W\right]\right)}{FFT\left(\sum_{y=0}^{Y-1}\sum_{z=0}^{Z-1}\underline{\underline{{}_kV_3^i}}(0,y,z)\sin\left[(y\Delta l+\Delta l/2)\pi/W\right]\right)}=\frac{\underline{\underline{{}_k\hat{V}_3^r}}}{\underline{\underline{{}_k\hat{V}_3^i}}}, \tag{9.16a}$$

$$\underline{S_{21}}=\frac{FFT\left(\sum_{y=0}^{Y-1}\sum_{z=0}^{Z-1}\underline{\underline{{}_kV_{11}^r}}(X-1,y,z)\sin\left[(y\Delta l+\Delta l/2)\pi/W\right]\right)}{FFT\left(\sum_{y=0}^{Y-1}\sum_{z=0}^{Z-1}\underline{\underline{{}_kV_3^i}}(0,y,z)\sin\left[(y\Delta l+\Delta l/2)\pi/W\right]\right)}=\frac{\underline{\underline{{}_k\hat{V}_{11}^r}}}{\underline{\underline{{}_k\hat{V}_3^i}}}. \tag{9.16b}$$

The values for the passive circuit equivalence were taken as $L_1 = 2.8\,\text{nH}$ and $L_2 = 2.95\,\text{nH}$, which are known to be achievable in the TLM model [9.5]. The transmission-line formulation given in Chapter five for the 2D case is used to compute the desired S parameters which are then compared with the TLM S parameters and the difference vector is derived. From Eqn.9.3, the perturbed time-reversal-mirrors for the particular solution for ports 3 and 11 are

$$\begin{aligned} \underline{\underline{{}_{3,11}V_{TRM\,P}}}^{F}(y,z,k)' &= (\alpha)\,\underline{\underline{{}_{3,11}V_{TRM\,P}}}^{F}(y,z,k) + \\ &(1-\alpha)\left(\underline{\underline{{}_{3,11}V_{TRM\,P}}}^{F}(y,z,k) - \underline{\underline{\phi}}(y,z)\otimes|\,\underline{G_{3,11}}(k)\,|\right), \end{aligned} \tag{9.17}$$

where the modal distribution of the dominant mode is

$$\begin{aligned} \underline{\underline{\phi}}(y,z) &= \sin\left((y\Delta l + \Delta l/2)\frac{n\pi}{W}\right)\cos\left((z\Delta l + \Delta l/2)\frac{m\pi}{H}\right) \\ &= \sin\left((y\Delta l + \Delta l/2)\frac{\pi}{W}\right), \qquad n=1, m=0. \end{aligned} \tag{9.18}$$

Since the field is uniform in z, the Poynting vector can be measured on any plane (x,y) in z, in which case $z=0$ was chosen for simplicity. The reverse time-reversal-mirror from Eqn.9.4 now reads

$$\underline{\underline{{}_{3,11}V_{TRM}}}^{R}(y,z,k) = \underline{\underline{{}_{3,11}V_{TRM\,P}}}^{F}(y,z,k)' - \underline{\underline{{}_{3,11}V_{TRM\,H}}}^{F}(y,z,k)\,. \tag{9.19}$$

The waveguide parameters are $W = 22.86\,\text{mm}$, $L = 20.05\,\text{mm}$ and $H = 10.16\,\text{mm}$. The TLM parameters are $Y = 57$ giving $\Delta l = 0.4\,\text{mm}$, $\Delta t = 6.69e-13\,\text{s}$. $X = 50$, $Z = 25$ and $N = 16384$. The threshold and damping values were $T_1 = 0.87$, $T_2 = 0.7$ and $\alpha = 0.4$. The filter is optimised within the bandwidth $10-14\,\text{GHz}$.

The time-reversal design begins with initial septa widths of $W_{S1} = W_{S2} = \Delta l = 0.4\,\text{mm}$ each, the convergence of the time-reversal process using the scalar figure of merit is shown in Figure 9-4. In this case it is seen that the convergence is found after 5 time-reversal iterations, and results in septa widths of $W_{S1} = 2.4\,\text{mm}$ and $W_{S2} = 2.79\,\text{mm}$. This design takes 9.5 hours to optimise using a $2\,\text{GHz}$ AMD processor. The S parameters from iterations 1, 4 and 5 of the time-reversal design process are shown in Figure 9-5.

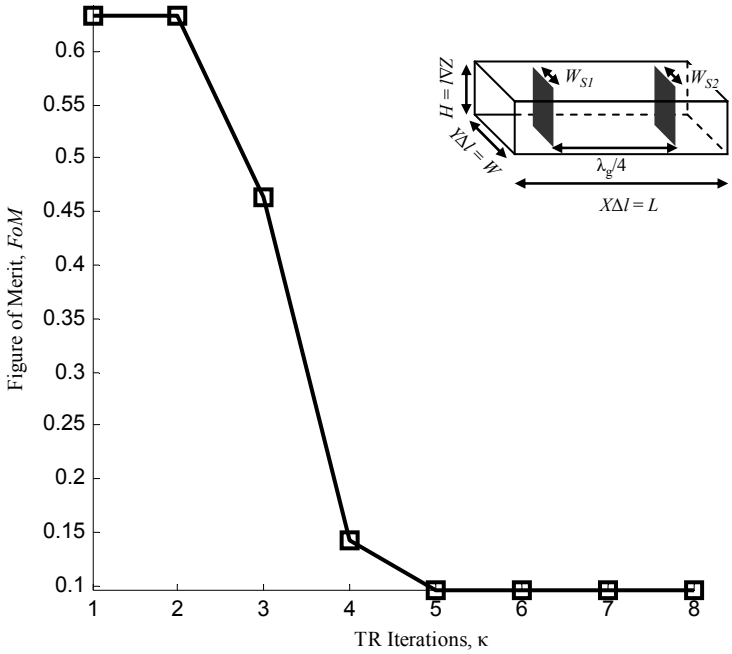

Figure 9-4 - Convergence of time-reversal design process of 3D 2nd order band pass filter, Δl = 0.4mm, Δt = 6.69e-13s, X = 50, Y = 57, Z = 25, L = 20.05mm, W = 22.86mm, H = 10.16mm and N = 16384. Optimised septa widths are W_{S1} = 2.4mm and W_{S2} = 2.79mm from initial configuration of $W_{S1} = W_{S2}$ = 0.4mm.

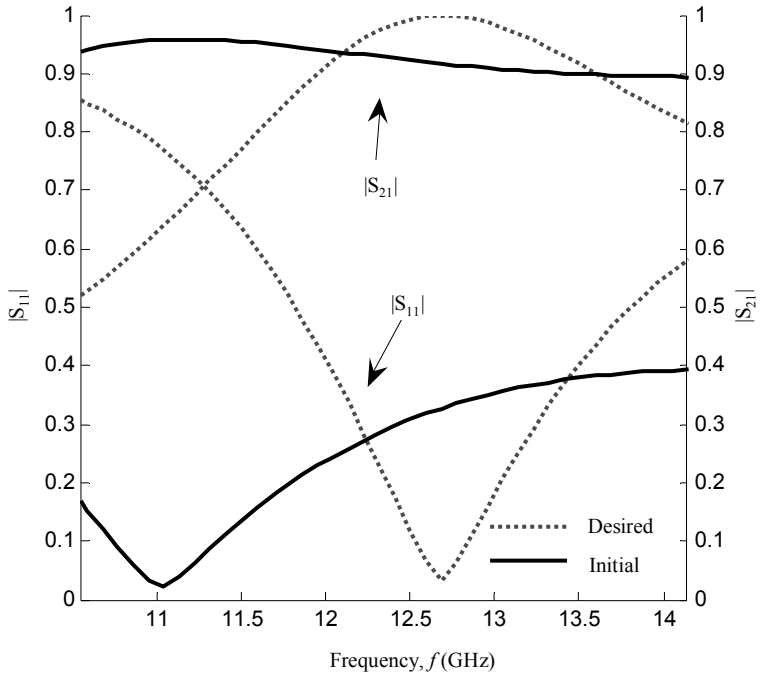
|S11|
|S21|
|S21|
|S11|
Desired
Initial
Frequency, f (GHz)

a)

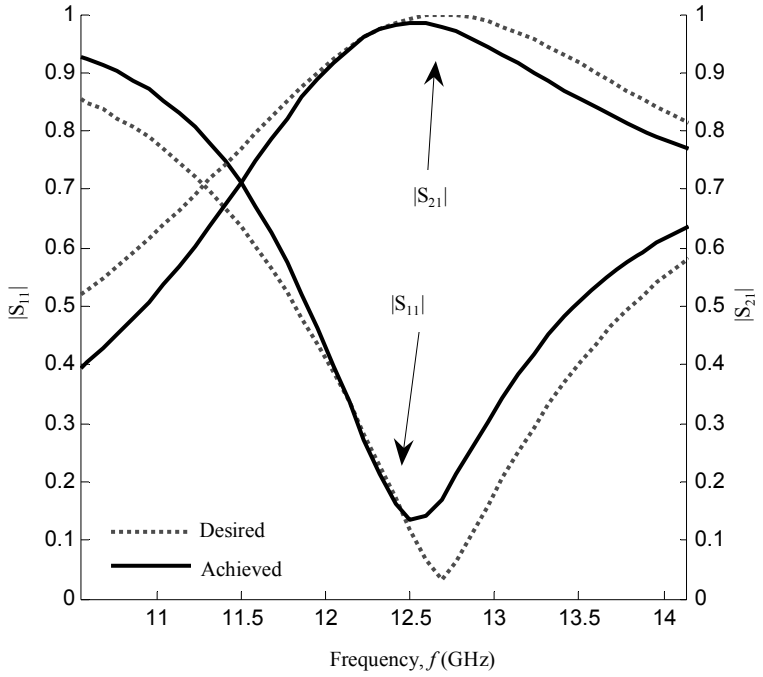
|S11|
|S21|
|S21|
|S11|
Desired
Achieved
Frequency, f (GHz)

b)

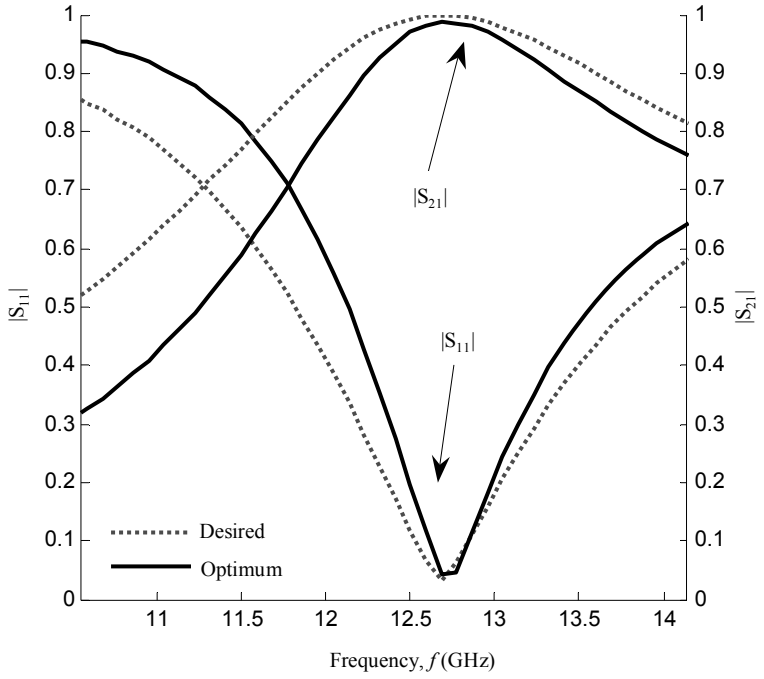

c)

Figure 9-5 - S parameters of 3D 2nd order microwave band pass filter optimised using time-reversal, a) initial configuration, b) iteration 4, c) final configuration found at iteration 5. Δl = 0.4mm, Δt = 6.69e-13s, X = 50, Y = 57, Z = 25, L = 20.05mm, W = 22.86mm, H = 10.16mm and N = 16384. Optimised septa widths are W_{S1} = 2.4mm and W_{S2} = 2.79mm.

9.3.2 Linear Dipole Antenna

This example serves to illustrate the application of the time-reversal design process to a radiating component in free-space, as apposed to the guided components designed so far.

A finite length linear dipole antenna is one of the simplest radiating structures in common use [9.6]. The radiating properties and design characteristics are already widely documented [9.6] [9.7] [9.8] and for these reasons, is an ideal candidate to investigate the use of the time-reversal design process with a radiating free space component.

A wire of length l, between nodes $(X/2-1, Y/2, z)$ and $(X/2, Y/2, z)$ is illustrated in Figure 9-6. The dipole will be optimised in the near field region,

$$k_0 r << 1 \tag{9.20}$$

where $k_0 = 2\pi/\lambda$ and r is the distance to the vertical time-reversal-mirrors.

In practical scenarios antenna systems are usually designed for use in the far field, however due to the need for eight time-reversal-mirrors in this case, it is not practical to increase the problem dimensions to the size necessary to reach the far field.

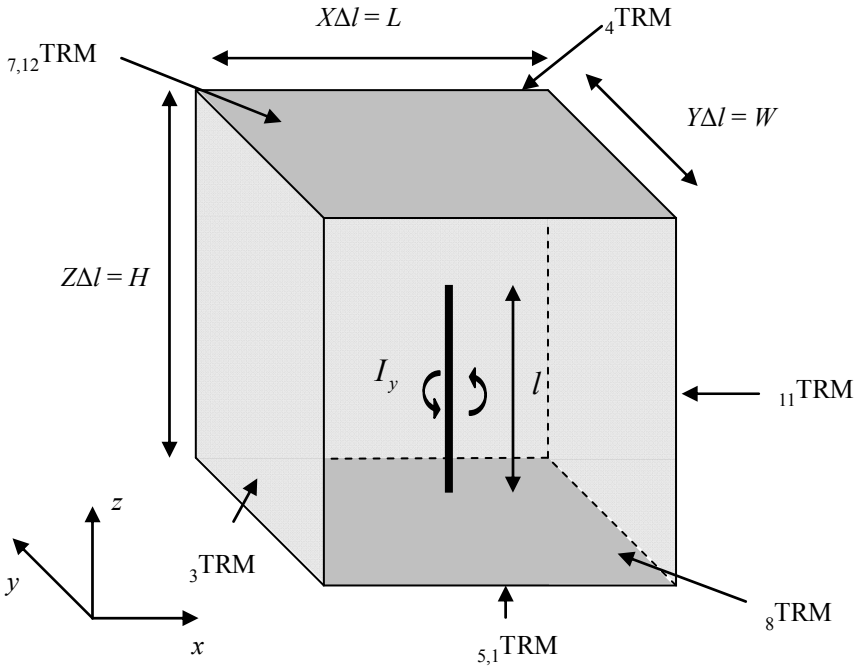

Figure 9-6 - Linear dipole antenna in free space, surrounded by eight time-reversal-mirrors, dark shading shows where two mirrors are needed. A current, I_y excites the dipole from nodes (X/2-1, Y/2, Z/2) and (X/2, Y/2, Z/2).

To excite a current in the wire, it is necessary to excite the relevant ports of the SCN bounding with the wire as,

$$\underline{\underline{V}}_{11}^{i}(X/2-1,Y/2,Z/2) = -\frac{\Delta l Z_0}{2}, \tag{9.21a}$$

$$\underline{\underline{V}}_{3}^{i}(X/2,Y/2,Z/2) = \frac{\Delta l Z_0}{2}, \tag{9.21b}$$

where the magnetic field in y between the nodes is given as [9.3]

$$H_y = \frac{-\underline{\underline{V}}_{11}^{i}(X/2-1,Y/2,Z/2) + \underline{\underline{V}}_{3}^{i}(X/2,Y/2,Z/2)}{\Delta l Z_0} = 1. \tag{9.22}$$

Similarly to the 2D shunt node described in Chapter three

$$I_y = H_y \Delta l, \tag{9.23}$$

and hence a current of amplitude Δl is excited in the wire. Since only the E_z field component is excited, only eight time-reversal-mirrors are required as shown in Figure 9-6, and are defined as

$$\underline{\underline{{}_3V_{TRM\,P}}}^{F}(y,z,k) = \underline{\underline{{}_kV_3^r}}(0,y,z), \tag{9.24a}$$

$$\underline{\underline{{}_4V_{TRM\,P}}}^{F}(x,z,k) = \underline{\underline{{}_kV_4^r}}(x,Y-1,z), \tag{9.24b}$$

$$\underline{\underline{{}_{11}V_{TRM\,P}}}^{F}(y,z,k) = \underline{\underline{{}_kV_{11}^r}}(X-1,y,z), \tag{9.24c}$$

$$\underline{\underline{{}_8V_{TRM\,P}}}^{F}(x,z,k) = \underline{\underline{{}_kV_8^r}}(x,0,z), \tag{9.24d}$$

$$\underline{\underline{{}_7V_{TRM\,P}}}^{F}(x,y,k) = \underline{\underline{{}_kV_7^r}}(x,y,Z-1), \tag{9.24e}$$

$$\underline{\underline{{}_{12}V_{TRM\,P}}}^{F}(x,y,k) = \underline{\underline{{}_kV_{12}^r}}(x,y,Z-1), \tag{9.24f}$$

$$\underline{\underline{{}_1V_{TRM\,P}}}^{F}(x,y,k) = \underline{\underline{{}_kV_1^r}}(x,y,0), \tag{9.24g}$$

$$\underline{\underline{{}_5V_{TRM\,P}}}^{F}(x,y,k) = \underline{\underline{{}_kV_5^r}}(x,y,0)\,. \tag{9.24h}$$

For simplicity and since the time-reversal-mirrors are within the near field, the beam pattern of the dipole is measured from $\underline{\underline{{}_3V_{TRM\,P}}}^{F}$ as

$$\begin{aligned}\underline{\underline{\hat{D}}}(z,f) &= FFT\left\{\frac{\underline{\underline{{}_3V_{TRM\,P}}}^{F}(Y/2,z,f)^2}{Z_0}\right\} \\ &= FFT\left\{\underline{\underline{{}_3V_{TRM\,P}}}^{F}(Y/2,z,f)^2\right\},\end{aligned} \tag{9.25}$$

where the desired frequency the dipole is to be optimised at is $1.95\,\text{GHz}$, and $Z_0 = 1$ in the normalised TLM.

In this case, the time-reversal design process is of primary interest, and so the desired beam pattern is first measured from a forward simulation with $l = \lambda$, using Eqn.9.25. In a practical scenario the desired beam pattern would be based upon some initial given criteria. The perturbation difference vector is

$$\underline{\underline{\hat{G}}} = \begin{cases}\underline{\underline{\hat{D}^d}}(z,f) - \underline{\underline{\hat{D}}}(z,f), & \text{if within bandwidth,} \\ 0, & \text{otherwise.}\end{cases} \tag{9.26}$$

Time-reversal at a single frequency does not always converge particularly well [9.9], for this reason the dipole is optimised within the bandwidth $1-10\,\text{GHz}$. This is a fairly large bandwidth, in comparison to the guided components designed so far. The time-reversal-mirrors upon walls 3, 4, 8 and 11 of the bounding computation space are perturbed as in Eqns.9.27a,b where $\underline{\underline{G}}$ is determined from the inverse Fourier transform of Eqn.9.26.

$$\underline{\underline{{}_{3,11}V_{TRM\,P}^{F}}}(y,z,k)' = (\alpha)\,\underline{\underline{{}_{3,11}V_{TRM\,P}^{F}}}(y,z,k) + (1-\alpha)\left(\underline{\underline{{}_{3,11}V_{TRM\,P}^{F}}}(y,z,k) - |\,\underline{\underline{G}}(z,k)\,|\right), \tag{9.27a}$$

$$\underline{\underline{{}_{4,8}V_{TRM\,P}^{F}}}(x,z,k)' = (\alpha)\,\underline{\underline{{}_{4,8}V_{TRM\,P}^{F}}}(x,z,k) + (1-\alpha)\left(\underline{\underline{{}_{4,8}V_{TRM\,P}^{F}}}(x,z,k) - |\,\underline{\underline{G}}(z,k)\,|\right). \tag{9.27b}$$

The homogenous solution is simulated with the wire removed and the time-reversal-mirror perturbation of Eqn.9.27 is applied with the corresponding Eqn.9.4 to determine the reverse mirrors.

The time-reversal-mirrors at the base and top of the simulation space remain unperturbed. The reverse simulation proceeds, identically to the guided 2D and 3D models, with the wire treated as the metal scatterer.

In the preceding chapters, the optimised scatterer enclosed one or more TLM nodes. In the case of the wire, the scatterer is placed between nodes. For this reason it is more accurate to measure the Poynting vector between nodes. The field components E_z and H_y between nodes are [9.3]

$$E_z = -\frac{\underline{\underline{V_{11}^{i}}}(x-1,y,z) + \underline{\underline{V_{3}^{i}}}(x,y,z)}{\Delta l}, \tag{9.28a}$$

$$H_y = \frac{-\underline{\underline{V_{11}^{i}}}(x-1,y,z) + \underline{\underline{V_{3}^{i}}}(x,y,z)}{\Delta l Z_0}, \tag{9.28b}$$

and

$$\vec{P} = \vec{E} \times \vec{H} = \begin{vmatrix} \vec{a}_x & \vec{a}_y & \vec{a}_z \\ 0 & 0 & E_z \\ 0 & H_y & 0 \end{vmatrix} = -\vec{a}_x E_z H_y . \tag{9.29}$$

The length of the dipole after time-reversal is measured from the absolute of the Poynting vector at $(X/2-1, Y/2, z)$. $H = 200\,\text{mm}$ and $L = W = 8\Delta l = 6.13\,\text{mm}$. The TLM parameters are $Z = 261$, giving $\Delta l = 0.77\,\text{mm}$ and $\Delta t = 1.28e-12\,\text{s}$. $X = 8$, $Y = 8$, and $N = 16384$. The dipole is excited as in Eqn.9.21, with the z coordinate at $(Z-1)/2$. The threshold and damping values are $T_1 = 0.025$, and $\alpha = 0.1$. The wire radius is $0.05\,\text{mm}$. In Figure 9-7a, the convergence of the time-reversal design process from an initial dipole length of $l = 151\Delta l = 115.71\,\text{mm}$ to a desired length of $154\,\text{mm}$ is shown, where the $3\,\text{dB}$ beam width is measured using Eqn.9.25 at $1.95\,\text{GHz}$. Theoretical analysis states the optimum $3\,\text{dB}$ beam width for a full wavelength dipole is approximately $48°$ [9.6], which verifies the time-reversal design result. In Figure 9-7b the initial beam pattern, and desired beam pattern are shown. Figure 9-7c shows the time-reversal convergence in terms of the wire length. This design takes approximately 7 hours to optimise using a $2\,\text{GHz}$ AMD processor.

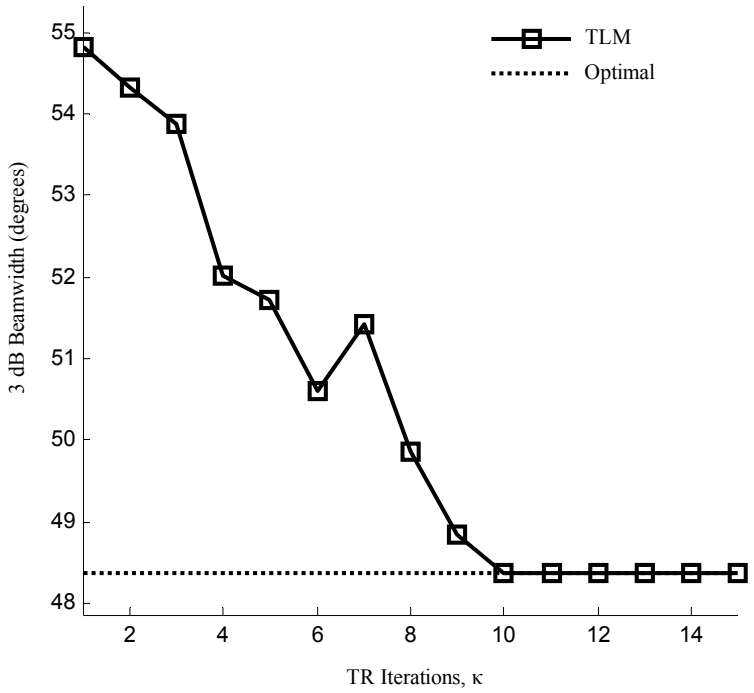

a)

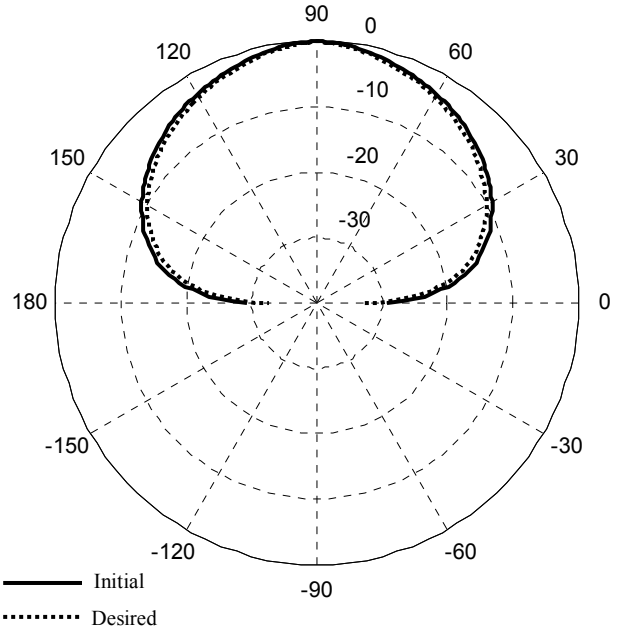

b)

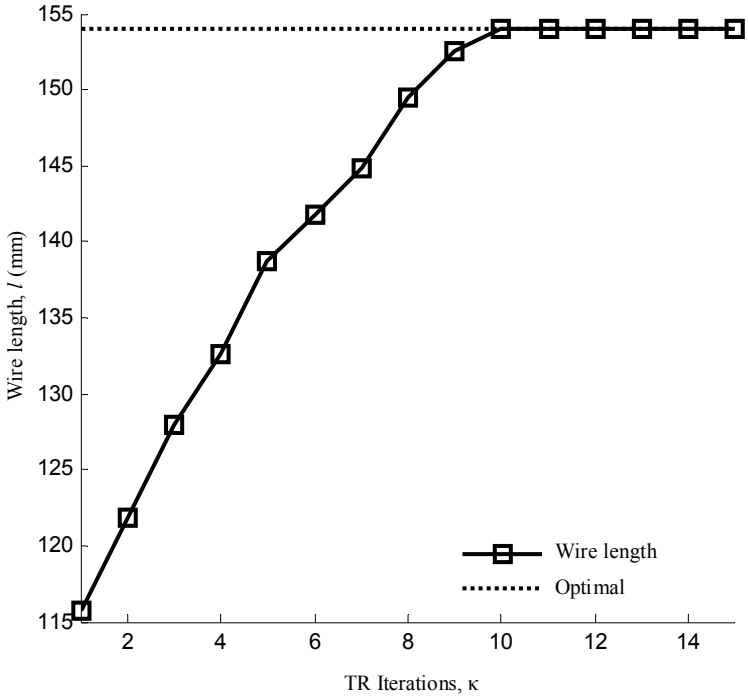

c)

Figure 9-7 - Convergence of 3D time-reversal design of linear dipole antenna optimisation. a) 3dB beam width with respect to time-reversal iteration, b) initial and desired beam patterns, c) wire length with respect to time-reversal iteration. Δl = 0.77mm, Δt = 1.28e-12s, X = 8, Y = 8, Z = 261, L = 6.13mm, W = 6.13mm, H = 200mm and N = 16384. The wire radius was 0.05mm.

The example has served to illustrate time-reversal for microwave component design is also applicable to radiating free space components.

9.4 Conclusion

This chapter has extended the time-reversal method to the optimisation of both guided and radiating 3D components. In both cases the time-reversal optimisation converges to the optimal solution. It is observed that fewer iterations were needed for the guided component (filter) in comparison to the dipole antenna design. 3D time-reversal may also benefit from internal-mirrors and the acceleration algorithms; however, this was not implemented due to time constraints. The following chapter concludes the thesis.

9.5 References

[9.1] A. J. Wlodarczyk and D. P. Johns, "New Wire Interface for Graded 3-D TLM," *Electronics Letters*, vol. 28, pp. 728–729, April 1992.

[9.2] P. Naylor and C. Christopoulos, "A New Wire Node for Modeling Thin Wires in Electromagnetic Field Problems Solved by Transmission Line Modeling," *IEEE Transactions on Microwave Theory and Techniques*, vol. 38, pp. 328–330, March 1990.

[9.3] C. Christopoulos, *The Transmission-line Modeling Method: TLM*. John Wiley & Sons/IEEE Publications, New York, NY, 1995.

[9.4] M. Khalladi, K. Bargach, and M. Essaaidi, "Efficient Modeling of Inclined Wire Structures Using the TLM Methods," *Microwave and Optical Technology Letters*, vol. 23, pp. 137–141, November 1999.

[9.5] R. E. Collin, *Foundations for Microwave Engineering*. John Wiley & Sons Inc, New York, NY, 2nd ed., 2001.

[9.6] C. A. Balanis, *Antenna Theory Analysis and Design*. John Wiley & Sons Inc, New York, NY, 2nd ed., 1997.

[9.7] C. A. Balanis, “Antenna Theory: A Review,” *Proceedings of the IEEE*, vol. 80, pp. 7–23, January 1992.

[9.8] P. Russer, *Electromagnetics, Microwave Circuit, and Antenna Design for Communications Engineering*. Artech House, Norwood, MA, 2nd ed., 2006.

[9.9] M. Forest and W. J. R. Hoefer, “A Novel Synthesis Technique for Conducting Scatterers Using TLM Time Reversal,” *IEEE Transactions on Microwave Theory and Techniques*, vol. 43, pp. 1371–1378, June 1995.

10. Conclusions

Research of electromagnetic component design methods that rely upon numerical simulation is of high importance due to the ever increasing need for automated design of complex components. This thesis began with a review of the time-reversal-cavity for time-reversal component design, and investigated problems inherent in the numerical implementation of the time-reversal algorithm. It was shown, using both analytical analysis and numerical computation, that a perfect numerical time-reversal model is not possible, due to the loss of evanescent information required for accurate reversal and the finite machine precision in the numerical scheme. Transmission-line modelling (TLM) was used, because of its inherent stability and electrical circuit equivalence which allowed for a simple derivation of the time-reversal-cavity, although it is expected that the same finite limitations will occur in all numerical schemes. The primary objective of this investigation was to prove the assumptions made for forward time models, for instance 'computation until steady state gives reasonable accuracy', do not necessarily hold for time-reversal due to the aforementioned limitations and as such it is necessary to understand the properties of time-reversal to successfully use the method.

The thesis demonstrated that it is necessary to ensure the field has been sufficiently sampled at the time-reversal-mirror before the forward phase is truncated. It was seen that, when the forward phase was heavily truncated,

the resolution of the time-reversal algorithm is impacted, hindering the characterisation of sources or scatterers.

Further, the effect of evanescent modal loss combined with the finite machine precision in lossless materials was shown to significantly impact the spatial resolution of the time-reversed source/scatterer. The successful development of internal-time-reversal-mirrors was shown to greatly improve the application of the time-reversal-cavity when used for component design and optimisation. As a result of this work, a higher order microwave band-pass filter, that was previously not possible to design using the traditional time-reversal-cavity, was successfully optimised with the addition of the internal-time-reversal-mirrors. The problem of conductive loss was briefly examined and it was shown that the performance of lossy materials with time-reversal is predictable.

The time-reversal-cavity approach to component design is heavily resource and time intensive. The memory requirement of the method was also seen as a limiting factor in the early work of Forest and Hoefer [10.1]. The thesis proposed to limit the memory of the time-reversal-cavity, through a selection of novel techniques. Linear interpolation, both spatial and temporal, was shown to be suitable for low interpolation values, typically saving around 10% of the memory, although the method is applicable to any component structure. If the modal content of the component is known, the memory requirements of the time-reversal-cavity can be reduced by only storing those modes known to exist, and resulted in memory reductions of 15 – 37%.

The derivation of linear acceleration methods for use with time-reversal to accelerate the convergence of the design procedure was demonstrated in Chapter seven. Stationary point successive over relaxation was shown as the simplest implementation, requiring only a single additional variable for application to time-reversal. The method resulted in considerable

computational reduction for all test cases of around 18 – 25 %. Further, non-stationary or Krylov subspace linear solvers, in particular conjugate gradients (CG) and generalised minimal residual (GMRES) were shown to be suitable for time-reversal, and their application to the example case studies resulted in convergence acceleration of around 27 – 55 %. Overall it was seen the CG method gave the most improved acceleration for the simple 2D sample demonstrations, although with more complex components, for example the third order filter, the GMRES solver performs better as expected and achieves convergence with a reduction of 42 %, or 5.5 hours on the 2 GHz processor.

The research focused mainly upon the 2D time-reversal-cavity. The bend was the easiest to design using time-reversal, since only a single variable, the post displacement, was optimised. This also allowed the analysis of the effect the starting position has on the convergence of the time-reversal design process.

In Chapter five, the spatial sampling of the numerical scheme used for the time-reversal implementation was shown to impact the design convergence. For the example of the directional coupler, a coarser spatial sampling was seen to cause oscillation at convergence. The oscillation was removed by increasing the spatial sampling.

In Chapter nine the 3D form of the time-reversal-cavity for use with the TLM method was derived, and its application to a waveguide filter, and dipole antenna optimisation was shown. In particular, the application of the time-reversal-cavity to the dipole antenna was shown to demonstrate the design of a radiating component in free space using the time-reversal-cavity.

10.1 Future Research

The primary investigation of the thesis was the accurate analysis of time-reversal methods when used at electromagnetic frequencies, and in

particular, development of the method for use as a component design and optimisation algorithm. In the process of achieving these goals, the case studies selected used lossless, linear, isotropic materials, to minimise the complexity and focus upon the properties of the time-reversal process. However, many microwave applications incorporate dielectric materials. In [10.2] imaging using time-reversal and dielectric materials was demonstrated.

The design of components with dielectric scatterers is more complex. The process of Chapter five is equally applied to determine the dimensions of a scatterer, however further investigation should be completed as to accurately calculate the dielectric permittivity of the material using time-reversal. Similarly further investigation of lossy materials is needed to determine their practicality for numerical time-reversal due to the instability created.

Scalability of the method from 2D to 3D was successfully demonstrated in Chapter nine. The acceleration and internal mirrors for 2D components should perform equally for 3D. A parallel implementation of the time-reversal algorithm would greatly accelerate the runtime. This could be done simply by parallelising the TLM nodes.

The time-reversal component design procedure is a valuable development tool, often leading to non-intuitive component configurations. With the improvements developed in the thesis, the method is more suited for use as an automated design procedure for complex electromagnetic components.

10.2 References

[10.1] M. Forest and W. J. R. Hoefer, “A Novel Synthesis Technique for Conducting Scatterers Using TLM Time Reversal,” *IEEE Transactions on Microwave Theory and Techniques*, vol. 43, pp. 1371–1378, June 1995.

[10.2] P. Kosmas and C. M. Rappaport, “Time Reversal With the FDTD Method for Microwave Breast Cancer Detection,” *IEEE Transactions on Microwave Theory and Techniques*, vol. 53, pp. 2317–2323, July 2005.